Acoustical Physics, Vol. 46, No. 3, 2000, pp. 243–248. Translated from Akusticheskiĭ Zhurnal, Vol. 46, No. 3, 2000, pp. 293–298.

Motion of Bodies under Vibration in Granular Media

V. N. Alekseev, A. N. Gromov, Yu. I. Gromov, A. T. Ovcharenko, and S. A. Rybak

Andreev Acoustics Institute, Russian Academy of Sciences, ul. Shvernika 4, Moscow, 117036 Russia

Received October 29, 1998

Abstract—Results obtained from experimental studies of the motion of solid bodies through a granular medium under a time-varying load are presented. Dependences of the average velocity of a body on the driving frequency are obtained, and the resonance behavior of these dependences is observed. It is established that the experimental value of the resonance frequency has a universal meaning and is fundamentally and closely related to the structure of the granular material. The structural features of a granular medium are qualitatively described, along with the correlation between them and the result of the study. © *2000 MAIK "Nauka/Interperiodica".*

Granular media, or loose granular materials, are widespread in nature and industry. They possess some specific properties that make them different from other bodies existing in the solid and liquid states. Because of the widespread occurrence and wide practical application of granular materials, studies of their properties and behavior under static and dynamic loads have been carried out for years and continue to this day [1–3]. These studies include both purely theoretical investigations and experiments. Many technological processes used in industry and construction are related to the motion of loose granular materials and the motion of solid bodies in granular media under vibrations. To increase the efficiency of such processes, it is necessary to know the structure of the granular materials and the mechanism of their interaction with solids. In this connection, the studies of such phenomena as the intergranular interactions, the friction forces, and the dissipation processes that occur in a granular medium and at the boundary between the medium and other bodies become especially important. In the last decade, the theory of friction has experienced a kind of rebirth: the most exciting results were obtained in the studies of the dynamics of the relative stick-slip motion of two pure crystalline surfaces separated by a thin liquid layer (a few molecules thick) [4–9]. In fact, some of the laws derived for this type of motion are universal in nature and are also valid for granular media. In this paper, we present the results of the experiments aimed at studying the specific features of the motion of solid bodies through granular media under time-varying forces. Although the work was initially of purely practical interest, some of the dependences obtained in the experiments seem to be closely related to the fundamental laws of particle interaction and are in conformity with the universal laws discovered in other fields of science and engineering.

In our experiments, the solid body moving through a granular medium was an empty metal cylinder with the outer diameter 2.5 cm and length 10 cm. To reduce the head resistance, conical surfaces were mounted at the cylinder ends; the cones were 2 cm high and had the same radius as the cylinder. The total length of the sample was about 14 cm, and its total mass varied from 400 to 500 g. The sample was set in a vertical position and completely buried in the granular medium. The linear dimensions of grains varied over wide limits: from fractions of a millimeter to several centimeters. We used different kinds of granular media: sand commonly used in construction (dry and wet sand), gravel, silica gel, and fine-disperse and granular carbon black. The cylinder was fastened to one end of an inextensible thread (or string) passing over a fixed block that was positioned above the surface of the granular material. The other end of the thread was fastened to a load whose mass was approximately equal to the cylinder mass. When the two masses were exactly equal to each other and both the cylinder and the counterbalance were in the air, the whole system was at rest. The equilibrium was not disturbed when the cylinder was preliminarily placed in the granular medium. This was true even in the case of a considerable difference between the masses of the cylinder and the counterbalance. Naturally, equilibrium was possible only when the static friction force arising in the granular material exceeded the difference between the weights of the sample and the load.

Longitudinal vibrations were excited in the cylinder. The excitation was performed by an eccentric mechanism, which consisted of a series of pins set normally to the surface of a rotating disk at some distance from its center. The pins deflected the thread thus jerking the cylinder and the counterbalance upward (the thread was fairly long). The disk was fixed at the shaft of an

1063-7710/00/4603-0243$20.00

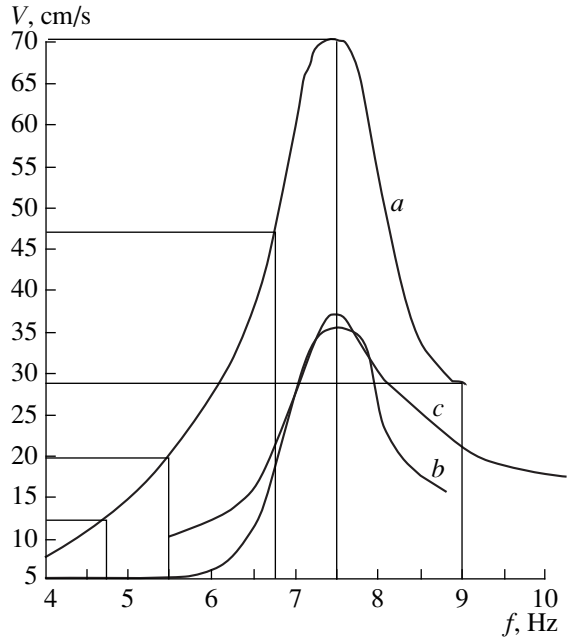

Fig. 1. Dependence of the velocity of the cylinder rise on the vibration frequency.

electric motor whose rotational speed was measured by a tachometer and could be varied over relatively wide limits. With the selected geometric parameters of the system (the thread length, the distance from it to the rotating pins, and the distance from the latter to the shaft center), the vibration amplitude of the load and the cylinder that were in balance in air varied from millimeters to several centimeters. As the cylinder was buried in the granular material, the initial symmetry of the body vibrations and the counterbalance ones was violated. The cylinder moved upward with jerks and finally emerged at the free surface of the granular material. The appearance of an upward motion of the sample should not seem unexpected, if one takes into account that in some sense it corresponds to the common downward motion observed in driving piles or other objects into the ground. In both cases, the necessary condition is that the external force applied to the body be greater than the friction force arising at the boundary between the body and the granular material.

The cylinder motion caused by the excitation of the thread vibrations was an intermittent-translational one. In fact, a vibrational force was applied to the body, and an unexpected effect for this kind of motion was the appearance of a minimum in the dependence of the time within which the body rose to the surface on the vibration frequency. As an example, in Fig. 1 we present a set of such dependences observed for different granular media: *a* sand, *b* silica gel, and *c* carbon black. The abscissa axis represents the frequency *f* characterizing the upward jerks applied to the cylinder, and the ordinate axis represents the average velocity *V* of the upward motion of the body, this velocity being inversely proportional to the time of the body rise. From the dependences, one can see that the frequency f_0 corresponding to the maximum average velocity is virtually the same for different granular media, and it is equal to 7.5 Hz. We will call it resonance frequency. For the materials under study, the linear dimensions of grains varied over more than one order of magnitude. For gravel, the resonance frequency was only 10% less than for carbon black, while the difference in the grain size of these materials was almost two orders of magnitude. Our experiments showed that noticeable variations in a number of geometric parameters of the system caused only minor variations in the resonance frequency. In particular, we studied the effect of the natural frequency of the thread carrying the load on the sought-for resonance frequency. It was found that, as the thread length was changed by a factor of two, the frequency varied by no more than 10%. The results of these measurements are illustrated in Fig. 2. This figure displays two curves obtained for sand: the dashed line corresponds to the thread length $L = 39$ cm, and the solid line corresponds to $L = 70.5$ cm.

The increase in the average velocity of the cylinder rise with frequency is natural and can be easily explained, if we assume that, with every jerk, the cylinder travels approximately the same distance. In the case of a strict equality, we should have a strictly linear dependence of the average velocity of the body rise on the vibration frequency. From Figs. 1 and 2, one can see that such a linear dependence is observed in the vicinity of the resonance frequency f_0, to the left of it. From the behavior of the curves *a* and *c* shown in Fig. 1, it follows that this linearity is most clearly defined for sand and carbon black. As for the nonlinear and slower decrease of the velocity with decreasing frequency, this phenomenon is closely related to the specific features of the load dynamics. Presumably, this can be explained by the specific way that the driving force is applied to the body under study and, in particular, by the lower acceleration experienced by the body. The decrease in the average velocity of the body rise that occurs with a considerable increase in the frequency of the driving force is likely to be related to the plastic properties of granular media and the finite time of the disruption of the microstructure of a granular material. The appearance of the maximum in the frequency dependence of the average velocity and the existence of the corresponding resonance frequency f_0, which varies only slightly from one experiment to another and with variations in different parameters, testify to the fundamental nature of the observed phenomenon and its relation to the structure of the granular material. We note that (as will be demonstrated below) the frequency f_0 and the corresponding period $\tau \approx 1/f_0$ are of the same order of magnitude as some characteristic values determined in other publications [7, 8, 11], and the phenomena under study are related not only to granular media, but also to entirely different systems.

Since there exists no rigorous theory for describing the behavior of a granular medium under dynamic and large static loads, we can neither rigorously justify the aforementioned statements nor obtain any adequate quantitative estimate for the quantity f_0 in this paper. However, proceeding from the existing concepts of the granular material structure, we will make an attempt to relate the measured value of the resonance frequency to some fundamental parameters of the granular material structure by using the data from other publications. It is well known that, in many cases, a granular material resembles a solid, and, formally, its behavior may be described to a first approximation by the equations valid for an elastic body. However, under large static loads, as well as under moderate forces acting within long time intervals, the behavior of a granular material becomes similar to that of a liquid, and it can be described on the basis of the hydrodynamical equations. For example, the model calculations in the constructional mechanics of granular materials are often made by using an equation analogous to the Navier–Stokes one with the stress tensor T_{ik} in the form [4]

$$T_{ik} = \sigma\left[\delta_{ik} + k\frac{V_{ik}}{|V|}\right], \text{ where } V_{ik} = \frac{\partial v_i}{\partial x_k} + \frac{\partial v_k}{\partial x_i}.$$

Here, σ and k are constants depending on the properties of the material. In this equation, the viscous term, which is proportional to the viscosity and the velocity gradient in the Navier–Stokes equation, is replaced by a term that is independent of the rate of shear. This fact expresses one of the fundamental properties of granular media: the stresses are independent of the velocities. The essential feature of the equation presented above is that the tensor V_{ik} is divided by $|V|$, so that the stress tensor does not depend on the absolute value of the velocity. Sometimes, in the mathematical description of a granular medium as an elastic body with allowance for its rheological and viscoelastic properties, the Hooke law is replaced by a more general equation relating the strain and the stress. In the case of strong vibrations and very large dynamic loads, when the value of the vibration overload parameter $\Gamma = A\omega^2/g$ (where g is the acceleration of gravity and A is some constant) is great, a granular material begins to "boil." In this case, the corresponding processes can be formally described by the gas dynamics equations and even with the use of the Boltzmann kinetic equation [10].

It should be noted that, in many cases, one of the most important properties of a granular material is its plasticity. This is the main property that distinguishes the granular material from classical solids, and it is a consequence of the very structure of the material. The plasticity of a granular medium fundamentally differs from the plasticity of solids. Recall that the particles (molecules) of a classical condensed matter are bound together by strong and mainly central forces. Therefore, in a solid, a crystal lattice is formed, and the plasticity of a solid is related to the lattice defects and the formation of, e.g., dislocations. In a granular material, the particles have macroscopic dimensions (as compared to the quantum dimensions), and their interaction is largely determined by transverse shearing forces and, specifically, friction forces. The characteristic feature of these forces manifests itself in the fact that any particle of the granular medium interacts with the surrounding particles in a highly nonuniform way. The force of the interaction with the closest neighbors may vary by an order of magnitude from one neighbor to another. As a result, in a granular material, although it looks very much like a solid, no crystal lattice can be formed. On the other hand, in contrast to a liquid whose structure possesses a short-range order, a granular medium develops a structure that is intermediate between liquid and fractal ones [11]. In fact, this leads to the formation of the so-called "chains," i.e., one-dimensional branching irregular structures, which penetrate the whole granular material and have linear dimensions much greater than those of individual grains. Along these chains, the stresses are transmitted with the values exceeding the average forces by an order of magnitude, and the existence of such chains is confirmed by the experiments [4, 11, 12]. In particular, the presence of a fully-developed chain-like structure in a granular material accounts for the well-known experimental fact consisting in the absence of the linear dependence of pressure on the thickness of the granular material [4]. This phenomenon is observed in tanks with granular materials beginning from a certain depth, and it can be easily explained by the transmission of the

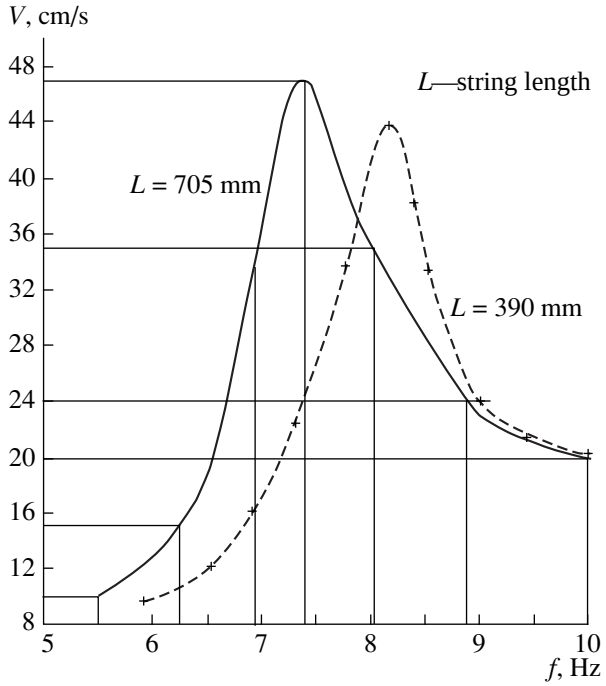

Fig. 2. Dependence of the velocity of the cylinder rise on the vibration frequency for different string lengths.

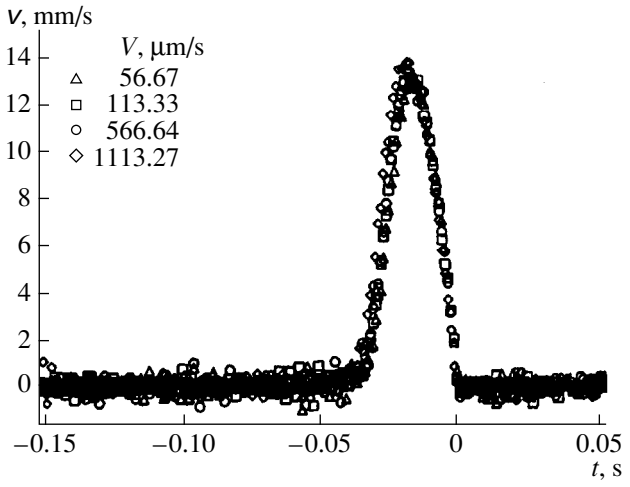

Fig. 3. Dependence of the instantaneous velocity of the plate *V* on time.

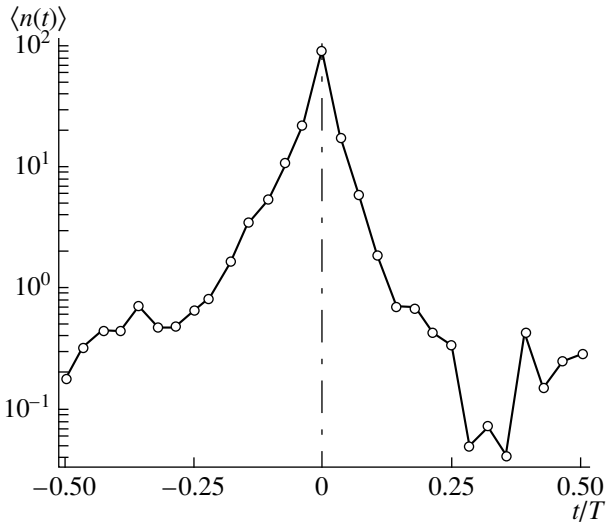

Fig. 4. Dependence of the average number of the displaced particles $\langle n \rangle$ on time.

weight of the upper layers of the material to the tank walls through the chain structures.

The application of external stresses to a granular material gives rise to internal stresses in this material with some average internal stress value. The aforementioned formal description of the material behavior is usually performed on the basis of these average values. However, in contrast to the classical condensed matter, a granular material is characterized by large stress fluctuations, which occur because of the formation of the chain-like structure. Their spatial frequency is anomalously high as compared to that of the fluctuations of internal forces in conventional bodies, while the stresses themselves exceed the average values by an order of magnitude [11]. The characteristic feature of the plasticity of a granular material is the gradual disruption of its irregular and chain-like structures under a load. In this process, the chain-like structure is likely to be responsible for the existence of a finite, and to some extent universal, value of the time of disruption.

The behavior of the friction force acting on bodies moving in granular materials has been studied in numerous experiments. For example, in some of them [7, 8], a flat plate was pulled along a horizontal layer of a granular material. The dependence of the friction force on the velocity was found to be ambiguous, with a hysteresis. A detailed study of the plate motion in time showed that, in a wide range of parameter variations, this motion was an intermittent-translational one. At low values of the average plate velocity *V*, the plate motion consisted of two phases, namely, the stick and slip phases, and it was purely regular in character. At the beginning, as the external force applied to the body increased from zero to the value of the static friction force, the body remained at rest; then, it was rapidly accelerated. After the beginning of the motion, the friction force decreased, and, as the shear stresses in the granular medium reached sufficiently small values, the body came to a stop. Within some interval of time, the process was repeated. When the average velocity was increased, the motion of the body became different: the length of every single plate displacement decreased, but the motion itself was no longer purely deterministic or stochastic. With a further increase in the velocity *V*, the displacements corresponding to individual jerks became still shorter, but the motion became more regular in character. As the velocity *V* exceeded some critical value, the plate motion, which initially was an intermittent and jump-like one, became totally irregular, but continuous.

The experiments described above included simultaneous measurements of the variation of the instantaneous velocity v of the body in the process of individual displacements. Figure 3 shows a set of such experimental dependences that were obtained for different values of the average velocity *V*. One can see that the maximum instantaneous velocity, which was about 1 cm/s in order of magnitude, was reached in the course of an individual jerk within the time $T \approx 40$–50 ms. This time was virtually independent of the average velocity *V* of the body in a wide range of its variation. The most remarkable fact was that the total time *T* of a single body slip was of the same order of magnitude as the characteristic period τ (the inverse of the resonance frequency f_0) determined in our experiment and presented at the beginning of this paper.

The aforementioned experiment [7] also included an optical visualization of the changes in the positions of individual grains of the granular material in the course of a single plate slip. Figure 4 taken from the cited paper [7] shows the experimental time dependence of the average number $\langle n \rangle$ of grains that changed their position within 4 mm^2 of the granular material surface contacting the body. The dependence $\langle n(t) \rangle$ is

presented on the logarithmic scale, and time is expressed in fractions of the slip period T. From this figure, it follows that, with an increase in stresses in the granular material, the number of particles changing their positions, $\langle n(t)\rangle$, substantially increases. The curve is asymmetric, and the number $\langle n(t)\rangle$ reaches its maximum at the slip stage. Here, it should be emphasized that the structural rearrangement of the medium begins before the slip onset.

Thus, from the experiments performed by Nasuno *et al.* [7], we derive two important conclusions: (1) from some critical value of the velocity V, the intermittent-translational motion of the body becomes continuous, but irregular; in a wide range of the velocity V variation, the motion possesses a characteristic time T whose value is virtually constant and related to the fundamental properties of the granular material; (2) within the time T, a structural rearrangement occurs in the granular material contacting with the body. Returning to our experiment, we can state that these two consequences provide a plausible explanation for the appearance of the maximum in the dependence $V(f)$ and for the existence of a nearly constant value of the resonance frequency f_0. In our opinion, the decrease observed in the velocity V at higher frequencies (Fig. 1) is explained by the fact that, as the average velocity of the cylinder moving through the granular medium increases, the spatial rearrangement of the material structure does not have enough time to occur during the jerks, and, therefore, the body cannot move through the material. The approximate (within an order of magnitude) coincidence of the values of T and $1/f_0$ and their relative constancy testifies to the universal character of the laws governing the rearrangement of the granular material structure. As for the certain numerical difference between the values obtained in our experiments and in the cited experiments [7], it can be explained by the specific features of the structural rearrangement that occurs in the granular material layer contacting the body. In contrast to the experiments [7] in which the body moved along the surface of the granular material, in our experiments the body moved through the granular medium and additionally experienced a head resistance. Therefore, to the time of the structural rearrangement of the granular medium in the vicinity of the lateral surface of the body, it is necessary to add the time of the particle transfer from the region in front of the body. The actual increase in the time of the structural rearrangement of the granular material in the vicinity of the moving body leads to a decrease in frequency. In our experiments, the time of disruption of the initial structure is almost by a factor of three greater than in the cited experiment [7]. We note that an increase in the region of the disruption of the material structure should inevitably lead to a decrease in the resonance frequency. It is precisely this effect that is observed when the vibrations of the body (both longitudinal and transverse ones) are amplified as the thread fixed to the cylinder is shortened. This effect is reflected in the behavior of the curves in Fig. 2.

In closing, we note once again the fundamental and to some extent universal character of the result obtained in this paper. The relation between the resonance frequency and the time of the disruption of the granular material structure is a general property not limited to granular media. A similar result is obtained for the relative stick-slip motion of two pure crystalline plates separated by a liquid layer several molecules thick [9]. It was found that the motion of these plates relative to each other is similar to the motion of a body in a granular medium and occurs much in the same way as described in this paper. Despite the difference in the nature of the materials and the great difference in the particle dimensions (the dimensions of molecules and grains differ by more than six orders of magnitude), not only a qualitative analogy takes place, but also a quantitative coincidence of the characteristic values. For low velocities of the plate slip, the plate motion is also a jump-like intermittent-translational one. In this case, it occurs in the form of a stick-slip motion, as in the case of a granular medium. At higher velocities, the plate motion becomes continuous, but irregular. The most remarkable fact is that the values of the critical velocity and the time of slip (fluctuation) T coincide in order of magnitude with the corresponding values obtained for granular materials. According to Thompson and Robins [9], in this case the slip mechanism is related to the thermodynamic instability of the lubricant and its jump-like transition from solid to liquid state. (Recall that when the lubricant is several molecular layers thick, its structure forms a crystal lattice that adjusts itself to the plate structure.) The phase transition in the lubricant layer plays the role of the structural rearrangement that occurs in a granular medium. Within the same time interval T, the crystal lattice of the molecular layers of the lubricant is destroyed, and the structural rearrangement of the substance leads to its transformation to a liquid.

It is well known that a unique but nonmonotone dependence of the friction force on the velocity of the contacting surfaces $F(v)$ leads to a periodic stick-slip motion for conventional bodies as well. In this case, one can hear the typical creak accompanying the velocity oscillations between zero and the value at which the derivative dF/dv becomes positive. A detailed study of the laws governing the friction between conventional bodies [6] shows that, in this case, the appearance of resonance frequencies is also possible for the bodies under a vibrational excitation. The imposition of the resonance frequency vibrations on the bodies slipping relative to each other makes it possible to increase the amplitude of the motion and to intensify the processes of cutting and penetration of one body into another. In this connection, numerous possibilities open up for the use of vibrations in science, engineering, and medicine. Specific examples of such applications can be found in the monograph written by Blekhman [5].

REFERENCES

1. *Disorder and Granular Media*, Ed. by D. Bideau and A. Hansen (North-Holland, Amsterdam, 1993).
2. G. K. Kleĭn, *Structural Mechanics of Loose Granular Bodies* (Stroĭizdat, Moscow, 1977).
3. *Granular Matter*, Ed. by A. Metha (Springer, Berlin, 1993).
4. H. M. Jaeger, S. R. Nagel, and R. P. Behringer, Phys. Today **49** (4), 32 (1996).
5. I. I. Blekhman, *Vibrational Mechanics* (Moscow, 1994).
6. *Vibrations in Engineering: Handbook* (Mashinostroenie, Moscow, 1978–1981), Vols. 1–6.
7. S. Nasuno, A. Kudrolli, and J. Gollub, Phys. Rev. Lett. **79**, 949 (1997).
8. G. B. Lubkin, Phys. Today **50** (9), 17 (1997).
9. P. A. Thompson and M. O. Robbins, Science **250**, 792 (1990).
10. Kh. I. Raskin, Dokl. Akad. Nauk SSSR **220**, 54 (1975).
11. C.-H. Liu, S. R. Nagel, D. A. Schecter, *et al.*, Science **269**, 513 (1995).
12. C. S. Campbell, Ann. Rev. Fluid Mech. **22**, 57 (1990).

Translated by E.M. Golyamina

Acoustical Physics, Vol. 46, No. 3, 2000, pp. 249–255. Translated from Akusticheskiĭ Zhurnal, Vol. 46, No. 3, 2000, pp. 299–305.

Nonlinear Equations for Quasi-Monochromatic Waves near a Caustic in a Dispersive Dissipative Medium with Cubic or Quadratic Nonlinearity

A. G. Bagdoev* and S. G. Saakyan**

** Institute of Mechanics, National Academy of Sciences of Armenia, pr. Marshala Bagramyana 24b, Yerevan, 375019 Armenia*

*** Yerevan Architecture-Construction Institute, ul. Teryana 105, Yerevan, 375009 Armenia*

e-mail: mechins@sci.am

Received March 11, 1999

Abstract—The behavior of a quasi-monochromatic nonlinear wave near a caustic is considered. Nonlinear ordinary differential equations for a dispersive dissipative medium with a cubic or quadratic nonlinearity are derived. For the latter medium, nonstationary equations describing it near the caustic are presented with allowance for the dissipative dispersive terms. These equations yield ordinary ones for quasi-monochromatic waves. The amplitude of the second harmonic is expressed in terms of the squared amplitude of the first harmonic. The amplitude of the second harmonic, as well as the solution as a whole, increases near the caustic. *© 2000 MAIK "Nauka/Interperiodica".*

INTRODUCTION

A linear solution to the wave equations with a variable sound (light) velocity for a monochromatic wave near a caustic was obtained by several authors [1–4]. Kravtsov [2] and Ludwig [4] found a uniformly exact solution in the form of a sum containing the Airy function and its derivative.

Bagdoev [1] and Gazaryan [3] found a solution to the problem of the incidence of a given wave on a caustic in the form of only one term containing the Airy function, i.e., a local asymptotics was found.

This asymptotics is associated with the fact that the factor of the derivative of the Airy function in the uniformly exact asymptotics, which is equal to the difference between the incident and reflected wave amplitudes at the caustic, is set equal to zero in the problems solved in [3, 1].

Since the order of magnitude of the linear solution near the high-frequency caustic is higher than that away from it, it is necessary in this specific region to allow for the nonlinear effects that, for a quasi-monochromatic wave, exhibit themselves in the form of a cubic or quadratic nonlinearity smoothed by low dissipation and dispersion present in the medium. In this case, in order to obtain a realistic picture of nonlinear wave fields near the caustic, one should take into account the second harmonic.

Paper [1] formulated the nonlinear problem for the quasi-monochromatic wave near a caustic by imposing the boundary conditions, which were derived from the linear solution expressed in terms of the Airy function, at a certain distance from it. The problem was reduced to an integral equation by the perturbation method and solved numerically.

In this paper, equations are derived for the quasi-monochromatic wave near a caustic in a dissipative dispersive medium with a cubic or quadratic nonlinearity.

Unlike the case of the medium with a cubic nonlinearity considered in [1], where dissipation was taken into account, here, we obtain a system of two equations for real amplitudes, which can be solved similarly to that in [1]. In contrast to the solution away from the caustic, the numerical solution near the caustic shows a substantial increase in the wave amplitude due to the nonlinearity. This solution is valid near the regular points of the caustic, i.e., at a distance from its cusp, where the problem should be studied separately.

Note that the numerical analysis of acoustic beam focusing away from the caustic on the basis of solving short-wave equations is considered in [8]. A two-wave solution for nonlinear waves near the caustic can be obtained by relying on the results provided in [9]. The parabolic-approximation method for solving the problems of acoustic wave propagation is developed in [10]. The acoustic wave attenuation and dispersion in a gas–liquid mixture are studied in [11]. A step-by-step approach to analyzing intense diffraction beams by matching the linear and nonlinear regions is given in [12].

1063-7710/00/4603-0249$20.00 © 2000 MAIK "Nauka/Interperiodica"

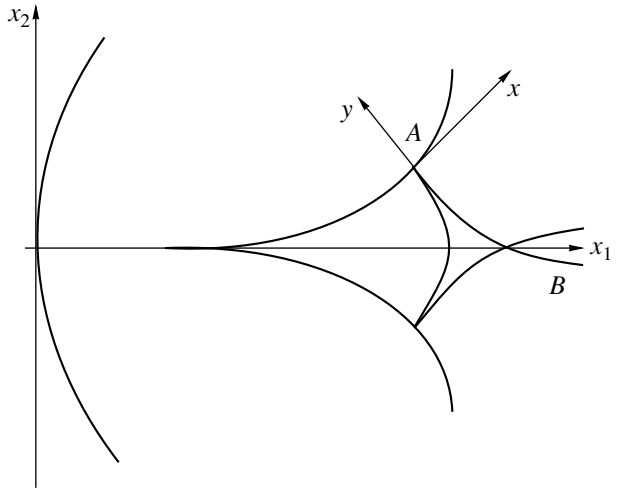

Wave behavior near the caustic.

LINEAR SOLUTION AND DERIVATION OF THE DIFFERENTIAL EQUATION FOR A MEDIUM WITH A CUBIC NONLINEARITY

Consider a quasi-monochromatic wave propagating in a dispersive dissipative medium with a cubic or quadratic nonlinearity. In the linear case, when the wave is concave or the medium is inhomogeneous, the rays have an envelope (or a caustic) at which the incident and reflected waves exist at a time moment t (figure). These waves intersect the caustic at the point A with the position vector $\mathbf{r}^0 = \mathbf{r}^0(t)$. The inspection of the linear solution to an arbitrary hyperbolic system of equations with variable coefficients [1, 2] and to the wave equation with variable wave velocity [3, 4], the principal order of the problem near the caustic is determined by the coordinates

$$x = (\mathbf{r} - \mathbf{r}^0)\mathbf{k}^1, \quad y = -(\mathbf{r} - \mathbf{r}^0)\mathbf{N}, \tag{1}$$

where $\mathbf{r}$ is the position vector of the point (x_i), $\mathbf{k}^1 = \{\alpha_j^1\}$ is the wave vector at the point A, $\mathbf{N}$ is the unit vector normal to the caustic at the point A in the direction of its convexity, x is the eikonal or the wave travel time from the point A to the projection of the given point on the wave normal, and $\mathbf{k} = \{\alpha_i\}$ is the wave vector at the given point.

First, we consider the linear problem. Let the medium equation be given by the expression

$$\Delta(ip_t, -ip_j, \mathbf{r})\Phi = 0, \tag{2}$$

where the hyperbolic operator Δ has higher derivatives of the order n, which affect equations near the caustic. The linear solution and the relationships at the characteristic [1] provide the dimensions of the region near the caustic

$$y \sim \varepsilon, \quad x \sim \varepsilon^{3/2}, \quad \omega \sim \frac{1}{x}, \tag{3}$$

where ω is the frequency of the process and ε is the order of the solution Φ near the caustic. Writing in the main order of smallness

$$p_t = \frac{\partial}{\partial t} = \frac{\partial x}{\partial t}\frac{\partial}{\partial x}, \quad p_j = \frac{\partial}{\partial x_j} = \alpha_j^1\frac{\partial}{\partial x} - N_j\frac{\partial}{\partial y}, \tag{4}$$

where $\dfrac{\partial x}{\partial t} = -1 + (\mathbf{r} - \mathbf{r}^0)\dfrac{\partial \mathbf{k}^1}{\partial t}$, and expanding Δ in series and neglecting the derivatives of orders higher than $\omega^{n-2/3}$, where $\Delta \sim \omega^n$, one can obtain the representation for the left-hand part of equation (2) in the linear problem:

$$\begin{aligned}\Delta(ip_t, -ip_j, \mathbf{r})\Phi &= \Delta\left(-i\frac{\partial}{\partial x}, -i\alpha_j^1\frac{\partial}{\partial x}, \mathbf{r}^0\right)\Phi \\ &+ \frac{\partial\Delta}{\partial x_k}(x_k - x_k^0)\Phi + i\Delta_{-i\frac{\partial}{\partial x}}(\mathbf{r} - \mathbf{r}^0)\frac{\partial \mathbf{k}^1}{\partial t}\frac{\partial\Phi}{\partial x} \\ &+ i\Delta_{-i\alpha_j^1\frac{\partial}{\partial x}}N_j\frac{\partial\Phi}{\partial y} - \frac{1}{2}\Delta_{-\alpha_i^1\alpha_j^1\frac{\partial^2}{\partial x^2}}N_iN_j\frac{\partial^2\Phi}{\partial y^2},\end{aligned} \tag{5}$$

where the index of Δ means differentiation. When deriving (5), terms of the order ω^{n-1} obtained as a result of the action of operators on the variable coefficients are omitted, which allows us to manipulate with operators as with numbers.

According to the linear solution [1–4], in the time-periodic problem one can assume $\Phi = \psi(y)\exp(i\omega x)$ and take into account the linear dispersion relation $\Delta(\omega, \tilde{\alpha}_j^1, \mathbf{r}^0) = 0$ at the point A and the ray equation $N_j\Delta_{\tilde{\alpha}_j^1} = 0$, where $\tilde{\alpha}_j^1 = \omega\alpha_j^1$. Then, for $\psi = \psi(y)$, the following equation can be derived from (5):

$$\begin{aligned}\tilde{\alpha}_k &= \omega\alpha_k, \\ \exp(-i\omega x)\Delta\Phi &= -\psi\Delta_\omega\omega(x_j - x_j^0)\left(\frac{\partial\alpha_j^1}{\partial t} - \frac{\partial\alpha_j}{\partial t}\right) \\ &- \frac{1}{2}\Delta_{\tilde{\alpha}_i\tilde{\alpha}_j}N_iN_j\frac{d^2\psi}{dy^2},\end{aligned} \tag{6}$$

where, according to the ray equation [1],

$$\frac{\partial x_j}{\partial t} = -\frac{\Delta_{\alpha_j}}{\omega\Delta_\omega}, \quad \frac{\partial\alpha_j}{\partial t} = \frac{1}{\omega}\frac{\Delta_{x_j}}{\Delta_\omega}. \tag{7}$$

Based on equation (1) and neglecting the term $\frac{\alpha_i}{|\alpha_i|^2}x$ with $x \sim y^{3/2}$, one can write accurate to the principal order

$$x_i - x_i^0 = -y\left(N_i - \frac{\alpha_j N_j}{\alpha_k \Delta_{\alpha_k}}\Delta_{\alpha_i}\right). \quad (8)$$

Using the notation

$$\lambda_1 y = -\omega\Delta_\omega(x_j - x_j^0)\left(\frac{\partial\alpha_j^1}{\partial t} - \frac{\partial\alpha_j}{\partial t}\right),$$

we obtain

$$\lambda_1 = \omega\Delta_\omega\left(N_j - \frac{\alpha_i N_i}{\alpha_k\Delta_{\alpha_k}}\Delta_{\alpha_j}\right)\left(\frac{\partial\alpha_j^1}{\partial t} - \frac{\partial\alpha_j}{\partial t}\right). \quad (9)$$

From equations $\Delta\Phi = 0$ and (6), we obtain for the linear problem:

$$\frac{d^2\psi_0}{dy^2} - \chi y\psi_0 = 0, \quad \chi = \frac{\lambda_1}{\frac{1}{2}\Delta_{\tilde\alpha_i\tilde\alpha_j}N_iN_j}. \quad (10)$$

A solution to this equation is the Airy function $v(\tilde y)$. The solution to the wave equation [2, 3] can be generalized to an arbitrary medium described by the hyperbolic system of equations [1, 4] to obtain the linear solution near the caustic:

$$\Phi_0 = \psi_0\exp(i\omega x),$$
$$\psi_0 = 2e^{-i\frac{\pi}{4}}A_1 v(\tilde y)\frac{\omega^{\frac{1}{6}}}{(-i\omega)^{k+1}}a_0^{\frac{1}{12}}, \quad (11)$$

where

$$\tilde y = y\sqrt[3]{\chi}, \quad a_0 = \chi/\omega^2. \quad (12)$$

Then, the linear solution to equation (10) can be written in the form

$$\psi_0 = e^{i\varphi_0}\tilde\psi_0, \quad \tilde\psi_0 = Cv(\tilde y),$$
$$C = 2a_0^{\frac{1}{12}}A_1\omega^{-k-\frac{5}{6}}, \quad \varphi_0 = \frac{\pi}{2}(k+1) - \frac{\pi}{4}. \quad (13)$$

The real constant A_1 can be found from the asymptotic formula for the Airy function at large $-y > 0$, which corresponds to the incident wave AB in the figure AB $\psi_0 = \psi_{\text{geom}}$,

$$\psi_{\text{geom}} = A_1(-\tilde y_1)^{-\frac{1}{4}}\frac{1}{(-i\omega)^{k+1}}\exp\left[-i\frac{2}{3}(-\tilde y)^{\frac{3}{2}}\right] \quad (14)$$

away from the caustic.

In order to calculate the nonlinear term that should be added to (10), one can assume that, at a certain distance away from the caustic, the summands corresponding to the incident and reflected waves can be separated, and one can assume $\tilde\psi_0 = \sum_{n=1}^{2} a_n e^{i\varphi_n}$. Then we drop the indices of a_n and φ_n and obtain from (10) in the linear approximation:

$$a\left(\frac{d\varphi}{dy}\right)^2 - \frac{d^2a}{dy^2} + \chi ya = 0, \quad a\frac{d^2\varphi}{dy^2} + 2\frac{da}{dy}\frac{d\varphi}{dy} = 0. \quad (15)$$

In order to obtain the nonlinear term that must be included into (10), for the medium with cubic nonlinearity, one should write the nonlinear dispersion relation [5] for the frequency Ω and eikonal F of the nonlinear wave:

$$\Omega = \omega_0(\mathbf{k}, \mathbf{r}) + \left(\frac{\partial\Omega}{\partial a^2}\right)_0 a^2, \quad a = |\tilde\psi|, \quad (16)$$

where

$$\omega = \omega_0(\mathbf{k}^1, \mathbf{r}^0), \quad \Omega = -\frac{\partial F}{\partial t}, \quad F = \omega x + \varphi(y). \quad (17)$$

The following relationships are valid (they assume that $\partial y/\partial t$ is small):

$$\frac{\partial F}{\partial t} \approx -\omega + \omega(\mathbf{r} - \mathbf{r}^0)\frac{\partial\mathbf{k}^1}{\partial t},$$
$$\tilde\alpha_j - \tilde\alpha_j^1 = \frac{\partial\varphi}{\partial x_j} = -\varphi'(y)N_j,$$
$$\omega_0(\mathbf{k}, \mathbf{r}) = \omega + \frac{\partial\omega_0}{\partial x_j}(x_j - x_j^0)$$
$$+ \frac{1}{2}\frac{\partial^2\omega_0}{\partial\tilde\alpha_i\partial\tilde\alpha_j}(\tilde\alpha_i - \tilde\alpha_i^1)(\tilde\alpha_j - \tilde\alpha_j^1) + \frac{\partial\omega_0}{\partial\tilde\alpha_j}(\tilde\alpha_j - \tilde\alpha_j^1). \quad (18)$$

Using relationships (7)–(9) and nonlinear dispersion relation (17), (18), one can obtain

$$\lambda_1 y + \frac{1}{2}\Delta_{\tilde\alpha_i\tilde\alpha_j}N_iN_j\varphi'^2(y) = \left(\frac{\partial\Omega}{\partial a^2}\right)_0 a^2\Delta_\omega. \quad (19)$$

Taking the real part of (6) with $\psi = ae^{i\varphi}$ away from the caustic and neglecting the diffraction term $\frac{d^2a}{dy^2}$, one can compare the result with (19) to show that, for the linear problem, the left-hand side of (6) must be complemented with the term $-\left(\frac{\partial\Omega}{\partial a^2}\right)_0|\psi|^2\psi\Delta_\omega$.

Then, the following nonlinear equation can be written:

$$\frac{1}{2}\Delta_{\tilde\alpha_i\tilde\alpha_j}N_iN_j\frac{d^2\psi}{dy^2} - \lambda_1 y\psi + \Delta_\omega\left(\frac{\partial\Omega}{\partial a^2}\right)_0|\psi|^2\psi = 0. \quad (20)$$

DETERMINATION OF THE COEFFICIENTS OF NONLINEAR EQUATIONS NEAR THE CAUSTIC

Since $\lambda_1 < 0$ and $\Delta_\omega > 0$, one should distinguish two cases. The conditions

$$\nu_1\left(\frac{\partial\Omega}{\partial a^2}\right)_0 > 0, \quad \nu_1 = \chi^{-\frac{1}{3}} > 0 \tag{21}$$

and

$$\nu_1\left(\frac{\partial\Omega}{\partial a^2}\right)_0 < 0 \tag{22}$$

define the defocusing and focusing media, respectively. Then, one can represent the function $\tilde{\psi}$, which is defined by $\psi = \tilde{\psi}\, e^{i\varphi_0}$ and satisfies (20), as

$$\tilde{\psi} = \mu\psi^*, \quad y = \nu_1 y^*, \quad \mu = \sqrt{\mp\frac{\lambda_1\nu_1}{\Delta_\omega\left(\frac{\partial\Omega}{\partial a^2}\right)_0}}, \tag{23}$$

where the "$\mp$" signs refer to media (21) and (22), respectively, and equation (20) can be written in the form

$$\frac{d^2\psi^*}{dy^{*2}} - y^*\psi^* \mp \psi^{*3} = 0. \tag{24}$$

It is necessary to find a solution to (24), which transforms into linear solution (11) at large $|y^*|$ and for which $\psi_0^* = \frac{C}{\mu} v(\tilde{y})$. When solving equations (24) with boundary conditions taken from (13), one should take into account that (24) is the Painleve equation and has two moving singularities. Therefore, when the Cauchy conditions are imposed, for example, at $y^* = -5$ for ψ^* and $\frac{d\psi^*}{dy^*}$ taken from (13), the problem will have no continuous solution. The problem of matching the solution to equations (24) with the linear solution can be approximately replaced by the boundary-value problem for ψ^* with the boundary conditions imposed, according to (11), at the ends of the segment (–5, 5), i.e.,

$$\begin{aligned} y^* &= -5, \quad \psi^* = \frac{C}{\mu} v(-5), \\ y^* &= 5, \quad \psi^* = \frac{C}{\mu} v(5). \end{aligned} \tag{25}$$

The choice $y^* = \pm 5$ for the universal coordinate y^*, where the linear and nonlinear solutions are matched, is, to a certain extent, arbitrary and made so as to obtain the best numerical result when integrating equations (24) [1].

Introducing the notation $\psi = \psi^* - \frac{C}{\mu} v(y^*)$, one can obtain the equation

$$\psi'' = \psi y^* \mp \left(\psi + \frac{C}{\mu} v\right)^3, \tag{26}$$

which can be solved under the conditions $\psi(-5) = 0$ and $\psi(5) = 0$.

This problem can be replaced by an integral equation whose kernel depends on two independent solutions to the Airy equation, which can be solved iteratively [1]. The solution shows that, when the upper sign is chosen in (24), i.e., for a defocusing medium, the nonlinear solution is only slightly different from the linear one. At the same time, for the lower sign in (24), i.e., for a focusing medium, the nonlinear solution near the caustic ($y^* = 0$) is by an order of magnitude greater than the linear one, and the solution for $\psi^*(y^*)$ exhibits soliton behavior.

Now, we determine the coefficients of equation (20) for an isotropic medium with $\omega_0 = \omega_0(k)$ and $k_2 = \tilde{\alpha}_i^2$. Since $\Delta_{\tilde{\alpha}_i} = -\omega_0'(k)\frac{\tilde{\alpha}_i}{k}\Delta_\omega$ and $N_i\,\Delta_{\alpha_i} = 0$, expression (9) yields

$$\lambda_1 = \omega\Delta_\omega N_j(\partial\alpha_j^1/\partial t - \partial\alpha_j/\partial t),$$

where $N_j\frac{\partial\tilde{\alpha}_j}{\partial t} = -N_j\frac{k}{\omega_0'(k)\Delta_\omega}\frac{\partial\Delta_{\tilde{\alpha}_j}}{\partial t}$ along the ray with allowance for the fact that $N_i\alpha_i = 0$.

Then, since the ray velocity is $v_\Lambda = \omega_0'(k)$, we obtain

$$\lambda_1 = \frac{k}{v_\Lambda}\left(\frac{\partial\Delta_{\tilde{\alpha}_j}}{\partial t} - \frac{\partial\Delta_{\tilde{\alpha}_j^1}}{\partial t}\right)N_j. \tag{27}$$

Additionally, along the ray,

$$N_j\frac{\partial\Delta_{\tilde{\alpha}_j}}{\partial t} = N_j v_\Lambda\Delta_\omega\frac{\partial t_j}{\partial t}, \text{ where } t_j = \Delta_{\tilde{\alpha}_j}/v_\Lambda\Delta_\omega, N_j\frac{\partial t_j}{v_\Lambda\partial t} = -\frac{1}{R_r}.$$

$1/R_r$ is the projection of the ray curvature vector onto the normal to the caustic, and $\frac{1}{R_s} = -N_j\frac{\partial t_j^1}{v_\Lambda\partial t}$ is the curvature of the normal section of the caustic along the ray. Then, (27) yields

$$\lambda_1 = -k v_\Lambda\frac{\Delta_\omega}{R}, \quad \frac{1}{R} = \frac{1}{R_r} - \frac{1}{R_s}, \quad \frac{1}{R} > 0, \tag{28}$$

which generalizes the result obtained in [3] for the wave equation. In addition, $\Delta_{\tilde{\alpha}_i\tilde{\alpha}_j}N_iN_j = -\frac{v_\Lambda}{k}\Delta_\omega$.

Thus, according to (10), for an isotropic medium in which $\omega_0 = \omega_0(k)$, we obtain

$$\chi = 2k^2/R, \tag{29}$$

where $\chi > 0$, and the signs in (23) and (24) are chosen according to the sign of $(\partial\Omega/\partial a^2)_0$. When $(\partial\Omega/\partial a^2)_0 > 0$, the medium is a defocusing one, and the upper signs in (23) and (24) are chosen; when $(\partial\Omega/\partial a^2)_0 < 0$, the medium is a focusing one.

DERIVATION OF NONLINEAR EQUATIONS FOR DISSIPATIVE DISPERSIVE MEDIA WITH QUADRATIC NONLINEARITY AND THE INVESTIGATION OF THESE BY THE PERTURBATION METHOD

In the particular case of the nonlinear optics problem, the Schrödinger equation for the nonstationary problem [7] yields

$$2ik\frac{1}{v_\Lambda}\frac{\partial A}{\partial t} + \Delta_\perp A + \varepsilon_2\frac{\omega^2}{c^2}Aa^2 = 0,$$
$$v_\Lambda = \frac{c}{\sqrt{\varepsilon_0}}, \quad A = ae^{i\varphi}, \tag{30}$$

where c is the light velocity, $\omega = ck$, ε_0 and ε_2 are the linear and nonlinear permittivities, and $\Delta_\perp$ is the transverse Laplacian. Taking into account that $\frac{\partial A}{\partial t} = \frac{\partial a}{\partial t}e^{i\varphi} + ai\frac{\partial\varphi}{\partial t}e^{i\varphi}$, for the one-dimensional problem for which $\Delta_\perp A = 0$, equation (30) yields

$$-\frac{2\omega}{v_\Lambda}\frac{\partial\varphi}{\partial t} + \varepsilon_2\frac{\omega^2}{c^2}a^2 = 0. \tag{31}$$

By virtue of (18), in the one-dimensional problem, $\Omega = -\frac{\partial F}{\partial t} = \omega - \frac{\partial\varphi}{\partial t}$ and $\Omega = \omega + \left(\frac{\partial\Omega}{\partial a^2}\right)_0 a^2$. Therefore, $\frac{\partial\varphi}{\partial t} = -\left(\frac{\partial\Omega}{\partial a^2}\right)_0 a^2$, and, for the optical medium, we obtain

$$\left(\frac{\partial\Omega}{\partial a^2}\right)_0 = -\varepsilon_2\frac{\omega}{2c\sqrt{\varepsilon_0}} < 0. \tag{32}$$

Hence, the optical medium is a focusing one, and the lower sign should be used in equations (24) and (26).

For waves on the water surface and flexural waves in shells and plates, the value of $(\partial\Omega/\partial a^2)_0$ is given in [5], which allows us to describe these problems by equation (20).

When the medium possesses a quadratic nonlinearity, as well as dispersion and dissipation, the determination of $(\partial\Omega/\partial a^2)_0$ is more complicated. For example, for an electrically conducting gas–fluid mixture, according to [6], a short-wave equation can be derived that describes the three-dimensional problem in the vicinity of the wave. In the ray coordinates t, τ, θ, ξ, where $\tau = x$ is the eikonal and conditions $\theta = \text{const}$ and $\xi = \text{const}$ imply ray equations, this equation has the form

$$\frac{\partial^2 u}{\partial t\partial\tau} - \frac{1}{2}H_1 L(u) = -\frac{1}{H_1}\frac{\partial}{\partial\tau}\left(\Gamma u\frac{\partial u}{\partial t}\right)$$
$$-\frac{E}{H_1}\frac{\partial^4 u}{\partial\tau^4} - \frac{D}{H_1}\frac{\partial^3 u}{\partial\tau^3}, \tag{33}$$

where u is the perturbed particle velocity normal to the wave; $L(u)$ is the transverse operator with respect to coordinates θ and ξ; Γ is the nonlinear coefficient in the formula for the normal wave velocity

$$c_n + v_n = H_1 + \Gamma u \tag{34}$$

and coefficients Γ, D, and E are expressed in terms of the mixture parameters [6].

For a quasi-monochromatic wave, one can assume in (33) that

$$u = U_0 + U_1\exp(i\alpha\tau - i\omega_1 t - \nu t)$$
$$+ U_2\exp[2(i\alpha\tau - i\omega_1 t) - 2\nu t] + \text{c.c.}, \tag{35}$$

where $\alpha = \omega$ is the original frequency and ω_1 is the modulated frequency in the linear formulation. Substituting (35) into (33) gives the linear dispersion relation and the attenuation factor

$$\omega_1 = -\frac{1}{H_1}E\alpha^3, \quad \nu = -\frac{D}{H_1}\alpha^2 \tag{36}$$

and the nonlinear Schrödinger equation for the amplitude of the first harmonic [6]

$$i\alpha\left.\frac{\partial U_1}{\partial t}\right|_\tau - \frac{H_1}{2}L(U_1) = -\frac{H_1}{\alpha}(\chi_1' + i\chi_2')|U_1|^2 U_1, \tag{37}$$

where

$$\chi_1' = -3\omega_1\xi, \quad \chi_2' = -\nu\xi, \quad \xi = \frac{\Gamma^2\alpha^3\exp(-2\nu t)}{2(9\omega_1^2 + \nu^2)H_1^3}. \tag{38}$$

When deriving (37), we took into account that, in the diffraction problem, we have $U_1 \sim \varepsilon$ and $U_0 \sim \varepsilon^3$, and, therefore, U_0 is not involved in equation (37).

When the problem is one-dimensional with respect to τ, we assume $U_1 = a_1 e^{i\varphi}$, where the eikonal φ is complex in the dissipative case, and obtain from (37) at $a_1 = \text{const}$ that

$$-\alpha\frac{\partial\varphi}{\partial t} = H_1 a_1^2(\chi_1' + i\chi_2').$$

On the right-hand side, dissipation in the factor $|e^{2i\varphi}|$ was neglected and it was assumed that $|e^{2i\varphi}| = 1$, which is admissible for small quantities on the order of a_1^4. Since, by virtue of (17) generalized to a dissipative

medium, we have $(\partial\Omega/\partial a_1^2)_0 a_1^2 = -\partial\varphi/\partial t$, we obtain $(\partial\Omega/\partial a_1^2)_0 = [H_1/\alpha](\chi_1' + i\chi_2')$.

Additionally, (35) implies that $U_1\exp(-i\omega_1 t - \nu t) = \psi$ and $\psi = a\exp(i\varphi)$; then, $a_1\exp(-\nu t) = a$, $(\partial\Omega/\partial a^2) = [H_1/\alpha](\chi_1 + i\chi_2)$, where $\chi_{1,2} = \chi_{1,2}'\exp(2\nu t)$.

Then, the nonlinear equation for the quasi-monochromatic wave near the caustic is given by (20). In the case of a gas–fluid mixture, it can be shown [6] that $E > 0$ and, for a dissipation-free medium, i.e., at $\chi_2 = 0$, we obtain $(\partial\Omega/\partial a^2)_0 > 0$, which means that the medium is a defocusing one.

Thus, a quasi-monochromatic wave in a dispersive dissipative medium with a quadratic nonlinearity can be described near a caustic by the equation

$$\frac{\partial^2\psi}{\partial y^2}\frac{1}{2}\Delta_{\tilde{\alpha}_i\tilde{\alpha}_j}N_iN_j - \lambda_1 y\psi + \frac{H_1\Delta_\omega}{\alpha}(\chi_1 + i\chi_2)|\psi|^2\psi = 0. \tag{39}$$

By calculating the coefficients for a dissipation-free gas-dynamical medium, one can obtain ($\omega = \alpha$)

$$\omega/k = H_1, \quad \alpha_j\Delta_{\alpha_j} = -\omega, \quad \lambda_1 = -kH_1/R,$$
$$\Delta_{\tilde{\alpha}_i\tilde{\alpha}_j}N_iN_j = -H_1/k,$$
$$-\frac{H_1^2}{2}\frac{d^2\psi}{dy^2} + \frac{\alpha^2}{R}y\psi + \Delta_\omega\frac{\Gamma^2}{6EH_1}|\psi|^2\psi = 0. \tag{40}$$

Equation (39) based on short-wave equations (33) can also be more rigorously deduced from the nonstationary-wave equation near the caustic for a medium with a quadratic nonlinearity [1], where the terms that are responsible for dispersion and dissipation and a term of the same order $\partial^2 u/\partial x\partial t$ are added as a result of comparison with (33), these terms being neglected when deriving the principal-order equations near the caustic [1]. In the one-dimensional (with respect to x) problem, they are the same for equations (33) and (39). With the inclusion of these terms, the equations have the form

$$\frac{\partial^2 u}{\partial x\partial t} + \frac{\lambda_1 y}{\alpha_j\Delta_{\alpha_j}}\frac{\partial^2 u}{\partial x^2} + \frac{1}{2\alpha_j\Delta_{\alpha_j}}\Delta_{\alpha_i\alpha_j}N_iN_j\frac{\partial^2 u}{\partial y^2} = -\frac{\Gamma}{H_1}\frac{\partial}{\partial x}\left(u\frac{\partial u}{\partial x}\right) - \frac{E}{H_1}\frac{\partial^4 u}{\partial x^4} - \frac{D}{H}\frac{\partial^3 u}{\partial x^3}, \tag{41}$$

where, by virtue of the homogeneity of $\Delta(\alpha_j, \omega)$, one can write $\alpha_j\Delta_{\alpha_j} = -\omega\Delta_\omega = -\alpha\Delta_\omega$.

As in (35), we seek a solution to (41) in the form

$$U = U_0 + U_1\exp(i\alpha x - i\omega_1 t - \nu t) + U_2\exp[2i(\alpha x - \omega_1 t) - 2\nu t] + \text{c.c.} \tag{42}$$

By equating the linear first-harmonic summands containing no derivatives in (41), one can obtain (36). By equating the summands associated with the second harmonic without regard for the derivatives of its amplitude, which is possible for $\omega_1 t \gg 1$, one can find

$$U_2 = \frac{\Gamma}{H_1}\frac{\alpha U_1^2}{-6\omega_1 + 2\nu i}. \tag{43}$$

Substituting the linear solution for U_1 (11) in (43), one can see that $|U_1|$ increases near the caustic as $\alpha^{1/3}$, whereas $|U_2|$ increases as $\dfrac{\alpha^{2/3}}{|\omega_1|}$.

Equating the first-harmonic terms in (41), we obtain

$$i\alpha\frac{\partial U_1}{\partial t} - i(\omega_1 - i\nu)\frac{\partial U_1}{\partial x} - \frac{\lambda_1 y}{\alpha}\frac{\partial^2 U_1}{\partial x^2} - \frac{1}{2\alpha\Delta_\omega}\Delta_{\alpha_i\alpha_j}N_iN_j\frac{\partial^2 U_1}{\partial y^2} - \frac{\Gamma}{H_1}\alpha^2 U_2U_1^*\exp(-2\nu t) = 0, \tag{44}$$

where the asterisk means complex conjugation.

Since, in the principal-order approximation for the quasi-monochromatic wave, $U_1 = \psi(y)\exp(i\alpha x)$, the first two summands in (44) can be omitted to obtain

$$\lambda_1 y\psi - \frac{1}{2\alpha^2}\Delta_{\alpha_i\alpha_j}N_iN_j\frac{d^2\psi}{dy^2} = -\frac{\Gamma^2\alpha^2}{2H_1^2}\frac{3\omega_1 + i\nu}{9\omega_1^2 + \nu^2}\exp(-2\nu t)|\psi|^2\psi, \tag{45}$$

which coincides with (39) and confirms that it was derived correctly. It should be noted that, in the principal order for fast variables x and y for an arbitrary wave in an inhomogeneous medium, the dependence of the coefficients on t can be neglected, which also refers to the factor A_1 in (13).

Thus, for a dispersive dissipative medium, one obtains equation (30) with the complex coefficient $\chi_1 + i\chi_2$, which makes it different from the case of the nondissipative medium described by (20). Then, universal variables (23) with $(\partial\Omega/\partial a^2)_0$ replaced by $\chi_1 H_1/\alpha$ can be introduced. Taking into account that $\psi = \tilde{\psi}\exp(i\varphi_0)$, $\tilde{\psi} = \mu\psi^*$, equation (39) yields the following equation for the defocusing ($\chi_1 > 0$) and focusing ($\chi_1 < 0$) media:

$$\frac{d^2\psi^*}{dy^{*2}} - y^*\psi^* \mp \psi^*|\psi^*|^2\left(1 + i\frac{\chi_2}{\chi_1}\right) = 0. \tag{46}$$

Here, in contrast to (24), $\psi^* = A + iB$ is complex, and A and B satisfy the system of equations

$$\frac{d^2A}{dy^{*2}} - y^*A \mp (A^2 + B^2)\left(A - \frac{\chi_2}{\chi_1}B\right) = 0,$$
$$\frac{d^2B}{dy^{*2}} - y^*B \mp (A^2 + B^2)\left(A\frac{\chi_2}{\chi_1} + B\right) = 0. \quad (47)$$

By introducing the new variable $\Psi = A - \nu(y^*)\frac{C}{\mu}$ as in (26), one can obtain a system of equations for Ψ and B with zero boundary conditions at $y^* = -5$ and 5.

As in [1], a solution can be obtained numerically by transforming (47) to integral equations and solving them by an iterative technique.

SUMMARY

The behavior of monochromatic waves near regular points of caustics in both linear and nonlinear problems is considered. The cases of cubic and quadratic nonlinearities are studied with allowances made for weak dispersion and dissipation. An electrically conducting fluid with gas bubbles [6] is a typical medium with a quadratic nonlinearity. Typical media with cubic nonlinearity are the optical medium [7], and plates and shells [5]. Ordinary nonlinear equations are derived for monochromatic waves near a caustic, the presence of dissipation leading to a system of two coupled equations. An expression for the amplitude of the second harmonic near the caustic is presented. Its value is an order of magnitude higher than the value of the amplitude far from the caustic. The formulation of the nonlinear problem in terms of matching with the linear solution and the result of numerical solution of the nondissipative problem are discussed.

REFERENCES

1. A. G. Bagdoev, *Wave Propagation in Continua* (Yerevan, 1981).
2. Yu. A. Kravtsov, Izv. Vyssh. Uchebn. Zaved. Radiofiz. **7** (4), 1964.
3. Yu. L. Gazaryan, in *Issues of the Dynamical Theory of Seismic Wave Propagation* (Leningrad State Univ., Leningrad, 1961), Vol. 5, pp. 73–114.
4. D. Ludwig, Commun. Pure Appl. Math. **19**, 215 (1966).
5. A. G. Bagdoev and L. A. Movsisian, Int. J. Nonlinear Mech. **19**, 245 (1984).
6. A. G. Bagdoev and L. G. Petrosyan, Izv. Akad. Nauk Arm. SSR. Mekh. **36** (5), 3 (1983).
7. J. K. Marburger and F. S. Felber, Phys. Rev. **A17**, 335 (1978).
8. N. S. Bakhvalov, Ya. M. Zhileĭkin, and E. A. Zabolotskaya, *Nonlinear Theory of Sound Beams* (Nauka, Moscow, 1982).
9. P. Carbonaro, ZAMP **37**, 43 (1986).
10. M. D. Collins, B. E. McDonald, K. D. Heany, *et al.*, J. Acoust. Soc. Am. **97**, 1567 (1995).
11. C. Feuillade, J. Acoust. Soc. Am. **99** (6), 3412 (1996).
12. K. A. Naugol'nykh, L. A. Ostrovskoĭ, and A. M. Sutin, in *Nonlinear Waves* (Nauka, Moscow, 1981), pp. 166–186.

Translated by A.D. Khzmalyan

Acoustical Physics, Vol. 46, No. 3, 2000, pp. 256–260. Translated from Akusticheskiĭ Zhurnal, Vol. 46, No. 3, 2000, pp. 306–311.

Noise Silencer in the Form of a Helmholtz Resonator at the Outlet of an Air Duct of Finite Length

D. V. Bazhenov, L. A. Bazhenova, and A. V. Rimskiĭ-Korsakov

Andreev Acoustics Institute, ul. Shvernika 4, Moscow, 117036 Russia

e-mail: bvp@akin.ru

Received February 25, 1999

Abstract—A new type of noise silencer with the original design of the air duct–resonator system is proposed. The design is free of the disadvantages that are inherent in the conventional design with a resonator placed inside the air duct. A physical model of the silencer is developed, and its efficiency is calculated for different geometrical and physical parameters of the resonator and the air duct. A comparison between the calculated characteristics and the experimental data is performed, and their agreement is demonstrated. *© 2000 MAIK "Nauka/Interperiodica".*

Helmholtz resonators are widely used for solving various technological problems [1–3]. In particular, these resonators are used for noise control in ventilation systems or in exhaust pipes of internal combustion engines. In these cases, the intake of a resonator is mounted flush with the inner surface of the air duct wall. The useful effect is attained due to the fact that the resonator has a very small impedance at the resonator frequency f_r and in its vicinity, and the sound waves propagating along the air duct are reflected from the place of the resonator mounting as from a soft boundary. More detailed studies of the physical processes occurring in air ducts of finite dimensions demonstrated that it is necessary to know the acoustic parameters of the noise source in order to use the resonator effectively [4, 5]. In the case of short air ducts ($kL < 1$), the efficiency of noise suppression decreases and tends to zero as kL tends to zero [6]. One more fact that one has to take into account in the case of the conventional design of the resonator is a possibility of its self-excitation under the action of a tangential airflow. The silencer design proposed in this paper and given in Fig. 1 provides an opportunity to avoid the difficulties indicated above and retain the silencer efficiency in the case of short air ducts. A silencer in the form of a Helmholtz resonator is placed at the end of an air duct, coaxially with it. The resonator intake shaped as a ring of radius R embraces a pipe of length L and radius r. The length of the cylindrical resonator neck l, the area of the neck cross-section S_r, the resonator volume V, and, hence, the resonance frequency f_r can be changed in such a way that the maximum effect of noise suppression is attained within a selected frequency range.

A mathematical model for describing the operation of a silencer of this kind is based on the known experimental fact [6] that a fan located at the intake of a pipe is a source of preset pressure, and the range of frequencies to be damped is such that an air duct may be considered as a narrow pipe.

Thus, we consider the following system: a narrow pipe of radius r with a resonator installed at its end in such a way that the pipe end and the edge of the resonator neck lie in the same plane. This plane is the boundary of the halfspace where sound is emitted to. The source of acoustic pressure (sound) is located at the beginning of the pipe. It is assumed that the pressure amplitude P_0 is constant within the whole considered frequency range independently of the load applied from the side of the air duct.

Let the volume velocity V_T arise at the outlet of the air duct under the action of the pressure P_0. Taking into account the smallness of the diameter of the air duct, we may assume that an equivalent point source of mass with the indicated volume velocity is located at the cen-

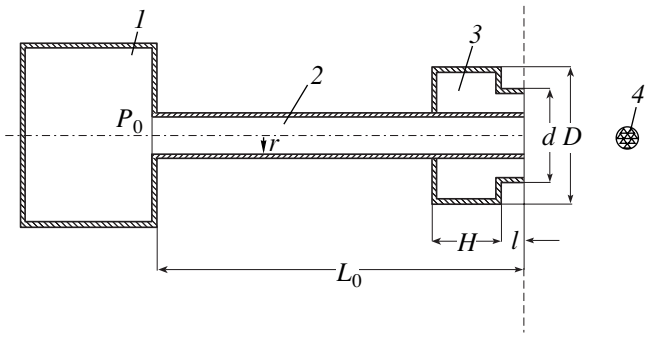

Fig. 1. Air duct with a silencer. (*1*) A source of preset pressure; (*2*) an air duct; (*3*) a resonator; and (*4*) a microphone.

1063-7710/00/4603-0256$20.00 © 2000 MAIK "Nauka/Interperiodica"

ter of the cross-section of the air duct. In this case, the acoustic pressure created by this source can be described by the known relationship

$$P_x = i\omega\rho V_T e^{-ikx}/(2\pi x), \quad k = \omega/c.$$

Here, x is the distance from the source, c is the sound velocity, and k is the wave number.

Further, we assume as usual that the resonator neck is closed by a massless piston, which lies freely on the neck edge. The acoustic pressure P_x affecting this piston gives rise to the force F_r that causes piston vibrations. The pressure force dF acts on an elementary ring of the area of the resonator neck, while the force applied from the side of the external source to the whole resonator neck is equal to

$$F_r = \rho c V_T M, \quad M = e^{-ikr} - e^{-ikR}. \tag{1}$$

The active component of radiation and the inherent loss of the resonator are taken into account by the introduction of the coefficient η. This coefficient determines the relative value of the halfwidth of the resonance band of the resonator at 0.7 of its peak amplitude. As it is done commonly in calculating the complex acoustic impedance, Z_{ac} is assumed to be equal to

$$\begin{aligned} Z_{ac} &= (i\omega\rho 1/S_r)[1 - (f_r/f)^2 - i\eta(f_r/f)] \\ &= i\omega\rho 1/S_r\alpha, \end{aligned} \tag{2}$$

where $\alpha = 1 - (f_r/f)^2 - i\eta(f_r/f)$.

Here, l is the length of the resonator neck with allowance for the associated mass of the radiation impedance and f is the frequency.

Knowing the acoustic impedance of the resonator (expression (2)) and the force (expression (1)), we can determine the volume velocity at the resonator neck

$$V_r := F_r/(S_r Z_{ac}) = V_T M/(ikl\alpha).$$

This velocity in its turn creates acoustic pressure in the surrounding medium. The pressure additionally affects the neck of the air duct.

The reaction force of the resonator neck upon the air duct F_a can be determined in the same way as the force F_r if we replace V_T by V_r in expression (1):

$$P_a := F_a/S_T = -i\rho c V_T M^2/(S_T kl\alpha).$$

Thus, the pressure at the outlet of the air duct depends on two factors: the pressure arising at the outlet of the free duct (without a resonator) P_1 and the additional pressure P_a caused by the reflection from the resonator.

In the absence of the resonator, the velocity V_1 at the outlet of the air duct is determined only by the reaction of the air duct itself and the regime at its inlet, i.e., the pressure P_0 in the case under study.

Representing a narrow pipe (an air duct) as a quadripole, i.e., a part L_0 of an acoustic long line, we can write

$$\begin{bmatrix} P_0 \\ V_0 \end{bmatrix} = \begin{bmatrix} \cos(kL_0) & iw\dfrac{\sin(kL_0)}{S_T} \\ iS_T\dfrac{\sin(kL_0)}{w} & \cos(kL_0) \end{bmatrix} \begin{bmatrix} P_1 \\ V_1 \end{bmatrix}.$$

Then, we obtain

$$\begin{aligned} P_0 &:= \cos(kL_0)P_1 + i\frac{w}{S_T}\sin(kL_0)V_1, \\ V_0 &:= i\frac{S_T}{w}\sin(kL_0)P_1 + \cos(kL_0)V_1, \end{aligned} \tag{3}$$

where $w = \rho c$.

The pressure P_1 and the velocity V_1 at the outlet of the air duct are interconnected by the impedance of radiation into free space

$$P_1 := V_1 Z_T = V_1\frac{w}{S_T}\beta,$$

$$Z_T := \frac{w}{S_T}\left[(kr)^2 + i\frac{8}{3\pi}kr\right],$$

$$\beta := (kr)^2 + i\frac{8}{3\pi}kr.$$

Taking into account expression (3), we have for V_1:

$$V_1 := P_0\frac{S_T}{w}\frac{1}{\beta\cos(kL_0) + i\sin(kL_0)}.$$

This expression determines the radiation from an air duct without a silencer (resonator).

If a resonator is present at the end of the air duct, the resonator reaction P_a is added to the pressure at the duct outlet, and, analogously to expression (3), we can write

$$\begin{aligned} P_0 &:= \cos(kL_0)(P_1 + P_a) + \frac{iw}{S_T}\sin(kL_0)V_T, \\ V_0 &:= \frac{iS_T}{w}\sin(kL_0)(P_1 + P_a) + \cos(kL_0)V_T. \end{aligned} \tag{4}$$

Taking into account P_1 and P_a determined earlier and expression (4), we obtain an expression for the volume velocity V_T at the outlet of the air duct with allowance

for the effect of the pressure field reradiated by the resonator upon the duct outlet:

$$V_T := P_0 \frac{S_T}{w} \frac{1}{\left(\beta + \frac{iM^2}{kl\alpha}\right)\cos(kL_0) + i\sin(kL_0)}. \quad (5)$$

The total acoustic field radiated by the air duct–resonator system is determined in this approximation by the sum of the volume velocities at the outlet of the air duct and at the resonator neck. However, in this case, the volume velocity at the neck should be taken with the reverse sign:

$$V_\Sigma := V_T - V_r = V_T\left(1 + \frac{iM}{kl\alpha}\right) = P_0 \frac{S_T}{w} \frac{1 + [iM/(kl\alpha)]}{\{\beta + [iM^2/(kl\alpha)]\}\cos(kL_0) + i\sin(kL_0)}. \quad (6)$$

If we determine the silencer efficiency as the ratio of the pressures created in the far wave field by a system with a resonator and a system without it, the silencer efficiency can be calculated according to the formula

$$W = 20\log|V_1/V_\Sigma| = 20\log\left|\frac{\{\beta + [iM^2/(kl\alpha)]\}\cos(k(1 + i\eta_1)L_0) + i\sin(k(1 + i\eta_1)L_0)}{\{1 + [iM/(kl\alpha)]\}[\beta\cos(k(1 + i\eta_1)L_0) + i\sin(k(1 + i\eta_1)L_0)]}\right|, \quad (7)$$

since, in the case of the limitations mentioned earlier (small dimensions), the ratio of acoustic pressures is precisely equal to the ratio of volume velocities.

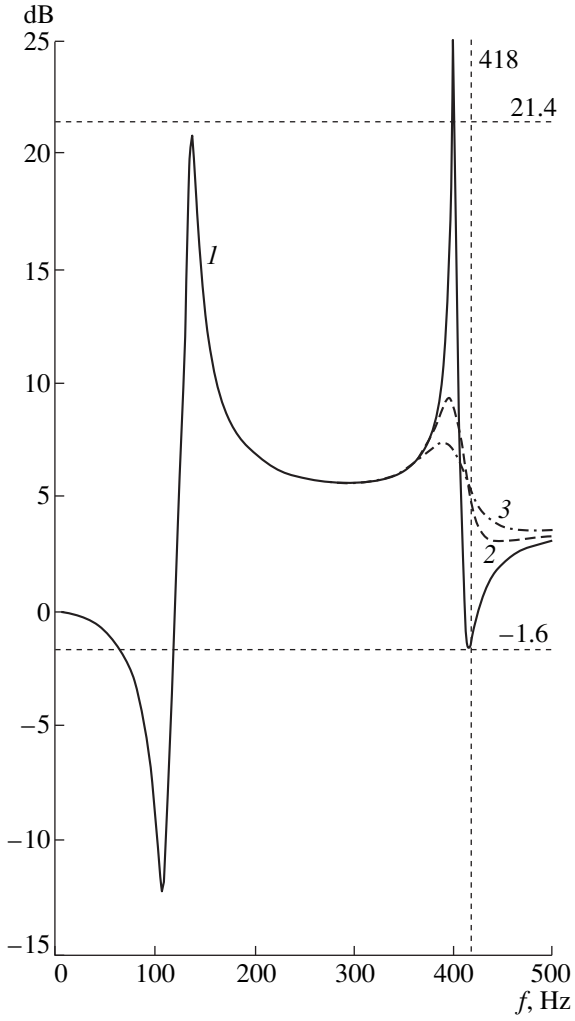

Fig. 2. Dependence of the silencer efficiency on frequency for different values of the attenuation coefficient in the air duct: η_1 = (*1*) 0.01, (W_1); (*2*) 0.05, (W_5); and (*3*) 0.08, (W_8).

The complex value of the wave number $k' = k(1 + i\eta)$ is introduced in formula (7) for taking into account the active loss in the air duct. The frequency range where W is positive corresponds to the positive effect when the radiation of the system with a resonator is less than without it. In the range where W is negative, the presence of a resonator enhances the radiation. Such a situation is characteristic of all jet silencers employed in air ducts of finite lengths.

We have to bear in mind that, in all calculations according to the formulas given above, the frequency range where these dependences are true is limited because of the geometrical dimensions of the resonator and its shape. For example, in the case of a cubic shape, the first natural resonance can manifest itself at the frequency $f = c/2\sqrt{3}\,V^{1/3}$. At much higher frequencies, such a resonator cannot be considered to possess acoustic stiffness.

Formula (7) includes several parameters, which cannot be calculated and must be determined from special experiments. Such parameters are the effective length of the neck l, the loss in the resonator η, and the loss in the air duct η_1. In addition, it is of interest to investigate how these parameters affect the final result. Some experimental estimates were obtained from the measurements of the frequency characteristics of a resonator and an air duct. It was found that, in a specific experiment, the value of η was close to 0.1, the value of η_1 was close to 0.01, and, according to the measured resonator frequency b_r, the effective length of the resonator neck was 0.07–0.08 m, with the physical length of the neck being l = 0.04 m. In calculating the silencer efficiency, the indicated parameters were varied within the limits close to the experimental data. The geometric dimensions of the air duct and the resonator used for calculation also corresponded to those investigated experimentally in order to simplify the comparison between theory and experiment. Thus, the length of the air duct was taken equal to L = 0.4 m, its radius was r = 0.0275 m, the radius of the cylindrical resonator was R_1 = 0.3 m, the

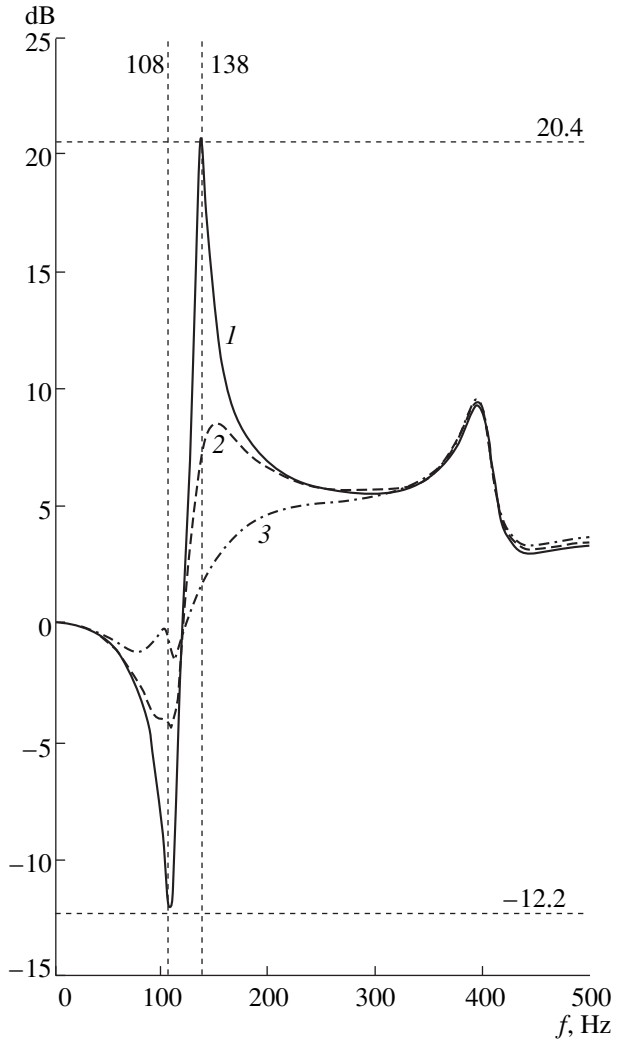

Fig. 3. Silencer efficiency versus frequency for different values of the attenuation coefficient in the resonator: η = (*1*) 0.1, (W_1); (*2*) 0.3, (W_3); and (*3*) 0.8, (W_8).

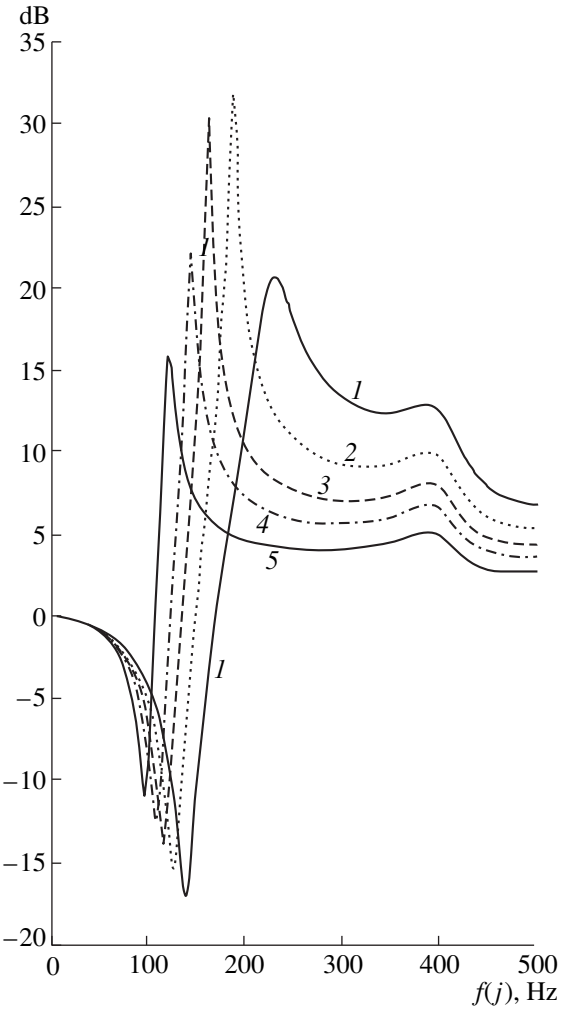

Fig. 4. Silencer efficiency versus frequency for different values of the length of the resonator neck: l = (*1*) 0.05, (W_1); (*2*) 0.06, (W_2); (*3*) 0.07, (W_3); (*4*) 0.08, (W_4); and (*5*) 0.1 m, (W_6).

radius and length of the resonator neck were $R = 0.06$ m and $l = 0.04$ m, and the resonator depth was $H = 0.1$ m.

Figure 2 presents the calculated frequency dependence of the resonator efficiency for three different values of the attenuation coefficient in the air duct η_1. One can see from the shapes of the curves that the peak of the silencing effect is observed at the frequency somewhat higher than the resonance frequency of the resonator f_r. A certain negative effect exists below this peak, precisely at the frequency f_r. And finally, a more or less smooth dependence with the positive effect increasing at the frequency of the first resonance of the air duct is observed at frequencies higher than that of the peak.

One can also see that the attenuation in the air duct affects the silencer efficiency only within a narrow frequency band near the resonance frequency of the air duct (400 Hz in our case), the silencer efficiency decreasing with the increase in attenuation.

The influence of the value of attenuation in the resonator η upon the silencer efficiency is illustrated in Fig. 3. In this case, the loss in the resonator also mainly affects the efficiency of noise suppression within a narrow resonance frequency band and have almost no effect on the wide-band region of the spectrum. One can see from these curves that it is possible to change (by 20–30 dB) the effect of noise suppression at its peak by varying the attenuation in the resonator. However, simultaneously with the increase in the silencer efficiency in the resonance region in the case of a decrease in attenuation in the resonator, the negative effect is enhanced, although to a lesser extent. Therefore, by changing purposefully the loss in the resonator, it is possible to considerably reduce the negative effect, while the positive effect will be reduced only insignificantly.

The silencer operation is most strongly affected by the variation in the length of the resonator neck, which can be seen clearly in Fig. 4. This figure shows the fre-

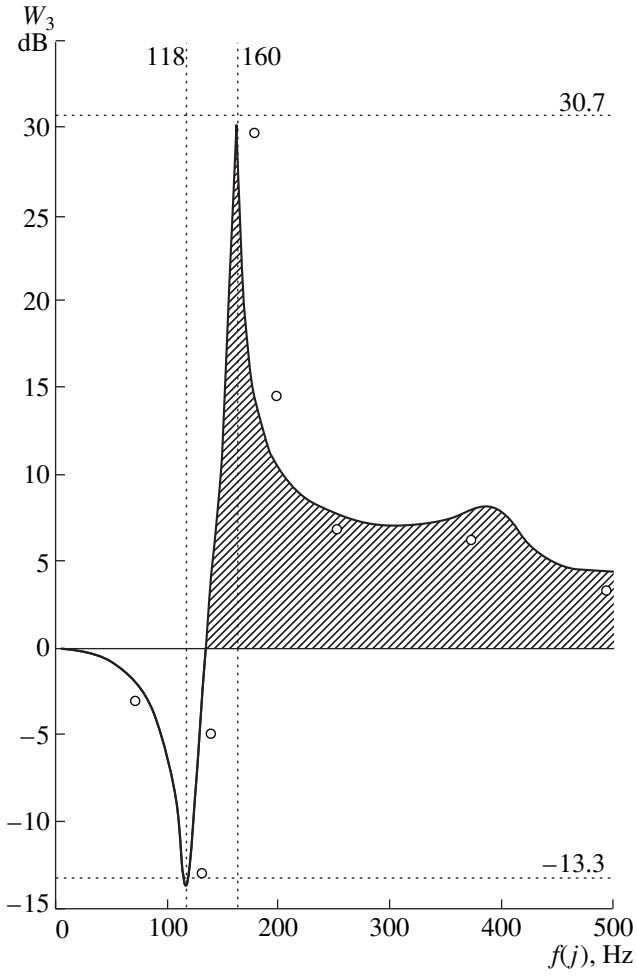

Fig. 5. Comparison between the theory and the experiment. The region of the positive effect of the resonator is hatched; the empty circles show the experimental data.

quency dependence of the silencer efficiency for five different values of the neck length, other geometric parameters including the resonator volume being constant. The losses in the resonator and in the air duct are $\eta = 0.1$ and $\eta_1 = 0.01$. In contrast to attenuation, the neck length affects the silencer operation in both the narrow resonance frequency band and in the wide-band region. The less the neck length, the greater the degree of noise suppression in the wide-band region (from 5 to 15 dB). As for the region of the maximum discrete action, there exists a certain optimum length of the neck that provides the maximum effect. We have to note that the resonance frequency of the resonator changes smoothly (in inverse proportion to l) with the change in the neck length, and, simultaneously, the resonance regions of the positive and negative effects are shifted. As for the negative effect, its maximum shifts smoothly to the lower frequency range with an increase in the neck length, and its amplitude is reduced. In the case of an increase in the neck length, the maximum of the positive effect also shifts to the low-frequency range, but a certain optimum neck length exists here providing the maximum effect. In this case, the effect attains a value of 30 dB and over in the given interval of the neck length variation. Thus, it is possible to tune the silencer to the necessary degree of noise suppression in narrow-band or wide-band frequency ranges.

We compared the experimental data for the designed silencer and the results of calculation according to the formulas given above in order to prove the validity of these formulas. In the experiments, we measured the pressure in the far wave field at the axis of the air duct in the presence of the resonator (P_1) and without it (P_2) at a given pressure at the intake of the air duct. After that, we calculated the efficiency in dB according to the formula $W = 20\log|P_2/P_1|$.

The results of this comparison are presented in Fig. 5, where the experimental data are denoted by circles near the calculated curve, and the region of the positive effect is hatched. One can see that the calculated and experimental data coincide not only qualitatively, but also quantitatively (the scatter is no greater than 2 dB). This coincidence justifies the approximations used in the calculations.

In conclusion, it should be noted that the proposed design of the air duct–resonator system has several advantages (which were mentioned above) over the conventional design with a resonator placed inside a long air duct. The proposed design is the most promising one for short air ducts.

REFERENCES

1. J. M. De Bedout, J. Sound Vibr. **202**, 109 (1997).
2. K. A. Velizhanina and V. A. Oborotov, Akust. Zh. **29**, 5 (1983) [Sov. Phys. Acoust. **29**, 3 (1983)].
3. R. Starobinski and J. Kergomard, J. Acoust. Soc. Am. **103**, 2968 (1998).
4. D. V. Bazhenov and L. A. Bazhenova, in *Aeroacoustics* (Nauka, Moscow, 1980), pp. 87–93.
5. A. V. Rimskiĭ-Korsakov, D. V. Bazhenov, and L. A. Bazhenova, *Physical Foundations of Sound Generation in Air Blowers* (Nauka, Moscow, 1988).
6. D. V. Bazhenov, L. A. Bazhenova, and A. V. Rimskiĭ-Korsakov, Akust. Zh. **41**, 22 (1995) [Acoust. Phys. **41**, 16 (1995)].

Translated by M. L. Lyamshev

Acoustical Physics, Vol. 46, No. 3, 2000, pp. 261–268. Translated from Akusticheskiĭ Zhurnal, Vol. 46, No. 3, 2000, pp. 312–319.

Numerical Calculation of the Correlation Moments of the Sound Field Scattered by a Rough Surface

V. F. Baranov and É. P. Gulin

Andreev Acoustics Institute, Russian Academy of Sciences, ul. Shvernika 4, Moscow, 117036 Russia

e-mail: bvp@akin.ru

Received April 12, 1999

Abstract—Numerically calculated two-dimensional correlation moments of the surface-scattered sound field are presented in the form of correlation surfaces and analyzed. The models of three-dimensional anisotropic and two-dimensional quasi-harmonic surface waves are considered. Data are presented on the angular dependence of the space-time correlation domains of the scattered sound field for receivers spaced across the propagation path in both horizontal and vertical directions, as well as on the shapes of the time-frequency and space-frequency correlation domains. © *2000 MAIK "Nauka/Interperiodica".*

In the previous paper [1], we derived a general expression for the frequency-space-time correlation moment of the sound field scattered by the water surface. The approximate expression obtained for a high smooth roughness was specified for the idealized model of two-dimensional quasi-harmonic surface waves and for a more realistic model of three-dimensional anisotropic ones. The obtained formulas are somewhat awkward, include a large number of parameters, and can therefore be hardly analyzed in the explicit form. We [1] also obtained the estimates that qualitatively characterize the behavior of the correlation moments for the surface-scattered sound field and the dimensions of the domains of combined correlation for the moments. Here, we consider the numerically obtained results that serve to visualize these domains in the form of the cross-sections of the correlation surfaces in the three-dimensional space, at the level of the correlation decrease by a factor of e.

In the computations, the PC MATLAB 5.2 program was used. The computed results were represented on the plane, as a set of closed curves that correspond to different values of the parameters. The coordinate axes represent the values of the shifts in time and space, time and frequency, or frequency and space, depending on the computation mode.

Figure 1 shows an example of the correlation surface corresponding to the absolute value $|B_P|$ of the two-dimensional space-time (ST) correlation moment of the scattered field calculated with the model [1] of the three-dimensional anisotropic surface waves. The waves are assumed to be high, i.e., the condition $\exp(-\Phi^2) \ll 1$ is met, where $\Phi = 2k\sin\Psi\sigma_\xi$ is the Rayleigh roughness parameter, $k = 2\pi/\lambda$, λ is the acoustic wavelength, σ_ξ is the rms height of the surface roughness, and ψ is the grazing angle for the ray specularly reflected from the mean surface plane. Figure 1 corresponds to the receivers spaced in the horizontal plane across the sound propagation path, i.e., along the Y coordinate. The angle ϑ_0 between the general propagation direction of the surface waves and the vector of the receiver spacing is specified to be 70°. In accordance with the shape of the correlation surface, its cross-section by the horizontal plane has an elliptic form in the case at hand.

Figure 2 shows the cross-sections of the correlation surfaces that are obtained by cutting off the absolute value of the ST correlation moment $|B_P(\Delta t, \Delta\mathbf{R})|$ of the scattered field at the I/e-level for the receivers spaced in

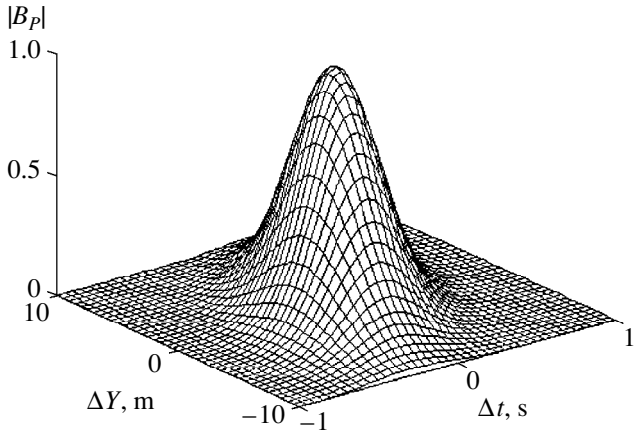

Fig. 1. Correlation surface for three-dimensional anisotropic surface waves (a two-dimensional correlation moment of the scattered field for the receivers spaced across the propagation path in the horizontal plane).

1063-7710/00/4603-0261$20.00 © 2000 MAIK "Nauka/Interperiodica"

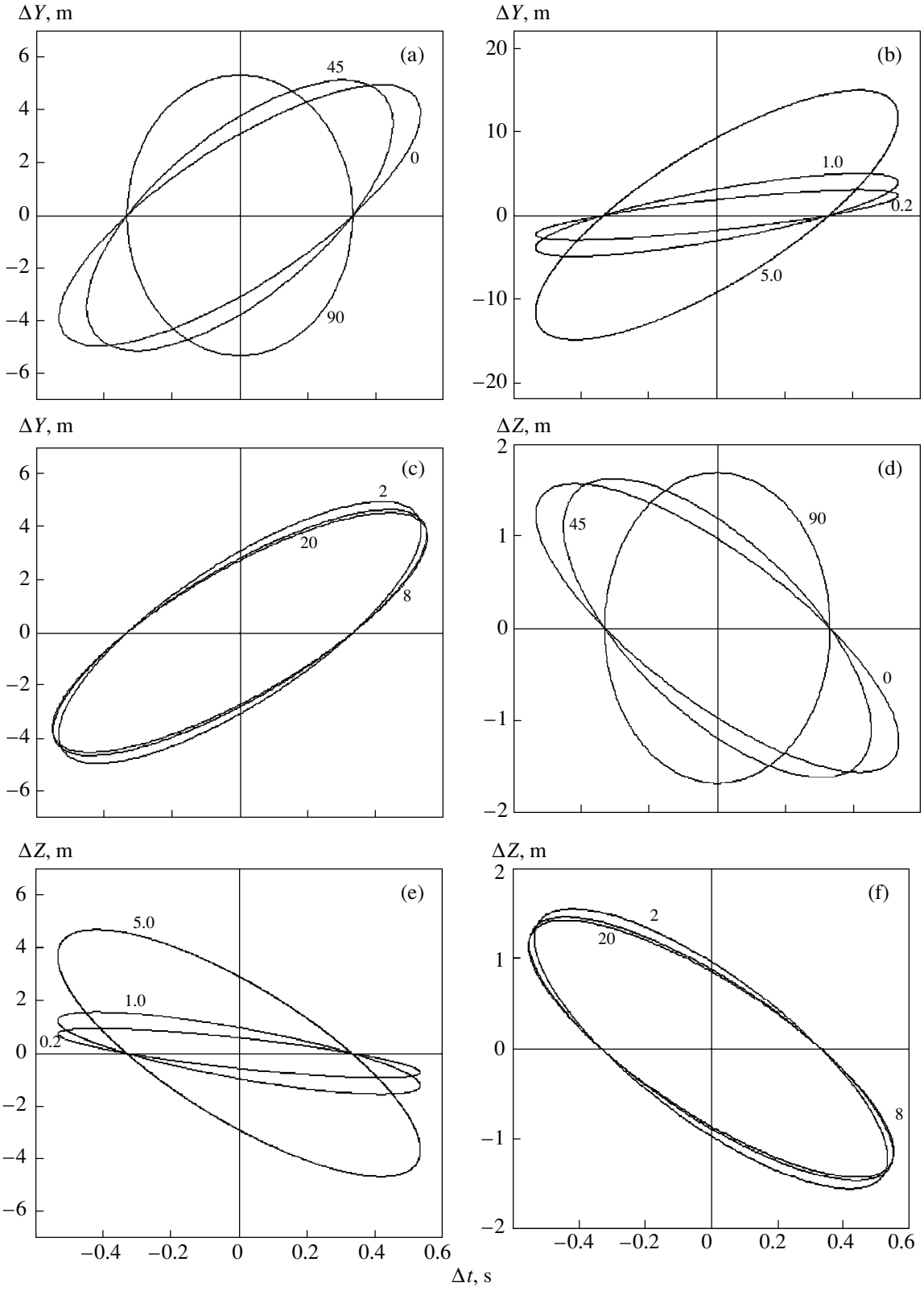

Fig. 2. Space-time (ST) correlation domains of the scattered field for three-dimensional anisotropic surface waves at different parameters: (a, d) angles ϑ_0; (b, e) ratios $d_z = Z/z$; and (c, f) values of l. Receivers are (a–c) horizontally and (d–f) vertically spaced across the propagation path: (a, d) $l = 2$, $d_z = 1$; (b, e) $l = 2$, $\vartheta_0 = 0$; (c, f) $d_z = 1$, $\vartheta_0 = 0$. The plots are labeled with the values of (a, d) ϑ_0 (in deg), (b, e) d_z, and (c, f) l.

the horizontal plane, perpendicularly to the sound propagation path (along the wavefront), and in the vertical. Here, the surface waves are three-dimensional, anisotropic, and follow the model [1] with the angular spectrum of the form $\theta_\zeta(\vartheta) = C_\zeta \cos^l(\vartheta - \alpha)$ at $|\vartheta - \alpha| \le \pi/2$ and $\theta_\zeta(\vartheta) = 0$ at $|\vartheta - \alpha| > \pi/2$, where $C_\zeta = \Gamma(l + 1)/[\sqrt{\pi}\,\Gamma(l + 1/2)]$, $l \ge 1$, $\Gamma(\cdot)$ is the gamma function, and α is the angle of the general direction of surface wave propagation; the frequency spectrum is specified as $G(\Omega) = a_1\Omega^{-n}\exp(-a_2\Omega^{-m})$ [2]. In the computations, the following formula was used:

$$|B_P\Delta(t, \Delta\tilde{X}, \Delta\tilde{Y})| = \exp\left\{-\left[(\Delta t)^2 + \frac{2(\Delta\tilde{R})^2}{v^2}\right.\right.$$
$$\left.\left.\times\left(1 + \frac{l}{l+2}\cos 2\vartheta_0\right) - \frac{8\sqrt{2}}{\pi\sqrt{\pi}}\frac{\Delta t\Delta\tilde{R}\cos\vartheta_0 q_l}{v}\right]/(\Delta t_c)^2\right\}, \quad (1)$$

where $\Delta t_c = \sqrt{2}/(\sqrt{\overline{\Omega^2}}\,\Phi)$– is the time correlation scale for the scattered field, $\overline{\Omega^2}$– is the mean squared (circular) frequency for the surface spectrum, v is the wind speed, $(\Delta\tilde{R})^2 = (\Delta\tilde{X})^2 + (\Delta\tilde{Y})^2$, $\Delta\tilde{R}\cos\vartheta_0 = \Delta\tilde{X}\cos\alpha + \Delta\tilde{Y}\sin\alpha$, $\Delta\mathbf{R} = \{\Delta X, \Delta Y, \Delta Z\}$ is the vector of the receiver spacing, $\Delta\tilde{X} = X_1\frac{z}{z + Z_1} - X_2\frac{z}{z + Z_2}$, $\Delta\tilde{Y} = Y_1\frac{z}{z + Z_1} - Y_2\frac{z}{z + Z_2}$, and z and Z are the transmission and reception depths; the distances between the imaginary source (specularly reflected relative to the plane $z = 0$) and the spaced receivers are $R_n = \sqrt{X_n^2 + Y_n^2 + (z + Z_n)^2}$, $n = 1, 2$; $q_l = [(l)!!/(l-1)!!]^2/(l-1)$. In expression (1), we use $m = 2$ and $n = 6$, which corresponds to the Neumann–Pierson spectrum of the fully developed seas. In this case, $\overline{\Omega^2} = 4g^2/(3v^2)$, where $g = 9.81$ m/s^2 is the gravity acceleration. For the cross-spaced (in Y) receivers, the shifts are symmetric about $Y = 0$: $Y_1 = \Delta Y/2$, $Y_2 = -\Delta Y/2$, and $\Delta\tilde{R} = \Delta\tilde{Y} = \Delta Y/(1 + d_z)$, where $d_z = Z/z$. For vertically spaced receivers, $\Delta\tilde{R} = \Delta\tilde{X} = -Xz\Delta Z/[(z + Z)^2 - (\Delta Z/2)^2]$, where $\Delta Z = Z_1 - Z_2$ and $Z = (Z_1 + Z_2)/2$. The following values of the parameters are specified: $\Phi = 3$; $v = 8$ m/s; $X = 1904$ m; $z + Z = 600$ m; $d_z = 1$, 0.2, and 5; and $l = 2$, 8, and 20.

The correlation cross-sections shown in Fig. 2 can serve to illustrate the dependence of the correlation scales of the scattered field on the angle ϑ_0, on the ratio $d_z = Z/z$ of the reception and transmission depths, and on the effective width of the angular surface spectrum, which is governed by the exponent l. The spatial correlation scales (the shifts $|\Delta Y|$ and $|\Delta Z|$ at $\Delta t = 0$) evidently increase as the angle ϑ_0 increases from 0° to 90° and as d_z increases, at a constant interval Δt_c of time correlation (the shifts $|\Delta t|$ at $\Delta Y = 0$, $\Delta Z = 0$). The ST correlation domain becomes broader (in the sense that the correlation is extended to the space and time shifts that exceed the corresponding time and space correlation scales of the scattered field) as the angle ϑ_0 decreases from 90° to 0°. In comparison with the time (Δt_c) and space (ΔY_c, ΔZ_c) correlation scales, the ST correlation domain is most (by approximately 60%) extended at $\vartheta_0 = 0°$ when the vector of the receiver spacing coincides with the general propagation direction of the surface wave. Of special importance are the signs of the space and time shifts at which their mutual compensation occurs, leading to the extension of the correlation domain. For instance, at $\vartheta_0 = 0°$ and $\Delta\tilde{R} = \Delta\tilde{Y} = \Delta Y/(1 + d_z) = (Y_1 - Y_2)/(1 + d_z) > 0$, the compensation can occur only for $t_1 - t_2 = \Delta t > 0$; at $\Delta Y < 0$, it can occur for $\Delta t < 0$. In contrast, for vertical spacings at $\vartheta_0 = 0°$, negative vertical shifts ($\Delta Z < 0$) must correspond to positive time shifts ($\Delta t > 0$), because $\Delta\tilde{R} \sim (-\Delta Z)$.

The vertical correlation scales, ΔZ_c, are about three times less than the horizontal ones, ΔY_c, in accordance with the well-known relation $\Delta Z_c/\Delta Y_c \simeq \tan\psi = (z + Z)/X$ (in our case, $\tan\psi \simeq 0.32$).

The scales of the space and ST correlations weakly depend on the effective width of the angular spectrum: as the exponent l increases from 2 to 20, the correlation scales decrease by about 10%.

Figures 3 and 4 illustrate the correlation domains of the scattered sound field numerically calculated with the model of two-dimensional quasi-harmonic surface waves. We used the expression for the absolute value of the frequency-space-time correlation moment [1], which can be expressed in the form:

$$|B_P| \simeq \frac{1}{\sqrt[4]{1 + b^2}}\exp\left[-\frac{(\Delta\Phi)^2}{2} - \frac{\varepsilon_{12}(D + F)}{(\Delta t_c)^2(1 + b^2)}\right]. \quad (2)$$

Here, $b = \varepsilon_{12}\Delta p^{-1}(v\Delta t_c)^{-2}$, where $\varepsilon_{12} = \Phi_1\Phi_2/\Phi_0^2$, $\Delta\Phi = \Phi_1 - \Phi_2$, $\Phi_0 = (\Phi_1 + \Phi_2)/2$, $\Delta t_c \simeq \sqrt{2}/(\Omega_0\Phi_0)$, $v = g/\Omega_0$, $\Omega_0 = 2\pi/T_\zeta$; T_ζ is the mean period of the surface waves; $\Phi_n = 2k_n\sigma_\zeta(z + Z_n)/R_n$, $n = 1, 2$;

$$\Delta p^{-1} = \frac{2zZ_1R_1^3}{k_1(z + Z_1)^4}\left[1 - \frac{1}{R_1^2}(X_1\sin\alpha - Y_1\cos\alpha)^2\right]$$
$$- \frac{2zZ_2R_2^3}{k_2(z + Z_2)^4}\left[1 - \frac{1}{R_2^2}(X_2\sin\alpha - Y_2\cos\alpha)^2\right];$$

$$D = (\Delta t - \Delta\tilde{U}/v)^2; \quad \Delta\tilde{U} = \Delta\tilde{X}\cos\alpha + \Delta\tilde{Y}\sin\alpha;$$

$$F = 2(\mu - 1)[b^2(\Delta t)^2 + (\Delta\tilde{U})^2/v^2]/\gamma^2;$$

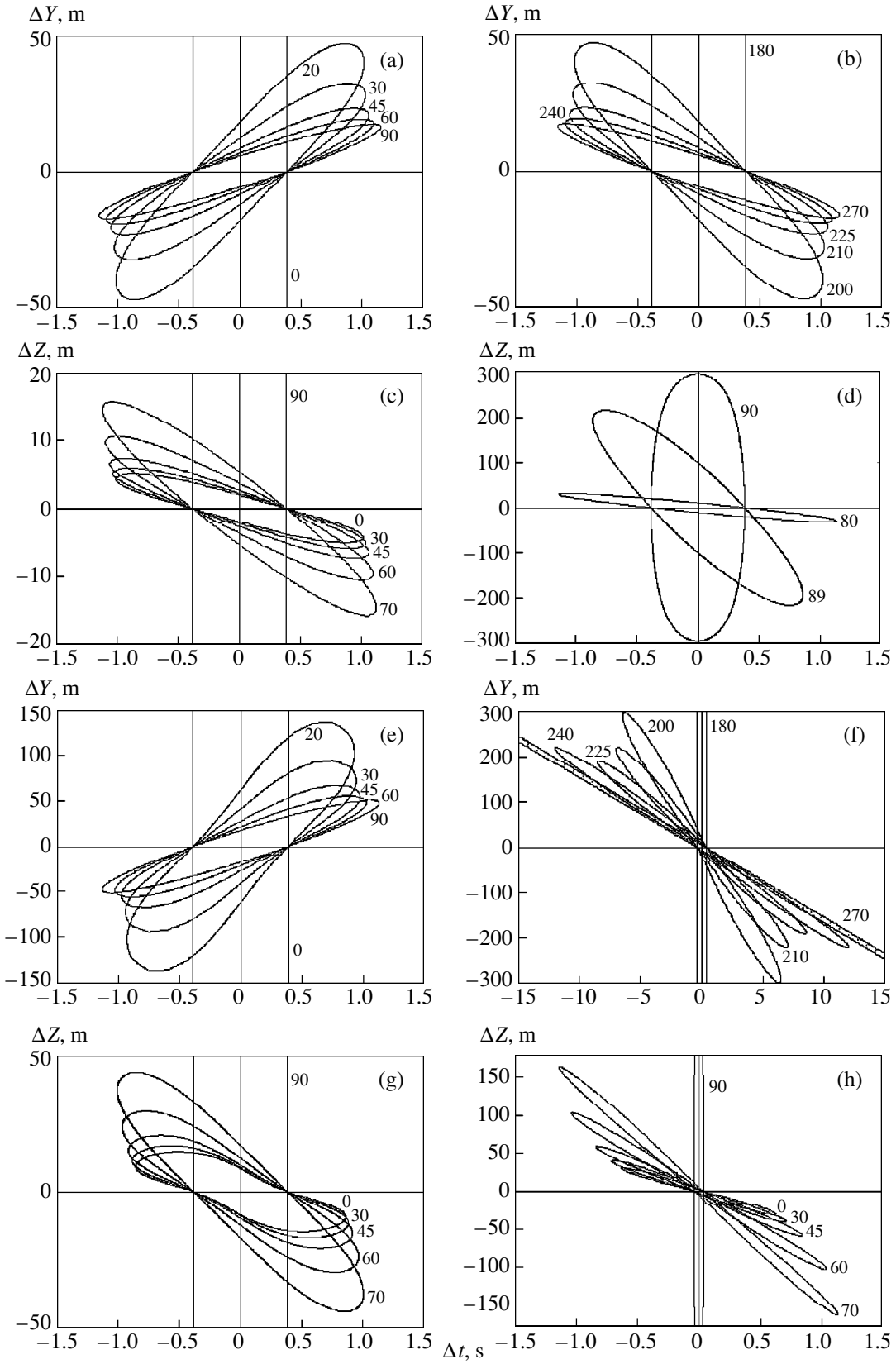

Fig. 3. ST correlation domains of the scattered field for two-dimensional quasi-harmonic surface waves propagating in different directions (at different angles α), (a–e, g) with the dispersion and (f, h) without it. Receivers are (a, b, e, f) horizontally and (c, d, g, h) vertically spaced across the propagation path: (a–d, f, h) $z = Z = 300$ m; (e, g) $z = 100$ m, $Z = 500$ m. The plots are labeled with the values of α (in deg).

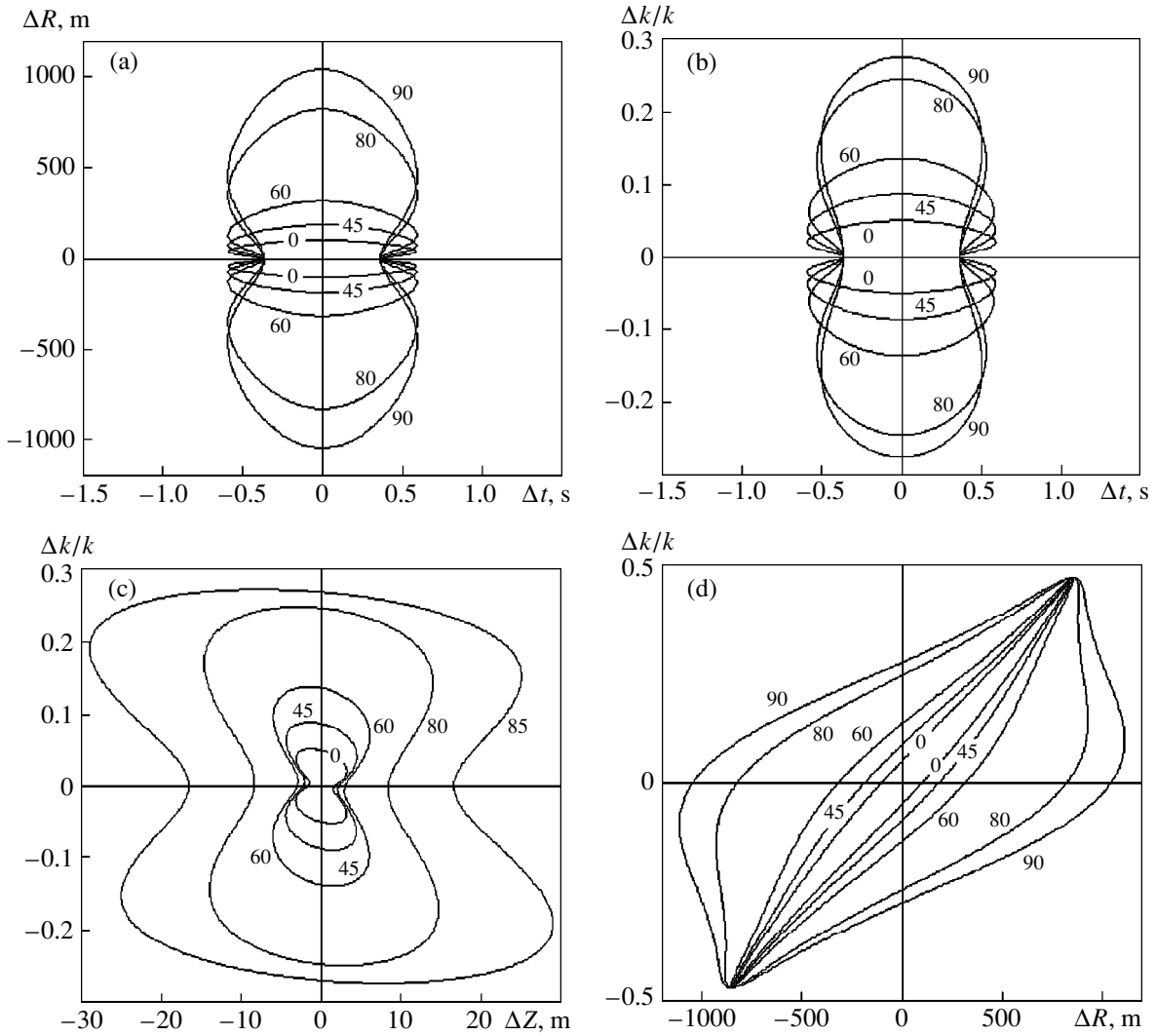

Fig. 4. Domains of (a) ST and (b) TF correlations for the receivers spaced along the specular ray; SF correlation domains for the receivers spaced (c) in the vertical direction and (d) along the specular ray, at different angles α. The model of two-dimensional surface waves with dispersion; $z = Z = 300$ m.

$\mu = 1$ when there is no dispersion of the surface waves (i.e., when these waves do not change their shapes in the course of the propagation); $\mu = 2$ when the deep-water dispersion relation is valid for the surface waves; $\gamma = \Omega_0 \Delta t_\zeta$; and Δt_ζ is the time correlation scale for the surface waves. In the visual representation of the calculations, the space and time shifts were introduced according to the following expressions: $Y_1 = Y + \Delta Y/2$, $Y_2 = Y - \Delta Y/2$, $Z_1 = Z + \Delta Z/2$, $Z_2 = Z - \Delta Z/2$, $X_1 = X + \Delta X/2$, $X_2 = X - \Delta X/2$, $k_1 = k + \Delta k/2$, and $k_2 = k - \Delta k/2$. The following values of the parameters were specified: $\Phi_0 = 3$, $k = 14.65\ \text{m}^{-1}$ ($f = 3.5$ kHz), $\sin\psi = 0.3$, $\sigma_\zeta = 0.34$ m, $v = 8$ m/s, $z + Z = 600$ m, $X = 1904$ m, $Y = 0$, and $\gamma = 4$.

Figure 3 illustrates the dependence of the ST correlation domains on the angle α, which characterizes the propagation direction of the surface wave and is measured counterclockwise from the positive direction of the X axis that coincides with the direction from the source to the receiver in the plane $z = 0$. The data presented in the figure are obtained both in view of the dispersion of the surface waves and without a dispersion, for the receivers spaced in the horizontal plane (in the Y coordinate) and in the vertical direction (in Z coordinate). According to Figs. 3a and 3b, the lateral correlation scale ΔY_c that is governed by the maximum (in terms of absolute value) shift along the axis ΔY noticeably increases as the angle α decreases from 90° to 0° and from 270° to 180°. The lowest values of ΔY_c correspond to the angles $\alpha = 90°$, 270° when the receivers are spaced along the normal to the wavefront of the plane surface wave. As α decreases from 90° to 60° and from 270° to 240°, the scale ΔY_c slightly increases; at $\alpha < 45°$ and $\alpha < 225°$, this increase is much more significant. At $\alpha = 0°$ and 180°, the full correlation is retained, this being true only for the shifts ΔY that are

symmetric about the Y axis when the receivers are located on the wavefront. In the general case of lateral spacing in the Y coordinate (for instance, at $Y_1 = \Delta Y$, $Y_2 = 0$), because of the deformation of the scattering area at large shifts ΔY, the correlation scale ΔY_c remains finite for the angles $\alpha = 0°$, 180° as well (for the specified parameters, this value is about 900 m when $z = Z =$ 300 m). Note that the correlation cross-sections shown in Fig. 3 will also characterize the ST correlation domains for the angle intervals $90° \le \alpha \le 180°$, $270° \le \alpha \le 360°$, if α is replaced by $180° - \alpha$ and $540° - \alpha$, respectively.

The angular dependence of the ST correlation scales Δt_c^{ST} and ΔY_c^{ST} has a different form. According to Figs. 3a and 3b, the quantity Δt_c^{ST} changes from $\Delta t_c^{ST} = \Delta t_c$ at $\alpha = 0°$, 180° to the maximum value that is approximately three times higher than Δt_c at $\alpha = 90°$, 270° when the propagation direction of the plane surface wave coincides with that of the vector of the receiver spacing. Within the angular ranges 1° to 90° and 181° to 270°, Δt_c^{ST} slightly (by about 17%) decreases as α decreases (earlier, we [1] argued that Δt_c^{ST} is independent of α and approximately equal to $\Delta t_c \gamma/\sqrt{2}$). A similar decrease caused by the increase in α takes place within the ranges 90° to 179° and 270° to 359°. In narrow angular bands near $\alpha = 0°$ and 180°, as $\alpha \longrightarrow 0°$ and $\alpha \longrightarrow 180°$, the time correlation scales Δt_c and Δt_c^{ST} increase because of the decrease in the Rayleigh parameter Φ_0. However, at $(\Delta Y)^2 \gg X^2 + (z + Z)^2$, the condition $\Phi_0^2 \gg 1$ can be violated, and expression (2) will not be valid.

The spatial dimensions of the ST correlation domain decrease as the angle α increases from 0° to 90° and from 180° to 270°, and increase as α increases from 90° to 180° and from 270° to 365°, the sharpest changes in the quantity ΔY_c^{ST} corresponding to the vicinities of $\alpha = 0°$ and 180°. For all angles α, except for the values $\alpha = 0°$ and 180° at which the full space correlation is retained, the ST correlation scales ΔY_c^{ST} are significantly higher than the scales ΔY_c of the space correlation. The size of the ST correlation domain is limited by the effect of the surface wave dispersion that leads to a waveform distortion in the course of the propagation. The deformation of the scattering surface area, which is caused by a displacement of the reception point, has a weaker effect. The latter conclusion can be confirmed by comparing the correlation cross-sections shown in Figs. 3b and 3h: in the absence of dispersion ($\mu = 1$), i.e., in the case of the unchanged waveform, the size of the ST correlation domain significantly increases (by a factor of 6–30 as α changes from 185° to 260°). The strongest changes occur near the values $\alpha = 90°$ and 270°, while the full correlation is retained at $\Delta t = \pm \Delta Y/(2v)$ for $\alpha = 90°$ and 270° in the case of $\mu = 1$. In accordance with the dependence $b^2 \sim \sin^2 2\alpha$, the spatial size of the ST correlation domain is minimal at $\alpha = \alpha_0 = (2n - 1)45°$ ($n = 1, 2, 3$) and increases as $|\alpha - \alpha_0|$ increases within each quadrant. The angular ranges $\Delta\alpha = |\alpha - \alpha_1|$ ($\alpha_1 = 0°$, 180°), within which the correlation scales Δt_c and Δt_c^{ST} grow as α approaches 0° or 180°, are significantly extended when $\mu = 1$, as compared to the case of $\mu = 2$, and cover about 5°.

When the receivers are spaced in vertical (Figs. 3c, 3d, 3g, and 3h), in contrast to the case of the horizontal spacing (in Y), the spatial correlation scales ΔZ_c and the spatial size of the ST correlation domains that are given by the quantity ΔZ_c^{ST} increase as the angle α increases from 0° to 90°. With the specified parameters, at the values of α from 0° to 70°, the quantity ΔZ_c^{ST} is about three times smaller than ΔY_c^{ST} at α changing from 90° to 20°. For these angular ranges, the ratio $\Delta Z_c^{ST}/\Delta Y_c^{ST}$ changes from 0.34 to 0.4. At sufficiently high spacings ΔZ, because of the deformation of the scattering area, the correlation scales ΔZ_c and ΔZ_c^{ST} corresponding to $\alpha = 90°$ are limited by a value of 300 m that is close to the specified values of z and Z.

At $\mu = 2$, the size of the ST correlation domain Δt_c^{ST} (in the time coordinate) slowly grows as α increases from 0° to 80°–85° and sharply decreases in the angular range 85°–90°, as α approaches 90°. For all angles except for the vicinity of $\alpha = 90°$, the size of the ST correlation domain is significantly greater than the correlation scales ΔY_c and Δt_c. This phenomenon is most pronounced at $\mu = 1$, when the correlation scales Δt_c^{ST} and ΔZ_c^{ST} corresponding to α changing from 0° to 70° are 6 to 10 times higher than those at $\mu = 2$. At $\mu = 1$, the angular dependence of Δt_c^{ST} is much more pronounced, Δt_c^{ST} increasing by a factor of 1.8 as α increases from 0° to 70°–75°. According to the calculations, further increase in α leads to a decrease in Δt_c^{ST}, and the latter quantity tends to Δt_c at $\alpha = 90°$.

Note that the correlation cross-sections shown in Fig. 3, which correspond to vertical receiver spacings, can be also attributed to the ST correlation within the fourth quadrant, if α is replaced by $360° - \alpha$. To convert to the second and third quadrants, one should replace α by $180° - \alpha$ and $180° + \alpha$, respectively, and change the sign of Δt.

The spatial dimensions ΔY_c^{ST}, ΔZ_c^{ST} of the ST correlation domain and the spatial correlation scales ΔY_c, ΔZ_c increase as z changes from 300 to 100 m and Z

changes from 300 to 500 m (i.e., as $d_z = Z/z$ increases); these dependences can be obtained from the comparison of Figs. 3a and 3e, 3c and 3g. The deviation from the dependence $\Delta Y_c, \Delta Z_c \sim 1 + d_z$, which is most pronounced at $d_z > 1$ and for vertical receiver spacings, is caused by the deformation of the scattering area, which manifests itself as an increase in ΔY_c and ΔZ_c with increasing b^2. As a result, within the angular ranges at hand, the change from 1 to 5 in d_z makes the scales ΔY_c and ΔZ_c increase by factors of 3–3.5 and 3.2–4.2, respectively, depending on α, rather than by a factor of 3. In this case, ΔY_c^{ST} and ΔZ_c^{ST} increase by a factor of 2.8–3, while the time scale Δt_c^{ST} slightly decreases (by less than 10–15%).

Figure 4 serves to illustrate the shapes of the time-frequency (TF) and space-frequency (SF) correlation domains, along with the ST correlation domain, for the degenerate case of the receivers spaced along the specular ray when $\psi = \text{const}$ and $\Delta R = R_1 - R_2 = \Delta Z/\sin\psi = \Delta X/\cos\psi$. The calculations were carried out with the modified formula for the model of two-dimensional quasi-harmonic surface waves and for a Gaussian time correlation function of the surface waves, at $Y_1 = Y_2 = 0$. If $\mu = 2$, this formula takes the form:

$$|B_P| = \frac{1}{\sqrt{1+\tilde{b}^2}}\exp\left[-\frac{(\Delta\Phi)^2}{2} - \frac{\varepsilon_{12}(\tilde{D}+\tilde{F})}{(\Delta\tilde{t}_c)^2(1+\tilde{b}^2)}\right]. \quad (3)$$

Here,

$$\tilde{b} = 0.5\varepsilon_{12}\Phi_0^2\,\overline{\Omega^4}\,\Delta p^{-1}/g^2 = b\overline{\Omega^4}/\Omega_0^4,$$

$$\Delta\tilde{t}_c = \sqrt{2}\,(\sqrt{\overline{\Omega^2}}\,\Phi_0), \quad \tilde{D} = [\Delta t - \Delta\tilde{U}\,\overline{\Omega^3}/(g\overline{\Omega^2})]^2,$$

$$\tilde{F} = [\tilde{b}^2(\Delta t)^2/(\overline{\Omega^2}\,\overline{\Omega^4})$$

$$+ (\Delta\tilde{U})^2/(g\overline{\Omega^2})][\overline{\Omega^4}\,\overline{\Omega^2} - (\overline{\Omega^3})^2].$$

The symmetry of the correlation cross-sections about the coordinates ΔR and Δt in Fig. 4a and $\Delta k/k$ and Δt in Fig. 4b means that the correlation moments do not depend on the signs of the shifts ΔR, Δt and Δk, Δt and testifies to the absence of the transport phenomenon. However, some spread of the ST and TF correlation domains in the time coordinate takes place, the value of $\Delta t_c^{ST} = \max\Delta t_c(\Delta R)$ being independent of α and equal to about $1.6\Delta t_c$, and the value of $\Delta t_c^{TF} = \max\Delta t_c(\Delta k)$ decreasing from $1.6\Delta t_c$ at $\alpha = 0°$–$45°$ to $1.4\Delta t_c$ at $\alpha = 90°$ (note that Δt_c corresponds to the values $\Delta R = 0$ and $\Delta k = 0$). Within the angular range $\alpha = 0°$–$90°$, the scales of the space (ΔR_c) and frequency (Δk_c) correlations increase as α increases varying from $\Delta R_c/R \simeq \Delta k/k \simeq 0.05$ at $\alpha = 0°$ to $\Delta R_c/R \simeq 0.52$ and $\Delta k_c/k \simeq 0.28$ (here, R stands for $R = (R_1 + R_2)/2$). In contrast to the case of spacing along the specular ray, the size of the frequency correlation domain and the spread of the TF correlation domain in Δt are governed by both the power-law and exponential factors involved in (3), the latter factor predominating at $\alpha \gtrsim 60°$.

As to the SF correlation domain (Fig. 4c) with vertical receiver spacings, a transport phenomenon can be noticed that leads to some extension of the SF correlation domain relative to the scales of the frequency (Δk_c) and space (ΔZ_c) correlations. In this case, the ratio $\Delta Z_c^{SF}/\Delta Z_c = \max\Delta Z_c(\Delta k)/\Delta Z_c$ decreases from 1.9 at $\alpha = 0°$–$60°$ to 1.75 at $\alpha = 80°$–$85°$, and to 1.28 at $\alpha = 90°$. The value of $\Delta k_c^{SF} = \max\Delta k_c(\Delta Z)$ is by as little as 2.5–4% greater than Δk_c for the entire angular range except for the close vicinity (1°–2°) of $\alpha = 90°$ where it sharply increases up to $1.85\Delta R_c$ at $\alpha = 90°$. At the same time, all correlation scales (frequency, spatial, and spatial-frequency ones) increase as the angle α increases from 0° to 90°. This is also true for receivers spaced along the specular ray. In the latter case, the SF correlation moment (Fig. 4d) evidences for the pronounced transport phenomenon that can be attributed to the mutual compensation of the space and frequency shifts: the deformations of the scattering area have different signs when the frequency and distance R increase. This phenomenon leads to a significant extension of the SF correlation domain, in comparison with the scales of frequency and space correlations for α varying from 0° to 60°. As α increases from 0° to 60°, the ratio $\delta_c = \Delta k_c^{SF}/\Delta k_c$ decreases from 8.4 to 3.4, and the ratio $\delta_R = \Delta R_c^{SF}/\Delta R_c$ decreases from 8.1 to 2.7. The lowest values $\delta_c \simeq 1.7$ and $\delta_R \simeq 1.06$ correspond to $\alpha = 90°$. According to Fig. 5d, the size of the SF correlation domain in the frequency coordinate is independent of α and equals to $\Delta k_c^{SF}/k \simeq 0.47$ in this case. This value coincides with the second scale of the frequency correlation, $\Delta k_c^{(2)}/k \simeq \sqrt{2}/\Phi_0$, that corresponds to the exponential decay of $|B_P(\Delta k)|$ [1]. The spatial size of the SF correlation domain is independent of α for $\alpha = 0°$–$70°$ and equals $\Delta R_c^{SF} \simeq 0.42\,R$; as α increases from 70° to 90°, it increases up to about $0.55\,R$. In this case, the values of ΔR_c^{SF} correspond to the vertical receiver spacings ΔZ that are comparable with the half-sum of the reception depths Z_1 and Z_2.

To conclude with, we emphasize that the presented geometric interpretation of the numerically calculated two-dimensional correlation moments of the scattered sound field can serve to visualize the features of the

space-time-frequency “medium filter” for the surface-reflected signals and to improve the explicit estimates [1] of the correlation domains.

ACKNOWLEDGMENTS

This work was supported by the Russian Foundation for Basic Research (project no. 96-02-18430-a).

REFERENCES

1. É. P. Gulin, Akust. Zh. **45**, 789 (1999) [Acoust. Phys. **45**, 711 (1999)].
2. I. N. Davidan, L. I. Lopatukhin, and V. A. Rozhkov, *Wind Waves in the Ocean* (Gidrometeoizdat, Leningrad, 1985).

Translated by E.A. Kopyl

Acoustical Physics, Vol. 46, No. 3, 2000, pp. 269–273. Translated from Akusticheskiĭ Zhurnal, Vol. 46, No. 3, 2000, pp. 320–324.

A Resonant Acoustic Level Gauge

V. I. Bardyshev, Yu. I. Gromov, A. N. Gromov, A. T. Ovcharenko, and A. V. Rimskiĭ-Korsakov

Andreev Acoustics Institute, Russian Academy of Sciences, ul. Shvernika 4, Moscow, 117036 Russia

e-mail: bvp@akin.ru

Received February 4, 1999

Abstract—A method and device for measuring the levels of liquids in reservoirs by using an acoustic resonance in a tube are considered. The main advantages of the proposed method are its noise immunity and high accuracy. © *2000 MAIK "Nauka/Interperiodica".*

Acoustic gauges for measuring the levels of liquids and loose materials in reservoirs on the basis of the method of pulsed echo sounding are widely used in industry and transport [1, 2]. Their main advantage is their high reliability in severe operating conditions, which is achieved owing to the absence of moving parts and the noncontact method of the level measurement. The electroacoustic transducers of these level gauges are not in contact with the monitored substance, which may be aggressive, e.g., chemically active, hot, abrasive, and so on. The disadvantage of the echo-sounding level gauges is their sensitivity to acoustic noise rather common in industry; noise interferes with the useful signals and disrupts the operation of gauges. The enhancement of the measurement accuracy is also desirable for such gauges [1].

Below, we describe a resonant acoustic level gauge (RALG) based on the resonance of acoustic waves in a tube resonator filled with air or some other gas [3]. Having all the advantages of echo-sounding level gauges, the RALG surpasses them in terms of noise immunity and accuracy. The main purpose of the RALG is to measure the levels of liquids. The measurement of the levels of some heavy and mobile loose materials is also possible.

The main part of the RALG is a tube resonator with a rigid wall. Its lower end is submerged in the monitored substance, and the upper end is closed with a rigid cover. In the upper part of the tube or in the cover, there is a narrow ventilation opening for the communication of the interior of the resonator with atmosphere or the part of the monitored reservoir above the monitored substance for maintaining the equality of gas pressure and the level of the substance in the reservoir and the resonator. A source of the noise signal and a receiving microphone are located under the cover in the resonator. We note that it is possible to manage without a microphone, by using a reversible electroacoustic transducer, as is done in a Pierce acoustic interferometer [4]. However, a microphone, in combination with an amplifier, makes it possible to expand the frequency band of the received signal and improve the accuracy of measurements. The sound waves form resonances in the upper part of the tube above the monitored substance level. The resonance frequencies depend on the length of the cavity and, hence, on the level of the substance. By measuring these frequencies, it becomes possible to determine the level of interest.

The sound waves are reflected from the rigid upper cover without loss of amplitude and phase [5]. The reflection coefficient of plane waves for perpendicular incidence from gas onto the surface of the monitored substance is described by the formula

$$R = (A - 1)/(A + 1), \quad A = \rho_1 c_1/\rho c, \tag{1}$$

where ρ, c, and ρc are the density, sound velocity, and acoustic resistance of gas, respectively, and ρ_1, c_1, and $\rho_1 c_1$ are the same quantities for the monitored substance. For a gas–liquid boundary, $A \gg 1$. For example, for the air–water boundary, $A = 3.2 \times 10^3$ and, for the air-oil boundary, $A = 2.3 \times 10^3$. Then, $R \approx 1$, and the sound waves are reflected from the monitored substance in the same way as from a rigid cover. In this case, the sound waves in the gas-filled cavity of length L are resonant at the frequencies [5]

$$f_n = cn/2L, \quad n = 1, 2, 3, \ldots, \tag{2}$$

where n is the number of resonance. The frequency spectrum of the received signal develops maxima that form a harmonic scale with the interval $f_1 = c/2L$. By measuring f_1, it becomes possible to compute L and the level of the monitored substance h:

$$L = c/2f_1, \quad h = l - c/2f_1, \tag{3}$$

where h is measured upward from any given level, for instance, from the bottom of the reservoir, and l is the distance from this level to the upper cover of the resonator. Only longitudinal waves are used. To eliminate the generation of oblique waves (modes of higher num-

bers), the following conditions for the internal cross-section of a circular resonator of diameter D should be satisfied [6]:

$$D < \lambda_h/1.706, \quad f_h < 0.586c/D, \tag{4}$$

where λ_h is the sound wavelength corresponding to the highest allowable frequency f_h of the operating range.

Analogous conditions for a rectangular resonator with the long side b of the internal cross-section are as follows [5]:

$$b < \lambda_h/2, \quad f_h < c/2b. \tag{5}$$

The ventilation opening should not shift the resonance frequencies, which means that its acoustic resistance should be sufficiently large. It requires the fulfillment of the following conditions

$$d \ll D, \quad d \ll \lambda_h = c/f_h, \tag{6}$$

where d is the diameter of the opening.

The sound velocity in gas is independent of pressure but strongly depends on its absolute temperature θ and molecular weight μ; it is given by the formula [5]

$$c = \sqrt{\gamma R_g \theta/\mu}, \tag{7}$$

where $R_g = 8.341$ J mol^{-1} deg^{-1} is the universal gas constant and γ is the ratio of heat capacities. For diatomic gases and air, $\gamma = 1.4$. The neglected changes in temperature $\Delta\theta$ and gas composition and, hence, in its molecular weight μ result in the relative error of the determination of L:

$$\Delta L/L = \Delta c/c = \frac{1}{2}\left(\frac{\Delta\theta}{\theta} - \frac{\Delta\mu}{\mu}\right). \tag{8}$$

Thus, at the mean temperature $\theta = 293$K (20°C), the increment $\Delta\theta = 30°$ leads to an error of 5% in the measurement of L. For removing the temperature error, the echo-sounding level gauges are provided with sensors of air temperature and appropriate electronics for correcting the sound velocity values [2]. For a fixed gas composition in the resonator, such a correction is efficient and can also be used in RALG. The most appropriate devices for RALG are the thermoelectric transducers, whose small size makes it possible to introduce them into the resonator. Their accuracy is sufficiently high. According to the JSA American standard, the tolerances for copper–constantan thermocouples are equal to ±0.8% in the range of temperatures T from –60 to +90°C [9], which corresponds to the relative standard (root-mean-square) error $\sigma T/T \approx 0.5\%$, or, for $T =$ 20°C, $\sigma\theta/\theta = 0.034\%$. According to (8), this results in the relative standard error $\sigma L/L = 0.017\%$. For $L = 1$ m, we have $\sigma L = 0.17$ mm.

At a small amplitude of sound waves, the dispersion of the sound velocity in gas is practically absent, and, as a consequence, there are no difficulties like those encountered in the design of level gauges based on transverse oscillations of a string [7] or a rod [8] characterized by a strong dispersion.

If the gas composition in the resonator changes due to, for example, vapor-gas emission of the monitored substance, an error arises owing to the change in μ. For example, the sound velocity in methane is 1.5 times greater than in air. This gas is emitted from oil. If the tube walls are compliant and thermally conducting, a reduction in the sound velocity inside the tube is possible [6]. All the mentioned errors can be compensated by introducing a supplementary reference resonator in the design of RALG. This resonator should be similar to the main one, but closed with rigid covers at both ends. For convenience, its length L_k may be less than the length of the main resonator. Its interior should communicate with the interior of the main resonator, or with the common gas medium, through a ventilation opening satisfying condition (6). In the reference resonator, a resonance scale with the interval f_{k1} is excited. Then,

$$c = 2L_k f_{k1}, \quad h = l - L_k f_{k1}/f_1. \tag{9}$$

This type of RALG will be called a double-resonator gauge. The system of signal processing may be unified, connected to the reference resonator by a switch when needed. Usually, the parameters θ and μ change slowly, and the connection to the reference resonator may be rare, practically without reduction in the rate of level measurement (h).

In the constructed prototypes of RALG, the signal processing was performed in digital form by several variants of algorithms and programs. The general flowchart of algorithms is shown in Fig. 1. The realization of a noise signal received by the microphone, $p(t)$, where $t \in [0, P]$, t is time, p is the sound pressure, and P is the length of realization, is fed to the input of an A/D converter. The digital sequence $\{p(t_i)\} = \{p(i)\}$, where $i = 0, 1, 2, \ldots, N-1$ is the number of reading, $t_i = i\Delta t$, $\Delta t = 1/f_s$, f_s is the sampling frequency, and $P = (N-1)\Delta t$, is passed from the output of the A/D converter to the unit *2*. There, the power spectral density averaged over m realizations is computed. The finite fast Fourier transform of the sequence $\{p(i)\}$ is calculated as

$$X_q(k) = \sum_{i=0}^{N-1} p_q(i) W_N^{ik}, \quad W_N^{ik} = \exp\left(-j\frac{2\pi ik}{N}\right), \tag{10}$$

where i, k are the numbers of readings, $k = 0, 1, 2, \ldots, N-1$, j is the imaginary unit, and q is the number of realization. The obtained sequence is smoothed by

using a Goodman window with seven weight coefficients

$$X_q(k) = \sum_{i=-3}^{3} a(i)X_q(k+i)$$
$$= X_q(k) + \sum_{i=1}^{3} a(i)[X_q(k-i) + X_q(k+i)], \quad (11)$$

$$a(0) = 1,\ a(1) = a(-1) = 0.35,\ a(2) = a(-2) = -0.0875,$$
$$a(3) = a(-3) = 0.0625.$$

The seven weight coefficients are a reasonable compromise between the complexity of calculations and quality of smoothing [10].

Then, the power spectral density is calculated with the coefficient corresponding to the Goodman smoothing:

$$S_q(k) = 1.267\frac{1}{P}|\tilde{X}_q(k)|^2, \quad k = 0, 1, 2, \ldots, \frac{N}{2}. \quad (12)$$

The obtained estimate of the power spectral density is averaged over m successive realizations:

$$\bar{S}(k) = \frac{1}{m}\sum_{q=1}^{m} S_q(k). \quad (13)$$

In single level measurements, we used a cepstrum method according to which the cepstrum of the power spectral density was calculated in the unit *3*

$$K(t) = |\Phi\{\log\bar{S}(k)\}|^2, \quad (14)$$

where Φ is the Fourier transform. The maximum of the cepstrum is formed at $t_k = 1/f_1$. According to (3), $L = ct_k/2$. Taking the logarithm of the power spectral density equalizes the levels of harmonics of the scale to some extent and assists in the detection of the maximum of the cepstrum.

In the continuous operation of RALG in the mode of tracking the level of the monitored substance, a simpler algorithm can be used according to which, in the unit *3*, the normalized cross-correlation function $R(L, L_T)$ of two power spectral densities, i.e., the measured power spectral density $\bar{S}(k, L)$ and theoretical one $S(k, L_T)$, is calculated. For $L = L_T$ $R(L, L_T) = 1$ and, for $L \neq L_T$ $R(L, L_T) < 1$. A set of spectra $S(k, L_T)$ is calculated for a number of values of L_T selected with a small step ΔL_T in the vicinity of the value of L obtained in the previous measurement. The value of L_T corresponding to the maximum of the correlation function is taken to be the true value. For a slow change in L, the required number of steps is not large.

The value of h is calculated in the unit *4* by equations (3) and (7) or (9). The unit *5* performs the visualization of the results of the measurement and generates a request signal for supplying the next ensemble of the signal realizations to the input of the A/D converter.

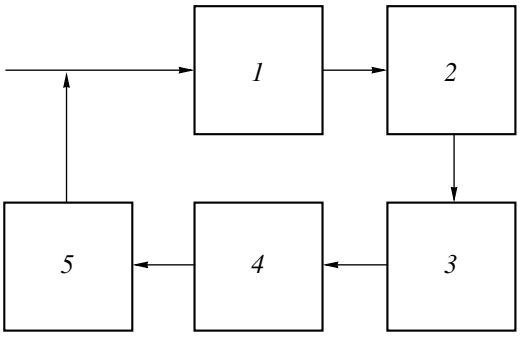

Fig. 1. Flow-chart of the algorithms of signal processing: (*1*) analog-to-digital converter, (*2*) calculation of power spectral density, (*3*) analysis of the power spectral density, (*4*) calculation of the level h, and (*5*) representation of the result on the display and the request for the input signal.

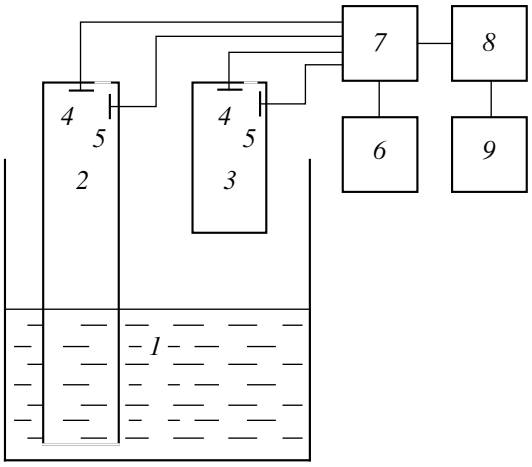

Fig. 2. Schematic diagram of a double-resonator RALG: (*1*) monitored substance, (*2*) measuring resonator, (*3*) reference resonator, (*4*) source of the noise signal, (*5*) microphone, (*6*) generator of the electric noise signal, (*7*) switch, (*8*) system of signal processing or PC, and (*9*) indicator of the level or a display.

A simplified schematic diagram of a double-resonator RALG is shown in Fig. 2. The external interfering noise has resonances at the same frequencies as the radiated signal, and, hence, the RALG is absolutely immune to it.

Random errors of measurement are connected with the boundedness of the intervals of averaging in time, frequency, and ensemble of realizations. With some assumptions, the standard error of determination of f_1 by N harmonics and m realizations is $\sigma f_1 \approx 1/3P\sqrt{Nm}$. From the relation $N \approx 2LF/c$, we obtain

$$\sigma f_1 \approx \frac{1}{3P}\sqrt{\frac{c}{2LFm}}. \quad (15)$$

Differentiating expression (3) with respect to f_1 and substituting df_1 for σf_1 according to (15), we obtain the relation for the standard error in the determination of h:

$$\sigma h_P = \sigma L_p \approx \frac{L}{3P}\sqrt{\frac{2L}{cFm}}. \quad (16)$$

Let the sound velocity be calculated by the measured value of gas temperature. The standard error of the temperature measurement $\sigma\theta$ results in the standard errors of the determination of sound velocity σc and level of the monitored substance σh_θ:

$$\sigma c = \frac{c}{2\theta}\sigma\theta, \quad \sigma h_\theta = \frac{L}{2\theta}\sigma\theta. \quad (17)$$

Assuming that the errors σh_P and σh_θ are independent, we obtain the relation for the standard error of measuring h by a single-resonator RALG:

$$\sigma h = [(\sigma h_P)^2 + (\sigma h_\theta)^2]^{1/2} = L\left[\frac{2L}{9cFP^2m} + \frac{(\sigma\theta)^2}{4\theta^2}\right]^{1/2}. \quad (18)$$

Similarly, we obtain the equation for σh for a double-resonator RALG:

$$\sigma h = \frac{L}{3P}[2(L + L_k)^2/cFm]^{1/2}. \quad (19)$$

For the purpose of testing the units of the RALG, evaluating its efficiency, and refining its characteristics, we manufactured and tested nine prototypes of the instrument with various types of radiators and receivers of noise signals, various resonators and data processing systems. The main unit of the RALG is enclosed in a cylindrical housing screwed onto the tube resonator. It consists of a generator and radiator of a noise signal, a microphone, and a microphone amplifier. We used small-sized electrodynamic and piezoceramic radiators and electret microphones. Metal and plastic tubes in 30–50 mm inner diameter and in 1–5 m length were used as measuring resonators. Water was used as the monitored substance. Its level was monitored by a glass-tube level gauge with a standard error of reading of about 0.3 mm. The temperature of water and air was measured by mercury thermometers with standard errors of about 0.3°. The water temperature was changed in the range from +18 to +80°C with an electric heater. In one of the experiments, the upper part of the tube was rolled into a ring of diameter 0.4 m. In all cases, the RALG operated properly.

The signal was processed on IBM PCs and Notebooks provided with A/D converter boards. The frequency spectra, the cepstra, and the measured level of water were shown on a display and recorded by a printer. The power of the electric signal supplied to the radiator did not exceed 0.1 W, which is lower than the level of inflammation of combustible materials of the PA group (propane, coal dust), and this fact makes the RALG comply with the fire safety regulations. In the course of the tests, the RALG was subjected to intense noise interference of the level up to 154 dB with a "pink" spectrum in the range 30–5000 Hz and to vibration in axial and transverse directions with the amplitude of the particle velocity up to 100 m/s in the frequency range 10–2000 Hz. Under these conditions, the RALG retained its accuracy.

An empirical estimate of the standard error of measurement was made as follows. At a fixed level of water, M measurements of L_i were made, $i = 1, 2, \ldots, M$ (M = 20) by a single-resonator RALG and by a glass-tube level gauge. The temperature of air and water was simultaneously measured by mercury thermometers. The value of σh was calculated by the formulas

$$\sigma h = \sigma L = \left[\frac{1}{M-1}\sum_{M-1}^{M}(L_i - \bar{L})^2\right]^{1/2}, \quad \bar{L} = \frac{1}{M}\sum_{i=1}^{M} L_i. \quad (20)$$

This procedure was repeated for several values of L in the range 0.5–1 m. The empirical value σh = 0.5 mm, or $\sigma h/\bar{L} \approx 0.05\%$, was obtained. The parameters of these measurements were as follows: P = 0.4 s, m = 10, f = 50–2000 Hz, F = 1950 Hz, T = +20°C, θ = 293K, $\sigma\theta$ = 0.3°, D = 3 cm, and d = 1 mm. According to formula (7), c = 343 m/s. Requirements (5) and (6) are satisfied. According to (18), the calculated estimate is $\sigma h \approx$ 0.3–0.8 mm, or, on the average, $\sigma h \approx$ 0.5 mm, which corresponds to the empirical estimate.

For a double-resonator RALG at the same conditions, for L_k = 1 m and $\bar{L}$ = 0.5–1 m, according to (20), we have $\sigma h \approx$ 0.3–0.6 mm and $\sigma h/\bar{L} \approx 0.06\%$. For comparison, the relative error of measurement by various modifications of the ÉKHO-5 echo-sounding level gauge lies in the range $\Delta h/L_{max}$ = 0.5–2.5%, or $\sigma h/L_{max} \approx$ 0.3–1.7% [2], where L_{max} is the upper limit of the range of measurements. The widely used float-type and hydrostatic gauges measuring the levels of liquids have a fundamental error of 1–5% of the upper limit of measurement [9]. The allowable level of noise interference for the ÉKHO-5 gauges is not greater than 60–80 dB [2].

The field tests of RALG were carried out aboard a river tanker and at a shore base of the inland water transport. The monitored substance was fresh water, L = 0.5–3 m, T = +15°C. The tests demonstrated the reliability of the RALG in field conditions and their accuracy being close to the rated value.

The positive results of laboratory and field tests allow us to recommend the RALG for industrial use.

REFERENCES

1. F. J. Berto, Oil Gas J. **95** (10), 63 (1997).
2. *ÉKHO-5 Acoustic Level Gauge. Service Manual* (Staraya Russa, 1991).
3. Patent of the Russian Federation No. 961,210.
4. H. J. McSkimin in *Physical Acoustics*, Ed. by W. P. Mason (Academic, New York, 1964), Vol. 1, Part A, pp. 271–334.
5. S. N. Rzhevkin, *Lectures on the Theory of Sound* (Mosk. Gos. Univ., Moscow, 1960).
6. B. P. Konstantinov, *Hydrodynamic Sound Formation and Propagation in a Bounded Medium* (Nauka, Leningrad, 1974).
7. M. S. Klyuev, V. V. Krasnoborod'ko, V. G. Selivanov, *et al.*, Akust. Zh. **44**, 470 (1998) [Acoust. Phys. **44**, 401 (1998)].
8. G. P. Ivanov, A. G. Trushchev, Yu. L. Savel'ev, and V. A. Malyshev, USSR Inventor's Certificate No. 1,619,051 (October 23, 1987).
9. D. I. Ageĭkin, E. N. Kostina, and N. N. Kuznetsova, *Transducers for Automatic-Control Systems* (Mashgiz, Moscow, 1959).
10. P. K. Otnes and L. Enockson, *Applied Time Series Analysis* (Wiley, New York, 1978).

Translated by A.V. Svechnikov

Acoustical Physics, Vol. 46, No. 3, 2000, pp. 274–283. Translated from Akusticheskiĭ Zhurnal, Vol. 46, No. 3, 2000, pp. 325–335.

Acoustic Field Structure in the First Oceanic Convergence Zone for Different Frequencies in the Audio Range

O. P. Galkin, E. A. Kharchenko, and L. V. Shvachko

Andreev Acoustics Institute, Russian Academy of Sciences, ul. Shvernika 4, Moscow, 117036 Russia

e-mail: bvp@akin.ru

Received December 25, 1999

Abstract—Experimental data on the angular and energy structures of the acoustic field generated in the first convergence zone by a source of continuous pseudo-noise radiation in the frequency range 0.5–4.0 kHz are presented. The experiments are carried out in a tropical region of the Central Atlantic. The acoustic field characteristics are studied with the omnidirectional and highly directional (~2°) reception in the vertical plane. Particular attention is given to studying the field structure at the entrance to the convergence zone at frequencies of 1.25 and 3.15 kHz. The experimental data are compared with the ray calculations. In the experiments, the origin of the convergence zone, which is determined by a sharp increase in the received signal intensity, is found to be about 1.2 km nearer to the source than in the calculations. At a frequency of 1.25 kHz, the convergence zone begins 300 m nearer than at the higher frequency (3.15 kHz). At distances of several kilometers to the zone origin, weak signals that arrive at the same angles as the signals forming the origin of the convergence zone are detected. © *2000 MAIK "Nauka/Interperiodica".*

In investigating the acoustic field structure in the ocean, one of the key problems is the degree of agreement between the experimental data and the computational results for a given waveguide model. The solution of this problem has many aspects, and, first of all, it depends on the requirements that are imposed on the aforementioned agreement in setting various specific problems. At the first stages of studying the energy characteristics of the total acoustic field (with omnidirectional reception), the approximate correlation was already established between the experimental data and the theoretical concepts of long-range sound propagation in the underwater sound channel. However, in the studies of the fine structure of acoustic fields, when the experiments with the directional reception in the vertical plane came into use and more severe requirements had been imposed upon the correlation between the experimental data and the computational results, significant distinctions were revealed, which showed that the problem considered is far from being solved [1–3]. The main discrepancies were observed in the spatial positions of the experimental and calculated boundaries of convergence zones, as well as in the fine (angle, time, energy, and correlation) structure of the acoustic field. In particular, during our experiments carried out in various regions of the ocean at frequencies of 0.5–4.0 kHz, we observed that the first convergence zone was located nearer to the source compared to the calculations (the difference varied from several hundreds of meters to ~1.5 km) [4–6]. In some publications related mainly to the studies of the total field with the omnidirectional reception, deviations by ~200 m are considered insignificant, and this accuracy of the calculations is deemed as quite acceptable [7]. However, for some applied problems, e.g., tomography, related to the prediction of the acoustic field structure and the solution of inverse problems, such deviations can be significant. In addition, the search for the reasons leading to these deviations allows one not only to develop the theory of sound propagation, but also to better understand the physical nature of the phenomena that occur in the ocean.

The problem under consideration was studied by introducing some changes and corrections in the existing models and by improving the metrological support of the experiments. Because the experiments were performed at relatively high frequencies, we used the ray model of waveguide sound propagation, that, as it was shown in [8], allows one to obtain results no worse than those given by the parabolic equation even in the case of a rapid variability of the sound velocity profile (for example, in the thermocline). The refinement of this model with allowance for the Earth curvature and wave corrections in the vicinity of caustics [5] somewhat reduced the discrepancies between experimental and calculated positions of the convergence zone, but did not eliminate them totally.

For improving the metrological support of the experiments, we used a specially developed hydroacoustic system for almost continuous measurements of the distance between the corresponding points (up to once a minute). The distance was measured between the radiation and reception points [9] rather than between the ships, as in the case of the satellite navigation.

1063-7710/00/4603-0274$20.00

In this paper, the main attention is given only to the discrepancies between the experimental and calculated positions of the origin of the first convergence zone at different frequencies from the audio range. In some experimental investigations of the angular and energy structures of the acoustic field, such discrepancies were really observed although, according to the ray theory, they must be absent at frequencies higher than several hundred hertz. For a detailed study of this question, we carried out special measurements in the course of the comprehensive investigations of the acoustic field structure by the research vessels *Sergei Vavilov* and *Petr Lebedev* of the Acoustics Institute. The experiments were carried out in April 1984 in one of the deep-water tropical regions of the Atlantic Ocean. Some results of these investigations were published in [6].

The dependence of the sound velocity c on the depth z in the test region is shown in Fig. 1. For such a profile $c(z)$ with a source in upper oceanic layers, the sound field in the waveguide was formed as a clearly defined sequence of convergence and shadow zones. The experiment was carried out along the track incorporating the three first convergence zones with the continuous variation of the distance between the ships. The rather slow variation of the distance was attained by the drift of the receiving ship and a slow motion of the transmitting ship in the direction opposite to the drift with operating acoustic systems lowered to a given depth. Pseudonoise wide-band radiation in the frequency range 0.5–4.0 kHz was used. The signals were received by an extended 40-m array that consists of 296 hydrophones less than 5 cm in diameter, which were arranged to form 74 phase centers. This allowed us to realize both the omnidirectional reception at any depth within a 40-m layer and the directional reception with the corresponding processing of the received signals. To obtain the data at different frequencies from a wide-band signal, we used 1/3-octave filters for singling out signals with the mid-frequencies f_m equal to 1.25 and 3.15 kHz. The directional pattern width in the vertical plane did not depend on frequency, because the signals with different f_m were received at different lengths of the receiving array. In both cases, the angular resolution was ~2°. The radiator and the center of the receiving array were at depths z = 200 m and z_1 = 190 m, which approximately corresponded to the lower boundary of the thermocline.

Among all results of investigations of the frequency dependence of the acoustic field characteristics that were obtained in this region, we will only consider data that refer to the first convergence zone. In this case, at the origin of the zone, the field structure is formed by signals transmitted through the water layers lying below the radiation and reception depths and, therefore, the influence of an unstable subsurface oceanic layer on the experimental results is eliminated.

The acoustic field structure in the first convergence zone was studied within two days. In this time interval, the zone was passed three times, which allowed us to estimate the stability of the characteristics obtained. Over the total extension of the zone, for both frequency ranges, we recorded the amplitudes and the arrival angles in the vertical plane (the angular field structure), as well as the energy characteristics for omnidirectional reception in a 40-m layer of the array location.

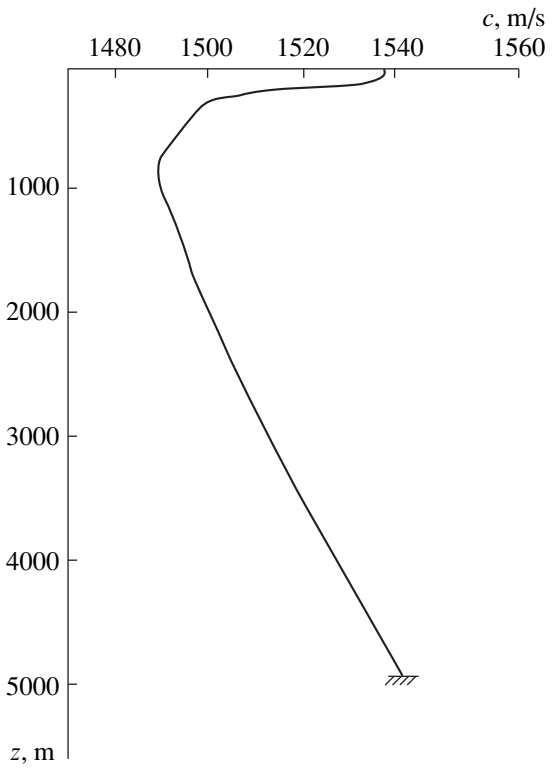

Fig. 1. Sound velocity profile $c(z)$.

Figure 2 shows the results of studying the angular field structure obtained in three passages along the zone for both frequency ranges. The distance r is represented by the abscissa axis, and the signal arrival angles in the vertical plane α are represented by the ordinate axis. The minus sign refers to the signals arriving at the point of reception from below, and the plus sign refers to signals arriving from above. The solid and dashed lines correspond to the calculated dependences $\alpha(r)$ for the water rays and bottom-surface reflections, respectively, and various symbols refer to the experimental data obtained in different passages of the zone. It should be noted that all experimental points in the plot are shifted upwards along the ordinate axis by ~1.5° in order to eliminate an array slope due to the drift of the receiving ship. From this plot, it follows that the general experimental structure for both the water rays and the bottom reflections is close to the calculated structure in the regions where the calculated field differs from zero. A significant deviation only occurs at distances from ~47 to 51 km, where, according to the calculations, no water signals must be present. In the experiment, these signals with a clearly pronounced angular spectrum (in

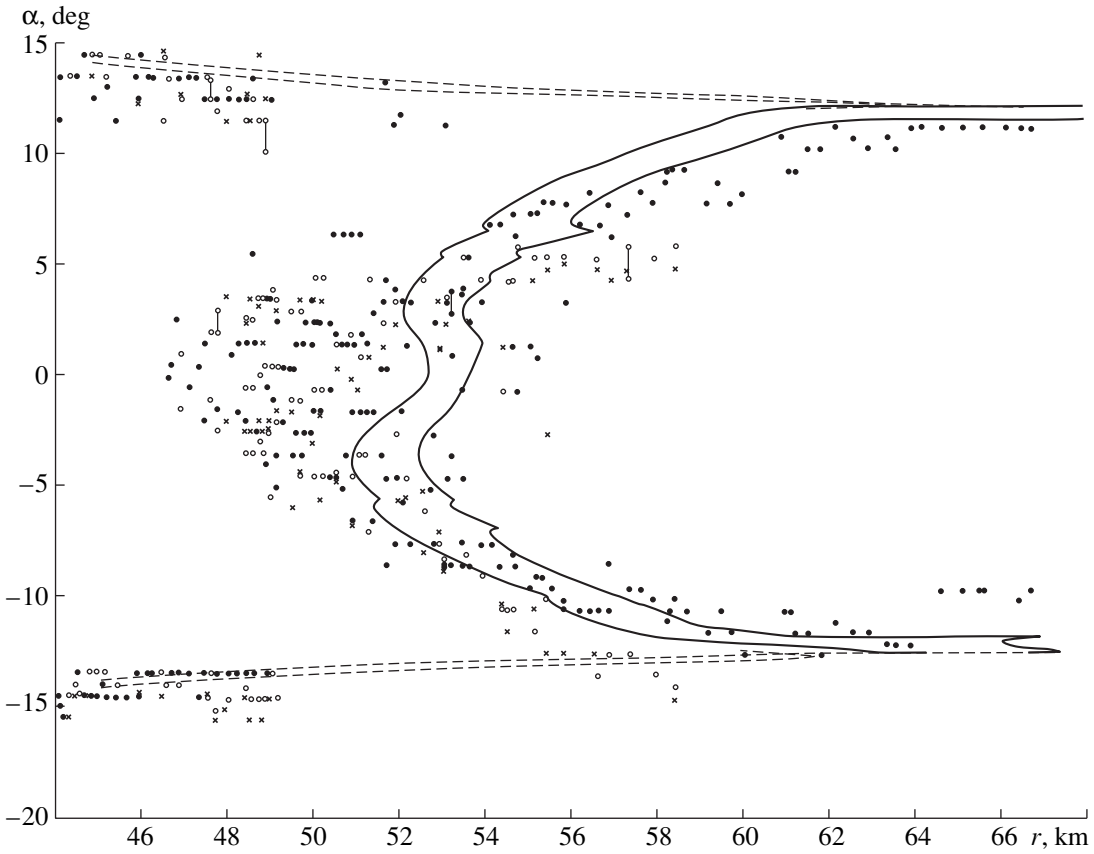

Fig. 2. Angular structure of the sound field in the first convergence zone; z = 200 m, z_1 = 190 m.

the range of arrival angles ±5°) were recorded much nearer to the source (by ~4 km) than the calculated origin of the convergence zone. However, it should be noted that the intensity of these signals was low, and their focusing factor was less than unity. (Some experimental data on the insonification of a shadow zone by water signals of the same frequencies at distances shorter than that of the first convergence zone are presented in [10] for a different region of the ocean.)

Figure 3 exhibits the experimental results obtained by measuring the energy structure over the total extension of the first convergence zone with the omnidirectional reception in the 1/3-octave frequency bands with f_m = 1.25 kHz and f_m = 3.15 kHz. The distance r is represented by the abscissa and the intensity J is the ordinate, where 0 dB corresponds to the signal level at a distance of 1 km for the spherical law of propagation. The solid curve (*1*) corresponds to the measured results, the dotted curve (*2*) to the calculations, and the dot-and-dash curve shows the spherical law $J(r)$ with allowance for the spatial attenuation calculated by the formula $\beta = 0.028f^{3/2}$ dB/km, i.e., 0.04 dB/km for f = 1.25 kHz and 0.16 dB/km for f = 3.15 kHz. The plots in Fig. 3 show that the general behavior of the experimental and calculated dependences $J(r)$ is almost the same; however, they are displaced in distance relative to each other. The calculated origin of the convergence zone ($r \approx 51$ km) "lags behind" the measured origin, which is determined from the rapid increase in the intensity of the received signals, by about 1.2 km for both frequency ranges. In the vicinity of the caustic (near the origin of the zone), the signal propagation anomaly is ~16μ dB for f_m = 1.25 kHz and ~ 22 dB for f_m = 3.15 kHz. The anomaly reaches its maximum level in the first half of the zone at a distance of 51.1–51.3 km, which is equal to 21–22 dB for the signals with f_m = 1.25 kHz and 22–23 dB for the signals with f_m = 3.15 kHz. In these plots, the local maxima and minima are caused by the interference effects arising because of the multipath character of the acoustic field.

In order to investigate in detail the field structure formed only by water signals, we used the directional reception in the vertical plane. Figure 4 compares the energy field structure $J(r)$ obtained at the entrance to the convergence zone at distances from ~48 to ~52 km with the directional and omnidirectional receptions for both frequency ranges considered. The intensity J is represented by the ordinate and the distance r (at the bottom) and the current time t (at the top) are shown on the abscissa axis. Curves with the index *1* obtained for the omnidirectional reception correspond to curves *1* in Fig. 3. Curves with the index *2* represent the depen-

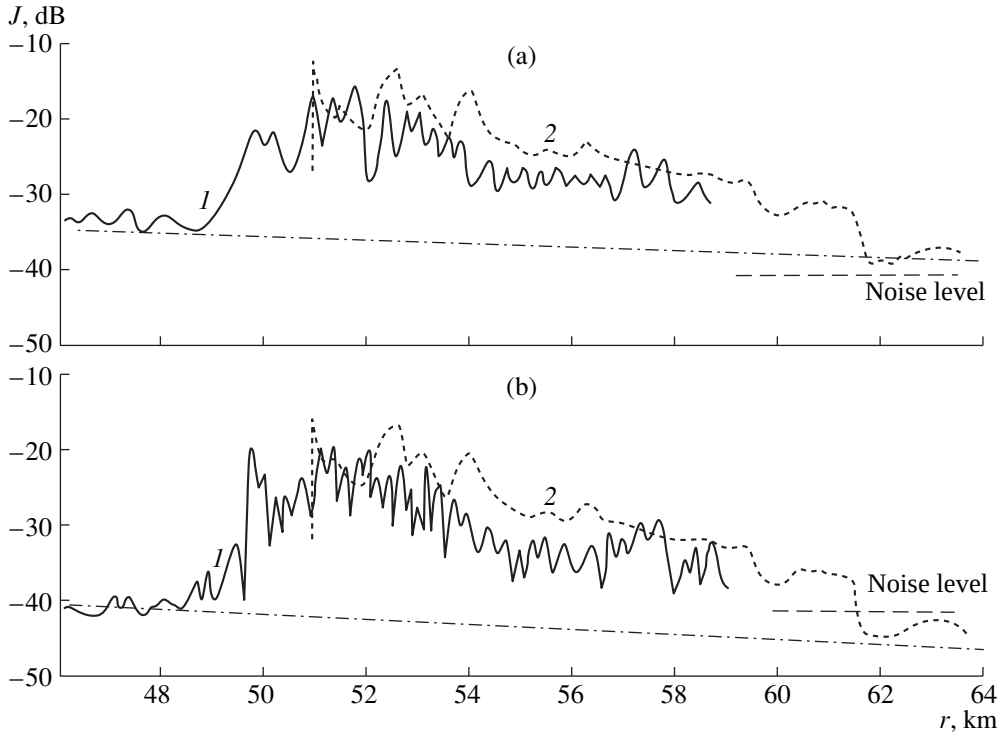

Fig. 3. Energy structure of the sound field in the first convergence zone for the omnidirectional reception; z = 200 m, z_1 = 190 m. The frequency range with f_m = (a) 1.25 and (b) 3.15 kHz.

dences $J(r)$ obtained for the directional reception in the vertical plane (the angular width of the directional pattern is ~2°). The guidance angle of the pattern α corresponded to the direction of the signal arrivals with the maximum intensity in the angular spectrum at each distance (by an angular spectrum the dependence of the amplitudes of signals on their arrival angle in the vertical plane is meant). The spherical law of sound propagation with allowance for the spatial attenuation is shown by a dot-and-dash line. It follows from these plots that the focusing factor of the signals received by the directional system at the entrance to the convergence zone is much less than unity (the intensity of the total signal within the array directional pattern falls by 20 dB below the dot-and-dash line at certain distances). As the distance increases, the amplitude of the received signals gradually increases, and, at a distance of $r \approx$ 49 km for the frequency f_m = 1.25 kHz and a distance of $r \approx$ 49.5 km for f_m = 3.15 kHz, the signal intensities become comparable for the directional and omnidirectional reception. This means that, at these distances, the main contribution to the total field in the omnidirectional reception is given by the signals that propagate not only over the water path, but arrive in the narrow angular range that is used in the directional reception. At longer distances within the convergence zone, a fairly correlated variation of both dependences $J(r)$ is observed.

In the hydrological conditions considered, the origin of the convergence zone is marked by a rapid increase in the amplitude of the received signal. As shown in Fig. 4b, such an increase in the amplitude for the signals with f_m = 3.15 kHz culminated in a well pronounced maximum at a distance of 49.73 km. For signals with f_m = 1.25 kHz, the corresponding maximum of $J(r)$ was less pronounced and observed at a distance of ~49.50 km. According to these data, one can speak about a tendency toward a nearer location of the convergence zone in the experiment at a frequency of 1.25 kHz as compared to a frequency of 3.15 kHz. In Fig. 4, the calculated origin of the convergence zone (50.95 km) is shown by a thick vertical line. Thus, the experimental origin of the convergence zone is ahead of the calculated one by $\Delta r \approx$ 1.45 km for the signals with f_m = 1.25 kHz and $\Delta r \approx$ 1.22 km for the signals with f_m = 3.15 kHz.

A more detailed angular field structure at the entrance to the first convergence zone was obtained from analyzing the continuous sequence of all recorded realizations of the angular spectrum. Fig. 5 exhibits (a) the examples of realizations of the angular spectrum and (b, c) the experimental angular structure of the field $\alpha(r)$ at the entrance to the zone for both frequency ranges. These examples of the angular spectra are photographs taken from an indicator of a sector display of the receiving system. To increase the accuracy of the determination of the signal arrival angles within the range from –20° to +20°, the indicator scale was extended about six times. The exterior scanning on the screen corresponds to the response of the total array length to the signals with f_m = 1.25 kHz, while the inte-

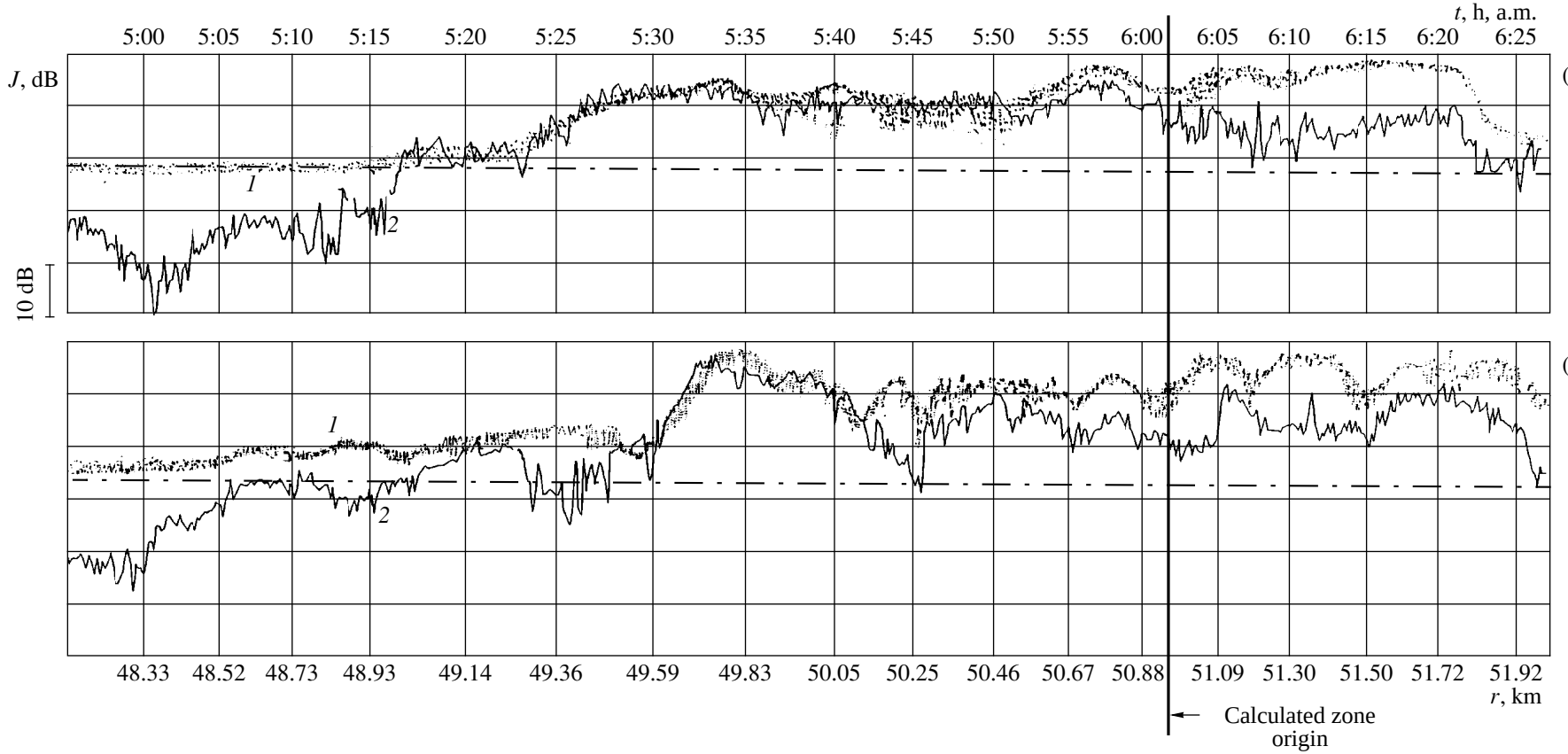

Fig. 4. Energy structure of the sound field at the entrance to the first convergence zone; z = 200 m, z =190 m. The frequency range with f_m = (a) 1.25 and (b) 3.15 kHz.

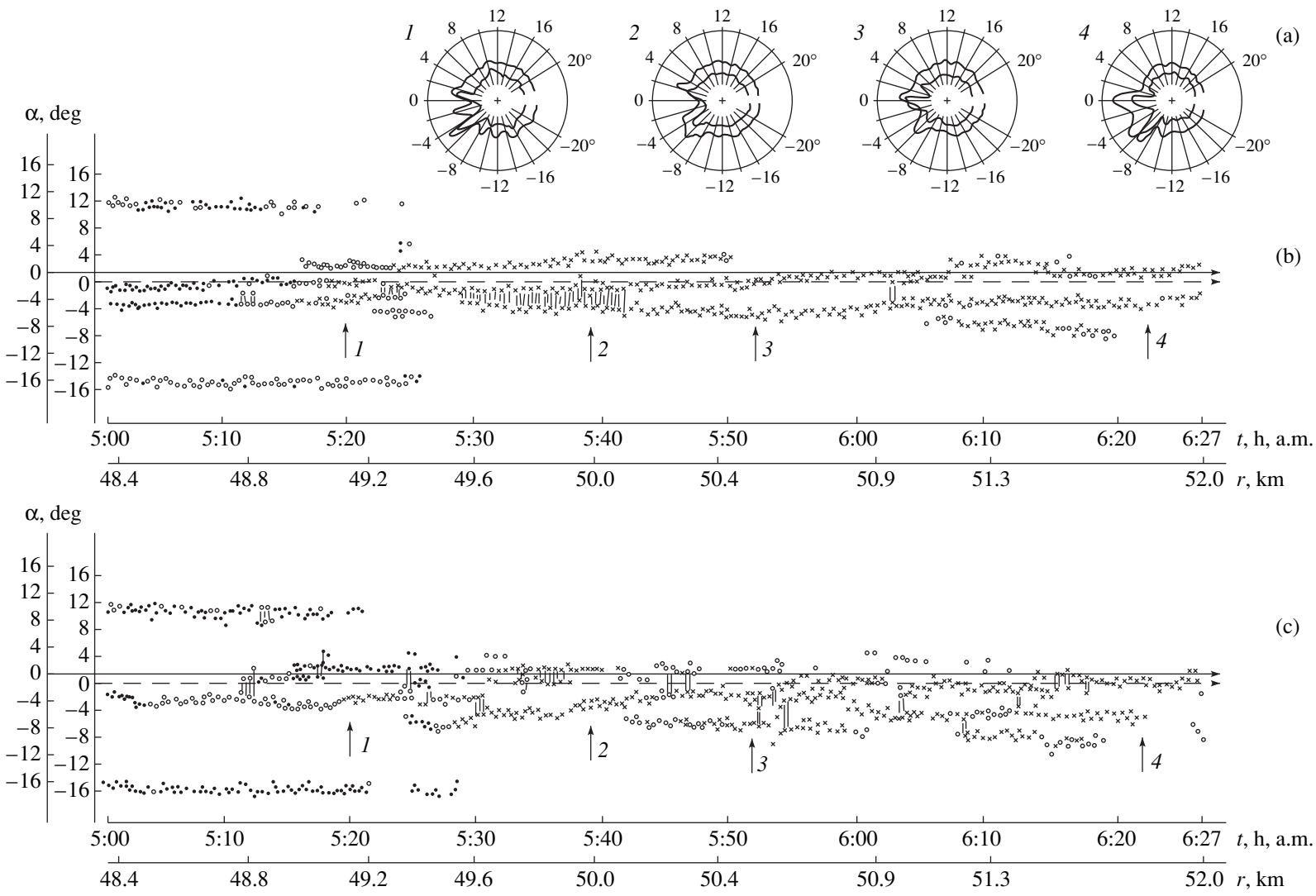

Fig. 5. Detailed angular structure of the sound field at the entrance to the first convergence zone; z = 200 m, z_1 = 190 m. (a) The realization of the angular spectrum of a signal; the experimental dependences $\alpha(r)$ for f_m = (b) 1.25 and (c) 3.15 kHz.

rior scanning refers to the response of the central part of the same array to the signals with the mid-frequency f_m = 3.15 kHz. In Figs. 5b and 5c, the observation time t and the distance to the source r are laid off on the abscissa and the signal arrival angles are plotted along the ordinate axis. The left scale refers to the arrival angles obtained directly from the processing of the angular spectra, while the right scale refers to the arrival angles corrected for the array slope, which was equal to ~1.5°. In order to obtain certain information on the energy relationships of the received signals from the dependences $\alpha(r)$, the experimental values of the arrival angles are shown by four different symbols arranged in the order of increasing signal amplitudes: points, circles, crosses, and stars. When rays are not resolved by the directional pattern but their presence is evident from the angular spectrum form, they were shown by a common oval curve on the plot. The angular spectrum realizations shown in Fig. 5a refer to the field segments that are marked in the plots by vertical arrows with indices *1–4* corresponding to the numbers of the angular spectra.

From the experimental dependences $\alpha(r)$, we can observe the dynamics of the variation of the angular field structure at different segments of the track at the entrance to the convergence zone. In spite of the similarity of the general behavior of the dependences $\alpha(r)$, the fine structure of the field at different frequencies slightly differs, which is confirmed by the photographs of the angular spectra presented in Fig. 5a.

As noted above, a steep increase in the intensity of the received signals is related to the origin of the convergence zone. At these distances, the signals arrive over rays with the grazing angles that slightly differ from each other, and, therefore, to resolve them even using a highly directional system is very difficult. In Figs. 5b and 5c, such segments of the angular structure characterizing the high signal level are located at distances ~49.5–49.6 km and designated by vertically elongated ovals and stars. Let us note that the increase in the signal amplitude with the frequency f_m = 1.25 kHz begins slightly nearer to the source than with the frequency f_m = 3.15 kHz. At distances exceeding ~50.1 km, a simpler angular structure is first formed, which is followed by a more complicated structure with fully resolvable and well observable ray congruences. From Figs. 5b and 5c, it also follows that the angular structure was already formed at the smallest distances (~48.4 km) shown in these plots, i.e., well before the origin of the convergence zone. The angular structure was characterized not only by two families of signals with the arrival angles (±12°–13°) that correspond to the first bottom reflections but also, what is more important, by the family of weak signals with the arrival angles from (+2°…3°) to (−4°…6°). These weak signals arrive at the point of reception over purely water paths. It should be noted that recording these signals with the use of an extened array was possible at shorter distances: according to Fig. 2, it was possible from a distance of ~47 km, the arrival direction being well resolved by the directional array. A pronounced angular dependence corresponding to the width of the directional pattern of the array testifies to a rather well defined front of the arriving signal. An example is the angular spectrum with the index *1* in Fig. 5a, which was recorded at a distance of ~49 km, i.e., before the origin of the convergence zone. The two-ray spectrum for the signals with f_m = 3.15 kHz and the three-ray spectrum for the signals with f_m = 1.25 kHz possess narrow and clearly defined maxima.

Figure 6 compares the experimental angular structure of the sound field at the entrance to the convergence zone with the calculated dependence $\alpha(r)$ for the signals within the frequency range with f_m = 1.25 kHz. The calculated dependence is shown by a solid curve. The distance r is shown on the abscissa, and the upper scale is related to the experiment, while the lower scale is related to the calculation. The calculated curve was imposed on the experimental points in such a way as to reach the best agreement between the experimental and calculated values at the field segments belonging to the convergence zone. The shift in distance between these two dependences is a measure of the difference between the experimental and calculated positions of the convergence zone boundary. With reference to Fig. 6, this shift is $\Delta r \approx 1.45$ km.

The boundary (origin) of the convergence zone was determined more precisely from the experimental data obtained with the directional reception, on the basis of the energy relationships for the recorded signals. Figures 7a and 7b exhibit the dependences of the sound field level on distance at the output of the array for water rays that determine the origin of the convergence zone and correspond to signals of both frequency ranges (f_m = 1.25 kHz and f_m = 3.15 kHz), with arrival angles close to ~−3° (see Figs. 5b, 5c). The distance r and the current time of the experiment t are plotted along the abscissa axis, and the ratio of pressures P/P_{max} is represented by the ordinate on the linear scale, where P_{max} is the maximum pressure at the site considered. In this case, the changes in the signal level, especially in the vicinity of the maximum, can be represented more clearly than on the logarithmic scale (see, e.g., Fig. 4). As noted above, the signals at the entrance to the convergence zone were recorded with the use of the complete length of the 40-m array, as well as by its separate hydrophones. The signals from a group of hydrophones (30 units) uniformly distributed in depth were recorded in the wide frequency band (0.5–4 kHz). Then, they were simultaneously introduced into an analyzer and summed up. The temporal variations of the sound pressure obtained by summing up signals from these hydrophones are shown in Fig. 7c. The comparison of this dependence with those in Figs. 7a and 7b shows a good agreement between the curves obtained for the same instants of time, which confirms the validity of various methods used for recording and processing the signals.

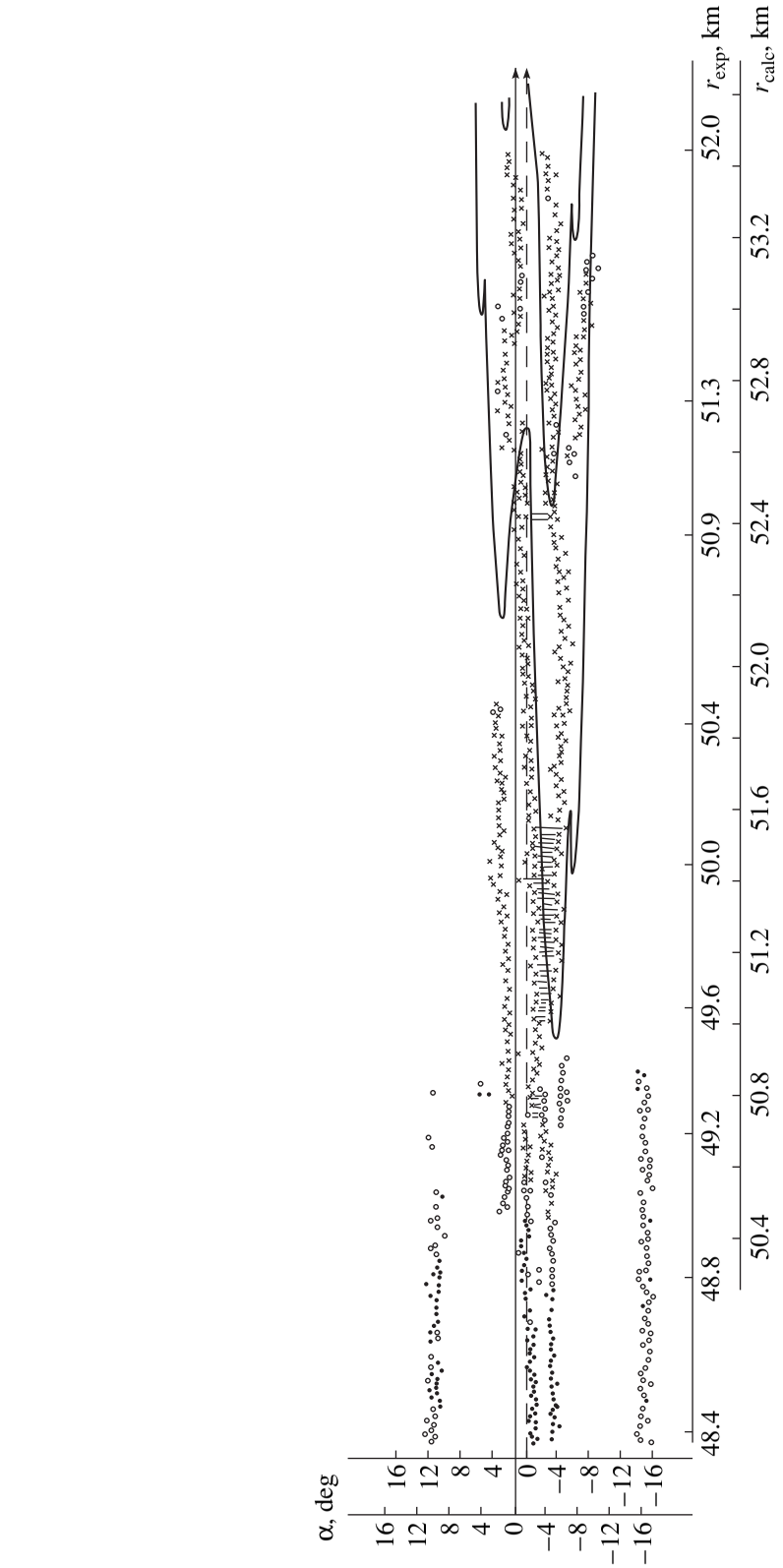

Fig. 6. Comparison of the calculated and experimental dependences $\alpha(r)$ at the entrance to the first convergence zone, $f_m = 1.25$ kHz.

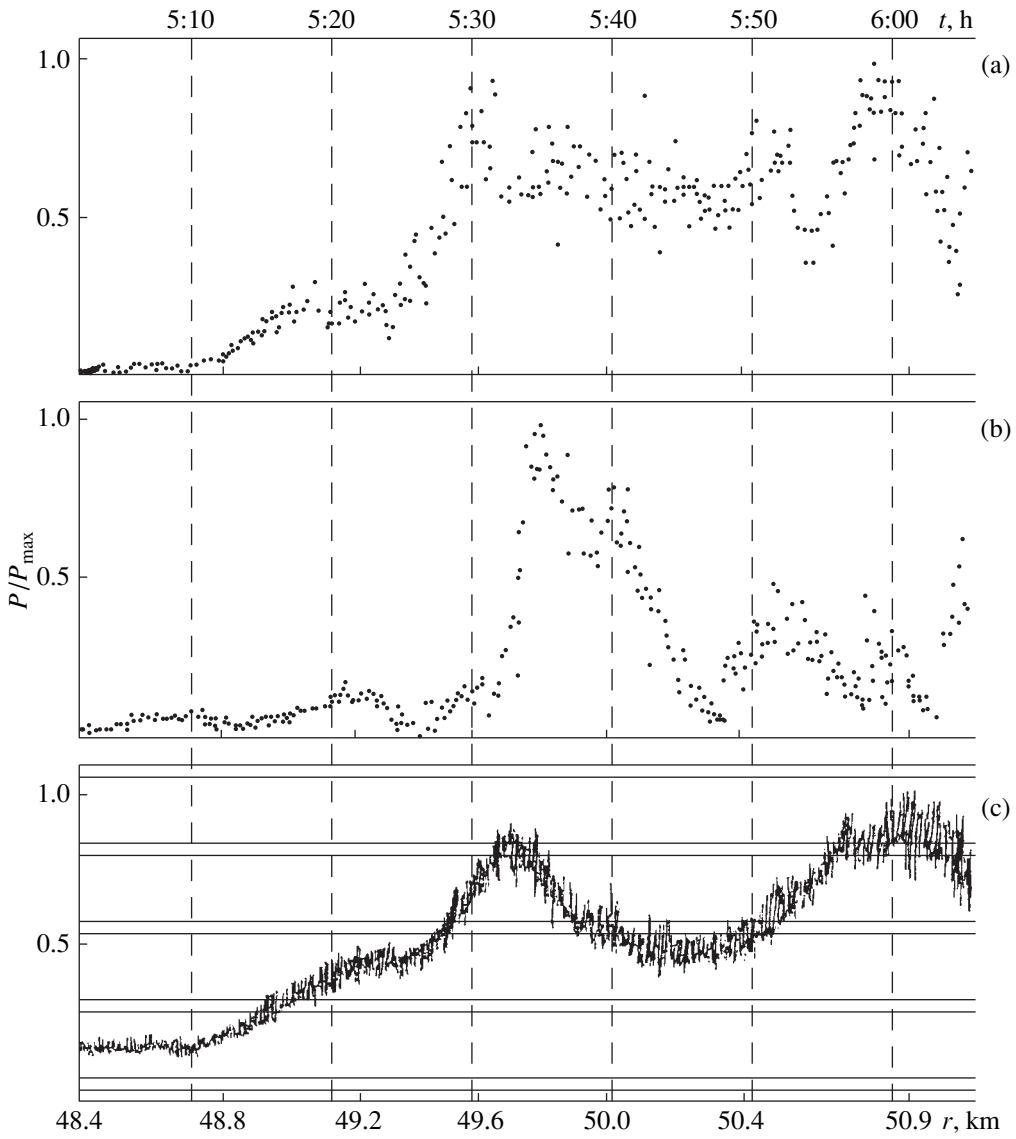

Fig. 7. Sound field level versus the distance for water rays determining the origin of the convergence zone. The frequency range with f_m = (a) 1.25 and (b) 3.15 kHz; (c) the frequency range 0.5–4.0 kHz.

In order to locate the origin of the convergence zone, we proceed from the fact that the field at a simple caustic is by a factor of 1.5 less than at the nearest maximum at the entrance to the convergence zone. The distance Δr_m from the caustic to this maximum can be found from the formula [11]

$$\Delta r_m = \frac{m\left|\partial^2 r/\partial\chi_0^2\right|^{1/3}}{2^{1/3}(k_0\sin\chi_0)^{2/3}}$$

$$= \left|\frac{1.02(\partial^2 r/\partial\chi_0^2)^{1/3}c^{2/3}}{2^{1/3}(2\pi f\sin\chi_0)^{2/3}}\right|,$$

where m is the Airy function argument whose modulus is equal to 1.02, r is the distance from the source, χ_0 is the grazing angle at the radiation point, f is the signal frequency, and c is the sound propagation velocity.

Thus, to determine the origin of the convergence zone from the calculated location of the caustic, it is necessary to find such a distance r in the energy dependences (Fig. 7) that the signal amplitude at this distance be by a factor 1.5 less than its value at the nearest maximum. Then, for the signals with the mid-frequency f_m = 1.25 kHz, we obtain r = 49.48 km, and, for the signals with f_m = 3.15 kHz, we obtain r = 49.79 km. Therefore, the origin of the convergence zone at lower frequencies is nearer to the source by ~300 m than at higher frequencies. A discrepancy between the calculated (50.95 km) and observed locations of the origins of the convergence zone is $\Delta r \approx 1.16$ km for the signals with f_m = 3.15 kHz and Δr = 1.47 km for the signals

with f_m = 1.25 kHz. The displacement of the origin of the convergence zone toward the source for the signals with $f_m \sim 1$ kHz compared to higher-frequency signals was observed by us in other experiments as well. True enough, sometimes the value of such a displacement was much smaller, but the tendency toward such a phenomenon was often observed. This fact somewhat differs from the theoretical results [11]. The ray calculations show that the location of the caustic does not depend on frequency, while the location of the field maximum at a distance of Δr_m is frequency dependent. Therefore, to obtain the signal maximum at a higher frequency, it is necessary to penetrate inside the convergence zone to a smaller distance Δr_m. Therefore, as the frequency decreases, the field maximum nearest to the origin of the convergence zone should move away from the source, rather than approach it as in the experiments.

It should be noted that a similar behavior of the frequency dependence of the convergence zone locations, i.e., the lower frequency, the nearer the convergence zone, was also reported by other authors [12] who analyzed the experimental data on the sound propagation at frequencies of 13.89 and 111.1 Hz along an extended track (from 400 to 2800 km). However, their conclusion was not quite correct, since the authors compared the signal propagation data obtained at different frequencies and radiation–reception depths (104 m for the low frequency and 21 m for the high frequency).

On the basis of the studies of the angular structure of the acoustic fields generated by continuous pseudonoise source in the frequency range 0.5–4.0 kHz in a tropical region of the Central Atlantic, the following conclusions can be drawn:

The field experiments confirm the fact of a discrepancy between the calculated and experimental positions of the origin of the convergence zone in the deep ocean, this discrepancy being observed in many previous investigations. For the hydrological conditions considered above, the origin of the first convergence zone was by about 1.1–1.4 km nearer to the source than in the calculations, which is close to the maximum discrepancy observed in earlier experiments.

As a result of detailed investigations of the angular and energy structures of the sound field in the one-third-octave bands with the mid-frequencies 1.25 and 3.15 kHz, it is shown that there exist a frequency dependence of the spatial position of the convergence zones: at lower frequencies, the first zone is by ~300 m nearer to the source than at higher frequencies.

Within several kilometers of the origin of the convergence zone, the experiments revealed the appearance of weak signals, which propagated without reflections from the waveguide boundaries and arrived at the same angles as the signals forming the origin of the first convergence zone. The mechanism of the weak signal excitation has yet to be understood.

ACKNOWLEDGMENTS

This work was supported by the Russian Foundation for Basic Research, project no. 96-02-19021.

REFERENCES

1. O. P. Galkin, E. A. Kharchenko, and L. V. Shvachko, in *Proceedings of the 9th All-Union Acoustical Conference* (Acoustics Institute, Moscow, 1977), Section D, pp. 1–4.
2. O. P. Galkin, L. V. Shvachko, and E. A Kharchenko, Vopr. Sudostr., Ser. Akust., No. 11, 80 (1978).
3. O. P. Galkin, in *Ocean Acoustics. The State of the Art*, Ed. by L. M. Brekhovskikh and I. B. Andreeva (Nauka, Moscow, 1982), pp. 92–106.
4. O. P. Galkin and L. V. Shvachko, Akust. Zh. **44**, 192 (1998) [Acoust. Phys. **44**, 153 (1998)].
5. O. P. Galkin, L. V. Shvachko, E. A. Kharchenko, *et al.*, in *Problems of Ocean Acoustics*, Ed. by L. M. Brekhovskikh and I. B. Andreeva (Nauka, Moscow, 1984), pp. 118–133.
6. O. P. Galkin, L. V. Shvachko, E. A Kharchenko, *et al*., in *Acoustics in the Ocean*, Ed. by L. M. Brekhovskikh and I. B. Andreeva (Nauka, Moscow, 1992), pp. 114–127.
7. R. A. Vadov, Akust. Zh. **43**, 470 (1997) [Acoust. Phys. **43**, 401 (1997)].
8. K. P. Bongiovanni and W. L. Siegmann, J. Acoust. Soc. Am. **100**, 3033 (1996).
9. A. E. Vedeneev, O. P. Galkin, I. S. Rogozhkin, *et al*., Vopr. Sudostr., Ser. Akust., No. 15, 122 (1982).
10. V. S. Gostev, V. I. Neklyudov, S. D. Chuprov, *et al.*, in *Acoustics of the Oceanic Medium*, Ed. by L. M. Brekhovskikh and I. B. Andreeva (Nauka, Moscow, 1989), pp. 88–97.
11. L. M. Brekhovskikh, *Waves in Layered Media* (Akad. Nauk, Moscow, 1973; Academic, New York, 1980).
12. A. N. Cuthrie, R. M. Fitzgerald, D. A. Nutile, *et al.*, J. Acoust. Soc. Am. **56**, 58 (1974).

Translated by Yu.P. Lysanov

Acoustical Physics, Vol. 46, No. 3, 2000, pp. 284–286. Translated from Akusticheskiĭ Zhurnal, Vol. 46, No. 3, 2000, pp. 336–339.

Laser Generation of Acoustic Waves at a Periodic Domain Structure in Lithium Niobate

A. V. Golenishchev-Kutuzov, V. A. Golenishchev-Kutuzov, and R. I. Kalimullin

Kazan Power Institute, Krasnosel'skaya 51, Kazan, 420066 Russia

e-mail: adm@kfmei.ksu.ru

Received June 30, 1999

Abstract—Generation of coherent acoustic oscillations due to the interaction of laser pulses with the periodic domain structure formed in a lithium niobate single crystal is observed. It is found that the excitation of acoustic waves is most efficient when the generated wavelength is equal to the period of the domain structure. The proposed mechanism of the optical generation of acoustic oscillations consists of the photogeneration of free carriers, which compensate the polarization fields within the domains, and the occurrence of alternating elastic stresses caused by the piezoelectric effect. © *2000 MAIK "Nauka/Interperiodica".*

The modern methods developed for the formation of periodic domain structures in ferroelectrics made it possible to derive new information on the interaction of coherent optical radiation with these structures and to extend the area of their application in nonlinear optics [1]. Most investigations concerned with this phenomenon center on the generation of the second harmonic of the laser radiation interacting with the domain structure. This effect was theoretically substantiated by Armstrong, Bloembergen, and Ducuing as early as 1962 [2]. However, in centrally asymmetric ferroelectrics such as lithium niobate, lithium tantalate, and barium titanate, which have pronounced piezoelectric properties, the interaction of an external field with a periodic domain structure should lead to a wider variety of manifestations.

In this paper, we report on the observation of coherent acoustic oscillations generated as a result of the interaction of laser pulses with a periodic domain structure formed in lithium niobate.

It should be noted that the possibility of a laser generation of acoustic waves at a spatial charge grating (called a holographic grating) was considered in a number of publications [3–5]. Such gratings can be formed by optical radiation in photorefractive crystals. Experimentally, the aforementioned effect was first observed by Pyatakov *et al.* [6]. In these experiments, it was found that the generation of pulses of acoustic waves occurred in the process of erasure of the charge structure under pulsed laser radiation. Thus, the following generation of acoustic waves was possible only after another act of the holographic grating formation by an auxiliary laser. Several years later, a new version of the generation of acoustic pulses was proposed: a photoconducting piezoelectric was irradiated by a laser pulse with a periodic intensity distribution [7]. In this case, the generation mechanism was also related to the process of recording or erasing the field of spatial charge. Below, we will show that the mechanism of the acoustic wave generation at a periodic domain structure has much in common with the generation at a holographic grating, but in this case no erasure of the domain structure takes place.

The experimental study of the laser generation of acoustic waves was performed on a rectangular plate of an *X*-cut lithium niobate crystal. The sample contained $\sim 10^{18}$ cm^{-3} iron ions with a concentration ratio $Fe^{2+}/Fe^{3+} \sim 0.3$. According to Vladimirtzev *et al.* [8], such conditions provide the maximum concentration of photoexcited electrons. A system of 50 ferroelectric domains was preliminarily formed in the middle part of the plate. The width of every domain was about 50 μm, and the domain boundaries were perpendicular to the polarization axis (Fig. 1). The formation of the periodic domain structure was performed by the method described by Mizuuchi and Yamamoto [9]. The plate ends were covered with metal to form electrodes that could be used for a broadband detection of acoustic waves. The optical effect was produced by a homogeneous beam of the second harmonic of a YAG : Nd^{3+} laser ($\lambda = 0.53$ μm). The beam was projected onto the sample surface to form a 10×2 mm^2 rectangular spot. The sample was irradiated with a sequence of pulses characterized by the power density10^4 W/cm^2, pulse duration 1.2×10^{-7} s, and pulse repetition frequency 10–50 Hz. To measure the jumps that occur in the electric field strength within the domains under the laser pulses, the electrooptic effect was used. The refraction index was measured with the help of a low-power He-Ne laser. As a laser pulse affected the region of the periodic domain structure, radio-frequency (r.f.) pulses were detected at both acoustic transducers. According to their travel times to the detectors, these pulses were attributed to the signals of a surface acoustic wave and

the longitudinal and transverse components of a subsurface acoustic wave (Fig. 2). The center of the frequency spectrum of these waves (the spectrum is shown in Fig. 3) corresponds to the condition of the equality between the acoustic wavelength and the period of the domain structure. The strain amplitude in the acoustic wave reached values of about $\sim 10^{-4}$.

According to Lyamshev [10], the generation of elastic waves under a modulated laser radiation is most efficient when it occurs at the expense of a periodic thermoelastic process. Our previous experiments [11] showed that, in such transparent materials as lithium niobate, the thermoelastic generation is effective only in the presence of an absorbing layer ($a_{abs} \geq 10^2$ cm^{-1}) applied to the sample surface, and the frequency range of the generated waves is determined by the duration of the laser pulses.

We propose another mechanism for the laser generation of acoustic waves: it consists of the photogeneration of a great number of electrons, which screen the polarization fields within the ferroelectric domains. Because of the opposite signs of the piezoelectric coefficients in neighboring domains, the jumps in the resulting electric fields cause alternating strains at the domain boundaries. Thus, a periodic domain structure can be represented (Fig. 1c) in the form of a system of periodically arranged sources of acoustic oscillations that propagate in both directions outward from the periodic domain structure. Because of the interference of the oscillations generated by individual sources, an efficient generation of acoustic waves is possible only at the frequencies satisfying the condition

$$f = nV/d, \quad n = 1, 2, 3\ldots \quad d = d_+ + d_-, \qquad (1)$$

where d_+ and d_- are the widths of the domains with direct and inverse polarizations and V is the velocity of the acoustic wave propagation.

After the termination of the laser pulse, a relaxation of the induced field takes place. At a certain ratio between the relative pulse duration and the relaxation time, the polarization fields inside the domains may recover to their initial values by the beginning of the next pulse of the sequence.

It is well known that lithium niobate belongs to the group of crystals that possess a strong photovoltaic field. This field is formed at the expense of the spatial recharging of impurity ions with variable valence, e.g., Fe^{2+} and Fe^{3+} ions. The strength of this field may reach values as high as 10^5 V/cm [12]. In our case, under a uniform irradiation, only the photogeneration of a great number of free electrons n takes place.

To estimate the jump that occurs in the polarization field E_0 under a short laser pulse of duration τ_p, we can use the known system of the Poisson and continuity equations [12]. This system of equations describes the evolution of the field of the spatial charge. When $\tau_p < \tau_r$ (the electron recombination time), the electron recombination processes that occur within the pulse duration can be neglected. Then, the varying polarization field obeys the equation

$$\frac{\partial E}{\partial t} + \frac{E}{\tau} = 0, \qquad (2)$$

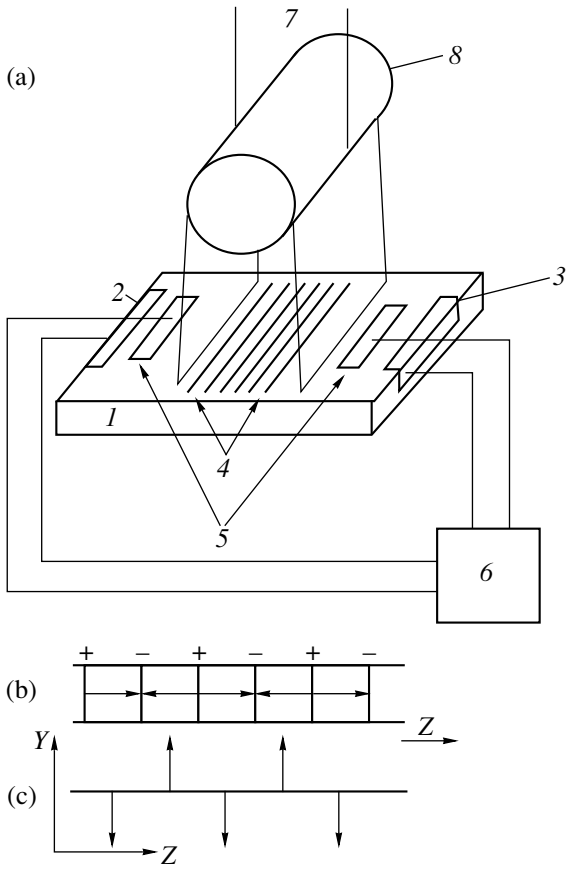

Fig. 1. (a) Experimental setup for the study of the optical generation of acoustic waves at a periodic domain structure; the directions of (b) the polarization fields and (c) piezoelectric axes in the domains. (*1*) Sample; (*2*, *3*) end transducers; (*4*) domain structure; (*5*) capacitive pickups; (*6*) oscilloscope; (*7*) laser beam; and (*8*) cylindrical lens.

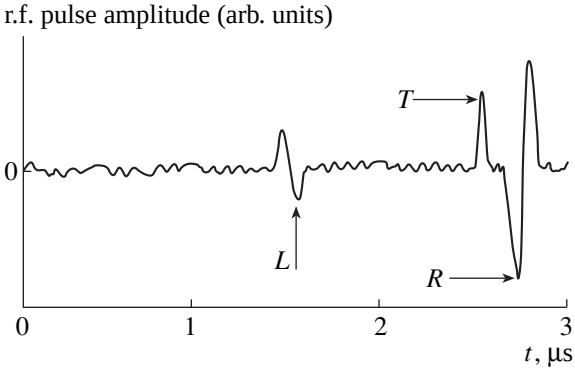

Fig. 2. Acoustic signals corresponding to the (*L*) longitudinal, (*T*) transverse, and (*R*) surface waves.

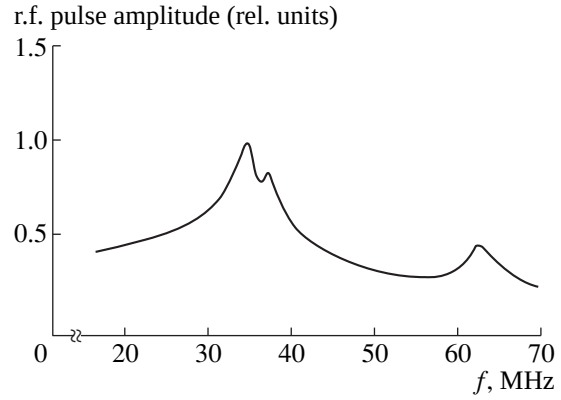

Fig. 3. Frequency spectrum of the acoustic waves excited at the periodic domain structure.

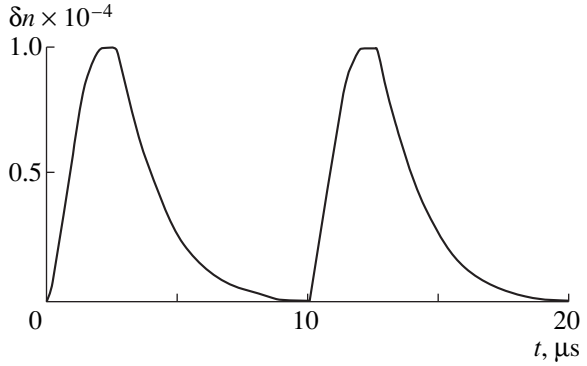

Fig. 4. Periodic variation of the refractive index under optical pulses.

where $\tau = \varepsilon\varepsilon_0/en\mu$; μ and n are the mobility and concentration of photoexcited electrons, respectively.

The solution to equation (2) in the form

$$\Delta E(t) = E_0 \exp(-t/\tau) \quad (3)$$

shows that the variation in the polarization field ΔE is proportional to the optical beam intensity I, because

$$n = g\tau_r; \quad g(t) = \alpha k I/\hbar\omega, \quad (4)$$

where α is the optical absorption coefficient, k is the quantum efficiency of the excitation, and g is the electron generation rate.

For the known material constants of lithium niobate, the aforementioned concentrations of iron ions, and $I \sim 10^4$ W/cm^2, the jump in the field strength may reach 10^4–10^5 V/cm. The proposed mechanism was experimentally verified by the observation of the periodic variation of the refraction index δn within the intervals of pulse duration. The values of δn presented in Fig. 4 correspond to electric field jumps of about $\sim 4 \times 10^4$ V/cm.

We emphasize the fundamental difference between the laser generation of acoustic oscillations and the generation under an alternating electric field applied to a periodic domain structure, the latter effect being also observed in lithium niobate [13]. Firstly, the laser generation provides the possibility to increase the strength of the excited electric fields by one or two orders of magnitude and, thus, to increase the efficiency of acoustooptic devices serving for signal processing. Secondly (this seems to be the most important result), a new possibility is opened up for studying the processes and mechanisms of the interaction between laser radiation and excited carriers.

ACKNOWLEDGMENTS

This work was supported by the Russian Foundation for Basic Research (project no. 99-02-17593).

REFERENCES

1. M. Gupta, W. Kozlovsky, and A. Nutt, Appl. Phys. Lett. **64**, 3210 (1994).
2. Y. Armstrong, N. Bloembergen, and J. Ducuing, Phys. Rev. **127**, 1918 (1962).
3. A. A. Chaban, Akust. Zh. **19**, 463 (1973) [Sov. Phys. Acoust. **19**, 298 (1973)].
4. T. E. Zelenskaya and S. M. Shandarov, Dokl. Akad. Nauk SSSR **289**, 600 (1986) [Sov. Phys. Doklady 31, 574 (1986)].
5. R. Alig, J. Appl. Phys. **46**, 3731 (1975).
6. V. N. Deev and P. A. Pyatakov, Akust. Zh. **34**, 621 (1988) [Sov. Phys. Acoust. **34**, 358 (1988)].
7. P. A. Pyatakov, Akust. Zh. **42**, 840 (1996) [Acoust. Phys. **42**, 744 (1996)].
8. Y. Vladimirtzev, V. Golenishchev-Kutuzov, S. Migachev, *et al.*, Ferroelectrics **22**, 653 (1978).
9. K. Mizuuchi and K. Yamamoto, Appl. Phys. Lett. **66**, 2943 (1995).
10. L. M. Lyamshev, Usp. Fiz. Nauk **135**, 637 (1981).
11. A. V. Golenishchev-Kutuzov, S. A. Migachev, and I. R. Yafaev, Akust. Zh. **31**, 671 (1985) [Sov. Phys. Acoust. **31**, 405 (1985)].
12. M. P. Petrov, S. I. Stepanov, and A. V. Khomenko, *Photorefractive Crystals in Coherent Optics* (Nauka, St. Petersburg, 1992).
13. Y. Zhu, N. Ming, and W. Jiang, Phys. Rev. B **40**, 8536 (1989).

Translated by E.M. Golyamina

Acoustical Physics, Vol. 46, No. 3, 2000, pp. 287–294. Translated from Akusticheskiĭ Zhurnal, Vol. 46, No. 3, 2000, pp. 340–347.

Momentum, Radiation Pressure, and Other Second-Order Quantities in Ideal Gas (Liquid) in Some Boundary-Value Problems

G. G. Denisov

Research Institute of Applied Mathematics and Cybernetics, ul. Ul'yanova 10, Nizhni Novgorod, 603005 Russia

Received July 23, 1998

Abstract—Problems related to such properties of sound waves as momentum, radiation pressure, and sound energy density and flux are investigated on the basis of the solutions of particular problems in the first- and second-order approximations using the Eulerian representation. Specifically, it is shown that a disturbance propagating in a continuous medium may have a nonzero momentum when the average density of the medium in the volume occupied by the wave coincides with the density of the undisturbed medium. In this case, the momentum and the related mass transfer and radiation pressure are caused by variations in the wave profile (envelope). Andreev's expression for the energy density that differs from the commonly used one is verified, and some other paradoxical consequences of the theory of sound are considered. The correctness of using the quantities averaged over time and space is discussed. © *2000 MAIK "Nauka/Interperiodica"*.

The problems dealing with the momentum and radiation pressure of sound waves and the sound energy density and flux, as well as with the relationships between the corresponding average quantities, have been discussed in scientific literature over many years. This issue attracted the attention of Andreev [1], who solved many fundamental problems of acoustics and, in particular, proposed an expression for the sound energy density that differs from the commonly used expression. Note that this problem still remains pressing [1–12], and its solution leads to a number of incomprehensible results. For example, some of the cited publications [3, 8, 10] contain the statement that waves necessarily have a nonzero momentum, while other publications [7, 9] say that this momentum must be zero. Another example is the paradoxical result obtained for a special case of sound wave propagation when the time-average energy density in the sound field is less than the energy density in the undisturbed medium [2, 5]. This paper solves these and other problems on the basis of the study of the planar motion of an ideal gas (liquid) enclosed in a tube with a unit cross-sectional area. We consider small vibrations of gas; however, we solve the equations to the terms of the second order of a small quantity, which is necessary, because many quantities of our interest include quadratic terms. In addition, equations of the second-order approximation contain secular terms; this fact restricts the applicability of the results to the time interval between the beginning of the process and the formation of the discontinuity. Below, we present the solutions of a number of particular problems. For some of the known problems, we use nonstandard formulations. We obtain both instantaneous and average quantities.

In the Eulerian representation, the equations of the planar motion of an ideal liquid (gas) without any external factors acting on it have the form

$$\rho_t + (\rho v)_x = 0, \quad \rho v_t + \rho v v_x + p_x = 0, \qquad (1)$$

where v is the velocity of flow at a given point of the medium, ρ is the density, and p is the pressure. Multiplying the first equation by v and adding the second equation to the result, we obtain

$$\rho_t + j_x = 0, \quad j_t + (j^2\rho^{-1} + p)_x = 0, \qquad (2)$$

where $j = \rho v$ is the density of momentum. As will be seen, these equations appear simpler and more convenient than the initial system. We will consider the propagation of a wave packet in an infinite medium, the interaction of the packet with a reflecting wall, the generation of wave motions in gas by a vibrating piston, the evolution of these motions, and other problems. Since our interest is in solving the problem to the second-order terms, we will seek ρ and j in the form $\rho = \rho_0 + \rho' + \rho'' + \ldots$ and $j = j' + j'' + \ldots$, where the number of primes corresponds to the order of smallness [1, 2]. Assuming that the pressure is a single-valued function of density, we write the Poisson equation

$$p = p_0(\rho/\rho_0)^\gamma,$$
$$p(\rho) \approx p_0 + c_0^2\rho' + \frac{1}{2}c_0^2(\gamma-1)\rho_0^{-1}\rho'^2 + c_0^2\rho'', \qquad (3a)$$

where γ is the adiabatic index and $c_0^2 = (\partial p/\partial \rho)_{\rho = \rho_0}$ is the squared velocity of sound. Equations of the first-order approximation and their obvious solutions are

$$\rho_t' + j_x' = 0; \quad j_t' + c_0^2 \rho_x' = 0,$$
$$\rho'/\rho_0 = f_1(\xi = x + c_0 t) + f_2(\eta = x - c_0 t), \qquad (2')$$
$$j'/\rho_0 = -c_0 f_1(\xi) + c_0 f_2(\eta).$$

Here, f_1 and f_2 are arbitrary functions that describe the waves propagating to the left and to the right, respectively, with a fixed velocity c_0 without any changes in the wave profile; these functions must be small (much less than unity) in magnitude. Below, we will consider, in particular, the case $\gamma < 0$, which is physically nonsense, because it leads to a decrease in pressure with increasing density. In this case, one can assume (for $\gamma = -1$) [3]

$$p = p_0 + \rho_0 c_0^2 (1 - \rho_0 \rho^{-1}). \qquad (3b)$$

With this assumption, the results obtained below will be valid for the γ of any sign.

Wave propagating in an unbounded medium. As follows from solution (2'), the momentum of a wave packet propagating to the left and described by a continuous function $f(x + c_0 t)$ taking finite values within the interval $0 \le x + c_0 t \le l$ and vanishing at the ends of this interval and outside it is completely determined by the deviation of density from its equilibrium value. In particular, if, at a moment t_1, the wave packet is enclosed between x_1 and $x_2 = x_1 + l$ and the excess of mass of the packet is $\rho_0 \int_{x_1}^{x_2} f(x, t_1) dx > 0$, then, the packet momentum will be $\int_{x_1}^{x_2} j'(x, t_1) dx < 0$, which means that the direction of the momentum coincides with the direction of the wave propagation. If the mass is deficient, the momentum will be positive, which means that the momentum and the wave propagation have opposite directions. Similar conclusions can be easily made for the wave propagating to the right. Therefore, according to the solution in the first-order approximation, the motion of a wave packet with a finite momentum is accompanied by a mass transfer in the direction that may not coincide with the propagation direction.

For the wave packet propagating to the left, equations of the second-order approximation have the form

$$\rho_t'' + j_x'' = 0, \quad j_t'' + c_0^2 \rho_x''$$
$$= -\rho_0^{-1}\left(j'^2 + \frac{1}{2}(\gamma - 1) c_0^2 \rho'^2\right)_x = -\varepsilon c_0^2 \rho_0 (f^2(\xi))_x, \qquad (2'')$$

where $\varepsilon = 0.5(\gamma + 1)$.

We will assume that the initial conditions for these equations are nonzero only within the interval $0 < x < l$:

$$\rho''(x, 0) = \rho_2^0(x), \quad j''(x, 0) = j_2^0(x),$$
$$\rho''(x, t) = \frac{\varepsilon}{4}\rho_0[-f^2(\xi) + 2c_0 t[f^2(\xi)]_x + f^2(\eta)]$$
$$+ \frac{1}{2}[\rho_2^0(\xi) + \rho_2^0(\eta) - c_0^{-1} j_2^0(\xi) + c_0^{-1} j_2^0(\eta)], \qquad (4)$$
$$j''(x, t) = \frac{\varepsilon}{4} c_0 \rho_0[-f^2(\xi) + 2c_0 t[f^2(\xi)]_x + f^2(\eta)]$$
$$+ \frac{1}{2}[j_2^0(\xi) + j_2^0(\eta) - c_0 \rho_2^0(\xi) + c_0 \rho_2^0(\eta)].$$

These solutions are obtained for an arbitrary continuous function $f(x, t)$ that has continuous derivatives with respect to x and t. Equations were solved by using the characteristics $\xi = x + c_0 t$, $\eta = x - c_0 t$ and substituting them into equations (2''). The resulting solution assumes that $t < t_d$, where t_d is the instant of the discontinuity formation.

From the solutions for the initial functions $\rho_2^0(x) = 0$ and $j_2^0(x) = 0$, it follows that the wave packet initially propagating to the left and described by the function $f(x)$ is later split into a group of waves propagating to the left and changing their envelopes (two first terms) and a wave propagating to the right (the third term). It appears that, if the initial packet was characterized by zero mass excess and momentum, which were determined by the integral $\int_0^l f(x) dx$, the resulting two groups of waves are characterized by finite mass excesses (or deficits) and momentums, which are determined by the integrals of $f^2(x \pm c_0 t)$, so that these quantities remain zero for the whole wave process. This is a manifestation of the mass and momentum conservation laws for the whole wave process.

Note that the wave propagating in the opposite direction disappears when

$$\frac{\varepsilon}{2} c_0 \rho_0 f^2(x) + c_0 \rho_2^0(x) + j_2^0(x) = 0. \qquad (5)$$

Taking this fact into account and eliminating $j_2^0(x)$, we obtain

$$\rho = \rho_0 + \rho_0 f(\xi) + \frac{\varepsilon}{2}\rho_0 c_0 t[f^2(\xi)]_x + \rho_2^0(\xi),$$
$$j = -c_0 \rho_0 f(\xi) \qquad (4a)$$
$$-\frac{\varepsilon}{2}\rho_0 c_0 \{f^2(\xi) + c_0 t[f^2(\xi)]_x\} - c_0 \rho_2^2(\xi).$$

Additionally, we present the formulas corresponding to $\rho_2^0(x) = -\frac{\varepsilon}{2}\rho_0[xf^2(x)]_x$:

$$\begin{aligned}\rho &= \rho_0 + \rho_0 f(\xi) - \frac{\varepsilon}{2}\rho_0[xf^2(\xi)]_x;\\ j &= -c_0\rho_0 f(\xi) + \frac{\varepsilon}{2}c_0\rho_0 x[f^2(\xi)]_x.\end{aligned} \tag{4b}$$

These solutions differ in the second-order terms that are proportional to $\sim t$ in the first case and to $\sim x$ in the second case; however, the behavior of the solutions is virtually the same, because $x \sim c_0 t$ for propagating waves. From (4a) and (4b), it follows that $\int_{x_1}^{x_2}(\rho' + \rho'')dx$ and $\int_{x_1}^{x_2} j\,dx$ cannot vanish simultaneously.

These formulas relate the momentum and density in a more complicated manner than the formulas of the first-order approximation. For a wave propagating to the right, we obtain the solutions by changing the sign of c_0. From the formulas derived above, it follows that, on the one hand, the wave cannot propagate without distortions (due to the term proportional to t or x) except for the case $\gamma = -1$, which is a well-known result. On the other hand, a nonsplitting wave necessarily has either a momentum or an excess (or deficit) of mass, or both. As an example, for $\rho_2^0(x) = -\varepsilon/2\rho_0 f^2(x)$, the wave packet has a zero momentum and a deficit of mass.

Special attention must be given to an additional fact of great importance that follows from formulas (4a). For $\rho_2^0(x) = 0$ and $\int_0^l f(x)dx = 0$, the wave packet has a zero mass excess, because $\int_0^l [f^2(x)]_x dx = 0$ by virtue of the condition $f(0) = f(l) = 0$, and, simultaneously, it has a finite momentum

$$\int_0^l j''(x)dx = -\frac{\varepsilon}{2}\rho_0 c_0 \int_0^l f^2(x)dx. \tag{6}$$

This brings up the question: How the packet with vanishing excess of mass can provide the mass transfer in view of its finite momentum? To resolve this paradox, let us calculate the momentum of the medium enclosed between the boundaries x_1 and x_2 where a wave packet with the leading edge at $x = -c_0 t$ and the trailing edge at $x = l - c_0 t$ propagates from the right to the left, so that $x_1 \le -c_0 t$ and $l - c_0 t \le x_2$. The center of mass x_c of this part of the medium x_c can be found from the formula

$$\rho_0(x_2 - x_1)x_c = \int_{x_1}^{x_2} x\rho(x, t)dx.$$

Substituting the density from (4a) for $\rho_2^0 = 0$ in this relationship, we obtain

$$\begin{aligned}\rho_0(x_2 - x_1)x_c &= \frac{1}{2}\rho_0(x_2^2 - x_1^2)\\ &+ \rho_0\int_0^l z\,f(z)dz - \frac{\varepsilon}{2}\rho_0 c_0 t\int_0^l f^2(z)dz.\end{aligned}$$

From this formula, it follows that, in the first-order approximation, the wave characterized by a zero average and propagating between x_1 and x_2 results only in a constant displacement of the center of mass of the considered part of the medium. The velocity of the center of mass is completely determined by the second-order term and is caused by the variation in the wave envelope:

$$\rho_0 l\dot{x}_c = -\frac{\varepsilon}{2}c_0\rho_0\int_0^l f^2(z)dz,$$

which coincides with momentum (6). This result can be extended to waves of finite amplitude.

Therefore, despite the wave packet being characterized by a zero mass excess, the packet momentum is related to the mass transfer due to the redistribution of density relative to the packet, i.e., due to the changes in the packet envelope. The momentum is proportional to $\gamma + 1$, and the denser portions have greater velocities then the portions with lower density [4]; as a result, the direction of the momentum coincides with the direction of the packet propagation when $\gamma > -1$. Different directions of the momentum and the velocity of packet propagation for a deficient mass and, in particular, the finite momentum for a packet with zero mass excess essentially distinguish the relation between the momentum and the velocity in a discrete system from that in a continuous medium. In a discrete system, the negative mass can be considered as an analog of the first fact; however, there is no analog of the second fact that is characteristic only of a continuous system and follows from its nonlinearity, the sign of the effect being coincident with the sign of $\gamma + 1$. Note that, for $\gamma = -1$, equations in the Lagrangian representation are linear [2], and the waves propagate without distortions (as in the Eulerian representation). In this case, the second aforementioned fact is absent, and a propagating wave with zero mass excess has a zero momentum [12].

It should be noted that the first-order approximation is insufficient for the determination of momentum (6), in contrast to the case considered by Landau and Lifshitz [4], namely, a wave occupying a finite region of the three-dimensional space with the velocity potential being constant outside the wave region. In the case of plane waves, the velocity potentials in front of the wave and behind it are different.

Thus, a wave propagating in an unbounded medium may have both nonzero and zero momentum, depending on the initial conditions, and a wave with a zero initial momentum is split into two waves propagating in opposite directions. The Brillouin's statement [7] that waves always have zero momentum is explained by the fact that he considered a sinusoidal propagating wave, i.e., a wave with an invariant envelope.

Interaction between a wave packet with an arbitrary envelope and an impenetrable wall. Let the wall be positioned at $x = 0$ and the wave packet be initially located in the region $x_0 < x < l + x_0$ and propagate toward the wall. The interaction between the packet and the wall occurs within the time interval determined by the condition $x_0 \le c_0 t \le x_0 + l$, and, at $x_0 + l \le c_0 t$, the completely formed reflected wave packet propagates away from the wall. Since the wall is assumed to be impenetrable, we can write the condition $j(0, t) = 0$. We will solve this boundary-value problem using a well-known procedure; namely, in the unbounded space, we consider a problem symmetric about $x = 0$. In this problem, $j(x, t) = -j(-x, t)$, $\rho(x, t) = \rho(-x, t)$, and the initial functions $j_0(x)$ and $\rho_0(x)$ are specified so as to generate nonsplitting wave packets symmetric with respect to the wall and propagating toward the wall. We write the solution to this problem in the form:

$$j = +\rho_0 c_0 \Big\{ -f(\xi) - \frac{\varepsilon}{2} f^2(\xi) - \frac{\varepsilon}{2}[f^2(\xi)]_x c_0 t - \rho_0^{-1}\rho_2^0(\xi) + f(\eta) + \frac{\varepsilon}{2} f^2(\eta) - \frac{\varepsilon}{2}[f^2(\eta)]_x c_0 t + \rho_0^{-1}\rho_2^0(\eta) + \frac{1}{4}(3-\gamma)[f_x(\eta)F(\xi) - f_x(\xi)F(\eta)] \Big\};$$

$$\rho = \rho_0 \Big\{ 1 + f(\xi) + \frac{\varepsilon}{2}[f^2(\xi)]_x c_0 t + \rho_0^{-1}\rho_2^0(\xi) + f(\eta) - \frac{\varepsilon}{2}[f^2(\eta)]_x c_0 t + \rho_0^{-1}\rho_2^0(\eta) + \frac{1}{4}(3-\gamma)[f_x(\eta)F(\xi) + f_x(\xi)F(\eta) + 2f(\xi)f(\eta)] \Big\}, \quad (7)$$

where $x_0 \le \xi \le l + x_0$, $-l - x_0 \le \eta \le -x_0$, $F_z(z) = f(z)$, and $\rho_2^0(x, 0)$ are the initial functions for the second-order approximation; $j(0, t) = 0$, because the functions $f(x, t)$ and $\rho_2^0(x, 0)$ are even with respect to $x = 0$.

There are two possible interpretations of the solutions for $j(x, t)$ and $\rho(x, t)$. The first one considers the solutions as two wave packets approaching each other. For $0 \le c_0 t \le x_0$, the packets do not overlap, and the last terms containing the products of the functions of ξ and η vanish. For $x_0 \le c_0 t \le l + x_0$, the packets interact, and all terms of the solutions are nonzero. For $x_0 + l \le c_0 t$, the wave packets move away from each other, and the last terms vanish again. The second interpretation considers the solutions as a description of a wave packet incident on the wall. For $0 \le c_0 t \le x_0$, the whole packet is located to the right of the wall, and one should take into account only the terms dependent on ξ. For $x_0 \le c_0 t \le x_0 + l$, the packet interacts with the wall, and one should take into account all terms for $0 < x$. For $l + x_0 \le c_0 t$, the reflected wave packet moves away from the wall, and one should take into account only the terms dependent on η.

Substituting $\rho(0, t)$ into formula (3a), we obtain the radiation pressure on the wall for any time, and the total effect will be

$$\int_{x_0/c_0}^{(x_0+l)/c_0} p(0, t)\,dt = [2\rho_0 \overline{f(c_0 t)} + \varepsilon\rho_0 \overline{f^2(c_0 t)} + 2\overline{\rho_2^0(c_0 t)}]c_0 l.$$

Now, we calculate the initial momentum of the wave packet for $x > 0$:

$$G(x, 0) = \int_{x_0}^{l+x_0} j(x, 0)\,dx = -\Big[\rho_0 c_0 \overline{f(x)} + \frac{\varepsilon}{2}\rho_0 c_0 \overline{f^2(x)} + c_0 \overline{\rho_2^0(x)}\Big] l.$$

For $x_0 + l < c_0 t_1$ and $0 < x$, the momentum of the reflected packet $G(x, t_1)$ will have the same magnitude but the opposite sign. In this case, $G(x, t_1) - G(x, 0)$ will determine the total force with which the wave packet acts on the wall. If the wave has a zero density excess, the its momentum and force acting on the wall depend on the length of the wave packet, the initial disturbance $f(x, 0)$, and the nonlinear properties of the medium. For $1 + \gamma > 0$, the wave produces positive pressure on the wall, and, for $1 + \gamma < 0$, the pressure is negative.

In parallel with its own significance, this problem immediately supports the idea of Rayleigh [12] that the packet can produce a total pressure on the wall only if it has a nonzero momentum. McEntire [9] considered this idea to be erroneous.

Wave generation in gas by a moving piston. We will consider the motion of gas both to the left and to the right of the piston, which is assumed to be at the origin of coordinates at the initial moment $t = 0$. We will assume that the initial velocities of the piston and the gas were zero everywhere, so that $j(x, 0) = 0$ and $\rho(x, 0) = \rho_0$ for all x. We derive the boundary conditions considering the problem of small vibrations of the piston. The gas velocity v at the piston located at $s(t)$ must coincide with the piston velocity:

$$v(s(t), t) = \dot{s}(t) \approx v'(0, t) + v''(0, t) + v'_x(0, t)s(t).$$

Taking into account the relationship $j(x, t) \simeq (\rho_0 + \rho')(v' + v'')$, we obtain

$$j'(0, t) = \rho_0 \dot{s}(t);$$

$$j''(0, t) = -j_x'(0, t)s(t) + \rho'(0, t)\dot{s}(t).$$

In the first-order approximation, the equations and the boundary and initial conditions are as follows:

$$\rho_t' + j_x' = 0; \quad j_t' + c_0^2 \rho_x' = 0;$$
$$j'(0, t) = \rho_0 \dot{s}(t); \quad 0 \le t \le \infty,$$
$$\dot{s}(0) = 0; \quad j'(x, 0) = 0; \quad \rho'(x, 0) = 0,$$
$$-\infty < x < +\infty.$$

For the second-order approximation, we have

$$\rho_t'' + j_x'' = 0;$$
$$j_t'' + c_0^2 \rho_x'' = -\frac{1}{2}[c_0^2 \rho_0^{-1}(\gamma - 1)\rho'^2 + j'^2 \rho_0^{-1}]_x,$$

$$j''(0, t) = \rho'(0, t)\dot{s}(t) - j_x'(0, t)s(t); \quad j''(x, 0) = 0.$$

In the first-order approximation, the solution to the problem is

$$j' = \Theta(x)\rho_0 s_t(z_-) + \Theta(-x)\rho_0 s_t(z_+),$$
$$c_0 \rho' = \Theta(x)\rho_0 s_t(z_-) - \Theta(-x)\rho_0 s_t(z_+),$$

where $z_\pm = t \pm x/c_0$, $\Theta(x)$ is the unit step function, and $\Theta(0) = 1/2$.

The solution is composed of two identical waves originating at $x = 0$, but propagating in opposite directions. The coordinate of the leading edge of the wave propagating to the right is $x = c_0 t$, and that of the wave propagating to the left is $x = -c_0 t$.

In the second-order approximation, equations for the wave propagating to the right are as follows:

$$\rho_t'' + j_x'' = 0;$$

$$j_t'' + c_0^2 \rho_x'' = -\varepsilon \rho_0 [s_t^2(z_-)]_x, \quad 0 \le x \le c_0 t.$$

For the wave propagating to the left, for $-c_0 t \le x \le 0$, one must replace c_0 by $-c_0$.

The initial conditions are $j''(x, 0) = 0$ and $\rho''(x, 0) = 0$. Taking into account the first-order solution, we bring the boundary conditions to the form:

$$j''(0, t) = \rho_0 c_0^{-1}[s(t)s_t(t)]_t = R_t(t).$$

For the wave propagating to the right, the solution is

$$j' + j'' = \rho_0 s_t(z_-) - \frac{\varepsilon}{2}\rho_0 c_0^{-1} x[s_t^2(z_-)]_x + R_t(z_-),$$

$$\rho' + \rho'' = \rho_0 c_0^{-1} s_t(z_-) - \frac{\varepsilon}{2}\rho_0 c_0^{-2}[x s_t^2(z_-)]_x + c_0^{-1} R_t(z_-).$$

For the wave propagating to the left, one must change the sign of c_0.

The first order solutions ρ', j' are complemented by waves, whose amplitude is proportional to $\gamma + 1$ and increases with increasing x, and waves, whose behavior is governed by the piston motion through the function $R_t(t)$. the terms proportional to x distort the wave envelope. In combination with the first-order terms, they are responsible for the wave momentum. If the piston motion is stopped at some instant $t = T$, two wave packets propagating in opposite directions are formed at this instant. For $t > T$, their leading edges are at $x = \pm c_0 t$, and their trailing edges are at $x = \pm c_0(t - T)$. Let us calculate the momentum and the mass excess of these packets for an arbitrary motion of the piston $s(t)$ under the conditions $s(0) = 0$; $s(t \ge T) = s(T)$; $s_t(0) = s_t(T) = 0$:

$$\int_{x_1}^{x_2} (j' + j'')dx = \rho_0 c_0 s(T) \pm \frac{\varepsilon}{2}\rho_0 \int_0^T s_t^2(\tau)d\tau,$$

$$\int_{x_1}^{x_2} (\rho' + \rho'')dx = \pm \rho_0 s(T),$$

where $x_1 = +c_0(t - T)$ and $x_2 = c_0 t$ for $x > 0$; $x_1 = -c_0 t$ and $x_2 = -c_0(t - T)$ for $x < 0$. The upper sign corresponds to the packet propagating to the right at $x > 0$, and the lower sign corresponds to the packet propagating to the left at $x < 0$. The first-order momentum is determined by the resulting displacement of the piston $s(T)$. In this case, the gas acquires the same momentum both on the right and on the left. In both cases, this momentum is directed along the piston displacement despite the fact that the wave packets propagate in opposite directions. The density excesses is also determined by the piston displacement $s(T)$ and has different signs for waves propagating in opposite directions. For $s(T) > 0$, the medium is compressed to the right of the piston and rarefied to the left of the piston.

In the above formulas for momentum, the second term is of the second order of smallness. However, this term predominates when $s(T) = 0$, i.e., when the piston is stopped at the initial point, or for long intervals T. The direction of the second-order momentum always coincides with the propagation direction of the wave packet for $\gamma + 1 > 0$, and it is opposite to the propagation direction for $\gamma + 1 < 0$. Let us determine the conditions under which the second-order term of the momentum considerably exceeds the first-order term. Consider a piston oscillating according to the law

$$s(t) = a(1 - \cos \omega t) \quad \text{for} \quad 0 \le t \le n\pi/\omega = T,$$
$$s(t) = s(T) \quad \text{for} \quad T < t.$$

In this case, the total time of the piston motion is composed of an integer number of half-periods of its oscil-

lations. For an odd n, the momentums of the wave packets will be given by

$$G_{\pm} = 2\rho_0 c_0 a \pm \frac{\varepsilon}{4}\rho_0 \omega^2 a^2 T,$$

and the desired conditions will have the form $n \gg 8c_0/\pi\varepsilon a\omega$. An estimate shows that this ratio is great even for high-power radiators, and the first term can be neglected only for long trains of waves. For $s(T) = 0$, wave packets are generated with zero mass excess, but with nonzero momentum. This fact agrees with the results obtained above for a wave propagating in an unbounded medium and is a consequence of the variations in the wave envelope. The mass transfer through an arbitrary cross-section x within the time interval between the arrival of the wave packet t_1 and its termination t_2 is equal to zero, i.e., $\int_{t_1}^{t_2} j(x, t)dt = 0$.

The results obtained in solving this problem are comparable with the Earnshaw solution [2, 5]. Here, we emphasize a significant difference between the average quantities. If $\overline{j(x)}^t T$ is the mass of the medium transferred through the cross-section x within the time T, then, $\overline{j(x)}^x l$ is the momentum of the wave packet of length l at the instant t corresponding to the mass transfer within the packet.

Two immobile walls. Consider the gas oscillations with the following boundary and initial conditions:

$$j(0, t) = j(l, t) = 0,$$
$$\rho(0, x) = \rho_0 + \rho_0 ak\cos kx, \quad j(0, t) = 0,$$

where $\sin kl = 0$, $ak \ll 1$, and $c_0 = \omega/k$. Then,

$$\rho = \rho_0 + \rho_0 ak\cos kx\cos\omega t + \frac{\rho_0 a^2 k^2}{4}\cos 2kx$$
$$\times[(2-\varepsilon)(1-\cos 2\omega t) - \varepsilon\omega t\sin 2\omega t],$$

$$j = \rho_0 a\omega\sin kx\sin\omega t + \frac{\rho_0 a^2 k\omega}{4}\sin 2kx$$
$$\times\left[\left(\frac{3}{2}\varepsilon - 2\right)\sin 2\omega t + \varepsilon\omega t\cos 2\omega t\right].$$

In this case, the average radiation pressure $\overline{\Pi}^t = \overline{p + \rho v^2}^t$ is determined as

$$\frac{1}{\tau}\int_{t_0}^{t_0+\tau}\Pi(x, t)dt$$
$$= p_0 + \frac{\varepsilon\rho_0 a^2\omega^2}{4}\left(1 + \frac{\cos 2\omega t_0}{2}\cos 2kx\right).$$

Here, τ is the averaging time equal to an integer number of periods of gas oscillations. As one can see, the average radiation pressure has two components, one constant and one varying in space [2]; however, the latter depends on the time t_0 at which the averaging process begins, and it is completely determined by the secular term of the solution $\rho(x, t)$. This means that the dependence of the average pressure on x is governed by the nonstationary character of oscillations.

For a number of experiments, the quantity t_0 can be considered as random. Then, the last term in the formula can be neglected, and the pressure will everywhere be constant and coincident with the result obtained by Rayleigh [12]. The instability of initial mode of oscillations in the ideal gas calls into question the result obtained in this section (see p. 200 in [2]); however, the result can be considered as a true one for a finite time and under the condition that the accepted idealizations are fulfilled. Additionally, we note that the first-order momentum $\int_0^l j(x, t)dx = \rho_0 ac_0(1 - \cos kl)\sin\omega t$ either is finite and periodically varies (for $\cos kl = -1$), or is always zero (for $\cos kl = 1$). Consequently, in a closed volume completely occupied by an oscillating medium, the pressure is unrelated to the momentum, but is caused by the nonlinearity of the system of equations ($\gamma \neq -1$) and by the wall response.

Sound energy. Zarembo and Krasil'nikov [2] give two expressions for the sound energy density E. In the second-order approximation, these expressions are

$$E_2 = \frac{\rho_0 v'^2}{2} + \frac{c_0^2\rho'^2}{2\rho_0} + \frac{c_0^2}{\gamma - 1}(\rho' + \rho''),$$

$$E_{2A} = \frac{\rho_0 v'^2}{2} + \frac{c_0^2\rho'^2}{2\rho_0} + \frac{c_0^2}{\gamma}(\rho' + \rho'').$$

The first expression is the commonly used formula, and the second expression was proposed by N.N. Andreev [1]. Note that, in the case of an invariable volume V_0, the integral $V_0\int_{V_0}(\rho' + \rho'')dV = 0$, and the total sound energy can be calculated by using only the two first terms that are identical in the above expressions. However, such an approximation is generally inappropriate (e.g., in the case of varying surfaces or in calculating the energy in a portion of the volume). Commonly, the potential energy density is defined as the difference between the energy densities in disturbed and undisturbed media: $w = \rho u - \rho_0 u_0$, where u is the potential energy per unit mass. Since the energy density is determined as the ratio of energy to the volume under consideration, this definition holds only for volumes that remain invariable in the presence of the disturbance. Andreev suggested another definition for the sound energy density by assuming that the potential portion of the energy density is approximately equal to the ratio of the difference between the energies in the presence and absence of sound to the disturbed volume:

$$w_A \approx (\rho uV - \rho_0 u_0 V_0)/V.$$

Andreev considered a fixed mass of the medium m that occupies the volume V_0 before the disturbance and V after the disturbance, so that $\rho V = \rho_0 V_0 = m$. If the mass and the volume are sufficiently small, the quantity w_A can be considered as the density at the point x at the instant t. Taking into account the last relationship, we obtain $w_A(x, t) = \rho(u - u_0)$. The relationship $w_A = w$ holds for $V = V_0$. Adding the kinetic energy, using the known expression for $u(\rho)$ [2, 4], and restricting our consideration to the second-order terms, we obtain the above formulas for E_2 and E_{2A}. A steep increase in E_2 at $\gamma \longrightarrow 1$ casts some doubt on the result. Andreev [1] derived the expression for the sound energy density E_A in the general case. There is no general agreement regarding the definition of E. Using our solutions, we can argue for one or another definition. The difference between the definitions is essential and is evident even in the first-order approximation. This fact considerably simplifies our task. As an example, we will use the result obtained for the wave generation in gas by a moving piston, specifically, the solution $\rho' = \rho_0 c_0^{-1} s_t(t - x/c_0)$. In this problem, in the first-order approximation, all the energy of the wave propagating to the right is determined by the work of the pressure forces acting on the wall and is equal to the product of the pressure p_0 and the wall displacement $s(T)$: $p_0 s(T) = (c_0^2 \rho_0/\gamma)s(T)$, where T is the instant when the piston comes to rest. On the other hand, this energy can be obtained by integrating the energy density of the generated wave with respect to x. With Andreev's energy density, we obtain

$$\int_0^{c_0 t} \frac{c_0^2}{\gamma}\rho' dx = \frac{c_0\rho_0}{\gamma}\int_0^{c_0 t} s_t(t - x/c_0)dx = \frac{\rho_0 c_0^2}{\gamma}s(T) \quad (T < t).$$

The coincidence of the calculated results is evidence in favor of Andreev's expression for the energy density. The same result was obtained for the energy of the disturbance generated by a piston moving with a constant acceleration in an infinite tube; this problem was exactly solved for small ρ' and v' in [4].

The case of a zero mass flux $\bar{j}^t = 0$ is of interest. Such situation corresponds to $\bar{s}_t^t = 0$ in the above problem of a moving piston. Let us take the solution for the wave propagating to the right and calculate the time-average energy density according to the common formula. We obtain

$$\bar{E}^2 = \rho_0 \overline{s_t^2}(t - x/c_0) - \frac{\varepsilon\rho_0}{2(\gamma - 1)}\bar{s}_t^2 = \frac{3\gamma - 5}{4(\gamma - 1)}\rho_0 \overline{s_t^2}.$$

This result casts great doubt upon its validity, because, for $1 < \gamma < 5/3$, i.e., for most gases, it means that the energy in the sound field is less than the energy in an undisturbed medium, which leads to an instability. Papers [2, 5], where this fact was pointed out, suggest different interpretations of this paradox. However, the paradox disappears if one uses Andreev's expression for the energy density. The corresponding calculation gives $\bar{E}_{2A}^t = \frac{3\gamma - 1}{4\gamma}\overline{s_t^2} > 0$ for all gases.

Average quantities. For the characterization of a wave or an oscillating process, the quantities averaged over time are usually more important than their instantaneous values. In most cases, the time-average quantities coincide with the space-average ones. However, this is not the case, for example, for waves whose envelope varies in the course of the wave propagation. To clarify the question as to what kind of average quantities should be used, we consider the equation relating the energy density to the energy flux q:

$$E_t + q_x = 0, \quad \int_{x_1}^{x_2}[E(x, t_2) - E(x, t_1)]dx + \int_{t_1}^{t_2}[q(x_2, t) - q(x_1, t)]dt = 0.$$

We consider the situation in which a wave disturbance propagates from the left to the right, so that its leading edge appears in the cross-section x_1 at $t = t_1$ and in the cross-section x_2 at $t = t_2$. Then, we have

$$\int_{x_1}^{x_2} E(x, t_2)dx = \int_{t_1}^{t_2} q(x_1, t)dt,$$

$$(x_2 - x_1)\bar{E}^x = (t_2 - t_1)\bar{q}^t.$$

Taking into account that $x_2 - x_1 = c_0(t_2 - t_1)$, we obtain from these expressions: $c_0\bar{E}^x = \bar{q}^t$. Thus, the widely used formula $c_0\bar{E}^t = \bar{q}^t$ is inappropriate for waves with varying profile. To calculate the energy in a given volume, one must use either the spatial energy density or the time-average energy flux through a given surface. The aforesaid also applies to the equations

$$\rho_t + j_x = 0, \quad j_t + \Pi_x = 0,$$

where one must use the average quantities $\bar{\rho}^x$ and $\bar{j}^t$ for calculating the mass and the mass flux (the first equation) and $\bar{j}^x$ and $\bar{\Pi}^t$ for calculating the momentum and the radiation pressure (the second equation). Additionally, we present the formula that expresses the radiation pressure in terms of the kinetic energy for the distance between the walls being invariant (the piston problem considered above) and for spring-loaded walls:

$$\overline{\Pi''}^t = \varepsilon\bar{\bar{E}}_k, \quad \overline{\Pi''}^t = \varepsilon\bar{\bar{E}}_k rl/(rl + \rho_0 c_0^2).$$

Note that radiation pressure strongly depends on the spring rigidity *r*.

The main results. An isolated wave may have a nonzero or zero momentum depending on the initial conditions. A wave with zero excess or deficit of density has a momentum caused by the nonlinearity and directed in the propagation direction when $\gamma + 1 > 0$. Variations in the wave envelope are an indication of the presence of a nonzero momentum. A mass transfer necessarily accompanies the propagation of a wave with a nonzero momentum.

One should distinguish between the factors responsible for the radiation pressure in the case of a closed volume completely filled with an oscillating medium and in the case of an isolated wave acting on a reflecting obstacle.

For undisturbed gas, the pressure behaves in accordance with the Poisson law $p_0 = p(\rho_0)$. In the presence of acoustic oscillations, by virtue of the nonlinear dependence $\Pi(\rho, v) = p(\rho) + \rho v^2$, the periodically varying density ρ' and velocity v' lead to an increase in the average pressure for $\gamma > -1$, i.e., to the appearance of the radiation pressure $\overline{\Pi - p_0}^t$. Hence, the volume of gas is increased, if the volume is bounded with surfaces held in pace by forces characterized by a finite rigidity. In this case, the radiation pressure is determined by the kinetic energy density of gas and the rigidity of the walls enclosing the volume, and it does not depend on the total momentum of gas. Here, we have a complete analogy with the thermal expansion of bodies due to the nonlinearity of interatomic bonds.

In the case of an isolated wave packet, the radiation pressure on a reflecting obstacle is completely determined by the variations in the packet momentum (as it is generally believed).

ACKNOWLEDGMENTS

I am grateful to V.A. Zverev for including my report in the agenda of his seminar and for useful discussions. This work was supported by the Russian Foundation for Basic Research, project nos. 96-01-00927 and 99-01-00061.

REFERENCES

1. N. N. Andreev, Akust. Zh. **1**, 3 (1955) [Sov. Phys. Acoust. **1**, 2 (1955)].
2. L. K. Zarembo and V. A. Krasil'nikov, *Introduction to Nonlinear Acoustics* (Nauka, Moscow, 1966).
3. J. Rayleigh, *The Theory of Sound* (Dover, New York, 1945; Gostekhizdat, Moscow, 1955), Vol. 2.
4. L. D. Landau and E. M. Lifshitz, *Fluid Mechanics* (Nauka, Moscow, 1986; Pergamon Press, Oxford, 1987).
5. L. A. Ostrovskiĭ, Akust. Zh. **14**, 82 (1968) [Sov. Phys. Acoust. **14**, 61 (1968)].
6. K. A. Naugol'nykh and L. A. Ostrovskiĭ, *Nonlinear Wave Processes in Acoustics* (Nauka, Moscow, 1990).
7. L. Brilloin, Ann. Phys. (Paris) **4**, 528 (1925).
8. B. B. Kadomtsev and V. I. Rydnik, *Waves around Us* (Znanie, Moscow, 1981).
9. M. McEntire, in *Journal of Fluid Mechanics. A Special Issue Celebrating the 25th Anniversary of the Journal*, Ed. By G. Batchelor and H. Moffatt (Cambridge University Press, Cambridge, 1981), Vol. 106; in *Modern Fluid Mechanics: Progress and Problems* (Mir, Moscow, 1984).
10. *Physics Encyclopedia* (Sov. Éntsiklopediya, Moscow, 1988), Vol. 1.
11. G. G. Denisov, Mekh. Tverd. Tela, No. 1, 42 (1994).
12. J. Rayleigh, Phil. Mag. **10**, 364 (1905).

Translated by A.G. Vinogradov

Acoustical Physics, Vol. 46, No. 3, 2000, pp. 295–301. Translated from Akusticheskiĭ Zhurnal, Vol. 46, No. 3, 2000, pp. 348–355.

Dissipation and Dispersion Properties of Microinhomogeneous Media

V. Yu. Zaĭtsev, V. E. Nazarov, and A. E. Shul'ga

Institute of Applied Physics, Russian Academy of Sciences, ul. Ul'yanova 46, Nizhni Novgorod, 603600 Russia

e-mail: nazarov@hydro.appl.sci-nnov.ru

Received June 8, 1999

Abstract—The propagation of a harmonic elastic wave in a microinhomogeneous (defect-containing) medium is considered in the framework of the rheological model that reperesents the medium in the form of a one-dimensional chain of masses connected by purely elastic elements and by Kelvin–Voigt viscoelastic elements. Analytical expressions are derived for the dissipation and dispersion characteristics of this medium for various distributions of the parameters of the viscoelastic elements. The dissipation and dispersion properties are found to obey the Kramers–Kronig relations. It is also shown that the damping decrement of the wave is almost constant, and the phase velocity monotonically increases in a sufficiently wide range of parameters of the viscoelastic elements in a wide frequency band. The derived expressions for the dispersion and dissipation are used to simulate the propagation of broadband pulses in this kind of medium. © *2000 MAIK "Nauka/Interperiodica".*

INTRODUCTION

It has been established experimentally that, in a wide frequency band, most microinhomogeneous (defect-containing) solids (in particular, rocks and metals) are described by an almost constant Q-factor [1–3]. The Kramers–Kronig relations [1, 4], which relate the dispersion and attenuation characteristics, show that these media must also exhibit noticeable dispersion. This conclusion is corroborated by experiments. They show that, in particular, the waveforms of propagating seismic pulses are asymmetric [1]. The problem of an adequate analytical description of the dissipation and dispersion properties of such media as functions of frequency is still under discussion [1, 3, 5, 6], because phenomenological approximations of these dependencies often do not fit each other and violate the causality principle.

A rheological model of a microinhomogeneous medium was proposed in our previous publications [7, 8]. This model explains why the Q-factor of such a medium is almost frequency-independent. We calculated the Q-factor on the basis of the energy approach, which allows for the absorption of the elastic wave energy by soft dissipative inclusions (defects) of different compliance. Clearly, this approach cannot directly determine the dispersion properties of the medium, though they can be found from the dissipation dependencies provided by the Kramers–Kronig relations.

In this paper, we derive the dissipation and dispersion properties of the microinhomogeneous medium in the framework of the rheological model [7, 8]. At first, we address the propagation of a harmonic elastic wave in this medium and find its attenuation factor and propagation velocity. Then, we show that the dissipation and dispersion properties thus derived satisfy the Kramers–Kronig relations. Finally, we study the propagation of broadband pulses by numerical simulation with the use of these dissipation and dispersion relations.

MODEL OF A MICROINHOMOGENEOUS MEDIUM AND THE BASIC EQUATIONS

Consider the propagation of a harmonic elastic wave in the framework of the model that represents the microinhomogeneous medium as a chain of masses and elastic and viscoelastic elements [7, 8] (Fig. 1). As in [7], we assume that the elastic elements of the chain are characterized by the elasticity coefficient K, and the dissipation effects are associated with the Kelvin–Voigt viscoelastic elements whose equations of state have the form

$$\sigma = k_j X + g\dot{X}, \tag{1}$$

where k_j and g are the elasticity and viscosity coefficients of the jth element ($k_j = \zeta_j K$, $\zeta_j \ll 1$), X is the variation of the defect length, and $\dot{X} = \partial X/\partial t$. Assume that a unit length of this chain contains a total of N elements of the length H, the number of viscoelastic elements being equal to N_1, so that the ratio $\nu = N_1/N$ characterizes the defect density. Also assume that the length of the elastic wave $\lambda = 2\pi/k$ (where k is the wave number) is much greater than the defect length H, so that $kH \ll 1$. These conditions allow one to regard the homogeneous regions of the chain as a continuum and assume that the elastic wave subjects each element to quasistatic deformations. Then, one can consider the interaction of the

1063-7710/00/4603-0295$20.00 © 2000 MAIK "Nauka/Interperiodica"

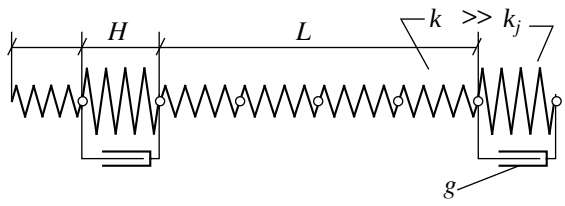

Fig. 1. Rheological model of a microinhomogeneous medium.

elastic wave with the defect of number j in terms of only the incident, reflected, and transmitted waves outside this defect and describe the deformation of the defect by the equations

$$\begin{aligned} \sigma_i + \sigma_r\big|_{x = x_j} &= \sigma_t\big|_{x = x_j + H}, \\ U_i - U_r\big|_{x = x_j} &= U_1, \\ U_t\big|_{x = x_j + H} &= U_2, \\ \sigma_t\big|_{x = x_j + H} &= k_j(U_2 - U_1) + g(\dot{U}_2 - \dot{U}_1), \end{aligned} \tag{2}$$

where $x = x_j$ and $x = x_j + H$ are the coordinates of the defect boundaries, and the stress and strain, σ_i, σ_r, σ_t and U_i, U_r, U_t, in the incident, reflected, and transmitted waves, respectively, are related through the elasticity coefficient K

$$\sigma_{i,r,t} = K\partial U_{i,r,t}/\partial x. \tag{3}$$

DISPERSION RELATION FOR THE MICROINHOMOGENEOUS MEDIUM

For a harmonic wave $\exp(-i\omega t \pm ikx)$ propagating in the homogeneous part of the chain in the positive (incident and transmitted waves) and negative (reflected wave) directions, respectively, equations (3) take the form

$$\sigma_i = ikKU_i, \quad \sigma_r = -ikKU_r, \quad \sigma_t = ikKU_t, \tag{4}$$

where $k = \omega/c_0$ and c_0 is the elastic wave velocity in a defect-free medium. Introduce the transmission T_j and reflection R_j factors for the jth defect:

$$\sigma_i\big|_{x = x_j} = R_j\sigma_r, \quad \sigma_t\big|_{x = x_j + H} = T_j\sigma_i. \tag{5}$$

Substituting expressions (4) and (5) into the system of equations (2), we obtain

$$R_j = \exp(2ikx_0)\left[\frac{2(\zeta - i\omega/\Omega)}{ikH} - 1\right]^{-1}, \tag{6}$$

$$T_j = \exp(-ikH)\left[1 - \frac{ikH}{2(\zeta - i\omega/\Omega)}\right]^{-1}, \tag{7}$$

where $\Omega = K/g$.

These expressions show that, when $kH \ll \zeta_j < 1$, the magnitudes of the transmission and reflection factors tend to unity ($|T_j| \longrightarrow 1$) and zero ($|R_j| \ll 1$), respectively. Under the assumption that reflection from each defect is negligible, the microinhomogeneous medium can be considered as an equivalent homogeneous (on average, on a scale much larger than the distance between the defects and covering a great number of them) medium with effective (spatially averaged) parameters [9]. In order to calculate the effective parameters of the equivalent homogeneous medium, which characterize the wave attenuation and the phase shift gained in the course of the propagation through the chain of the length $L = NH$ containing a large number of defects, let us find their effect on the wave amplitude and phase. Clearly, for this purpose one should find a product of the transmission factors of all elements of the chain. As a result, we obtain the following formula for the total transmission factor T_{total} of the wave transmitted through the chain of length L:

$$T_{\text{total}} = \exp(-ikL)\prod_{j=1}^{N_1}\tilde{T}_j, \tag{8}$$

where the factor $\exp(-ikL)$ describes the phase delay of the wave transmitted through the chain of length $L = NH$ consisting of N elements, N_1 of which contain defects, and the factors $\tilde{T}_j$ are given by the expression

$$\tilde{T}_j = \left[1 - \frac{ikH}{2(\zeta_j - i\omega/\Omega)}\right]^{-1}. \tag{9}$$

By equating expression (8) to the transmission factor of the equivalent homogeneous medium defined as $T_0 = \exp(-i\tilde{k}L)$, we obtain an equation for the complex wave number $\tilde{k} = \tilde{k}(\omega)$ of the homogeneous medium

$$\exp(-ikL)\prod_{j=1}^{N_1}\tilde{T}_j = \exp(-i\tilde{k}L), \tag{10}$$

which yields

$$(\tilde{k} - k)L = -i\ln\left(\prod_{j=1}^{N_1}\tilde{T}_j\right) = -i\sum_{j=1}^{N_1}\ln(\tilde{T}_j). \tag{11}$$

Next, we take into account that, for the part of defects that are described by the same parameter ζ_j, $\sum_{j=1}^{N_j} H/L = \nu_j$ characterizes their linear concentration. When the number of defects is great, the distribution function $\nu = \nu(\zeta)$ can be introduced, so that $\nu(\zeta)d\zeta$ is the number of defects belonging to the interval $[\zeta, \zeta + d\zeta]$ per unit length of the chain. Then, in view of (9), expression (11) takes the form

$$\tilde{k} - k = i\int_0^1 \ln\left[1 - \frac{ikH}{2(\zeta - i\omega/\Omega)}\right]\nu(\zeta)d\zeta. \tag{12}$$

When $kH \ll \zeta < 1$, this equation yields the dispersion relation for the microinhomogeneous medium:

$$\tilde{k} - k = \frac{kH}{2}\int_0^1 \left[\frac{\zeta}{\zeta^2 + (\omega/\Omega)^2} - \frac{i(\omega/\Omega)}{\zeta^2 + (\omega/\Omega)^2}\right]\nu(\zeta)d\zeta. \quad (13)$$

The first summand in the integrand determines the frequency-dependent phase correction, and the second one determines the wave attenuation. Using the relationship $\theta(\omega) = \alpha(\omega)\lambda$ between the wave attenuation factor $\alpha(\omega)$ and the damping decrement $\theta(\omega)$ in equation (13), we obtain

$$\theta = \pi\int_0^1 \nu(\zeta)\frac{\omega/\Omega}{\zeta^2 + (\omega/\Omega)^2}d\zeta. \quad (14)$$

(A similar expression was obtained in [7, 8] by summing the losses due to individual inclusions.) Equation (13) can be used to obtain the dispersion correction to the phase velocity $\Delta c(\omega) = c(\omega) - c_0$ (when $\Delta c/c_0 \ll 1$):

$$\frac{\Delta c(\omega)}{c_0} = -\frac{1}{2}\int_0^1 \nu(\zeta)\frac{\zeta}{\zeta^2 + (\omega/\Omega)^2}d\zeta. \quad (15)$$

According to [7, 8], the independence of the Q-factor from frequency can be explained under the assumption that the defect distribution in the parameter ζ is wide, which is likely to be valid for actual microinhomogeneous media. (Taking additionally into consideration the defect distribution in the parameter Ω does not change the main conclusions. Therefore, for the time being, we can assume that the parameter Ω is constant.) Let the defect distribution in the parameter ζ in equations (14) and (15) be described by a Π-shaped function

$$\nu(\zeta) = \nu_0 \text{ for } \zeta \in [a, b], \quad a \ll \zeta \ll b,$$
$$\nu(\zeta) = 0 \text{ for } \zeta \notin [a, b]. \quad (16)$$

In this case, integral (14) yields

$$\theta = \pi\nu_0 \arctan\left[\left(\frac{b\Omega}{\omega} - \frac{a\Omega}{\omega}\right)\Big/\left(1 + \frac{ba\Omega^2}{\omega^2}\right)\right]. \quad (17)$$

From expression (17), we obtain

$$\theta \approx \pi\nu_0(\omega/2a\Omega), \text{ for } \omega/\Omega < a, \quad (18)$$

$$\theta \approx \pi^2\nu_0/2, \text{ for } a < \omega/\Omega < b, \quad (19)$$

$$\theta \approx \pi\nu_0(b\Omega/2\omega), \text{ for } \omega/\Omega < b. \quad (20)$$

In a similar manner, we use expression (15) for the dispersion correction to obtain

$$\frac{\Delta c(\omega)}{c} \approx -\frac{\nu_0}{4}\ln\frac{b^2 + (\omega/\Omega)^2}{a^2 + (\omega/\Omega)^2}. \quad (21)$$

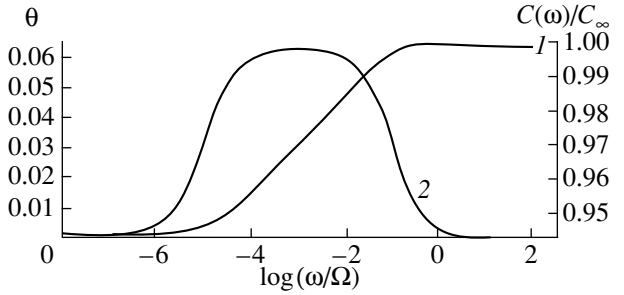

Fig. 2. (*1*) Dispersion and (*2*) dissipation characteristics of the medium for $a = 10^{-5}$, $b = 10^{-1}$, $\Omega = 10^8$ Hz, $\nu = 1.3 \times 10^{-3}$, and $c_0 = 3000$ m/s.

This correction is negative and tends to zero as $\omega \longrightarrow \infty$; therefore, c_0 has the meaning of the high-frequency limit of the phase velocity in the microinhomogeneous medium. Figure 2 displays the damping decrement and the phase velocity of the elastic wave against frequency. These plots show that a wide defect distribution in elasticity leads to a wide frequency region $a < \omega/\Omega < b$ where the damping decrement is almost constant and the phase velocity gradually increases. It is of interest that, in this region, the decrement is independent of the viscosity of the defects and is determined by their density alone. The relative change in the wave phase velocity $\Delta c/c_0 = [c(\omega \gg b\Omega) - c(\omega \ll a\Omega)]/c_0 \approx (\nu_0/2)\ln(b/a)$ is also determined by the defect density and by the range $d = b/a$ where $\theta \approx$ const.

ALLOWANCE FOR THE DEFECT DISTRIBUTION IN VISCOSITY

Expressions (17) and (21) were derived under the assumption that the defects possess identical viscous properties, i.e., that the parameter Ω is the same for all defects. In real microinhomogeneous media, the viscoelastic inclusions are not only distributed in their elastic parameters, but also in their viscous properties. It can be expected that these distributions are statistically independent, i.e.,

$$\nu = \nu(\zeta, \Omega) = \nu(\zeta)\nu(\Omega). \quad (22)$$

In this case, in order to find the contribution of all defects, the integrals in (14) and (15) should be taken with respect to both parameters ζ and Ω:

$$\theta = \pi\iint \nu(\zeta, \Omega)\frac{\omega/\Omega}{\zeta^2 + (\omega/\Omega)^2}d\Omega d\zeta, \quad (23)$$

$$\frac{\Delta c(\omega)}{c_0} = -\frac{1}{2}\iint \nu(\zeta, \Omega)\frac{\zeta}{\zeta^2 + (\omega/\Omega)^2}d\Omega d\zeta. \quad (24)$$

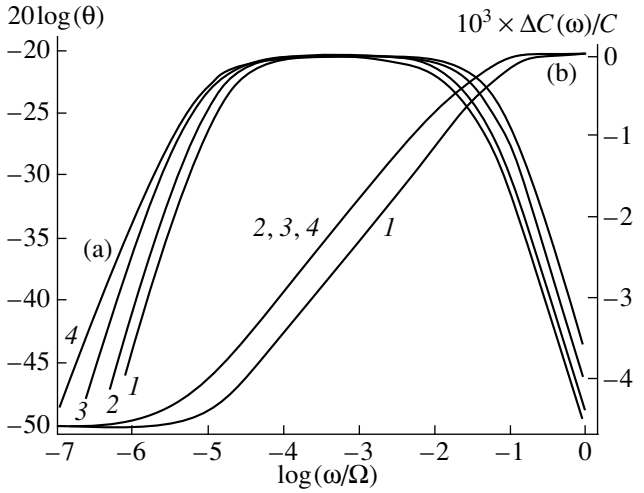

Fig. 3. (a) Dissipation and (b) dispersion characteristics of the medium for Ω_b/Ω_a = (*1*) 1, (*2*) 2, (*3*) 10, and (*4*) 10^5.

For a Π-shaped distribution function $\nu = \nu(\zeta, \Omega)$ in the form

$$\begin{aligned} \nu(\zeta, \Omega) &= \nu_0 \quad \text{for} \quad \zeta \in [a, b], \quad \Omega \in [\Omega_a, \Omega_b], \\ \nu(\zeta, \Omega) &= 0 \quad \text{for} \quad \zeta \notin [a, b], \quad \Omega \notin [\Omega_a, \Omega_b]. \end{aligned} \tag{25}$$

expressions (23) and (24) yield

$$\theta(\omega) = \pi\nu_0\Omega\left[\arctan\left(\frac{b\Omega}{\omega}\right) - \arctan\left(\frac{a\Omega}{\omega}\right)\right] + \frac{\pi\nu_0\omega}{2}\left[\frac{1}{a}\ln\left(\left(\frac{a\Omega}{\omega}\right)^2 + 1\right) - \frac{1}{b}\ln\left(\left(\frac{b\Omega}{\omega}\right)^2 + 1\right)\right]\Bigg|_{\Omega = \Omega_a}^{\Omega = \Omega_b}, \tag{26}$$

$$\frac{\Delta c(\omega)}{c_0} = -\frac{\Omega\nu_0}{4}\ln\left(\frac{b^2 + (\omega/\Omega)^2}{a^2 + (\omega/\Omega^2)}\right) + \frac{\omega\nu_0}{2b}\arctan\left(\frac{b\Omega}{\omega}\right) - \frac{\omega\nu_0}{2a}\arctan\left(\frac{a\Omega}{\omega}\right)\Bigg|_{\Omega = \Omega_a}^{\Omega = \Omega_b}. \tag{27}$$

Figure 3 shows the frequency dependencies (26) and (27) at various Ω_b/Ω_a and a fixed total defect density ν_t:

$$\begin{aligned} \nu_t &= \int \nu(\zeta, \Omega) d\Omega d\zeta \\ &\approx (b - a)(\Omega_b - \Omega_a)\nu_0 = \text{const}. \end{aligned} \tag{28}$$

These plots show that, first, a wide region where the damping decrement (or the Q-factor of the medium) is almost constant is present in every curve. Second, at a fixed total density ν_t, the decrement remains almost unchanged in this region, and the frequency boundaries of this region are weakly sensitive to the parameter Ω_b/Ω_a; namely, when Ω_b/Ω_a changes from 1 to 10^4 (curves *1–4* in Fig. 3a), the boundaries of the frequency band move towards lower frequencies (approximately by half an order of magnitude in frequency for curve *4*, which has the maximum displacement). Dispersion curves *1–4* plotted in Fig. 3b for the same values of Ω_b/Ω_a exhibit a similar behavior. These results once again show that the distribution of the elastic properties of the soft defects is the key factor that primarily determines the frequency dependencies of attenuation and dispersion.

DISSIPATION AND DISPERSION PROPERTIES AND THE KRAMERS–KRONIG RELATIONS

It is well known that the requirement for the causality principle to be fulfilled leads to the integral Kramers–Kronig relations [1, 4], which relate the frequency behavior of the real and imaginary parts of the wave number $\tilde{k}(\omega) = k(\omega) + i\alpha(\omega)$, i.e., the dissipation and the dispersion. In the case under study, it is convenient to introduce the following notation: $\tilde{k}(\omega) = \frac{\omega}{c_0} + k'(\omega) + ik''(\omega)$, where $k'(\omega) = k(\omega) - \frac{\omega}{c_0}$ is the dispersion correction and $k''(\omega) = \alpha(\omega)$. In terms of this notation, the Kramers–Kronig dispersion relations have the form [1]

$$k'(\omega) = \frac{1}{\pi}\int_{-\infty}^{+\infty}\frac{k''(\omega')}{\omega - \omega'}d\omega', \tag{29}$$

$$k''(\omega) = -\frac{1}{\pi}\int_{-\infty}^{+\infty}\frac{k'(\omega)}{\omega - \omega'}d\omega'. \tag{30}$$

By virtue of integral (29) and expression (13), one obtains the relation

$$\frac{\omega}{c(\omega)} - \frac{\omega}{c_0} = \frac{1}{2\pi c_0}\int_{-\infty}^{+\infty}\int_a^b \frac{\nu(\zeta)(\omega'/\Omega)^2}{(\omega'/\Omega)^2 + \zeta^2}\frac{1}{(\omega' - \omega)}d\zeta d\omega' = \frac{1}{2c_0}\omega\int_a^b \frac{\nu(\zeta)\zeta}{\zeta^2 + (\omega/\Omega)^2}d\zeta,$$

which is equivalent to dispersion relation (21) when $\Delta c(\omega)/c_0 \ll 1$. In a similar manner, it can also be shown that the second Kramers–Kronig relation (30) is identically satisfied.

The structure of integrals (29) and (30) shows that, for example, the dispersion correction at a particular frequency is related to the behavior of the attenuation factor in the entire frequency range from zero to infinity, and the requirement that the integral be convergent imposes constraints, which determine the physically admissible frequency behavior of the decrement at low and high frequencies [1, 5]. It is clear that a simple approximation of the decrement, for example, by a constant does not satisfy relationships (29) and (30) and is unsuitable for estimates both at low and at high fre-

quencies. It should be noted that some other more complex approximations of the decrement [10], which agree well with the experiments, also fail to fit the causality principle. Nevertheless, in the frequency range where the Q-factor of the medium is approximately constant, it was found that the following approximate relationship for the ratio of the phase velocities at two frequencies ω_1 and ω_2 is valid [1]:

$$\frac{c(\omega_1)}{c(\omega_2)} \approx 1 + \frac{1}{\pi Q}\ln\left(\frac{\omega_1}{\omega_2}\right). \tag{31}$$

One can easily verify that the relationships derived above agree well with this approximate result. In particular, for $a < \omega/\Omega < b$, expression (21) yields

$$\Delta c(\omega) = -\frac{\nu_0}{4}c_0\ln\frac{b^2 + (\omega/\Omega)^2}{a^2 + (\omega/\Omega)^2} \approx -\frac{\nu_0}{2}c_0\ln\frac{b\Omega}{\omega},$$

which, when used with (19), gives

$$\frac{C(\omega_1)}{C(\omega_2)} \approx \left(1 - \frac{\nu_0}{2}\ln\frac{b\Omega}{\omega_1}\right)\Big/\left(1 - \frac{\nu_0}{2}\ln\frac{b\Omega}{\omega_2}\right)$$
$$\approx 1 + \frac{1}{\pi Q}\ln\left(\frac{\omega_1}{\omega_2}\right).$$

Thus, expressions for the dispersion and the damping decrement obtained from the solution to the one-dimensional propagation problem satisfy the causality principle. Furthermore, since the same expression for the decrement can be obtained from energy considerations, which do not require that the medium be one-dimensional, the derivation of the dispersion correction from the Kramers–Kronig relations also allows us to extend these results to the three-dimensional medium, for which the propagation problem cannot be solved that easily.

NUMERICAL SIMULATION OF THE PROPAGATION OF BROADBAND PULSES

Let us use expressions (17) and (21) for the attenuation factor and phase velocity of a harmonic elastic wave to study the propagation of broadband pulses in a medium for which the wave number has the form

$$\tilde{k}(\omega) = \frac{\omega}{c_0} + \frac{\nu_0\omega}{4c_0}\ln\left|\frac{b^2 + (\omega/\Omega)^2}{a^2 + (\omega/\Omega)^2}\right|$$
$$+ i\nu_0\frac{\omega}{2c_0}\arctan\left[\left(\frac{b\Omega}{\omega} - \frac{a\Omega}{\omega}\right)\Big/\left(1 + \frac{ba\Omega^2}{\omega^2}\right)\right]. \tag{32}$$

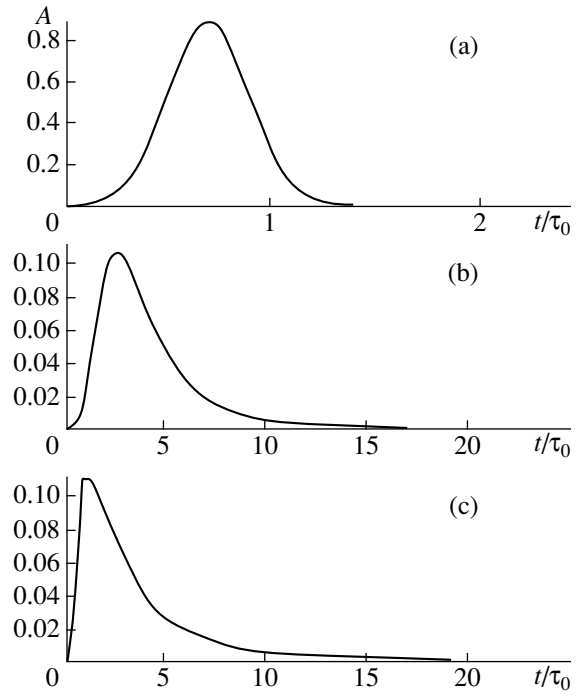

Fig. 4. Pulse waveforms in the medium for $f(t) = \exp(-(t/2\tau_0)^2)$, $x = 400\lambda$, and τ_0 = (a) 5×10^{-2}, (b) 5×10^{-5}, and (c) 10^{-7} s.

The shape of the pulse that passed a distance x in the medium can be found from the equation [4]

$$f'(t, z) = \int_{-\infty}^{+\infty}\tilde{f}(\omega)\exp(-i[\omega t - \tilde{k}(\omega)z])d\omega$$
$$= \int_{-\infty}^{+\infty}\tilde{f}'(\omega)\exp(-i\omega t)d\omega, \tag{33}$$

where $\tilde{f}(\omega) = \frac{1}{2\pi}\int_{-\infty}^{+\infty} f(t)\exp(i\omega t)dt$ is the spectrum of the initial pulse $f = f(t)$ and $\tilde{f}'(\omega) = f'(\omega)\exp(i\tilde{k}(\omega)z)$ is the spectrum of the pulse in the medium.

Below, we present the results of the simulation for initial pulses of three types.

In the first case, we consider a Gaussian unipolar initial pulse: $f(x) = \exp(-(t/2\tau_0)^2)$. Figure 4 presents the pulse waveforms in the medium calculated for three durations of the initial pulse. The long pulse whose spectrum completely falls into the dispersion-free region of the phase velocity is symmetrically broadened due to attenuation (Fig. 4a). The pulse whose spectrum covers part of the region where the Q-factor is constant experiences dispersion effects: its leading edge becomes steeper, while the trailing edge is spread (Fig. 4b). The short pulse whose spectrum completely covers the region of the constant Q-factor experiences

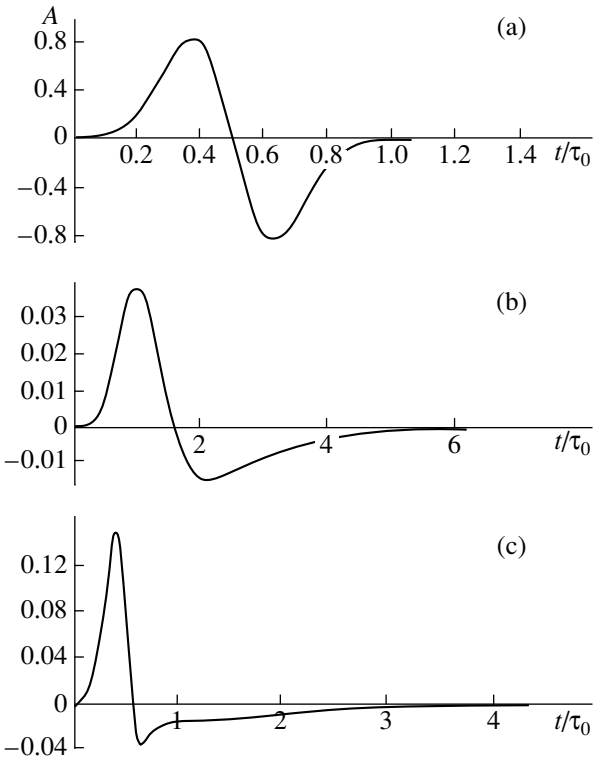

Fig. 5. Pulse waveforms in the medium for $f(t) = (-\tau_0 \exp(0.5))\frac{d}{dt}\exp(-(t/2\tau_0)^2)$, $x = 400\lambda$, and τ_0 = (a) 5×10^{-2}, (b) 5×10^{-5}, and (c) 10^{-7} s.

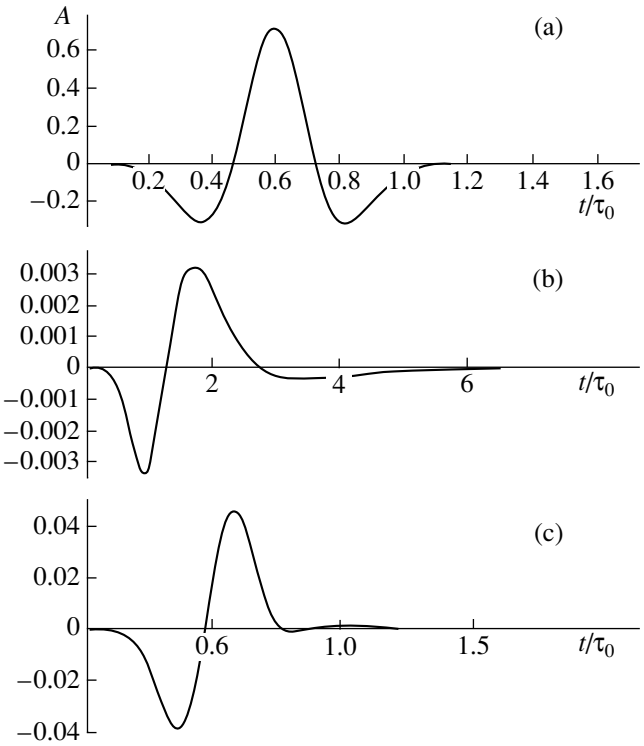

Fig. 6. Pulse waveforms in the medium for $f(t) = \tau_0^2\frac{d^2}{dt^2}\exp(-(t/2\tau_0)^2)$, $x = 400\lambda$, and τ_0 = (a) 5×10^{-2}, (b) 5×10^{-5}, and (c) 10^{-7} s.

similar but more pronounced dispersion effects (an essentially asymmetric pulse shape, as shown in Fig. 4c).

In the second and third cases, we consider bipolar pulses in the form of the first and second time-derivatives of the Gaussian pulse:

$$f(t) = (-\tau_0 \exp(1/2))\frac{d}{dt}\exp(-(t/2\tau_0)^2),$$

$$f(t) = \tau_0^2\frac{d^2}{dt^2}\exp(-(t/2\tau_0)^2).$$

(Such pulses are generated as a result of the self-demodulation of the high-frequency pulses in nonlinear media and can be radiated by parametric acoustic sources operating in the Berktay and Westervelt modes [11].)

The respective pulse waveforms in the medium calculated for three characteristic durations of the initial pulse are plotted in Figs. 5 and 6. For long pulses whose spectrum is localized in the region of the square-law frequency behavior of the attenuation factor, only the attenuation and the corresponding pulse broadening are significant (Figs. 5a, 6a). The pulses whose major part of spectrum falls into the region of the constant Q-factor experience noticeable dispersion effects: as they travel through the medium, their leading edge becomes steeper, and the trailing edge becomes flatter (Figs. 5b, 6b). For a short pulse, similar but more pronounced dispersion effects are observed, which make the pulse asymmetric, so that the negative part of the trailing edge almost disappears (Figs. 5c, 6c).

CONCLUSIONS

The origin of the frequency-independent decrement observed for the elastic wave attenuation in various microinhomogeneous media had been a problem under discussion for a long time [1–3, 5]. A number of phenomenological models of this effect (the best of them, Gurevich's [12] and Liu's [13] models, are in essence identical and based on the introduction of the spectrum of relaxation times of the type $1/\tau$) left open the question of their physical realization and, therefore, the question of the relationship between the model parameters and the microstructure characteristics of the medium.

The rheological model proposed above for describing a microinhomogeneous medium occupies an intermediate position between the physical models of elastic and dissipative properties of media and the phenomenological approximations that describe the empirical data. This model is based on the assumption that the

elastic properties of the defects are characterized by a wide distribution, which, in terms of the relaxation times, is equivalent to the phenomenological models [5, 13]. The rheological model proposed above allows us to assign the physical meaning to the parameters introduced earlier and used in the phenomenological approaches [1, 5, 13, 14] and to relate these parameters to the microstructural characteristics of the medium. An important result of our analysis is the conclusion that, for the Q-factor to be almost frequency-independent, only a small number of microinhomogeneities are necessary. In fact, the only important factor is the presence of highly compliant defects whose size is small as compared to the wavelength of the elastic waves and whose elastic parameters are characterized by a wide distribution. It was found that, in the frequency region where the Q-factor is almost constant, its value is primarily determined by the geometric properties of the microstructure and is almost independent of both the effective viscosity and the elasticity of the defects (though these parameters determine the boundaries of this frequency region). Clearly, such defects are typical of a wide class of microinhomogeneous media; therefore, it is no wonder that materials, which at first glance appear to be wildly different (for example, many metals and rocks), exhibit similar dissipation and dispersion properties. The effective viscosity introduced in the model can be associated with thermal loss at the defects due to high temperature gradients (because the defects are small [15]) and the high rate of material deformation near the defects (intergranular contacts, cracks, etc.).

Our results agree well with the known experimental data on the dissipation and dispersion properties of microinhomogeneous elastic media [1, 2, 5, 6]. In particular, the simulation of the propagation of broadband pulses has shown that the pulse edges are asymmetric due to the dispersion distortions, which is known to be typical of real seismic pulses [1]. Finally, our results (unlike some phenomenological approximations [1, 5]) do not violate the physical limitations imposed on the relationship between attenuation and dispersion: the consequences of the physically realizable model proposed above satisfy the Kramers–Kronig relations, which directly follow from the causality principle.

ACKNOWLEDGMENTS

This work was supported by the Russian Foundation for Basic Research, (project nos. 98-02-17686 and 98-05-64683).

REFERENCES

1. K. Aki and P. G. Richards, *Quantitative Seismology: Theory and Methods* (Freeman, San Francisco, 1980), Vol. 1.
2. *Physical Acoustics: Principles and Methods*, Ed. by W. P. Mason (Academic, New York, 1968; Mir, Moscow, 1968), Vol. 3, Part B.
3. V. N. Nikolaevskiĭ, *Hydromechanics and Fluidodynamics* (Nedra, Moscow, 1996).
4. M. B. Vinogradova, O. V. Rudenko, and S. P. Sukhorukov, *Theory of Waves* (Nauka, Moscow, 1979).
5. S. Ya. Kogan, Fiz. Zemli, No. 11, 3 (1966).
6. M. J. Buckingham, J. Acoust. Soc. Am. **102**, 2579 (1997).
7. V. Yu. Zaĭtsev and V. E. Nazarov, Preprint No. 403, IPF RAN (Institute of Applied Physics, Russian Academy of Sciences, Nizhni Novgorod, 1996).
8. V. Yu. Zaitsev and V. E. Nazarov, Acoust. Lett. **21** (1) 11 (1997).
9. M. A. Isakovich, *General Acoustics* (Nauka, Moscow, 1978).
10. Sh. A. Azimi, A. V. Kalinin, V. V. Kalinin, *et al.*, Fiz. Zemli, No. 2, 42 (1968).
11. B. K. Novikov, O. V. Rudenko, and V. I. Timoshenko, *Nonlinear Hydroacoustics* (Leningrad, 1981).
12. G. I. Gurevich, in *Problems of the Dynamical Theory of Seismic Wave Propagation*, Issue VI (1962), Issue VII (1964).
13. H. P. Liu, D. L. Anderson, and H. Kanamori, Geophys. J. Roy. Astron. Soc. **47**, 41 (1976).
14. G. M. Lundquist and V. C. Cormier, J. Geophys. Res. **85**, 5244 (1980).
15. L. D. Landau and E. M. Lifshits, *Theory of Elastisity* (4th ed., Nauka, Moscow, 1987; 2nd ed., Pergamon, Oxford, 1970).

Translated by A.D. Khzmalyan

Acoustical Physics, Vol. 46, No. 3, 2000, pp. 302–309. Translated from Akusticheskiĭ Zhurnal, Vol. 46, No. 3, 2000, pp. 356–364.

Calculation of Temporal, Angular, and Intensity Characteristics of the Sound Field in a Coastal Area with an Arbitrary Bottom Relief and a Constant Sound Speed in the Medium

N. N. Komissarova

Andreev Acoustics Institute, Russian Academy of Sciences,
ul. Shvernika 4, Moscow, 117036 Russia
e-mail: bvp@akin.ru

Received June 17, 1999

Abstract—Computational algorithms and some computed data are presented for the total sound field in a waveguide whose depth arbitrarily depends on two horizontal coordinates. The sound speed is supposed to be constant, and the bottom slopes are considered as small. The algorithm involves three steps. First, horizontal rays, i.e., horizontal projections of the real rays multiply bottom- and surface-reflected, are calculated. Second, the horizontal rays are set up to a point. Third, the real rays are set up to a point. The computational accuracy is analyzed for a homogeneous wedge lying on a halfspace. Calculations are carried out for a coastal region of the ocean. © *2000 MAIK "Nauka/Interperiodica".*

In recent years, a significant progress has been achieved in the development of three-dimensional models of sound propagation in the ocean. Most models use the approximation of a parabolic equation [1, 2]. Among the earliest successful attempts to solve the problem of long-range low-frequency propagation in a three-dimensional medium, the approach is known that is based on the sound field representation in the form of the sum of adiabatic modes which are calculated in the parabolic approximation. This method follows the theory of horizontal rays and vertical modes of Weinberg and Burridge [3]. Heany *et al.* [4] used this theory to interpret the experimental data on the global propagation of low-frequency sound (from the western coast of Australia to the Bermuda Islands). Collins [5] made a next step by developing a method for calculating the low-frequency sound field on the basis of the computation of adiabatic modes in the parabolic approximation. Later, in a number of joint studies [6, 7], the aforementioned researchers obtained excellent results that explained the global low-frequency propagation observed in the HIFT (Head Island Feasibility Test), which was carried out in 1991 to study the feasibility of monitoring global warming. The method used in these studies is advantageous in that it allows one to solve the long-range propagation problem in view of the real dependence of the parameters of the medium on the spatial coordinates. Though this approach is approximate, the calculation errors seem to be comparable with those in the determination of the parameters of the medium. Abawi *et al.* [8] considered the mode interaction by using the parabolic approximation to solve the horizontal wave equation that involves the summands governing the interaction of modes.

Three-dimensional models for high-frequency sound propagation are developed to a lesser extent. Good results are achieved in developing the calculation methods based on the ray considerations for the case of a sound speed in the medium depending on three spatial coordinates (e.g., in sea currents, oceanic fronts, and internal waves). Thus, Chiu *et al.* [9] analyzed the HIFT by using the HARPO computer program (Hamiltonian Raytracing Program for the Ocean) developed in 1986 [10]. The program computes the rays by the numerical integration of the Hamilton equations of motion. The sound speed that depends on three spatial coordinates is expanded in orthogonal functions.

Nevertheless, one often faces difficulties in applying the classical ray theory to three-dimensional high-frequency propagation when the bottom profile significantly contributes to the sound field formation. These difficulties are related to the limited computer abilities. In particular, the calculation of the sound field in a shallow sea corresponds to the case of the sea depth depending on both horizontal coordinates, and the ray being multiply bottom- and surface-reflected and refracted in the horizontal plane. Recently, such a refraction has been called the "bathymetric" one [11] in contrast to the refraction caused by the sound speed dependence on the horizontal coordinates. In the theoretical studies of the bathymetric refraction, combined methods are frequently used that involve elements of both ray and mode techniques. Thus, the interpretation of the effects observed in the coastal zone [12] in terms of mode considerations and equivalent rays made it possible to explain the noticeable difference in the azimuth angles of the refracted and direct arrivals (the observed angular difference was as high as 25°). A

1063-7710/00/4603-0302$20.00

number of theoretical studies [13–16] used the ray invariant and considered the reflection from the inclined bottom. However, such studies are based on simplified models for the medium: the sea depth H is supposed to depend on a single horizontal coordinate [15, 16].

On the other hand, to obtain the sound field parameters for natural environments, one should take into account the dependence of the sea depth on both horizontal coordinates. An efficient method was proposed [17–20] for calculating the high-frequency sound field for an arbitrary (but smooth) depth dependence on both coordinates. This method is based on an approximate technique for calculating the horizontal rays (i.e., projections of the real rays on the horizontal plane). At the same time, the three-dimensional problem of determining the horizontal projections of the rays is reduced to two-dimensional ray calculations in a two-dimensionally inhomogeneous medium with the effective refractive index $\tilde{n}(x, y)$ that depends on two horizontal coordinates and is governed by the bottom relief and sound speed profile [17, 18]. This approach has been implemented in computer codes to calculate the rays for the cases of a constant sound speed [19] and an arbitrary dependence of the sound speed on the vertical coordinate [20].

The computation of the horizontal rays is the first step in solving the problem of the sound field calculation in an oceanic waveguide with an arbitrary depth dependence on both horizontal coordinates. The next step consists in computing the total sound field at an arbitrary point $S(x_s, y_s, z_s)$ along with its spatial and temporal spectra. The main problem here is to set up the rays to a point, i.e., to determine the ensemble of the rays that connect the sound source and receiver, this problem being much more complicated for the three-dimensional model than for the two-dimensional one. In this paper, we report on the algorithm and some results of computing the parameters of the total sound field in a waveguide whose depth $H(x, y)$ arbitrarily (but smoothly) depends on two horizontal coordinates. We assume that the bottom slopes are small and the sound speed c_o is constant (considering the vertical dependence of the sound speed is the subject of further studies).

The way of specifying the medium parameters is described in [19]. The bottom relief is set by the isobaths. The bottom is approximated by osculating triangles, so that the water column above each triangle is an element of a wedge-like domain. Accordingly, the horizontal ray propagates as if the medium is stratified and has the effective refractive index $\tilde{n}(H) = \sqrt{1 - H_p^2 \sin^2 \vartheta_p / H^2}$, where ϑ_p is the grazing angle of the ray at the sound source (at the point $P(x_p, y_p, z_p)$), $H_p = H(x_p, y_p)$, and $H(x, y)$ is the dependence of the sea depth on the horizontal coordinates x, y.

The algorithm of calculating the total sound field in a waveguide with a three-dimensional bottom relief involves the following steps.

1. The first step consists in computing the parameters of the horizontal rays that emanate from the source. The horizontal trajectories of the real rays are determined for each given grazing angle ϑ_p, i.e., the current coordinates of the horizontal ray are calculated as a function of the propagation time t:

$$x = X(\varphi_p, t|\vartheta_p), \quad y = Y(\varphi_p, t|\vartheta_p), \tag{1}$$

where φ_p is the azimuth departure angle of the ray. (This procedure is described in [17, 19].) As a result of computing, two-dimensional arrays are calculated for each ϑ_p varying with the increment $\Delta\vartheta_p$. These arrays are defined on a two-dimensional grid $\{T, A\}$, where A is a one-dimensional array containing the values of the azimuth departure angles φ_{pj} (the angle increment is $\Delta\varphi_p$), and T is a one-dimensional array containing the propagation times t_i for the ray (the time increment is Δt). The elements of the jth column of the array XAT and those of the jth column of the array YAT determine the trajectory of the horizontal ray with the azimuth departure angle φ_{pj}. The elements of the ith row of the arrays XAT and YAT determine the projection of the curve of constant propagation time, $t = t_i$, on a horizontal plane. The horizontal projections of the rays and the constant-propagation-time curves form a curved grid on the (xy) plane with the cells C_{ij}, each cell being formed by two portions of the horizontal rays with the departure angles φ_{pj} and φ_{pj+1}, which are bounded by the projections of the curves $t = t_i$ and $t = t_{i+1}$. Each grazing angle ϑ_p leads to its own curved grid.

In addition to the trajectory of the horizontal ray (1), for each current point of this ray, the time dependences of the grazing angle $\vartheta(\varphi_p, t|\vartheta_p)$ and the azimuth angle $\varphi(\varphi_p, t|\vartheta_p)$ of the real ray are calculated along with the intensity $l(\varphi_p, t|\vartheta_p)$ of the sound field associated with the ray and the sea depth $h(\varphi_p, t|\vartheta_p)$ for the current ray point at the instant t. The number $N(\varphi_p, t|\vartheta_p)$ of ray cycles that are produced by the real ray before it comes to the current point are also calculated. Here, the ray cycle means the trajectory of the real ray between the adjacent points of reflection from the surface or from the bottom. The horizontal length of the ray cycle can be approximately (within the order of the small bottom slope) expressed as

$$L(\varphi_p, t|\vartheta_p) = 2h(\varphi_p, t|\vartheta_p)\cot\vartheta(\varphi_p, t|\vartheta_p),$$

where the quantity L is a slowly varying function of the propagation time t. Denote the ray length in the horizontal plane as σ and the number of cycles produced by the ray as N. The change $\Delta\sigma$ in a single cycle ($\Delta N = 1$) is the cycle length L: $\Delta\sigma/\Delta N = 1$. Hence, assuming that N is a real and continuous function of σ, in view of the

slow variation of L, we obtain $d\sigma/dN = L$. Then, we have

$$N = \int_0^{\sigma} \frac{d\sigma}{L} = \frac{c_0}{2}\int_0^t \frac{\sin\vartheta}{h}dt. \quad (2)$$

The latter formula was used to compute the number of cycles of the real ray simultaneously with the parameters of the horizontal ray. By computing the number N of ray cycles, we managed to set the rays to a point without calculating the trajectory of the real ray in three dimensions.

The number $N(\varphi_p, t|\vartheta_p)$ of ray cycles is a monotonically increasing function of the ray propagation time t. For instance, if $z_p = 0$, the values $N = 1, 2, 3, \ldots$ correspond to the first, second, third, etc time that the ray comes to the surface, and the values $N = 0.5, 1.5, 2.5, \ldots$ correspond to the first, second, third, etc time that the ray touches the bottom. The value N can be expressed as a sum of the integer and fractional parts:

$$N = m + \mu.$$

The integer part m is the number of full cycles produced by the ray, and the fractional part μ corresponds to the last incomplete ray cycle and depends on the vertical coordinate z_s of the point S. It can be shown that, at $z_p = 0$ (within the order of the small bottom slope), we have

$$\mu(z) = 0.5z/h \text{ for the ray propagating from above, (3)}$$

$$\mu(z) = 1 - 0.5z/h \text{ for the ray propagating from below. (4)}$$

Here, z is the vertical coordinate of the current point of the real ray and h is the sea depth under this point. If one knows the fractional part of N, expressions (3) and (4) can be used to obtain the vertical coordinate z of the current point of the real ray at the instant t. Thus, the calculated trajectory of the horizontal ray, i.e., the quantities $x = X(\varphi_p, t|\vartheta_p)$ and $y = Y(\varphi_p, t|\vartheta_p)$, and the number $N(\varphi_p, t|\vartheta_p)$ of the ray cycles carry complete information on the trajectory of the real ray with the departure angles ϑ_p and φ_p.

The grazing angle of the real ray as a function of time t was calculated with the use of the Weston invariant $H|\sin\vartheta| = H_p|\sin\vartheta_p|$ for the trajectory of the horizontal ray (1). In calculating the intensity $I(t)$ of the ray-associated sound field, we transformed the sum of the reflected ray contributions into the integral over its horizontal trajectory. For the intensity $I(t)$ expressed in decibels, the following expression is valid:

$$I(t) = 10\log\left[\tau^{-2}e^{-\beta\tau}\prod_{\nu=1}^{\nu_t} V_\nu^2\right] = -20\log\tau + 10\log e^{-\beta\tau} + 20\sum_{\nu=1}^{\nu_t}\log V_\nu, \quad (5)$$

where $\tau = c_o t$ is the path length along the real ray; β is the attenuation coefficient; ν is the ordinal number of bottom reflection ($\nu = 1, 2 \ldots \nu_t$); ν_t is the number of bottom reflections experienced by the ray till the instant t; $V_\nu = |V(\gamma_\nu)|$ is the absolute value of the bottom reflection coefficient; and γ_ν is the grazing angle of the reflected ray relative to the bottom, which is approximately equal to the ray grazing angle: $\gamma_\nu \approx \vartheta_\nu$. In the latter summand of (5), we replace the summation by the integration and use the facts that the real ray grazing angle slowly varies along its trajectory and that $d\nu = dN = d\sigma/L = c_o\sin\vartheta dt/(2h)$:

$$20\sum_{\nu=1}^{\nu_t}\log V_\nu = 20\int_0^N \log V(\vartheta_N)dN = 20\int_0^{\sigma}\log V(\vartheta)\frac{d\sigma}{L} = 10c_o\int_0^t \log V[\vartheta(t)]\frac{\sin\vartheta}{h(t)}dt, \quad (6)$$

where $h(t) = H(x(t), y(t))$ is the sea depth at the current ray point. This expression was used to calculate the parameters of the horizontal rays. As a result, two-dimensional arrays were obtained on the two-dimensional grid $\{TA\}$, which contain the ray parameters.

2. The second step of the algorithm consists in setting the horizontal rays to the point $S_o(x_s, y_s, 0)$, which is the projection of the observation point $S(x_s, y_s, z_s)$ on the horizontal plane. For each grazing angle at the source, $\vartheta_{pk} = \vartheta_{po} + k\Delta\vartheta_p$ ($k = 0, 1, 2, \ldots$ and ϑ_{po} is the initial angle at the source, which is close to zero), the departure angle $\varphi_{ps}(\vartheta_{pk})$ is calculated for the horizontal ray that passes through the point S_o, i.e., the azimuth departure angle $\varphi_{ps}(\vartheta_{pk})$ of the real ray that passes under the point S_o. To do so, for each ϑ_{pk}, a cell C_{ij} is found that contains the point S_o. Then, by using the coordinates x, y of the cell nodes and by the inverse interpolation, the departure grazing angles φ_{ps} are determined for the horizontal ray that passes through the point $S_o(x_s, y_s, 0)$, along with the time $t_s(\vartheta_{pk})$ of propagation of the associated real ray from the source. After that, with the parameters ϑ, φ, I, h, and N calculated at the cell nodes, the values of these parameters are computer-interpolated to the point S_o. By implementing the aforementioned procedures for all ϑ_{pk} (with the specified increments $\Delta\vartheta_p$), we obtain one-dimensional arrays that characterize the dependence of the ray parameters on the grazing angle ϑ_p at the point S_o: $\varphi_s(\vartheta_p)$, $\vartheta_s(\vartheta_p)$, $I_s(\vartheta_p)$, and $N_s(\vartheta_p)$.

3. The third step consists in setting up the real rays to the point S, i.e., in determining the departure angles ϑ_{pm} and φ_{pm} for the real rays emanating from the source and arriving at the point $S(x_s, y_s, z_s)$. Till now, the vertical coordinate z_s of the reception point was not used in the calculations. In fact, the calculated parameters determine all physical rays passing under the point S_o. From these rays, only those should be selected that pass

through the point $S(x_s, y_s, z_s)$ with the specified vertical coordinate z_s. One must solve the equation:

$$N_s(\vartheta_p) = m + \mu(z_s), \quad m = 0, 1, 2 \ldots. \tag{7}$$

In other words, for the specified value of z_s, a number of ϑ_{pm} should be found that serve as the departure angles for the rays arriving at the point S. Then, by interpolation, the parameters t_m, ϑ_m, φ_m, and I_m corresponding to these real rays are calculated. Thus, the temporal and angular spectra of the sound field are computed for the point S.

The proposed algorithm of setting the rays to a point needs no calculation of trajectories for the three-dimensional reference rays and no determination of the coordinates for multiple points of bottom reflections. Instead, it is sufficient to compute the horizontal trajectories and solve equation (7). A number of problems do not require even this equation to be solved. In particular, to determine the total intensity I of the sound field at the point S, one can transform the summation over the ray number m into the integration:

$$I = \sum I_m = \int I_s(\vartheta_p)\left[\frac{dm}{d\vartheta_p}\right]_s d\vartheta_p.$$

The derivative $[dm/d\vartheta_p]_s$ means the number of rays arriving at the point S and belonging to a unit interval of the grazing angles at the source. This derivative is given by equation (7), where z_s = const:

$$\frac{dm}{d\vartheta_p} = \frac{dN_s(\vartheta_p)}{d\vartheta_p}.$$

Then, we have

$$I = \int I_s(\vartheta_p)\frac{dN_s(\vartheta_p)}{d\vartheta_p}d\vartheta_p, \tag{8}$$

i.e., the summation of intensities of all rays arriving at the point S is reduced to the integration of the function that is specified by the computed array. One can expect that this algorithm will be more advantageous for the problems which require sound fields of many sources to be calculated, e.g., estimation of ambient-noise and reverberation interference.

The proposed algorithm can be successfully accomplished on condition that the sea depth is a slowly varying function of the horizontal coordinates. This condition was used in deriving the equation for horizontal rays [17] and in passing from the sum to the integral in expressions (2) and (6). To illustrate the accuracy of the aforementioned computer program, a uniform wedge can be considered, for which the ray parameters can be precisely calculated by using the method of imaginary sources [21]. In the previous paper [19], we compared the data of the horizontal-ray calculations with those of the accurate calculations of the horizontal projections of real rays for a wedge with an angle of 3°. The relative error proved to be approximately 10^{-3}. For this wedge, Fig. 1 shows the calculated departure angles φ_{pm} and

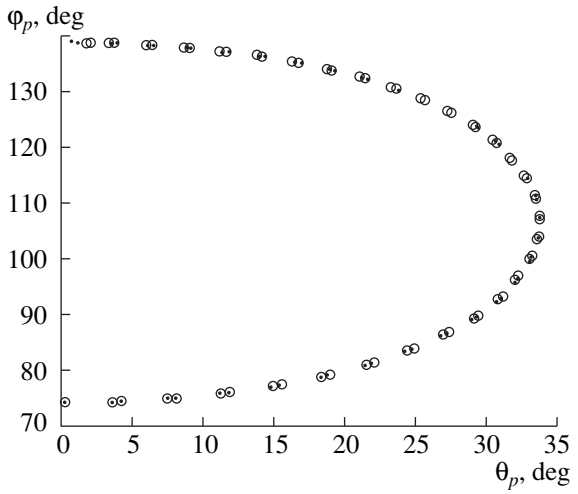

Fig. 1. Grazing (ϑ_{pm}) and azimuth (φ_{pm}) departure angles for the rays arriving at the point S (50, 110, 0.4) within the wedge: (○) the approximate calculation with the method of horizontal rays and (·) the exact calculation with the imaginary-source method.

ϑ_{pm} for the rays that emanated from the source P(30, 40, 0) and arrived at the point S(50, 110, 0.4) (the corresponding horizontal trajectories and the positions of the points P, S are shown in Fig. 2). In Fig. 1, the circles mark the departure angles φ_{pm} and ϑ_{pm} calculated after the proposed algorithm. The dots show the same quantities calculated with the computer program that uses accurate explicit expressions (obtained by applying the imaginary-source method [21] to the wedge) for the ray parameters. The agreement is good, especially for the lower set of points corresponding to the most intense rays. The presented comparison testifies to the applicability of the approximate expressions (2) and (7) to the calculations of the rays connecting the source and the receiver. The horizontal rays connecting the points P and S in the wedge (Fig. 2) are computed with the use of the proposed algorithm. Some trajectories can hardly be distinguished in Fig. 2. Each solid curve corresponds to a pare of rays with close grazing angles at the source. One can see that the algorithm based on the approximate approach allows a sufficiently good setting of the rays to the reception point. The comparison of the accurate and approximate calculations for the intensity of rays connecting the points P and S showed that the relative accuracy was, e.g., equal to 10^{-3} for a singly bottom-reflected ray and 4×10^{-3} for a seven times bottom-reflected one. For a sand bottom, the total sound field intensities at the point S were –28.43 dB (the exact value) and –28.50 dB (the approximate value). A conclusion can be drawn that expressions (5) and (6) are good approximations for the intensity computations when the sea depth is a slowly varying function of the horizontal coordinates.

Below, we present the angular and temporal structures of the sound field calculated for a coastal region of the ocean. The region has a sand bottom, and its

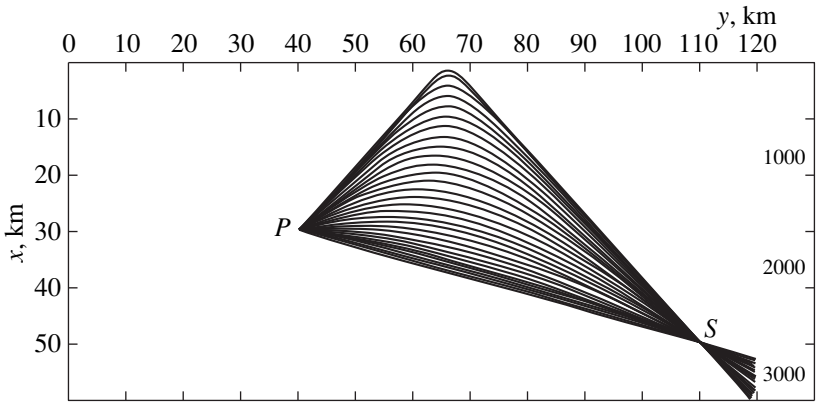

Fig. 2. Horizontal rays connecting the source *P* and the point *S* (50, 110, 0.4) within the wedge (the approximate calculation). The numbers on the right indicate the depths for the isobaths *x* = 20, 40, and 60 km.

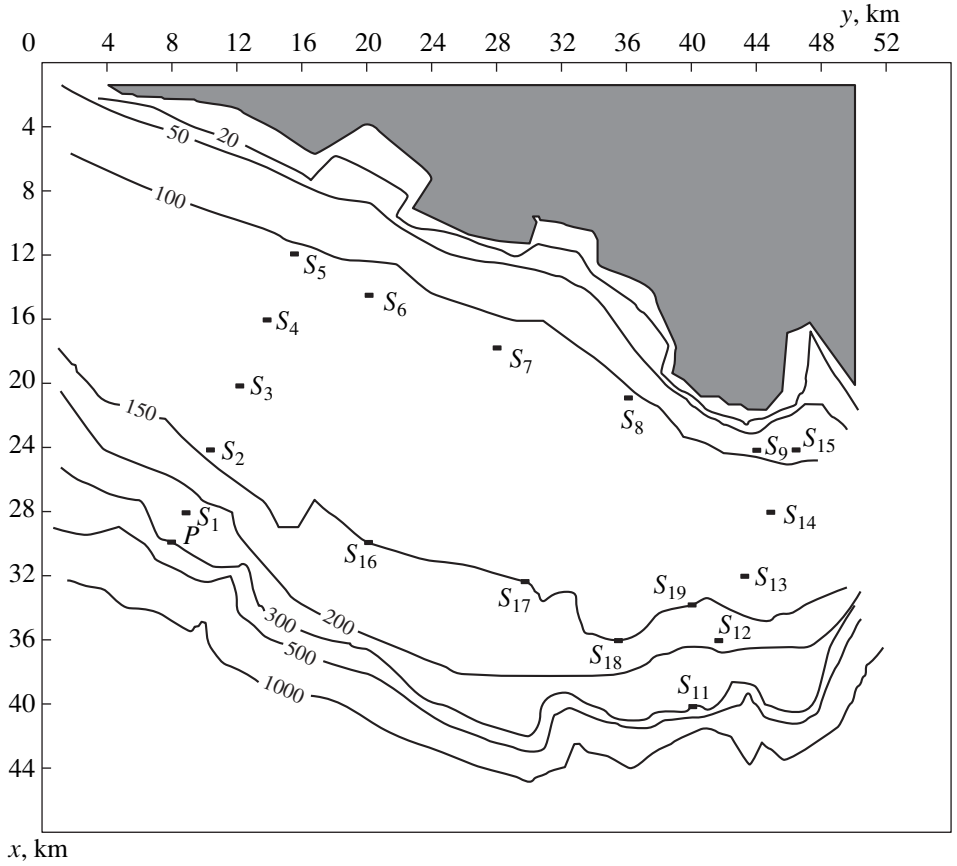

Fig. 3. Bottom topography for the coastal region and the positions of the source *P* and the reception points S_n used in the calculations.

topography is shown in Fig. 3. A set of points S_n at which the field was calculated is also shown in this figure. The point *P*(30, 8, 0) indicates the source position. The reception depth was z_s = 75 m. The points S_n lie in four propagation paths. Two of the paths are oriented approximately along the isobaths (path 2, points S_6–S_9 and path 4, point S_{16}–S_{19}, see Fig. 3), and the two other paths are nearly perpendicular to the isobaths (path 1, points S_1–S_6 and path 3, point S_{11}–S_{16}).

The calculations were carried out for two bottom topographies. The first case is illustrated in Fig. 3: the bottom slope is about 0.2° at the bottom area between the 100- and 150-m isobaths. The second case is characterized by the same isobath positions, but they correspond to other depth values (instead of the 150-, 200-, 300-, and 500-m depths, the values 500, 600, 700, and 800 m are used), the bottom slope being about 1.5° between the 100- and 500-m isobaths.

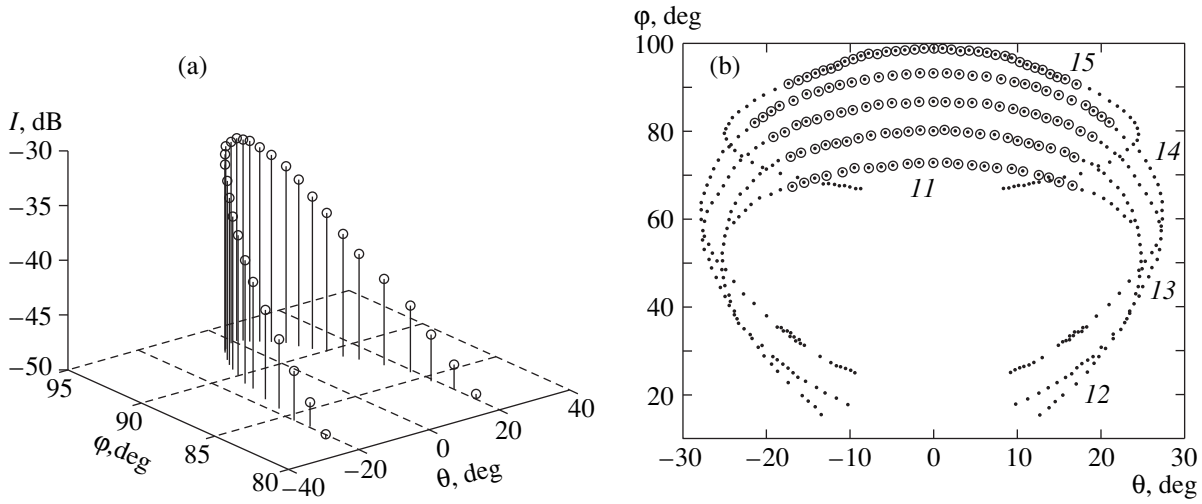

Fig. 4. Angular structure of the signal (a steep bottom slope): (a) at the point S_{14}; (b) at the points S_{11}–S_{15}.

Figure 4 shows the angular spectrum of the sound field calculated for the point S_{14} of the sea region under study (case 2, steep slope). Parameters are shown only for the rays with the intensities higher than –50 dB. Each vertical line in the figure corresponds to a ray that arrives at the point S_{14} from the direction determined by the angles φ_m and ϑ_m, and with the intensity I_m. The computations show that the most intense signals arrive from the directions close to that of the direct arrival, $\varphi_0 \approx 93°$. The range of the grazing angles of the arriving rays is wider than that of the azimuth angles. Figure 4b shows the arrival angles φ_m and ϑ_m for five points of path 3. The numbers *11–15* denote the calculated data for the points S_{11}–S_{15}. The circled points correspond to the rays with intensities higher than –50 dB. Other points illustrate the arrival angles for the rays with intensities from –300 to –50 dB. The maximum $|\vartheta_m|$ corresponds to the ray with a turning point that is close to the reception point S_n in the horizontal plane. The rays associated with the points of the lower portions of curves *11–15* arrive at the point S_n after turning back from the coast, their intensities being small. As the distance between the observation point and the coast grows, the range of the azimuth arrival angles increases.

The range of the azimuth arrival angles $\Delta\varphi$ is governed by the bottom topography and seems to be the most pronounced feature determined by the three-dimensional geometry of the problem. If the sea depth were constant, all rays would arrive at the same azimuth angle ($\Delta\varphi = 0$). For the data shown in Fig. 4a, $\Delta\varphi$ reaches a value of 11° for the rays with intensities higher than –50 dB. If one considers rays of lower intensities, this range will increase. Figure 5 illustrates the second case of the bottom topography. The values of $\Delta\varphi$ are shown for the points S_n of all four paths, only the rays with intensities $I_m > -50$ dB being taken into account. The data show that the values of $\Delta\varphi$ increase as the distance from the source increases. A trend can be also noticed to increasing $\Delta\varphi$ for the observation points approaching the coast line. The computations yield a broader range $\Delta\varphi$ when the bottom slope is steep compared to the smooth one. This is a consequence of the fact that, with the steep slope, the rays experience a lesser number of bottom reflections and are more intense than those observed in the case of a smooth bottom, this effect leading to broader range of the azimuth arrival angles for intense rays.

The calculations showed that the signal duration is considerably greater for the steep bottom slope than for the smooth one. Figure 6 presents the temporal signal structure at the point S_{13} (a steep slope). The direct ray (with the highest intensity) is the first to arrive at the observation point. The comparative data on the ray parameters for the points S_{11}–S_{15} are summarized in the table for both a steep and a smooth bottom slope.

The performed calculations lead to the following conclusions for the steep bottom slope:

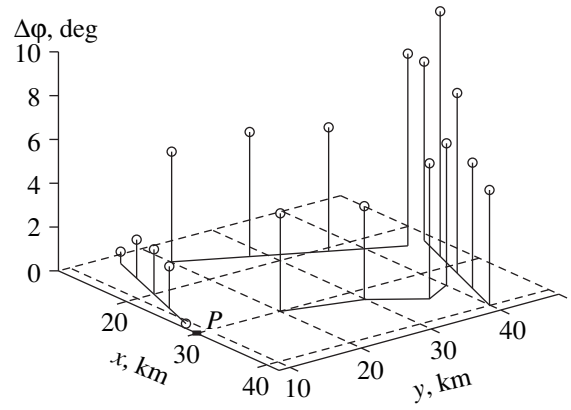

Fig. 5. Range of the azimuth arrival angles at the points S_n for the coastal region with a steep bottom slope.

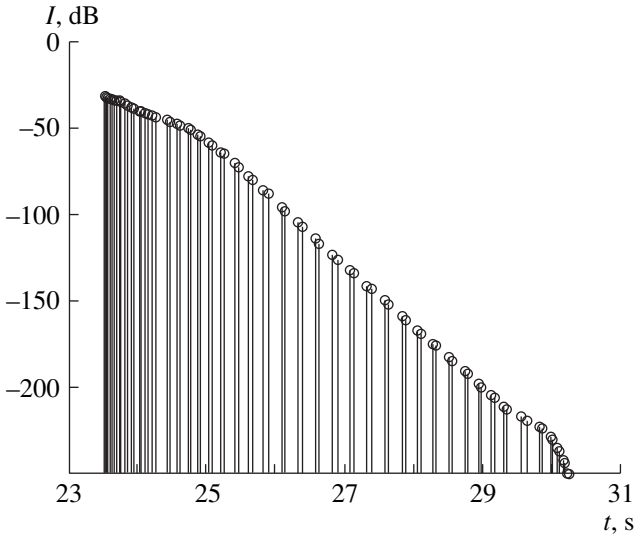

Fig. 6. Temporal structure of the signal at the point S_{13} (a steep bottom slope, z_s = 0.4 km).

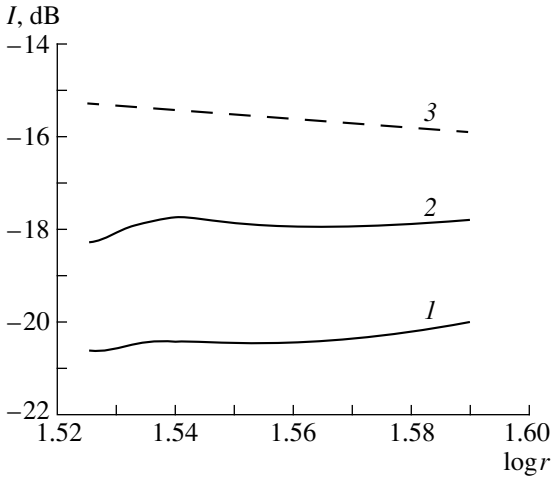

Fig. 7. Sound field intensity on path 3 for (*1*) a smooth bottom slope, (*2*) a steep bottom slope, and (*3*) a cylindrical decay law, $I = -10\log(r/r_0)$, where r_0 = 1 km.

the number of rays forming the received signal is less;

the range $\Delta\varphi$ of the azimuth arrival angles is broader;

the range $\Delta\vartheta$ of the grazing arrival angles is broader;

the range $\Delta\varphi_p$ of the azimuth departure angles is broader;

the range $\Delta\vartheta_p$ of the grazing departure angles is broader; and

the signal duration Δt is longer.

The table illustrates how the signal duration Δt increases, as the distance of the observation point from the coast grows (the points from S_{15} to S_{11}).

According to the calculations, the total sound field intensity (obtained by summation of the ray-associated intensities) is by ~2–3 dB higher for the steep slope than for the smooth one. This intensity difference is a consequence of the lower number of bottom reflections of the ray in the steep-bottom case. The intensity range dependence is most interesting for path 3, which is perpendicular to the isobaths and passes away from the source (Fig. 7). For this path, the distance from the source increases from 33.5 km (point S_{11}) to 38.5 km (point S_{15}), and the total intensity even becomes somewhat higher for longer ranges. The reason is the increase in the number of intense rays (see table). On path 1, which is also perpendicular to the isobaths but

Range of the ray parameters (at the –50-dB intensity level) for the reception points S_{11}–S_{15} and for two cases of the bottom topography in the coastal zone (a sand bottom)

	Case no. 1 or 2	Reception points				
		S_{15}	S_{14}	S_{13}	S_{12}	S_{11}
Number of rays connecting the source and the receiver	I	51	47	45	43	39
	II	35	31	27	25	23
Range of azimuth arrival angles $\Delta\varphi$, deg	I	3.0	1.3	1.4	2.3	3.1
	II	8.3	11.3	8.2	5.8	5.2
Range of grazing arrival angles $\Delta\lvert\vartheta\rvert$, deg	I	11.5	10.8	10.8	9.5	7.2
	II	17	21	19	17	17
Range of azimuth departure angles $\Delta\varphi_p$, deg	I	0.6	1.0	1.3	2.2	3.3
	II	1.0	2.8	3.9	4.4	5.7
Range of grazing departure angles $\Delta\vartheta_p$, deg	I	3.2	4.2	5.0	6.0	7.8
	II	2.0	6.9	10.6	14.0	6.9
Signal duration Δt, s	I	0.27	0.32	0.35	0.41	0.5
	II	0.26	0.81	1.1	1.3	1.5

passes through the source, the sound field decays with distance.

The proposed algorithm for calculating the high-frequency sound field in the sea with a three-dimensional bottom is based on ray considerations, but requires neither the reference rays to be computed in the three-dimensional space, nor the multiple points of bottom reflections to be found. At a number of procedure steps, the problem is reduced to two dimensions. One can expect that thereby higher efficiency of computing may be attained, especially when sound fields of many sources are to be combined (e.g., the calculations of surface-generated ambient noise or reverberation). The approach used above is approximate and imposes some constraints on the parameters of the problem. First, the general validity conditions of the geometrical optics should be met. Second, the bottom slope should be low. The latter requirement can hardly be formulated in a more formal way. To be more specific, we have compared the approximate results with the exact ones obtained for the wedge. A typical feature of the problems associated with the bathymetric refraction is that one cannot specify the bottom relief and the slopes in detail. This fact seems to justify the inaccuracy of our computations.

REFERENCES

1. M. D. Collins and S. A. Ching-Bing, J. Acoust. Soc. Am. **87**, 1104 (1990).
2. D. Lee, G. Botseas, and W. L. Seigmann, J. Acoust. Soc. Am. **91**, 3192 (1992).
3. H. Weinberg and R. Burridge, J. Acoust. Soc. Am. **55**, 63 (1974).
4. K. D. Heaney, W. A. Kuperman, and B. E. McDonald, J. Acoust. Soc. Am. **90**, 2586 (1991).
5. M. D. Collins, J. Acoust. Soc. Am. **94**, 2269 (1993).
6. B. E. McDonald, M. D. Collins, and W. A. Kuperman, J. Acoust. Soc. Am. **96**, 2357 (1994).
7. M. D. Collins, B. E. McDonald, K. D. Heaney, and W. A. Kuperman, J. Acoust. Soc. Am. **97**, 1567 (1995).
8. A. T. Abawi, W. A. Kuperman, and M. D. Collins, J. Acoust. Soc. Am. **102**, 233 (1977).
9. Ch.-S. Chiu, A. J. Semtner, C. M. Ort, *et al.*, J. Acoust. Soc. Am. **96**, 2380 (1994).
10. R. M. Jones, J. P. Riley, and T. M. Georges, *HARPO—A Versatile Three-Dimensional Hamiltonian Ray-Tracing Program for Acoustic Waves in an Ocean with Irregular Bottom* (NOAA Wave Propagation Laboratory Report, 1986).
11. S. A. L. Glegg, J. M. Riley, and A. LaVigne, J. Acoust. Soc. Am. **103**, 2989 (1998).
12. R. Doolittle, A. Tolstoy, and M. Buckingham, J. Acoust. Soc. Am. **83**, 2117 (1988).
13. D. E. Weston, Proc. Phys. Soc. (London) **73**, 365 (1959).
14. D. M. Milder, J. Acoust. Soc. Am. **46**, 1259 (1969).
15. D. E. Weston, Proc. Phys. Soc. (London) **78**, 46 (1961).
16. C. H. Harrison, J. Acoust. Soc. Am. **62**, 1382 (1977).
17. N. N. Komissarova, Akust. Zh. **41**, 617 (1995) [Acoust. Phys. **41**, 542 (1995)].
18. N. N. Komissarova, Akust. Zh. **41**, 902 (1995) [Acoust. Phys. **41**, 799 (1995)].
19. N. N. Komissarova, Akust. Zh. **44**, 68 (1998) [Acoust. Phys. **44**, 54 (1998)].
20. N. N. Komissarova, Akust. Zh. **44**, 801 (1998) [Acoust. Phys. **44**, 698 (1998)].
21. N. N. Komissarova, Akust. Zh. **33**, 43 (1987) [Sov. Phys. Acoust. **33**, 25 (1987)].

Translated by E.A. Kopyl

Acoustical Physics, Vol. 46, No. 3, 2000, pp. 310–316. Translated from Akusticheskiĭ Zhurnal, Vol. 46, No. 3, 2000, pp. 365–372.

Spectral Intensity Oscillations of a Sound Field in a Randomly Inhomogeneous Ocean

V. M. Kuz'kin

Center of Wave Investigations, General Physics Institute, Russian Academy of Sciences, ul. Vavilova 38, Moscow, 117942 Russia

e-mail: petniko@kapella.gpi.ru

Received January 27, 1999

Abstract—The correlation description of the fluctuations of the frequency shifts, which occur in the sound field interference pattern of a shallow sea because of the spatial variability of the medium, is presented. The frequency shifts of the spectral intensity oscillations are estimated for a number of models of large-scale inhomogeneities. The possibilities for using this phenomenon for monitoring shallow-water ocean regions are discussed. © *2000 MAIK "Nauka/Interperiodica".*

INTRODUCTION

The frequency shift of the sound field interference pattern in waveguide channels due to the variability of the propagation conditions along the track is a well-known effect in ocean acoustics. The study of this shift is of interest in relation to the investigation of the characteristic features of the sound field propagation in the ocean that are associated with interference phenomena, as well as from the point of view of its possible applications.

Most of the theoretical and experimental investigations were devoted to the study of the sound reception at points separated in space and frequency in horizontally homogeneous oceanic waveguides (e.g., [1–4]). However, in most cases, the spatial characteristics of the water medium vary along the track. Due to this fact, the development of a more general theory has become a necessity. This problem was not discussed in the literature, although there are some publications that consider its particular aspects [2, 5, 6].

The first description of the spectral intensity oscillations caused by the temporal variability of the propagation conditions was given in the previous paper by Kuz'kin [7]. The theory developed there was confirmed by the experimental data [8].

This paper develops the results obtained by Chuprov [2] and Kuz'kin [5, 6]. It provides the correlation description of the fluctuations of the spectral intensity oscillations caused by the spatial variability of the ocean. The characteristic scales of such variations are estimated for a number of perturbation models. The possibility of using this effect for remote sensing of the inhomogeneity parameters of oceanic waveguides is discussed.

FREQUENCY SHIFTS OF SOUND INTENSITY

For the subsequent analysis, we need the expression for the shift of the signal frequency spectrum in a somewhat different form than it was given by Chuprov [2]. Therefore, we briefly consider its derivation. We restrict ourselves to considering longitudinal and transverse separations of the points of reception (relative to the direction of sound wave propagation) only in the (x, y) horizontal plane. Assume that sound propagates along the x axis.

Longitudinal Separation

At a long distance x from the point source, the intensity of a monochromatic field of frequency ω is represented as a sum of modes

$$I = \sum_m \sum_n A_m(x) A_n^*(x) \exp\left[i \int_0^x \xi_{mn}(\omega, x')dx' \right], \quad (1)$$

where $\xi_{mn} = \xi_m - \xi_n$, and A_m and ξ_m are the amplitude and the propagation constant (the horizontal component of the wave vector) of the mth mode. In the vicinity of the point (ω_0, x_0) of a local extremum of the sound intensity, the following expression is valid:

$$\frac{\partial I(\omega_0, x_0)}{\partial \omega} \Delta\omega_{\|} + \frac{\partial I(\omega_0, x_0)}{\partial x} \Delta x = 0. \quad (2)$$

The sound propagation conditions in the ocean are such [3] that the local interference pattern, which is stable to the variations of the propagation conditions, is formed efficiently by a small number of one-type modes excited in phase (constructive interference). In this interval of mode numbers, we expand ξ_m in a power

series in the vicinity of the lth mode and retain only the linear terms

$$\xi_m = \xi_l + (m - l)\alpha, \tag{3}$$

where $\alpha = \partial\xi_l/\partial l = -2\pi/S_l$ and S_l is the ray cycle length corresponding to the lth mode [9]. Assuming that the mode amplitude is a slower function of its arguments as compared to the phase and using relations (1)–(3), we obtain for the frequency shift of the oscillations:

$$\Delta\omega_{\parallel} = -\int_{x_0}^{x_0+\Delta x} \alpha(\omega_0, x)dx \Big/ \int_0^{x_0} \frac{\partial\alpha(\omega_0, x)}{\partial\omega}dx. \tag{4}$$

Expression (4) can be derived in a different way by using the condition of the phase constancy of the field excited by a group of one-type modes: $\int_0^x \xi_{mn}(\omega, x')dx' = \text{const}$ [4]. Expanding the phase in the vicinity of the point (ω_0, x_0) in a Taylor series and retaining only the linear terms, we find

$$\Delta\omega_{\parallel} = -\int_{x_0}^{x_0+\Delta x} \zeta_{mn}(\omega_0, x)dx \Big/ \int_0^{x_0} \frac{\partial\xi_{mn}(\omega_0, x)}{\partial\omega}dx.$$

With allowance for expansion (3), the right-hand member of the obtained expression does not depend on mode numbers and coincides with the right-hand member of expression (4).

Note that expression (4) can also be transformed in a different way by using the definitions of the group c_{gl} and phase c_{phl} velocities of the lth mode: $c_{gl} = \partial\omega/\partial\xi_l$ and $c_{phl} = \omega/\xi_l$. As a result, equality (4) takes the form

$$\frac{\Delta\omega_{\parallel}/\omega_0}{\Delta x/x_0} = -\frac{d[1/c_{phl}(x_0)]}{d\langle 1/c_{gl}\rangle},$$

which corresponds to the relationship used in [2]. Here, $c_{phl}(x_0)$ is the mean phase velocity of a group of one-type modes received at the distance x_0 from the source; the quantity $\langle 1/c_{gl}\rangle$ is the value of $1/c_{gl}$ averaged over the track, i.e., $1/c_{gl}$, $\langle 1/c_{gl}\rangle = (1/x_0)\int_0^{x_0}[1/c_{gl}(x)]dx$, and $c_{gl}(x)$ is the local value of the group velocity of the lth mode.

Transverse Separation

Assume that the points of reception are located at the distance x from the source and are separated by the interval y in the transverse direction. If we perform calculations similar to those used to derive expression (4), we obtain for the frequency shift of the spectral oscillations:

$$\Delta\omega_{\perp} = -\left(\int_0^x [\alpha(\omega, x', y) - \alpha(\omega, x', 0)]dx'\right) \Big/ \int_0^x \frac{\partial\alpha(\omega, x', 0)}{\partial\omega}dx'. \tag{5}$$

It is clear that in waveguides with the horizontal stratification, $\Delta\omega_{\perp} = 0$.

The frequency shifts of the interference extrema can be used, in particular, for controlling the field focusing in oceanic waveguides on the basis of the principle of phase conjugation (wave front inversion) [10–12] and for monitoring shallow-water ocean regions [4].

STATISTICAL PROPERTIES OF THE FREQUENCY SHIFTS

In the framework of the correlation theory, we describe the fluctuations of the spectral intensity oscillations caused by random variations of the oceanic medium. The quantity α is represented as the sum of the mean value $\bar{\alpha}$ and its fluctuations $\tilde{\alpha}$:

$$\alpha(\omega, \boldsymbol{\rho}) = \overline{\alpha(\omega, \boldsymbol{\rho})} + \tilde{\alpha}(\omega, \boldsymbol{\rho}), \tag{6}$$

where $\bar{\alpha} = \alpha_0 + \alpha_1$, α_0 is the unperturbed value corresponding to a horizontally-homogeneous waveguide channel, and α_1 is the perturbation caused by the regular inhomogeneities, the latter quantity satisfying the condition $\bar{\tilde{\alpha}} = 0$ and $|\bar{\alpha}| \gg |\tilde{\alpha}|$; $\boldsymbol{\rho} = \boldsymbol{\rho}(x, y)$ is the radius-vector of the point of observation in the (x, y) horizontal plane. The overbar means statistical averaging of the quantity considered. Assume that the random field $\tilde{\alpha}(\boldsymbol{\rho})$ is an isotropic and homogeneous one. The corrections α_1 and $\tilde{\alpha}$ to the unperturbed value α_0, which is assumed to be known, can be found in the WKB approximation from the perturbation theory [13]. In this case, the corrections are explicitly expressed in the integral form and can be related to the behavior of the field of oceanic inhomogeneities. Further, it is convenient to write $\tilde{\alpha}$ as the product of a deterministic function $\nu(\omega)$ and a random function $\mu(\rho)$:

$$\tilde{\alpha}(\omega, \rho) = \nu(\omega)\mu(\rho). \tag{7}$$

We will describe the random field μ by the correlation function $B_{\mu}(\rho)$. Consider the fluctuations of the frequency shift of the field interference pattern for longitudinal and transverse separations of the points of observation in the (x, y) horizontal plane.

Longitudinal Correlation

Using expressions (4), (6), and (7), for a random frequency shift of the spectral intensity fluctuations within the interval $(x, x + s)$, we obtain the expression

$$\varphi_{\parallel}(x, s) = \Omega(x + s) - \Omega(x) = \overline{\varphi_{\parallel}(x, s)} - \left[x\left\langle\frac{\partial\bar{\alpha}}{\partial\omega}\right\rangle\right]^{-1} \times\left\{\nu(\omega)\int_{x}^{x+s}\mu(x')dx' + \overline{\varphi_{\parallel}(x, s)}\frac{\partial\nu}{\partial\omega}\int_{0}^{x}\mu(x')dx'\right\}, \tag{8}$$

where $\Omega(x)$ is the random field of the frequency shifts of the local intensity extrema on the x axis, and $\langle\partial\bar{\alpha}/\partial\omega\rangle$ is the mean value of $\partial\bar{\alpha}/\partial\omega$ within the interval $(0, x)$. The mean value of the frequency shift $\bar{\varphi}$ is determined by expression (4) in which we need to set $x_0 \equiv x$, $\Delta x \equiv s$, and $\alpha \equiv \bar{\alpha}$. Consider a fluctuation of the field increments for the field $\Omega(x)$, i.e., the quantity $\tilde{\Omega}(x) = \Omega(x) - \overline{\Omega(x)}$. According to (8), for the mean square modulus of the increment of the fluctuation component $\tilde{\Omega}$ of the field Ω, which we denote by $D_{\Omega}(x, s)$, we obtain

$$D_{\Omega}(x, s) = \left[x\left\langle\frac{\partial\bar{\alpha}}{\partial\omega}\right\rangle\right]^{-2}\left\{\nu^2(\omega)\int_{x}^{x+s}\int B_{\mu}(x'' - x')dx''dx' + [\overline{\varphi_{\parallel}(x, s)}]^2\left(\frac{\partial\nu}{\partial\omega}\right)^2\int_{0}^{x}\int B_{\mu}(x'' - x')dx''dx'\right\}. \tag{9}$$

The one-dimensional spatial spectral density $W_{\mu}(\kappa)$ of the homogeneous and isotropic field μ along the chosen direction is related to its correlation function $B_{\mu}(s)$ through the Fourier transformations [14]:

$$B_{\mu}(s) = \int_{-\infty}^{\infty} W_{\mu}(\kappa)\cos(\kappa s)d\kappa,$$
$$W_{\mu}(\kappa) = (2\pi)^{-1}\int_{-\infty}^{\infty} B_{\mu}(s)\cos(\kappa s)ds. \tag{10}$$

Using spatial spectrum (10), we can express the structure function (9) as the integral

$$D_{\Omega}(x, s) = 2\left[x\left\langle\frac{\partial\bar{\alpha}}{\partial\omega}\right\rangle\right]^{-2}\left\{\nu^2(\omega)\int_{-\infty}^{\infty} W_{\mu}(\kappa)\frac{1 - \cos\kappa s}{\kappa^2}d\kappa + [\overline{\varphi_{\parallel}(x, s)}]^2\left(\frac{\partial\nu}{\partial\omega}\right)^2\int_{-\infty}^{\infty} W_{\mu}(\kappa)\frac{1 - \cos\kappa x}{\kappa^2}d\kappa\right\}. \tag{11}$$

If the spectrum width $\Delta\kappa$ of the random field μ is large compared to that of the main maximum of the factor $(1 - \cos\kappa x)/\kappa^2$, i.e., $\Delta\kappa \gg 2\pi/x$, and $W_{\mu}(0) \neq 0$, expression (11) can be reduced to the form

$$D_{\Omega}(x, s) = 2\left[x\left\langle\frac{\partial\bar{\alpha}}{\partial\omega}\right\rangle\right]^{-2}\left\{\nu^2(\omega)\int_{-\infty}^{\infty} W_{\mu}(\kappa)\frac{1 - \cos\kappa s}{\kappa^2}d\kappa + [\overline{\varphi_{\parallel}(x, s)}]^2\left(\frac{\partial\nu}{\partial\omega}\right)^2 x\sigma_{\mu}^2 l_{\text{int}}\right\}, \tag{12}$$

where σ_{μ}^2 and l_{int} are the mean square and the integral correlation radius of the field fluctuations μ, respectively; $l_{\text{int}} = (1/\sigma_{\mu}^2)\int_0^{\infty} B_{\mu}(s)ds$. The condition, at which expression (12) holds, can be given in the correlation form. If, for isotropic random fields, we use the uncertainty principle (or "smearing") $\Delta\kappa l_{\text{int}} \geq 1$ in which $\Delta\kappa = \vartheta/l_{\text{int}}$, where $\vartheta = 2\pi$, we arrive at the condition $x \gg l_{\text{int}}$. In particular, in the absence of regular perturbations of the oceanic medium ($\alpha_1 = 0$), formula (12) yields

$$D_{\Omega}(x, s) = 2\left[x\frac{\partial\alpha_0}{\partial\omega}\right]^{-2}\left\{\nu^2(\omega)\int_{-\infty}^{\infty} W_{\mu}(\kappa)\frac{1 - \cos\kappa s}{\kappa^2}d\kappa + \alpha_0^2 s^2(x)^{-1}\left(\frac{\partial\alpha_0}{\partial\omega}\right)^2\sigma_{\mu}^2 l_{\text{int}}\right\}. \tag{13}$$

We now estimate the influence of the braced terms of the right-hand member of (12) on the behavior of the structure function. For subsequent estimates, it is sufficient to use any model of the correlation function μ, for example, an exponential function

$$B_{\mu}(s) = \sigma_{\mu}^2\exp(-|s|/l),$$

for which, in particular, the field correlation radius l coincides with the integral radius, $l = l_{\text{int}}$. According to (10) and using (13), we determine the spectral density of the random field μ and substitute it in (12). As a result, we obtain

$$D_{\Omega}(x, s) = 2\left[x\left\langle\frac{\partial\bar{\alpha}}{\partial\omega}\right\rangle\right]^{-2} l\sigma_{\mu}^2 \times\left\{\nu^2[s - l(1 - e^{-|s|/l})] + [\overline{\varphi_{\parallel}(x, s)}]^2 x\left(\frac{\partial\nu}{\partial\omega}\right)^2\right\}. \tag{14}$$

Consider the two limiting cases:

(i) For the spatial intervals $s \ll l$, the total rms frequency shift is described by the square-law dependence

$$D_{\Omega}(x, s) = \left[x\left\langle\frac{\partial\bar{\alpha}}{\partial\omega}\right\rangle\right]^{-2} s^2\sigma_{\mu}^2 l \times\left\{(\nu^2(\omega)/l) + 2x(\bar{\alpha})^2\left[x\left\langle\frac{\partial\bar{\alpha}}{\partial\omega}\right\rangle\right]^{-2}\left(\frac{\partial\nu}{\partial\omega}\right)^2\right\}$$

in which the first term predominates over the second term, provided that $x \gg 2l$.

(ii) For the spatial intervals $s \gg l$, we obtain

$$D_\Omega(x, s) = 2\left[x\left\langle\frac{\partial\bar{\alpha}}{\partial\omega}\right\rangle\right]^{-2}\sigma_\mu^2 l$$

$$\times\left\{\nu^2(\omega)s + (\bar{\alpha})^2 s^2 x\left[x\left\langle\frac{\partial\bar{\alpha}}{\partial\omega}\right\rangle\right]^{-2}\left(\frac{\partial\nu}{\partial\omega}\right)^2\right\}.$$

The behavior of the structure function is now determined by the diffusion law, on condition that $x \gg s$.

In deriving these estimates, we took into account the condition $[\bar{\alpha}/\nu]^2/[\langle\partial\bar{\alpha}/\partial\omega\rangle/(\partial\nu/\partial\omega)]^2 \sim 1$. Thus, at large distances $x \gg l$ in the case of both the narrow spectrum, i.e., a long-lived correlation ($s \ll l$), and the wide spectrum, i.e., a short-lived correlation ($s \gg l$), the structure function of the frequency shifts of the local extrema is determined by the expression

$$D_\Omega(x, s) = 2\left[x\left\langle\frac{\partial\bar{\alpha}}{\partial\omega}\right\rangle\right]^{-2}\nu^2(\omega)$$

$$\times\int_{-\infty}^{\infty} W_\mu(\kappa)\frac{1-\cos\kappa s}{\kappa^2}d\kappa,$$

or in the other form

$$D_\Omega(x, s) = \left[x\left\langle\frac{\partial\bar{\alpha}}{\partial\omega}\right\rangle\right]^{-2}\nu^2(\omega)D_\gamma(s),$$

where

$$D_\gamma(s) = 2\int_{-\infty}^{\infty}(1-\cos\kappa s)W_\gamma(\kappa)d\kappa$$

is the spectral density of the structure function of the random field $\gamma(x)$ [14] and $\mu(x) = d\gamma/dx \times (W_\gamma(\kappa) = W_\mu(\kappa)/\kappa^2)$.

It is clear that these conclusions are unrelated to the special choice of the exponential correlation function (13) for μ. An important point is only whether this correlation function is sufficiently sharp within the interval s, i.e., $l \ll s$, or this interval is too small, $s \ll l$. Certainly, this result can be obtained directly from expression (12) by considering short-correlated and long-correlated fluctuations μ. Thus, at distances x far exceeding the integral correlation radius l_{int}, $x \gg l_{\text{int}}$, in the limiting cases of slow and fast fluctuations μ, the spectrum of the frequency shifts of the local intensity extrema reproduces the spectrum of the random field γ within the factor $\nu^2(\omega)[x\langle\partial\bar{\alpha}/\partial\omega\rangle]^{-2}$. The value of this factor depends on the track length and the dispersion characteristic of the waveguide.

Transverse Correlation

Consider the mean square $\varphi_\perp(x, y) = \tilde{\Omega}(x, y) - \tilde{\Omega}(x, 0)$ (referred to as $D_\perp(x, y)$) of the increments of the frequency shift fluctuations $\tilde{\Omega}(x, y) = \Omega(x, y) - \overline{\Omega(x, y)}$ of the local intensity extrema on the y axis. If these extrema are observed at the distance x from the source, then, according to (5)–(7), we obtain

$$D_\perp(x, y) = \left[x\left\langle\frac{\partial\overline{\alpha(x, 0)}}{\partial\omega}\right\rangle\right]^{-2}\left\{2\nu\left(\nu - \overline{\varphi_\perp}\frac{\partial\nu}{\partial\omega}\right)\right.$$

$$\times\int_0^x\int[B_\mu(x''-x', 0) - B_\mu(x''-x', y)]dx''dx' \qquad (15)$$

$$\left.+ (\overline{\varphi_\perp})^2\left(\frac{\partial\nu}{\partial\omega}\right)^2\int_0^x\int B_\mu(x''-x', 0)dx''dx'\right\},$$

where

$$\overline{\varphi_\perp} = -\left(\int_0^x[\overline{\alpha(x', y)}\right.$$

$$\left.-\overline{\alpha(x', 0)}]dx'\right)/\int_0^x(\partial\overline{\alpha(x', 0)}/d\omega)\,dx'$$

is the mean value of the frequency shift of the interference pattern for a transverse separation of the points of observation. If the transverse (with respect to the direction of sound wave propagation) gradient of the regular perturbation equals zero, i.e., $\partial\overline{\alpha(x, 0)}/\partial y = 0$, we have $\overline{\varphi_\perp} = 0$.

Now, in expression (15), we go over to new variables of integration, $s = x'' - x'$ and $\eta = (x' + x'')/2$, and take into account that the correlation function markedly differs from zero only for the values of $|s|$ that do not exceed the correlation radius of the fluctuations μ. At distances $x \gg l_{\text{int}}$, the limits of the integration with respect to s can be extended to infinity, and the integral with respect to η can be calculated in the limits from 0 to x. Since $B_\mu(\rho) = [D_\mu(\infty) - D_\mu(\rho)]/2$, we obtain

$$D_\perp(x, y) = 2x\left[x\left\langle\frac{\partial\overline{\alpha(x, 0)}}{\partial\omega}\right\rangle\right]^{-2}$$

$$\times\left\{\nu\left(\nu - \overline{\varphi_\perp}\frac{\partial\nu}{\partial\omega}\right)\int_0^\infty[D_\mu(s, y) - D_\mu(s, 0)]ds \qquad (16)\right.$$

$$\left.+ (\overline{\varphi_\perp})^2\left(\frac{\partial\nu}{\partial\omega}\right)^2\sigma_\mu^2 l_{\text{int}}\right\}.$$

Structure function (16) can be expressed in terms of the spatial spectrum of fluctuations. Substituting the spectral density [14]

$$D_\mu(r) = 8\pi\int_0^\infty\left(1-\frac{\sin\kappa r}{\kappa r}\right)\Phi_\mu(\kappa)\kappa^2 d\kappa,$$

where $r = \sqrt{x^2+y^2+z^2}$, in expression (16) and integrating with respect to s, we obtain

$$D_\perp(x,y) = 8\pi^2 x\left[x\left\langle\frac{\partial\overline{\alpha(x,0)}}{\partial\omega}\right\rangle\right]^{-2}\left\{\nu\left(\nu-\overline{\varphi_\perp}\frac{\partial\nu}{\partial\omega}\right)\right.$$
$$\left.\times\int_0^\infty\Phi_\mu(\kappa)[1-J_0(\kappa y)]\kappa d\kappa+(\overline{\varphi_\perp})^2\left(\frac{\partial\nu}{\partial\omega}\right)^2\sigma_\mu^2 l_{\text{int}}\right\}. \quad (17)$$

Here, $J_0(x)$ is the zero Bessel function, and $\Phi_\mu(\kappa)$ is the three-dimensional spatial spectrum of the homogeneous isotropic field μ, which is related to the one-dimensional spectrum $W_\mu(\kappa)$ by the relationship [14]

$$\Phi_\mu(\kappa) = -\frac{1}{2\pi\kappa}\frac{\partial W_\mu(\kappa)}{\partial\kappa}.$$

From (17) it follows that, in the absence of regular inhomogeneities ($\varphi_\perp = 0$), we have

$$D_\perp(x,y) = 8\pi^2(x)^{-1}\left(\frac{\partial\alpha_0}{\partial\omega}\right)^{-2}\nu^2(\omega)$$
$$\times\int_0^\infty\Phi_\mu(\kappa)[1-J_0(\kappa y)]\kappa d\kappa. \quad (18)$$

From this expression, we derive

$$B_\perp(x,y) = (2\pi)^2(x)^{-1}\left(\frac{\partial\alpha_0}{\partial\omega}\right)^{-2}\nu^2(\omega)$$
$$\times\int_0^\infty J_0(\kappa y)\Phi_\mu(\kappa)\kappa d\kappa. \quad (19)$$

The variance of fluctuations Ω has the form

$$\sigma_\Omega^2 = (1/2)D_\perp(x,\infty) = B_\perp(x,0)$$
$$= 2(x)^{-1}\left(\frac{\partial\alpha_0}{\partial\omega}\right)^{-2}\nu^2(\omega)\sigma_\mu^2 l_{\text{int}}. \quad (20)$$

Thus, the mean square of the frequency shifts of the spectral intensity oscillations is determined by the track length, the dispersion characteristic of the unperturbed waveguide channel, and the variance and the integral correlation radius of the fluctuations μ. It is worth noting that, as the distance decreases, the fluctuations of the frequency shifts of the spectrum increase as $(1/x)$. From expression (19) it follows that the transverse correlation of the frequency shifts of the oscillation spectrum extends over distances of the order of the correlation radius l of the random field μ, i.e., $l_\perp \sim l$. This fact is evident from the example of the Gaussian correlation function

$$B_\mu(\rho) = \sigma_\mu^2\exp(-\rho^2/2l^2),$$

for which one can show that

$$B_\perp(x,y) = \sigma_\Omega^2(x)\exp(-y^2/2l^2),$$

where the variance $\sigma_\Omega^2(x)$ is determined by expression (20). In this case, we obtain $l_\perp = l$.

In particular, if the transverse correlation function $B_\perp(x, y)$ of the frequency shifts of the local intensity extrema is known, then, inverting formula (19), we obtain an expression for the spatial spectrum of fluctuations

$$\Phi_\mu(\kappa) = (2\pi)^{-2}x(\partial\alpha_0/\partial\omega)^2\nu^{-2}(\omega)$$
$$\times\int_0^\infty B_\perp(x,y)J_0(\kappa y)y dy.$$

ESTIMATES OF THE FREQUENCY SHIFTS

The relationships obtained above allow us to estimate the effect of various parameters of the oceanic medium (for a known oceanic medium model) on the frequency shift of the sound field interference pattern. As an illustration, we consider some examples of both regular and random spatial perturbations in a waveguide channel with perfectly reflecting boundaries. Here, we accept a model with a rigid bottom. The use of a more complex bottom model as an impedance medium does not significantly affect the estimates of the frequency shift (see [2] and the literature cited there).

Regular Perturbations

Example 1. Plane slope bottom, isovelocity channel. Let the waveguide depth vary with distance along the x axis as

$$H(x) = \begin{cases} H_1, & 0 \le x \le x_1 \\ H_1 + \varepsilon(x-x_1), & x_1 \le x \le x_2 \\ H_2, & x \ge x_2 \end{cases}$$

and the track length x_0 exceed the distance x_2, $x_0 > x_2$. Using the dispersion relation for a perfectly homogeneous waveguide [9]and expression (4), we obtain an expression for the relative frequency shift

$$\frac{\Delta\omega_\parallel}{\omega} = \frac{\Delta x H_1^2}{x_1 H_2^2 + (x_2-x_1)H_1H_2 + (x_0-x_2)H_1^2}.$$

Setting, for example, $x_1 = x_2 - x_1 = x_0 - x_2 = 10$ km (the total track length is $x_0 = 30$ km), $\varepsilon = 10^{-2}$, and $H_1 = 100$ m, we obtain $\Delta\omega_\parallel/\omega \approx 1.4 \times 10^{-5}\Delta x$. Note that, in the absence of depth variations along the track ($H(x) = \text{const}$), we have $\Delta\omega_\parallel/\omega \approx \Delta x/x_0 \approx 3.3 \times 10^{-5}\Delta x$ [2]. The quantity Δx is expressed in meters.

Example 2. Frontal zone. Assume that the frontal zone is a transition region between two regions with range-independent stratifications. We limit our consideration to a two-layer model of the sound channel in the transition region $0 \le x \le L$, which is described by the sound velocity profile

$$c(x, z) = \begin{cases} c_0(x), & -h \le z \le 0 \\ c_0(x)[1 + \chi(x)(h + z)], & -H \le z \le -h \end{cases}$$

and assume that the parameters $c_0(x)$ and $\chi(x)$ vary linearly with the distance x:

$$c_0(x) = c_1 + (\Delta c/L)x, \quad \chi(x) = \chi_1 + (\Delta\chi/L)x.$$

The sea depth H, the thickness of the homogeneous layer h, and the sound velocity near the bottom $c(-H)$ are assumed to be invariable along the track. Assume also that the track is normal to the frontal zone boundaries and its length exceeds the width of the transition region, $x_0 > L$. We use the following values of the sound channel parameters: $\Delta c \sim 13.8$ m/s, $c_1 \sim 1480$ m/s, $\Delta\chi \sim 4.6 \times 10^{-5}$ 1/m, $\chi_1 \sim 1.7 \times 10^{-5}$ 1/m, $H \sim 250$ m, $h \sim 50$ m, and $L \sim 10$ km, which roughly correspond to the polar frontal zone of the western part of the Barents Sea [15, 16]. We estimate the frequency shifts of the local extrema of the field interference pattern formed by a group of modes associated with the bottom rays. According to [9], we have

$$\alpha = -\frac{(3\pi)^{2/3}}{3}\omega^{1/3}\chi^{2/3}(x)c_0^{-1/3}(x)\left(l - \frac{3}{4}\right)^{-1/3}.$$

The substitution of this expression in (4) yields

$$\frac{\Delta\omega_\parallel}{\omega} = \frac{-3\chi_2^{2/3}c_2^{-1/3}\Delta x}{\chi_2^{2/3}c_2^{-1/3}x_0 - (\chi_1^{2/3}c_1^{-1/3}x_1 - \chi_2^{2/3}c_2^{-1/3}x_2) + (3/5)(\chi_2^{5/3} - \chi_1^{5/3})Lc_1^{-1/3}(\Delta\chi)^{-1}},$$

where x_1 and $x_0 - x_2$ represent the track length in the first and second horizontally homogeneous regions, respectively; $x_2 = x_1 + L$, $c_2 = c_1 + \Delta c$; and $\chi_2 = \chi_1 + \Delta\chi$. Setting $x_1 = x_0 - x_2 = 10$ km (the total track length is $x_0 = 30$ km), we obtain the estimate: $\Delta\omega_\parallel/\omega \approx -5.6 \times 10^{-5}\Delta x$. Note that, in the absence of the transition region, the relative frequency shift would be $\Delta\omega_\parallel/\omega = -3\Delta x/x_0 \approx -10^{-4}\Delta x$ [2]. The quantity Δx is expressed in meters.

Random Inhomogeneities

On the assumption that regular inhomogeneities are absent, we estimate the relative fluctuations of the frequency shift of the spectrum oscillations, σ_Ω/ω (20).

Example 3. Isovelocity channel with a rough lower boundary. In our case, we have

$$\alpha_0 \approx -\frac{\pi^2(l + 1/2)c}{\omega H^2}, \quad \nu(\omega) \approx -\frac{2\alpha_0}{H}, \quad \mu(\rho) = \tilde{h}(\rho),$$

where H and $\tilde{h}$ are the mean value and the random fluctuations of the depth, respectively, and c is the sound velocity. Assume that the roughness is described by the Gaussian correlation function $B_\mu(\rho) = \sigma_\mu^2 \exp(-\rho^2/2l^2)$. Then, from expression (20), we obtain

$$\sigma_\Omega/\omega = 2\sqrt[4]{2\pi}(\sigma_\mu/H)\sqrt{l/x}.$$

The validity of this relationship is limited by the condition that the size of the Fresnel zone is small compared to the correlation radius of roughness, which allows us to ignore the amplitude fluctuations as compared to the phase fluctuations [17]. Setting, for example, $H = 200$ m. $x = 30$ km, $\sigma_\mu = 2$ m, and $l = 1$ km (mesoscale bottom roughness), we obtain $\sigma_\Omega/\omega \approx 4.7 \times 10^{-3}$.

Example 4. Random inhomogeneities of the medium. Consider an isovelocity channel in which the sound velocity fluctuates about the mean (unperturbed) value c. Assume that the variance of the sound velocity fluctuations does not depend on the channel depth. In this case, according to (20), we arrive at the estimate

$$\sigma_\Omega/\omega = \sqrt{2l_{\text{int}}/x}(\sigma_\mu/c).$$

Setting x =30 km, $c = 1500$ m/s, $\sigma_\mu = 1$ m/s, and $l_{\text{int}} = 300$ m [18], we obtain $\sigma_\Omega/\omega \approx 10^{-4}$.

CONCLUSIONS

The estimates presented above for the frequency shifts of the spectrum oscillations provided reassuring results. These estimates reach noticeable values, which testifies to the feasibility of their reliable measurements. Under the conditions of multimode propagation, the interference effects often make it difficult, if not impossible, to obtain any definite conclusions about the relation between the parameters of the oceanic medium and the observed variability of the sound field characteristics. In the case under study, the statistical characteristics of the frequency shifts of the interference pattern, as indicated above, are completely determined by the dispersion characteristic of an unperturbed sound channel and by the correlation function of fluctuations of the inhomogeneity parameters. From this standpoint,

the effect of the frequency shifts of the local interference extrema at small distances offers considerable promise for solving an inverse problem, i.e., the construction of models of the spatial variability of the oceanic medium on the basis of the data obtained by recording the frequency shifts of the spectrum oscillations. The results are obtained on the assumption that the emitting and (or) receiving arrays provide spatial filtering of a group of one-type modes whose interference pattern is sensitive to oceanic perturbations of the type under study. The problems of the synthesis of acoustic field in waveguide systems have been widely discussed in the literature (see, e.g., [19, 20]). The feasibility of the spatial filtering of a given set of modes in a shallow sea was demonstrated by Lynch *et al*. [16].

ACKNOWLEDGMENTS

This work was supported by the Russian Foundation of Basic Research, project no. 97-05-64878.

REFERENCES

1. S. D. Chuprov and N. E. Mal'tsev, Dokl. Akad. Nauk SSSR **257** (2), 475 (1981).
2. S. D. Chuprov, in *Ocean Acoustics. The State of the Art*, Ed. by L. M. Brekhovskikh and I. B. Andreeva (Nauka, Moscow, 1982), pp. 71–91.
3. V. N. Kulakov, N. E. Mal'tsev, and S. D. Chuprov, Akust. Zh. **29**, 74 (1983) [Sov. Phys. Acoust. **29**, 41 (1983)].
4. *Interference of Wide-Band Sound in the Ocean*, Ed. by V. A. Zverev and E. F. Orlov (Institute of Applied Physics, Academy of Sciences of the USSR, Gorki, 1984).
5. G. A. Grachev, Akust. Zh. **39**, 67 (1993) [Acoust. Phys. **39**, 33 (1993)].
6. V. M. Kuz'kin, Akust. Zh. **41**, 344 (1995) [Acoust. Phys. **41**, 300 (1995)].
7. V. M. Kuz'kin, Akust. Zh. **45**, 258 (1999) [Acoust. Phys. **45**, 224 (1999)].
8. V. M. Kuz'kin, A. V. Ogurtsov, and V. G. Petnikov, Akust. Zh. **44**, 94 (1998)[Acoust. Phys. **44**, 77 (1998)].
9. L. M. Brekhovskikh and Yu. P. Lysanov, *Fundamentals of Ocean Acoustics* (Gidrometeoizdat, Leningrad, 1982; 2nd ed., Springer, Berlin, 1991).
10. W. A. Kuperman, W. S. Hodgkiss, and H. C. Song, J. Acoust. Soc. Am. **103**, 25 (1998).
11. H. C. Song, W. A. Kuperman, and W. S. Hodgkiss, J. Acoust. Soc. Am. **103**, 3234 (1998).
12. W. S. Hodgkiss, N. C. Song, and W. A. Kuperman, J. Acoust. Soc. Am. **105**, 1597 (1999).
13. I. K. Kobozev, Yu. A. Kravtsov, and A. V. Ogurtsov, Akust. Zh. **34**, 109 (1988) [Sov. Phys. Acoust. **34**, 58 (1988)].
14. S. M. Rytov, Yu. A. Kravtsov, and V. I. Tatarskiĭ, *Principles of Statistical Radiophysics* (Nauka, Moscow, 1978; Springer, Berlin, 1989), Part 2.
15. A. R. Parsons, R. H. Bourke, and R. D. Muench, J. Geophys. Res. **101**, 14201 (1996).
16. J. Lynch, G. Jin, R. Pawlowich, *et al.*, J. Acoust. Soc. Am. **99**, 803 (1996).
17. F. G. Bass and I. M. Fuks, *Wave Scattering from Statistically Rough Surfaces* (Nauka, Moscow, 1972; Pergamon, New York, 1979).
18. M. Schulkin, G. R. Garrison, and T. Wen, J. Acoust. Soc. Am. **77**, 465 (1985).
19. C. Gazanhes, J. P. Sessarego, and J. L. Garnier, J. Sound Vibr. **56**, 251 (1978).
20. V. I. Talanov, Izv. Vyssh. Uchebn. Zaved., Radiofiz. **28**, 872 (1985).

Translated by Yu.P. Lysanov

Acoustical Physics, Vol. 46, No. 3, 2000, pp. 317–326. Translated from Akusticheskiĭ Zhurnal, Vol. 46, No. 3, 2000, pp. 373–383.

Reflection of Transverse Waves in a Structure "Dielectric–Piezoelectric Semiconductor with Current"

L. M. Lyamshev* and N. S. Shevyakhov**

** Andreev Acoustics Institute, ul. Shvernika 4, Moscow, 117036 Russia*
e-mail: lyamshev@kapella.gpi.ru
*** Institute of Radio Engineering and Electronics, Ul'yanovsk Division, Russian Academy of Sciences, ul. Goncharova 48, Ul'yanovsk, 432011 Russia*
e-mail: ufire@mv.ru

Received July 24, 1999

Abstract—Reflection of a plane monochromatic transverse wave by the boundary of the acoustic contact of a dielectric with a hexagonal piezoelectric semiconductor in the presence of a longitudinal charge drift is treated in the small-signal approximation within the framework of the hydrodynamic description of a charge carrier plasma. A procedure of selecting the branches with allowance for the conversion of the quasi-acoustic mode (a refracted transverse wave) into plasma-acoustic disturbances, both in-leaking at the boundary or out-leaking from it, is proposed for the determination of the solution under the conditions of a supersonic drift and "overcritical" angles of incidence. Beyond the restrictions of White's theory of ultrasonic wave propagation in piezoelectric semiconductors, it is demonstrated that this technique removes the defects of the solutions obtained earlier in the form of discontinuities in angular dependences of the modulus of the reflection coefficient of a transverse wave in the vicinity of the "critical" angle of incidence and leads to a solution that does not contain a resonance singularity of a polar type. © *2000 MAIK "Nauka/Interperiodica".*

Reflection of ultrasonic waves from the boundaries of layered structures of the "piezoelectric–semiconductor" and "dielectric–piezoelectric semiconductor with current of charge carriers" types was discussed quite extensively in the 1970s and 1980s. The case of the wave reflection in structures with separated piezoelectric and semiconductor properties was studied in detail [1–5]. This case attracted the attention of researchers because of the good prospects for its applications in the development of nonlinear acoustoelectronic devices [6]. Naturally, further efforts were concentrated on the analysis of nonlinear effects [7–9].

The reflection properties of the boundary of a monolithic structure "dielectric–piezoelectric semiconductor with current" with respect to acoustic waves incident from the dielectric was also considered by many researchers [10–15]. Despite many attempts, the problem has not been solved adequately. The major theoretical difficulties in studying this case are connected first of all with the singularities in the angular dependences of the modulus of the reflection coefficient near the "critical" angle of incidence under the conditions of supersonic drift.[1] They are similar to those existing in optics in the case of reflection of light waves from the boundary of an amplifying medium of a lower density [16, 17]. A similar situation exists also in the case of the reflection of sound waves from the boundary between equilibrium and nonequilibrium oscillatory-excited gases [18].

As applied to the boundary-value problems of the refraction of electromagnetic waves at the contact between passive and active media, the existence of these singularities is connected commonly [19] with insufficient adequacy of a single-frequency representation of wave fields for expressing the cause-and-effect relationships at overcritical angles of incidence. This does not answer the question, since, in the case of the monochromatic way of describing the establishment of the chain of events, "cause–effect" is not canceled in general but transformed into a corresponding causal form, i.e., the radiation principle. On the other hand, in an active medium, we cannot ignore the possibility of conversion of a refracted wave into field disturbances, which not only transfer energy, but also contribute to the energy "extraction" from the active medium. Then, the radiation principle is replaced (or complemented) by the conditions of the process existence corresponding to the causal considerations and grounded upon a specified mechanism of field interaction with the active medium. In this case, the latter plays the role of a distributed source of energy, and, in this connection, possible singularities (jumps) of the modulus of the reflection coefficient[2] must be connected (if they exist at all) with the change of not a geometrical quantity, i.e., the

[1] It is necessary to note that in our previous paper [10] (see also [20]), such singularities were not noticed because of a mistake in interpolation in the case of a too large step of change of the incidence angle.

[2] We should remind the reader that in fact, the modulus of the reflection coefficient is the energy characteristic of the refraction process.

1063-7710/00/4603-0317$20.00 © 2000 MAIK "Nauka/Interperiodica"

angle of incidence (the characteristic of the spatial spectrum), but the parameter expressing the specific features of the "energy exchange" between the wave and the active medium. In our opinion, the inability to understand this fact and the absence of nonformalized models of the field interaction with an active medium (see [11, 16, 17]) are the primary causes for the arising difficulties.

A paper by Filippov [13] is indicative in this respect. It considers the reflection of a transverse wave by a "dielectric–semiconductor layer with current" boundary for the 45°-cut of a crystal of the class $\bar{4}3m$. The continuity of the calculated angular dependences of the energy reflection coefficient $|R|^2$ gives an impression of successful results. However, the selection of solution that is motivated only by the radiation principle is questionable. The fact that the value $R = 1$, which is common for the reflection of a transverse wave by a free boundary of an isotropic solid in the case of the thickness of a piezoelectric semiconductor layer tending to zero, does not follow from the paper results (despite the statements made by the author) makes such opinions about this paper more justified. In particular, in the case of this limit, the amplitude coefficient R of the reflected wave retains in an incomprehensible way the dependence on the electromechanical coupling coefficient (already eliminated by the gradual "stripping" of the layer) of the semiconductor and on the dielectric permeabilities of the materials.

The purpose of this paper is to critically revise the theoretical data on the reflection of a transverse wave from an acoustic contact between an isotropic dielectric and a piezoelectric semiconductor of the class 6*mm* with current [10, 14, 15] on the basis of the concept of conditionality of the "critical" reflection by the energy characteristics of the process of the interaction of a refracted wave with an active medium. Correspondingly, the condition of a continuous change of the solution as a function of the angle of incidence is adopted as the main concept for the selection of the quasi-acoustic branch of the solution in a piezoelectric semiconductor in the process of the transition to the "overcritical" reflection and active behavior of the medium (a supersonic drift). This condition allows us to alternatively combine the requirement of boundedness of the solution (which used to be the only criterion for the selection of a solution [10, 14, 15]) with the radiation principle (the only criterion for the selection of a solution used by Filippov [13]). The limitation due to the requirement of the low level of electromechanical coupling, which is characteristic of White's theory of acousto-electronic interaction [21], as well as the traditional relation between the "critical" reflection and the idea of the critical angle of the total reflection, is removed from the description of the dispersion properties of a piezoelectric semiconductor with current in this paper. This provides an opportunity not only to extend the theoretical results to the case of strong piezoelectric materials but also to remove the additional mistake, which was present in many preceding papers [10, 13–15]. The "smallness" of this mistake is far from being evident under the conditions of "critical" reflection, even in the case of piezoelectric semiconductors with weak electromechanical coupling. The necessary data on the spectral properties of the modes of a piezoelectric semiconductor with current are taken from our previous paper [22], where the hydrodynamic approximation was used to describe the effects of kinetics of charge carriers, and the quasi-static approximation of an electric field was also applied. The effect of these approximations is completely transferred to this paper.

We consider the next geometry of the problem: the region $y > 0$ in the rectangular coordinates $x0yz$ is filled with an isotropic dielectric ($\nu = 1$), and the region $y < 0$ is filled with a piezoelectric semiconductor of the class 6*mm* with the axis $6 \| z$ ($\nu = 2$). The "pulling" field $E_0 \| x$ is applied to the semiconductor. Let a plane monochromatic transverse wave with the frequency ω and particle displacements $u \| z$ be incident at the angle θ upon the boundary $y = 0$ of the acoustic contact between the materials from the side of the dielectric. The interaction of the wave with the boundary in these conditions does not change the polarization of the elastic displacements. Therefore, the equations of the piezoelectric effect together with the Maxwell equations in the quasi-static approximation and the motion equations of the theory of elasticity complemented with the equation of continuity and the linearized expression for the current density in the piezoelectric semiconductor [21] (see also [8, 15]) lead to the next system of initial equations:

$$\begin{aligned} p_\nu \ddot{u}_\nu &= \lambda_\nu \nabla^2 u_\nu + (\nu - 1)\beta \nabla^2 \varphi_\nu, \\ \nabla^2 \varphi_\nu &= (\nu - 1)\left(\frac{4\pi\beta}{\varepsilon_\nu}\nabla^2 u_\nu + \frac{4\pi e}{\varepsilon_\nu} n\right), \qquad (1) \\ (\nu - 1)\left[f\mu\left(E_0 \frac{\partial}{\partial x}\right) + f D_0 \nabla^2 - \frac{\partial}{\partial t}\right] en &= \sigma_0 \nabla^2 \varphi_\nu. \end{aligned}$$

Here, u_ν is the elastic displacement, φ_ν is the electric potential, n is the density of charge carriers induced in the process of shear deformation of the piezoelectric semiconductor, $\nabla^2 = \partial^2/\partial x^2 + \partial^2/\partial y^2$ is the Laplacian, ρ_ν is the density, λ_ν is the shear modulus, ε_ν is the dielectric permeability, β is the piezoelectric modulus, μ is the mobility of charge carriers, D_0 is the diffusion coefficient of charge carriers, σ_0 is the conductivity of the piezoelectric semiconductor, f is the trap factor, e is the

elementary charge, and t is time. Let us add the boundary conditions to equations (1):

$$\begin{gathered} u_1\big|_{y=0} = u_2\big|_{y=0}, \\ \lambda_1\frac{\partial u_1}{\partial y}\bigg|_{y=0} = \lambda_2\frac{\partial u_2}{\partial y}\bigg|_{y=0} + \beta\frac{\partial \varphi_2}{\partial y}\bigg|_{y=0}, \\ \varphi_1\big|_{y=0} = \varphi_2\big|_{y=0}, \\ \varepsilon_1\frac{\partial \varphi_1}{\partial y}\bigg|_{y=0} = \varepsilon_2\frac{\partial \varphi_2}{\partial y}\bigg|_{y=0} - 4\pi\beta\frac{\partial u_2}{\partial y}\bigg|_{y=0}, \\ \sigma_0\frac{\partial \varphi_2}{\partial y}\bigg|_{y=0} - fD_0e\frac{\partial n}{\partial y}\bigg|_{y=0} = 0, \end{gathered} \tag{2}$$

which mean the continuity of shear displacements and stress, electric potentials and normal components of electric inductions, and the requirement of the absence of charge carrier flow from the piezoelectric semiconductor to the dielectric, respectively.

Oscillations and waves arising as a result of boundary disturbance by an incident wave are in spatial (in the x axis) and time synchronism at the boundary points. Therefore, if $\xi = k_x x - \omega t$ is the phase of oscillations of the incident wave at $y = 0$, then, u_ν, φ_ν, and $n \sim \exp(i\xi)$. Using this fact, we obtain (in the way similar that used earlier [10, 14, 15]) from equations (1) at $\nu = 1 (y > 0)$:

$$u_1 = Ue^{i\xi}(e^{-ipy} + Re^{ipy}), \quad \varphi_1 = Fe^{i\xi}e^{-k_x y}, \tag{3}$$

where U is the amplitude of particle displacements in the incident wave, R is the coefficient of reflection of the transverse wave, $p = (k_1^2 - k_x^2)^{1/2}$, $k_1 = (\rho_1\omega^2/\lambda_1)^{1/2}$ is the wave number for transverse waves in the dielectric, $k_x = k_1\sin\theta$, and F is the amplitude of oscillations of the electric field potential induced in the dielectric by piezoelectric charges from the surface of the piezoelectric semiconductor. We should remind that, in the process of the selection of solutions (3), we followed the standard requirement of limitation for the potential and the Sommerfeld radiation principle.

In the case of a piezoelectric semiconductor ($\nu = 2$), the process of solution construction is analogous. By virtue of proportionality of the quantities u_2, φ_2, and n to the phase factor $\exp(i\xi)$, equations (1) are transformed into a system of homogeneous differential equations, which establishes the dependences of the fields u_2 and φ_2 on the transverse coordinate and the distribution of charge carriers n along it. The characteristic equation of this system has the known form [15, 20]

$$\begin{gathered} s(s + k_2^2)\left[\frac{\omega_c}{\omega} - \left(i\gamma + s\frac{\omega}{\omega_D k_2^2}\right)\right] \\ - K^2 s^2\left(i\gamma + s\frac{\omega}{\omega_D k_2^2}\right) = 0, \end{gathered} \tag{4}$$

where $s = q^2 - k_x^2$, q is the characteristic coefficient, $k_2 = (\rho_2\omega^2/\lambda_2)^{1/2}$ is the wave number of transverse waves in the piezoelectric semiconductor without taking into account the piezoelectric effect, $\gamma = 1 - v_d k_x/\omega$ is the drift parameter, $v_d = -f\mu E_0$ is the drift velocity, $\omega_c = 4\pi\sigma_0/\varepsilon_2$ is the frequency of the conductivity relaxation, $\omega/\omega_D = fD_0k_2^2/\omega$, ω_D is the diffusion frequency, and $K^2 = 4\pi\beta^2/\varepsilon_2\lambda_2$ is the square of the factor of the static electromechanical coupling.

In the case of a piezoelectric semiconductor, the solution to equation (1) for the sequence of the values of the characteristic coefficients q_j, $j = 1, 2, \ldots$, obtained from equation (4) can be represented in the form

$$\begin{gathered} u_2 = e^{i\xi}\sum_j UA_j e^{q_j y}, \quad \varphi_2 = e^{i\xi}\sum_j F_j e^{q_j y}, \\ n = e^{i\xi}\sum_j N_j e^{q_j y}. \end{gathered} \tag{5}$$

In this case, the amplitude coefficients to be determined, i.e., A_j, F_j, and N_j from expressions (5), for each single value of q_j are connected by the relationships

$$\begin{gathered} (k_2^2 + s_j)UA_j = -\frac{\beta}{\lambda_2}s_j F_j, \\ \frac{4\pi\beta}{\varepsilon_2}s_j UA_j + \frac{4\pi e}{\varepsilon_2}N_j = s_j F_j, \\ \left(i\gamma + \frac{\omega}{\omega_D k_2^2}\right)eN_j = \frac{\sigma_0}{\omega}s_j F_j. \end{gathered} \tag{6}$$

Expressions (4)–(6) demonstrate that oscillations of three types are excited under the action of the incident wave: purely electrical ones with the simple root $s_1 = 0$ of equation (4), oscillations at the only possible (because of the boundedness of the solution at $y < 0$) characteristic coefficient $q_1 = k_x$, where $k_x > 0$, and mixed plasma-acoustic oscillations connected by electric fields with the roots of equation (4)

$$s_{2,3} = \frac{k_2^2}{1 + K^2}\frac{\omega_D}{2\omega}\left[\Gamma_- \pm \sqrt{\Gamma_+^2 + 4\frac{\omega_c}{\omega_D}K^2}\right], \tag{7}$$

where $\Gamma_\pm = \omega_c/\omega \pm \omega/\omega_D - i\gamma(1 + K^2)$.

Electric oscillations describe the boundary piezoelectric polarization field of the type φ_1 from expression (3). Its properties are well known (see [15, 20] for example). Plasma-acoustic oscillations are less studied and have been considered as a rule in the approximation of low electromechanical coupling $K^2 \ll 1$ and for low-frequency ultrasound $\omega \ll \omega_D$. For the case of such an approximate approach, they were classified in our previous paper [20] as oscillations of mostly the plasma (the root s_2 in the case of the sign "plus" in formula (7))

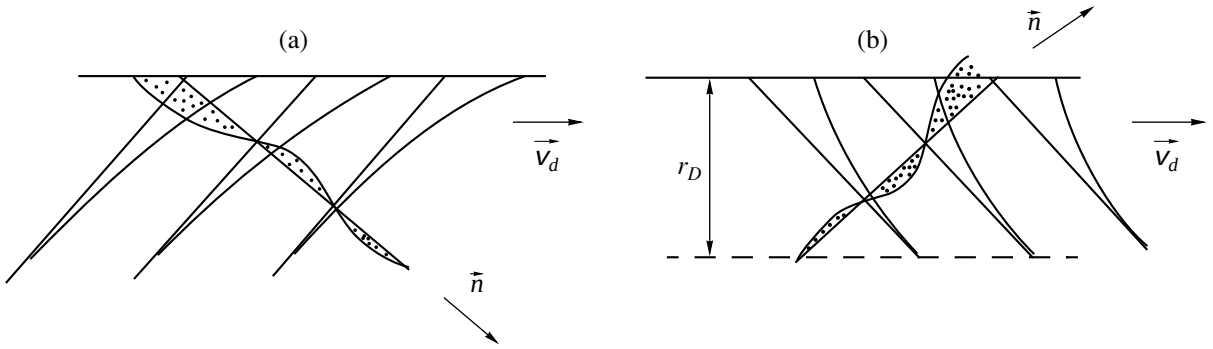

Fig. 1. Structure of boundary quasi-plasma oscillations in the cases of (a) subsonic and (b) supersonic drift. Inclined lines correspond to wave fronts, and curves show the distribution of the oscillation amplitudes along the fronts. Disturbances of the cubic density of charge carriers in the direction of the wave normal *n* are shown by the dotted regions.

or acoustic (the root s_3 in the case of the sign "minus" in formula (7)) nature. In this case, the behavior of the quasi-acoustic mode obeys White's theory [21], and the excitation of quasi-plasma oscillations is explained by the additional (because of the boundary mode coupling) disturbance of the plasma subsystem of the piezoelectric semiconductor under the action of the field of the boundary piezoelectric-polarization oscillations.

The specific features of plasma-acoustic oscillations mentioned above also remain valid in the case of both strong electromechanic coupling and frequencies ω comparable to ω_D, which provides grounds to follow a common tradition in naming them. However, one will be able to see from the following analysis that just the approximate (White's) description of the quasi-acoustic mode is in fact the main reason for the utilization of the concept of "critical" reflection on the basis of the idea of the critical angle of "total" reflection [10, 14, 15, 20]. The inadequacy of the approximate approach is explained by the fact noted by Shevyakhov [22], that the mutual influence of nontunable branches of the spectrum of plasma and acoustic modes of an infinite piezoelectric semiconductor (this effect being fundamentally important for the correct determination of the conditions of "critical" reflection) can be detected reliably only in the higher orders of the approximation with respect to the coupling parameter $\mathcal{K}^2\omega_c/\omega_D$, where $\mathcal{K}^2 = K^2/(1 + K^2)$, because of the "weakness" of the interaction specific to them. This specific feature also remains in the conditions of the boundary mode coupling.[3]

Before the determination of the characteristic coefficient $q_2 = \pm(s_2 + k_x^2)^{1/2}$ of quasi-plasma oscillations, we have to remind the basic properties of the plasma mode for an infinite piezoelectric semiconductor [22] and dwell on its differences from quasi-plasma oscillations arising due to boundary mode coupling. First, let us note that they interrelate as natural and forced oscillations. The role of the latter is played by the quasi-plasma oscillations excited in the piezoelectric semiconductor by the wave incident from outside. The second characteristic feature is the fact that they are "tied" to the boundary, i.e., they are localized boundary disturbances. It is important that in this case we do not contradict their interpretation as a plasma mode proper to a piezoelectric semiconductor. Indeed, according to Shevyakhov [22], plasma waves do not have anomalies in the dispersion spectrum and attenuate at any pulling fields. As the distance from the boundary of the piezoelectric semiconductor grows, they attenuate independently of the value of the pulling field and the conditions of the boundary excitation.

It follows from the stated above that, in the process of the determination of the sign of the characteristic coefficient q_2, one has to be guided by the condition $\mathrm{Re}\,q_2 > 0$, i.e., $q_2 = (s_2 + k_x^2)^{1/2}$. In fact, this means that, despite the presence of the component $\mathrm{Im}\,q_2 \neq 0$ in the wave vector of quasi-plasma disturbances, they demonstrate first of all the properties of localized boundary oscillations in their behavior and obey not the radiation principle but the requirement of boundedness. The details of the structure of boundary plasma oscillations can be demonstrated using a piezoelectric semiconductor with low electromechanical coupling as an example. In this case, together with the relationship $\omega_c \ll \omega_D$, which is usually valid, we obtain an expression from relationship (7):

$$q_2 \approx \left[k_x^2 + k_2^2\frac{\omega_D}{\omega}\left(\frac{\omega_c}{\omega} - i\gamma\right)\right]^{1/2}, \qquad (8)$$

which being substituted into expression (5) shows, first, the criticality of the inclination of the equiphase planes of quasi-plasma oscillations with respect to the sign of the drift parameter, and, second, the boundedness of the depth of their localization by the Debye length r_D (see Fig. 1).

[3] In the conditions of boundary mode coupling, the nontunability of the plasma and acoustic branches of the spectrum is expressed as the absence of multiple degeneracy of the roots of equation (7).

The first of these features follows from the fact that the plasma mode is subjected to the governing action of the pulling field to a greater extent as compared to the acoustic mode [22]. The mechanism of the formation of the inclination of the equiphase planes of quasi-plasma oscillations under the action of drift is as follows. Wisps of quasi-plasma oscillations at the surface of a piezoelectric semiconductor have a strictly "sonic" velocity of longitudinal displacements because of the coupling with the boundary disturbances caused by an incident wave. At the same time, in the in-depth layers of the crystal, they move at the velocity v_d in conformity with the "drift" nature of plasma waves and thus, they either fall behind (Fig. 1a, subsonic drift) or advance (Fig. 1b, supersonic drift) the surface wisps. This leads to the inclination of the equiphase planes and gives the quasi-plasma oscillations the form of the waves leaking from the boundary ($\gamma > 0$) or to it ($\gamma < 0$). It is expedient to note that, in the conditions of "active" behavior of the medium $\gamma < 0$, the boundary plasma oscillations are an example of the "typical" violation of the radiation principle in active media. We mentioned this fact in the introductory part of the paper.

Let us turn to the determination of the characteristic coefficient q_3. Considering the inequality $\mathrm{Re}\Gamma_+ > \mathrm{Re}\Gamma_-$, we have according to expression (7) $\mathrm{Re}s_3 < 0$. Under the condition $k_1 > k_2$, which provides the total reflection of the transverse wave from a piezoelectric semiconductor in the dielectric limit $\omega_c/\omega \longrightarrow 0$, $\omega/\omega_D \longrightarrow 0$, and $\gamma \longrightarrow 1$, there is the fundamental possibility of the sign of $\mathrm{Re}q_3^2 = \mathrm{Re}s_3 + k_x^2$ changing as the angle θ grows. The same possibility of a change of sign of the quantity $\mathrm{Im}q_3^2 = \mathrm{Im}s_3 \sim -\gamma$ is present within the range of drift velocities $v_d > \omega/k_1$. In the characteristic conditions of the formation of singularities in the dependences $|R(\theta)|$ [14, 15] (the "overcritical" angles of incidence and supersonic drift), one has to take into account both possibilities, which indicates the existence of the branch point $q_3 = 0$.

This fact was ignored in preceding papers [10, 14, 15, 20], where the "overcriticality" of reflection of a transverse wave by a piezoelectric semiconductor was traditionally connected (though with reservations) only with the realization of the total reflection in the limiting case of a dielectric medium. We can assume that, in the case of a piezoelectric semiconductor with current, just the branch point $q_3 = 0$ determines the conditions of the mode of "critical" reflection without mixing it with the concept of total reflection, which does not have a physical meaning. Revision of the results of the preceding papers [10, 14, 15, 20] on these grounds is also promising because it avoids the limitations of White's theory [21]. This theory was used to one or another extent in the attempts to utilize the concept of the angle of limiting reflection as the indicator of the "criticality" of reflection.

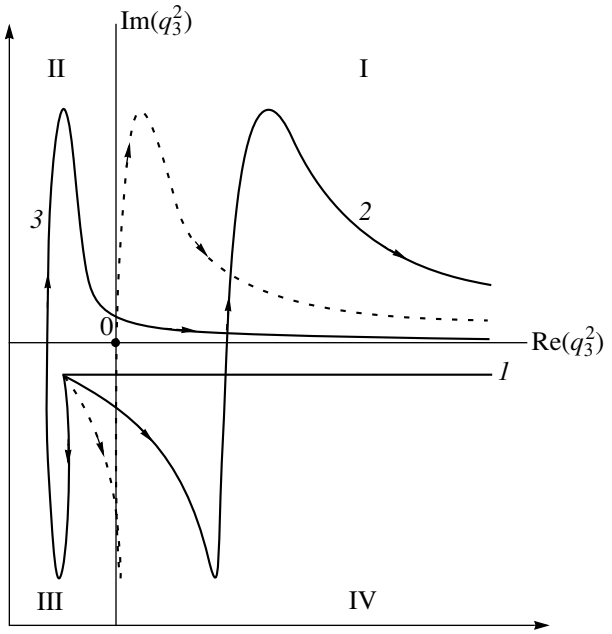

Fig. 2. Pattern of parametric phase trajectories of the image point for the quasi-acoustic mode in the complex plane q_3^2 in the process of the variation of the incidence angle from 0 to $\pi/2$. (*1*) $v_d = 0$, (*2*) $v_d < v_d^*$, and (*3*) $v_d > v_d^*$.

The position of the branch point $q_3 = 0$ in the plane (θ, v_d) can be determined from the combined solution of the equations $\mathrm{Re}s_3 + k_x^2 = 0$ and $\gamma = 0$. Designating its coordinates as θ^* and v_d^* and taking into account expression (7), we obtain

$$v_d^* = \frac{\omega}{k_1}\left(\frac{\lambda_2\rho_1}{\lambda_1\rho_2}\right)^{1/2}\sqrt{2\frac{\omega}{\omega_D}(1+K^2)} \times\left[\sqrt{\left(\frac{\omega_c}{\omega}+\frac{\omega}{\omega_D}\right)^2+4\frac{\omega_c}{\omega_D}K^2}+\left(\frac{\omega}{\omega_D}-\frac{\omega_c}{\omega}\right)\right]^{-1/2}. \quad (9)$$

The corresponding value of θ^* is calculated according to the formula $\sin\theta^* = \omega/k_1 v_d^*$.

The meaning of the quantity v_d^* in expression (9) can be revealed considering the behavior of the parametric (at $v_d = \mathrm{const}$) trajectories described in the complex plane q_3^2 by the image point of the quasi-acoustic mode in the process of the θ variation from 0 to $\pi/2$. According to the typical pattern given in Fig. 2, one can see that the trajectory corresponding to the "critical" value of v_d^* (the dashed line) is the only possibility for the direct transition of the image point from the quadrant III of the plane q_3^2 to the quadrant I bypassing the

intermediate quadrants II (at $v_d > v_d^*$, curve *3*) or IV (at $v_d < v_d^*$, curve *2*). Intersection of the branch line $(-\infty, 0]$ by the trajectory with the transition of the type III $\longrightarrow$ II $\longrightarrow$ I means its extension to another sheet of the Riemannian surface q_3^2.

Thus, we can treat v_d^* as the threshold value of the drift velocity $v_d > \omega/k_1$. If the value of the drift velocity lies lower than this threshold, the parametric trajectory lies completely within the initial sheet of the Riemannian surface, and if the threshold is exceeded, the trajectory ends at another sheet.

We can assume that if a medium is active (quadrants I and II), the radiation principle and the requirement of boundedness of the solution acquire a contradictory character in homeomorphic mapping $\{q_3^2\} \longrightarrow \{q_3\}$, and the choice between them in order to select the branches of the solution must be made proceeding from the previous history of the behavior of the parametric trajectory. The existence of such mutual exclusion was demonstrated already by the behavior of the solution for the boundary quasi-plasma oscillations. However, this question did not arise, since the attenuation always proper to the plasma mode allowed us to accept the requirement of boundedness of the solution as the self-contained one. It is expedient here to monitor the changes in the structure of the quasi-acoustic mode in the process of the movement of the image point along the parametric trajectories of the three chosen types ($v_d < v_d^*$, $v_d = v_d^*$, and $v_d > v_d^*$) by concentrating our attention at the continuity of the change of the value q_3 in the transitions between the quadrants. Let us denote

$$q_3^2 = \chi' + i\chi'', \quad |q_3^2| = |\chi|, \tag{10}$$

where, in correspondence with the representation $q_3^2 = k_x^2 + s_3$ and formula (7), for s_3 we have $\chi'' \sim -\gamma$. Taking into account expression (10), we can write (according to the definition of the signum function):

$$q_3 = \pm\frac{1}{\sqrt{2}}[\sqrt{|\chi| + \chi'} + i\,\mathrm{sign}(\chi'')\sqrt{|\chi| - \chi'}]. \tag{11}$$

In the quadrant III (small incidence angles $\theta < \theta^*$ and subsonic drift $\gamma > 0$), we have $\chi' < 0$, $\chi'' < 0$, which gives $\sqrt{|\chi| + \chi'} \ll \sqrt{|\chi| - \chi'}$ or at least $\sqrt{|\chi| + \chi'} \leq \sqrt{|\chi| - \chi'}$. Physically, this means the obvious prevalence of the radiation principle $\mathrm{Im}\,q_3 < 0$ in the process of the selection of branches. This condition takes into account the absence of dispersion anomalies in the acoustic spectrum of the modes of a piezoelectric semiconductor [21, 22]. We should add that the above inferences are also valid in the process of the selection of branches in the quadrant II, which also belongs to the quadrants with the wave type of solution.

In the quadrant IV $\chi' > 0$, if at the beginning (at $\chi' \ll 1$) the values of $\mathrm{Re}\,q_3$ and $\mathrm{Im}\,q_3$ are close to each other, the real part of q_3 becomes dominant as χ' grows. In relation to the clearly nonwave character of the solution, now we have to consider the requirement of boundedness $\mathrm{Re}\,q_3 < 0$ as the criterion for the selection of the solution branches. Analogously, the selection of branches in the quadrant I should obey the same condition. However, we should recall that, here, they may belong to different sheets of the Riemannian surface. Therefore, the extension of this criterion to the quadrant I is admissible only with the proviso that the selected solution belongs to the sheet of the Riemannian surface common with the quadrant IV. This condition is consistent with the solution obtained for the case $v_d < v_d^*$.

In the case of an inactive medium, the governing role of the radiation principle (in the case of the subordinate meaning of the requirement of boundedness, quadrant III) or, conversely, the requirement of boundedness (in the case of the subordinate meaning of the radiation principle, quadrant IV) might not be stressed, since, in the process of the selection of the positive root (11), they are satisfied simultaneously because of the general condition $\chi'' < 0$ ($\mathrm{Re}\,q_3 > 0$, $\mathrm{Im}\,q_3 < 0$):

$$q_3 = \frac{1}{\sqrt{2}}[\sqrt{|\chi| + \chi'} - i\sqrt{|\chi| - \chi'}]. \tag{12}$$

The validity of this approach is not exhausted by the considerations of only methodological character but originates from the essential physical differences in the structure of solution (5) of the quasi-acoustic mode of branch (12) lying in the quadrants III ($\chi' < 0$) or IV ($\chi' > 0$). For example, in the quadrant III, we have $\mathrm{Re}\,q_3 \ll |\mathrm{Im}\,q_3|$, and the corresponding solution (5) describes a monochromatic wave refracted in the piezoelectric semiconductor and attenuating weakly because of the acoustoelectronic absorption as the distance from the boundary grows. In the case of the transition to the quadrant IV, the quantities $\mathrm{Re}\,q_3$ and $\mathrm{Im}\,q_3$ exchange their places so to say, and, from expression (5) taking into account expression (12), it follows that the quasi-acoustic mode acquires the dominant features as $\chi' > 0$ increases, these features being characteristic of the boundary plasma-acoustic oscillations of the out-leaking type (see Fig. 1a). We should stress that here we do not mean the identical coincidence of solutions (5) for q_2 and q_3 in the quadrant IV. However, their closeness is doubtless, and, naturally, the following transition from the quadrant IV to the active quadrant I at $v_d < v_d^*$ (i.e., along curve *2* in Fig. 2) is performed according to the same rules that were established above for the selection of the root q_2. The condition $\mathrm{Re}\,q_3 > 0$ is imposed just by virtue of the "violation" of the radiation principle because of the active character of the medium. An explicit expression for q_3 is obtained in this case from

expression (12) with a change of sign of the imaginary part:

$$q_3 = \frac{1}{\sqrt{2}}[\sqrt{|\chi| + \chi'} + i\sqrt{|\chi| - \chi'}], \quad \chi' > 0, \quad \chi'' > 0, \tag{13}$$

and, according to expression (5), it determines the solution in the form of the boundary plasma-acoustic oscillations of the in-leaking type (Fig. 1b). Finally, we have to note that q_3 expressed by formulas (12) and (13) at different sections of the single-sheet trajectory *2* in Fig. 2 are determined by a common formula (11), where the selection of the positive root corresponds to the initial sheet.

Now let us discuss the specific features of the selection of the solution for the quasi-acoustic mode under the conditions $v_d > v_d^*$. The value of q_3 in the initial quadrant III is already known and determined by formula (12). The transition of the trajectory *3* (Fig. 2) from the quadrant III to the active quadrant II is connected with the extension of the branch to another sheet of the Riemannian surface, as we have mentioned above. Therefore, we have not just to take $\mathrm{sgn}(\chi'') = 1$ in formula (11) but also to select the negative sign, i.e.,

$$q_3 = -\frac{1}{\sqrt{2}}[\sqrt{|\chi| + \chi'} + i\sqrt{|\chi| - \chi'}]. \tag{14}$$

The negativeness of the quantity $\mathrm{Re}\,q_3$ in expression (14) shows that this branch of the solution is selected in contradiction with the requirement of boundedness but in consistency with the radiation principle. It is characteristic that, in the intersection point of the trajectory *3* and the semi-axis $\mathrm{Re}\,q_3^2 < 0$ in Fig. 2, the values of q_3 determined by formulas (12) and (14) coincide. On the contrary, if we follow the way of selecting the solution used previously [10, 14, 15, 20], then, with the transition to the quadrant II, we should change the sign of only the imaginary part of q_3 in expression (12). In this case, we obtain expression (13) for q_3. This expression in combination with expression (12) does not provide a continuity of its change in the process of the transition between the quadrants. The violation of the radiation principle here was not perceived earlier [10, 14, 15, 20] as a defect of solution because of the lack of the differentiation of reflection modes by the condition $v_d > v_d^*$.[4] It seemed natural in this case to extend the universality of the requirement of boundedness for boundary quasi-plasma oscillations (the root q_2) also to the quasi-acoustic mode under the conditions of "overcritical" reflection. The singularities in the dependences $|R(\theta)|$ mentioned above arose because of this. According to expression (14), where the imaginary part numerically exceeds the real part due to the condition $\chi' < 0$, solution (5) represents the quasi-acoustic mode (as in the quadrant III) in the form of a refracted monochromatic wave, which is not attenuated but amplified (a supersonic drift) with the propagation within the piezoelectric semiconductor bulk. Thus, at this stage, the requirement of boundedness is quite reasonably excluded from consideration because of the typical wave behavior of the quasi-acoustic mode in the conditions of the medium activity [21, 22]. The transition from the quadrant II to the quadrant I along trajectory *3* in Fig. 2 is accompanied only by the change of sign of χ' in formula (14). This leads to the decrease in $|\mathrm{Im}\,q_3|$ and growth of $|\mathrm{Re}\,q_3|$. The quasi-acoustic mode finally acquires the form of the wave, which is amplified but, at the same time, out-leaking weakly into the piezoelectric semiconductor.

If $v_d \equiv v_d^*$ at $\theta < \theta^*$, the coefficient q_3 is unambiguously determined by relationship (12), and the quasi-acoustic mode has the form of a refracted transverse plane wave attenuating as it propagates in a piezoelectric semiconductor. As the wave reaches the branch point $q_3 = 0$ in the process of motion along the trajectory indicated by a broken line in Fig. 2, this attenuation stops because of the establishment of the strictly "sonic" drift velocity (at $\theta \longrightarrow \theta^*$, $\gamma \longrightarrow 0$), and the refracted wave with a plane homogeneous front starts to propagate along the boundary, as it occurs under the conditions of "critical" reflection from a common ideal medium. As the condition $\theta > \theta^*$ becomes valid, further motion along the trajectory shown by the dashed line in Fig. 2 into the quadrant I does not allow us anymore to make the unambiguous choice between the values of q_3 from expressions (13) and (14) at $\chi' > 0$. The ambiguity of the result symptomatically indicates the conditionality of the "critical" reflection caused by just the energy side of the process of wave interaction with an active medium.

After the determination of q_j ($j = 1, 2, 3$), only F_1, A_2, and A_3 of the whole set of the amplitude coefficients of solution (5) may be considered independent because of expression (6). After the substitution of expressions (3) and (5) into expression (2) and the solution of the obtained system of algebraic equations, we obtain

$$R = \frac{i\cos\theta\lambda_1(L_2 + L_3) - \lambda_2(L_3M_2 - L_2M_3)}{i\cos\theta\lambda_1(L_2 + L_3) + \lambda_2(L_3M_2 - L_2M_3)},$$
$$A_3 = \frac{2i\cos\theta\lambda_1 L_2}{i\cos\theta\lambda_1(L_2 + L_3) + \lambda_2(L_3M_2 - L_2M_3)}. \tag{15}$$

[4] This was indicated by Filippov [13], but again, another extremity arose because of the lack of the distinction between the reflection modes according to the drift, i.e., a complete neglect of the requirement of boundedness of the solution for the quasi-acoustic mode.

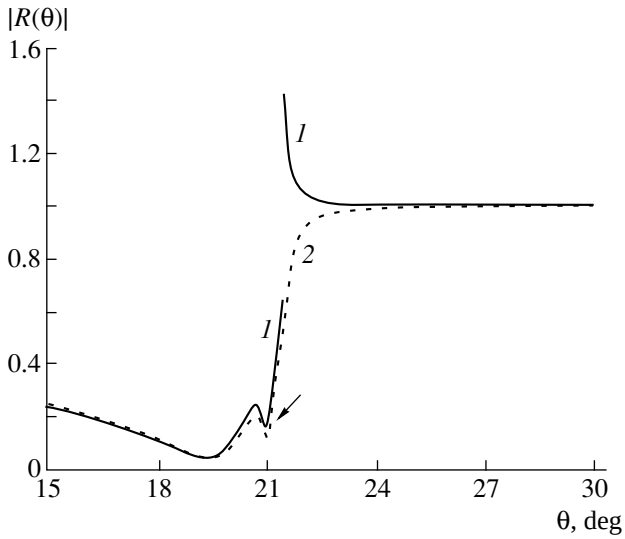

Fig. 3. Angular dependences $|R(\theta)|$ for the As_2Se_3–ZnO boundary at $\omega_c/\omega = 0.005$, $\omega/\omega_D = 0.001$, and $v_d/c_t = 2.8$. The quantity $c_t = \omega/k_1$ is the velocity of transverse waves in the dielectric.

Here, $A_2 = -A_3L_3/L_2$ and

$$L_j = \frac{1}{k_1(1+\Delta_j)}\left[q_j\left(1+\Delta_j\frac{\omega^2}{\omega_D\omega_c}\frac{s_j}{k_2^2}\right)\right.$$
$$\left.+\left(1+\frac{\varepsilon_1}{\varepsilon_2}\right)^{-1}\left(q_j\Delta_j-\frac{\varepsilon_1}{\varepsilon_2}k_x\right)\right],$$

$$M_j = \frac{1}{k_1(1+\Delta_j)}\left[q_j(1+\Delta_j+K^2)\right. \qquad (16)$$
$$\left.+K^2\left(1+\frac{\varepsilon_1}{\varepsilon_2}\right)^{-1}\left(q_j\Delta_j-\frac{\varepsilon_1}{\varepsilon_2}k_x\right)\right],$$

$$\Delta_j = i\frac{\omega_c}{\omega}\left(\gamma - is_j\frac{\omega}{\omega_D k_2^2}\right)^{-1}.$$

According to expression (8), we have from expressions (16) in the low frequency limit: $1 + \Delta_2 \longrightarrow 0$ (in this case $1 + \Delta_3 \neq 0$). This leads to $L_2/L_3 \longrightarrow 0$ and, correspondingly, to $A_2/A_3 \longrightarrow 0$. This implication could be foreseen because of the mainly plasma nature of the oscillations described by partial solution (5) at $j = 2$.

We restrict ourselves to expressions (15), omitting the formulas for the amplitudes of the potentials F and F_1. If, in the process of the determination of the quantities q_j and s_j from expressions (15) and (16), we use White's approximation and select the "overcritical" region by the limiting angle of the total reflection for a dielectric medium, then, in the process of selecting the branches of q_3 by formula (13) in the conditions of the activity of a piezoelectric semiconductor, we arrive at the results obtained earlier [10, 14, 15, 20], as it could be expected. The rejection of White's approximation and the concept of the limiting angle of total reflection developed on its basis as the criterion of the "criticality" of reflection while maintaining the representation of q_3 under the conditions $\gamma < 0$ by formula (13) removes the polar singularities in the dependences $|R(\theta)|$. At the same time, their finite jumps-singularities at the "critical" point do not vanish at all, but, on the contrary, they may be amplified with the change in the pulling field. Such a behavior of $|R(\theta)|$ for the boundary of a piezoelectric semiconductor crystal ZnO with a chalcogenide glass As_2Se_3 ($\lambda_1/\lambda_2 = 0.18$, $\rho_1/\rho_2 = 0.8$, $\varepsilon_1/\varepsilon_2 = 1.0$, and $K^2 = 0.08$; the material parameters are taken from a handbook [23] and a paper by Kul'bitskaya and Shutilov [24]) is shown in Fig. 3 by line *1* consisting of dots virtually merged into a continuous line.

The total elimination of all defects of the solution is attained in the case $v_d > v_d^*$ only by way of application of formula (14) instead of formula (13). The corresponding dependence $|R(\theta)|$ is given in Fig. 3 by the dashed curve *2*. The absence of the sharp peak of the resonance acoustoelectronic amplification of the reflected wave in the curves in Fig. 3, i.e. the peak that transforms (according to the earlier data [10, 14, 15, 20]) into the polar singularity of $|R(\theta)|$ at a certain value of supersonic drift, is evidence of inadequacy of the use of the concept of the limiting angle of total reflection on the basis of White's approach even in the case of weak piezoelectric materials like ZnO. One can see also from Fig. 3 that in the case of an exact calculation of $|R(\theta)|$ according to formula (15) in the range of angles $\theta < \theta^*$ (they precede the singularity in curve *1*), the acoustoelectronic interaction leads to the formation of a "gap" in the reflection (indicated by an arrow) because of the optimization of the acoustic coupling of the dielectric and the piezoelectric semiconductor on account of conductivity and drift. This result agrees well with the described behavior of the quasi-acoustic mode in a piezoelectric semiconductor (before the transition of the image point along the phase trajectory *3* in Fig. 2 from the quadrant III to the quadrant II) as that of an attenuating wave refracted into the volume.

As the image point gets into the quadrant II, the attenuation of the refracted wave is changed for the amplification that does not influence qualitatively the character of the energy transfer by the wave with respect to the boundary. Therefore, the "gap" in the reflection in the form of a local minimum in the dependence $|R(\theta)|$ remains. However, there is a new detail, which manifests itself by the fact that a narrow peak of total reflection corresponding to the intersection point of the phase trajectory *3* in Fig. 2 with the negative semiaxis $\mathrm{Re}\,q_3^2$ arises in the reflection gap. Such peaks of total reflection are present in curve *1* in Fig. 4 at v_d

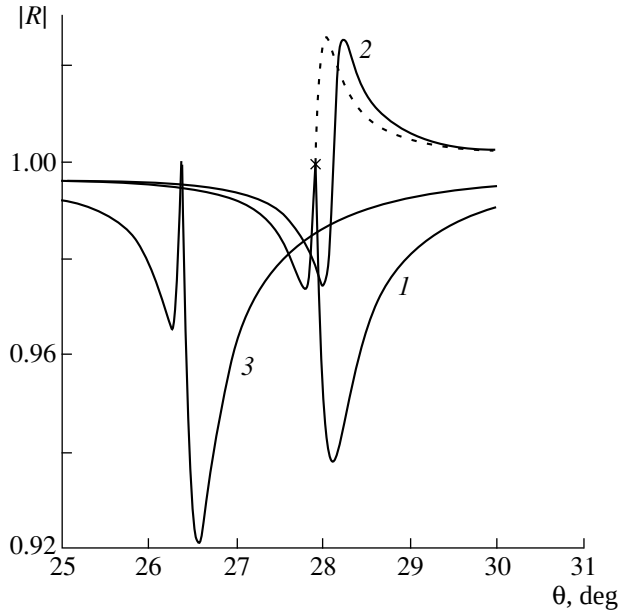

Fig. 4. Angular dependences $|R(\theta)|$ for the As_2Se_3–ZnO boundary for the same characteristics of the electronic plasma as in Fig. 3. (*1*) $v_d/c_t \simeq 2.13$, (*2*) $v_d/c_t = 2.12$, and (*3*) $v_d/c_t = 2.25$.

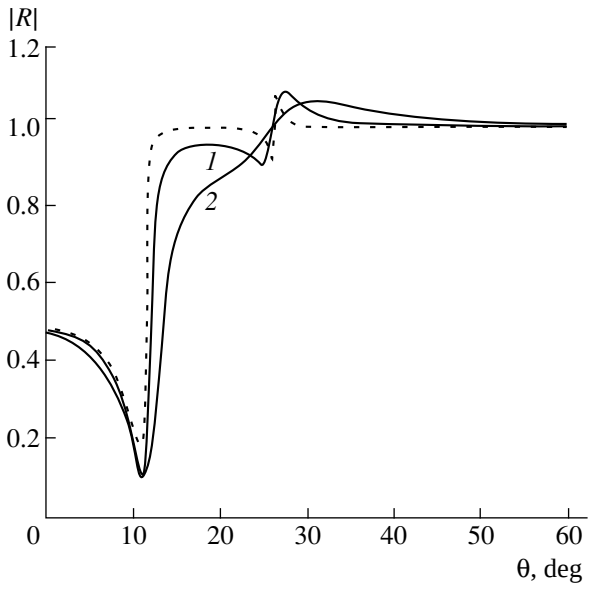

Fig. 5. Angular dependences $|R(\theta)|$ for the boundary "dielectric–semiconductor" with the parameters $\lambda_1/\lambda_2 = 0.11$, $\rho_1/\rho_2 = 0.58$, $\varepsilon_1/\varepsilon_2 = 0.73$, and $K^2 = 0.55$ at $\omega/\omega_D = 0.001$ and $v_d/c_t = 2.28$. (*1*) $\omega_c/\omega = 0.1$ and (*2*) $\omega_c/\omega = 0.5$. The dashed curve is obtained for $\omega_c/\omega = 0.01$.

slightly exceeding $v_d^* \approx 2.13$ with the offset $(v_d - v_d^*)/v_d^* = 10^{-11}$ and in curve *3* when v_d is noticeably greater than v_d^*.

The dashed curve, which is obtained for the small negative offset of v_d from v_d^* ($(v_d^* - v_d)/v_d^* = 10^{-11}$) and, therefore, almost coincides with curve *1* at the angles $\theta < \theta^*$, and curve *2* in Fig. 4 correspond to the case $v_d < v_d^*$. Now, by virtue of the passage of the image point in the transitions of the type III $\longrightarrow$ IV $\longrightarrow$ I through the "nonwave" quadrant IV into the "nonwave" (according to the condition of positioning of the phase trajectory *2* in Fig. 2 totally in the initial sheet of the Riemannian surface q_3^2) quadrant I, the dependences $|R(\theta)|$ reproduce a typical acoustoelectronic change in the signal level under the effect of drift [21]. In the case of the image point being in the "inactive" quadrant IV, when the quasi-acoustic mode in a piezoelectric semiconductor is a wave out-leaking from the boundary (because of $\gamma > 0$) like quasi-plasma oscillations in Fig. 1a, the acoustoelectronic attenuation of reflection occurs, and $|R(\theta)|$ passes through the minimum. At the moment when the image point intersects the positive semiaxis $\mathrm{Re}\, q_3^2 = 0$ (see curve *2* in Fig. 2), we have $\mathrm{Im}\, q_3 = 0$ ($\gamma = 0$) and $|R| \equiv 1$. The corresponding point in the dashed curve in Fig. 4 is indicated by a cross. It is of interest, because it represents in fact the branch point of the solution $q_3^2 = 0$ (the point "0" in the phase plane in Fig. 2) since the phase trajectory for the dashed curve in Fig. 4 almost coincides with the dashed trajectory in Fig. 2. This fact is confirmed by the comparison of the dashed curve and curve *1* in Fig. 4 obtained at the values of v_d very close to v_d^*: they coincide at $\theta < \theta^*$ and diverge essentially at $\theta > \theta^*$.

After the transition of the image point from the quadrant IV to the quadrant I, the acoustoelectronic attenuation of the reflected wave is changed by amplification: $\gamma < 0$. This is explained physically by the fact that, in the case of the position of the image point in the quadrant I on the initial sheet of the Riemannian surface q_3^2, the quasi-acoustic mode in the piezoelectric semiconductor is the wave in-leaking to the boundary like quasi-plasma oscillations in Fig. 1b. Thus, applying energy to the boundary, it provides an energy transfer to the reflected wave and, therefore, contributes to the amplification of the latter.

The acoustoelectronic amplification of the reflected wave is small. Even in the case of strong electromechanical coupling (see Fig. 5), it does not attain 10% of the level of total reflection. Comparing curves *1* and *2* with the dashed curve in Fig. 5, one can see that an increase in conductivity of a piezoelectric semiconductor causes the broadening and decrease of the peaks of acoustoelectronic amplification. In the dielectric limit $\omega_c/\omega \longrightarrow 0$, they become narrower and smaller. Therefore, the dependence $|R(\theta)|$ acquires a characteristic break with the transition into the typically horizontal section of the total reflection after passing through the "Brewster" minimum and a sharp growth up to unity.

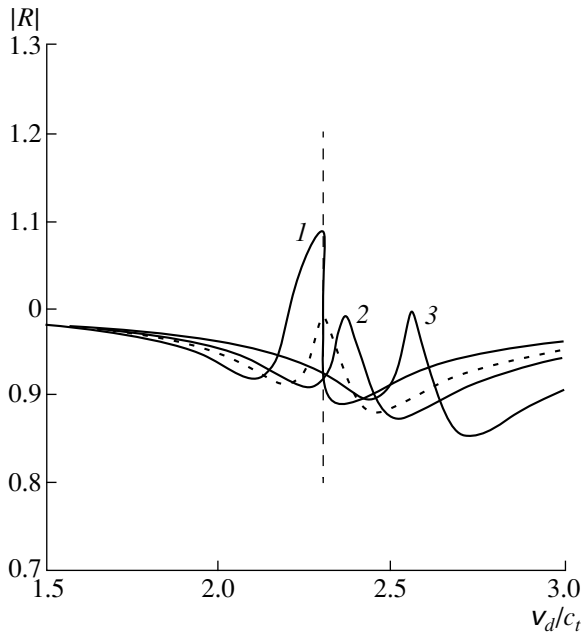

Fig. 6. Dependence of $|R|$ on v_d/c_t for the boundary "dielectric–semiconductor" with the same parameters as in Fig. 5 for $\omega_c/\omega = 0.1$ and $\omega/\omega_D = 0.001$. (*1*) $\theta = 27°$, (*2*) $\theta = 25°$, and (*3*) $\theta = 23°$. The dashed curve is obtained for $\theta = 25.77°$ ($\theta \approx \theta^*$). The vertical dashed line corresponds to the value $v_d^*/c_t \approx 2.3$.

Turning to Fig. 4, we can see that the jump-like transition from curve *1* to the dashed curve at the angles $\theta > \theta^*$ with the increase in v_d in the vicinity of v_d^* reflects the presence of jumps-singularities in the dependences $|R(v_d)|$ in the obtained solution at fixed θ, at the point $v_d = v_d^*$. Figure 6 illustrates this fact. In contrast to the jumps-singularities in the angular dependences $|R(\theta)|$ characteristic of the previous results [10, 14, 15, 20] (see Fig. 3), the discussed jumps-singularities manifest themselves with the change in the activity factor of the piezoelectric semiconductor and can be treated as the consequence of the insufficient adequacy of the adopted model of acoustoelectronic interaction. The experimental study of these phenomenon looks promising in this connection.

About 40 years have passed after the publication of the first papers devoted to the propagation of acoustic waves in semiconductors. However, this problem is still important and garners the attention of researchers (see [25, 26] for example).

ACKNOWLEDGMENTS

The work is supported by the Federal Target Program "Integration" (grant no. A 0066) and by the Russian Foundation for Basic Research (project no. 99-02-16334).

REFERENCES

1. L. M. Lyamshev and N. S. Shevyakhov, Akust. Zh. **19**, 918 (1973) [Sov. Phys. Acoust. **19**, 592 (1973)].
2. M. K. Balakirev and I. A. Gilinskiĭ, Fiz. Tverd. Tela **16**, 3144 (1974) [Sov. Phys. Solid State **16**, 2038 (1974)].
3. Yu. V. Gulyaev and V. P. Plesskiĭ, Pis'ma Zh. Tekh. Fiz. **3**, 1028 (1977) [Sov. Tech. Phys. Lett. **3**, 422 (1977)].
4. M. K. Balakirev and A. V. Gorchakov, in *Proceedings of the 10th All-Union Conference on Quantum Acoustics and Acoustoelectronics* (FAN, Tashkent, 1978), p. 76.
5. L. M. Lyamshev and N. S. Shevyakhov, Akust. Zh. **32**, 198 (1986) [Sov. Phys. Acoust. **32**, 117 (1986)].
6. V. G. Mozhaev, Akust. Zh. **27**, 285 (1981) [Sov. Phys. Acoust. **27**, 156 (1981)].
7. V. V. Bozhenko, T. G. Viskun, O. K. Naĭdov-Zhelezov, *et al.*, Akust. Zh. **30**, 162 (1984) [Sov. Phys. Acoust. **30**, 95 (1984)].
8. F. Josse, J. Acoust. Soc. Am. **81**, 1767 (1987).
9. I. Yu. Solodov, Vestn. Mosk. Gos. Univ. Ser. Fiz. Astron. **35** (6), 13 (1994).
10. O. A. Kosolapova, L. M. Lyamshev, and N. S. Shevyakhov, in *Proceedings of the Eighth All-Union Acoustical Conference* (AKIN, Moscow, 1973), Vol. 2, p. 202.
11. V. N. Belyĭ and I. Z. Dzhilavdari, Pis'ma Zh. Tekh. Fiz. **6**, 1073 (1980) [Sov. Tech. Phys. Lett. **6**, 460 (1980)].
12. V. N. Belyĭ and G. A. Pashkevich, Izvestiya AN BSSR, No. 4, 88 (1981).
13. V. V. Filippov, Vestnik AN BSSR, Ser. Fiz. Matem., No. 4, 81 (1982).
14. V. N. Beluĭ, I. Z. Dzhilavdari, and G. A. Pashkevich, Izvestiya AN BSSR, Ser. Fiz. Matem., No. 4, 79 (1983).
15. V. N. Belyĭ and G. A. Pashkevich, Preprint No. 324, Institut Fiziki AN BSSR (Institute of Physics, Academy of Sciences of Belorussian SSR, Minsk, 1984).
16. G. N. Romanov and S. S. Shakhidzhanov, Pis'ma Zh. Éksp. Teor. Fiz. **16**, 298 (1972) [JETP Lett. **16**, 210 (1972)].
17. B. B. Boĭko, N. S. Petrov, and I. Z. Dzhilavdari, Zh. Prikl. Spektrosk. **18**, 727 (1973).
18. E. Ya. Kogan and N. E. Molevich, Akust. Zh. **33**, 252 (1987) [Sov. Phys. Acoust. **33**, 151 (1987)].
19. L. A. Vaĭnshteĭn, Usp. Fiz. Nauk **118** (2), 339 (1976) [Sov. Phys. Usp. **19** (2), 189 (1976)].
20. N. S. Shevyakhov, Candidate's Dissertation in Physics and Mathematics (Andreev Acoustics Institute, Moscow, 1980).
21. D. L. White, J. Appl. Phys. **32**, 2547 (1962).
22. N. S. Shevyakhov, Akust. Zh. **35**, 934 (1989) [Sov. Phys. Acoust. **35**, 541 (1989)].
23. *Acoustic Crystals. Handbook*, Ed. by M. P. Shaskol'skaya (Nauka, Moscow, 1982).
24. M. N. Kul'bitskaya and V. A. Shutilov, Akust. Zh. **22**, 793 (1976) [Sov. Phys. Acoust. **22**, 451 (1976)].
25. V. X. Zhang, J. E. Lefebvre, and T. Gryba, J. Appl. Phys. **86**, 3361 (1999).
26. J. Wauer, J. Acoust. Soc. Am. **106**, 626 (1999).

Translated by M.L. Lyamshev

Acoustical Physics, Vol. 46, No. 3, 2000, pp. 327–333. Translated from Akusticheskiĭ Zhurnal, Vol. 46, No. 3, 2000, pp. 384–391.

Periodic Spatial Rearrangement of the Interference Structure and the Diffraction Focusing of Acoustic Fields in Oceanic Waveguides

Yu. V. Petukhov

Institute of Applied Physics, Russian Academy of Sciences,
ul. Ul'yanova 46, Nizhni Novgorod, 603600 Russia
e-mail: petukhov@hydro.appl.sci-nnov.ru

Received April 15, 1998

Abstract—It is demonstrated that the periodic (along the path) rearrangement of the spatial (in depth and horizontal distance) interference structure of the acoustic field generated in an oceanic waveguide by a CW point source is accompanied by a diffraction focusing of the field with the corresponding spatial period. It is found that, in an oceanic waveguide with a monotone angular dependence of the Brillouin ray cycle, the spatial period of both the rearrangement of the interference structure and the diffraction focusing of the field is directly proportional to the square of the characteristic vertical scale of the waveguide and inversely proportional to the wavelength; in a waveguide with a nonmonotone dependence, the corresponding spatial period is directly proportional to the cube of the aforementioned waveguide scale and inversely proportional to the square of the wavelength. *© 2000 MAIK "Nauka/Interperiodica".*

The periodic focusing of the acoustic field generated by a CW point source in a constant-velocity oceanic waveguide is a well-known phenomenon [1–5]. In the framework of the simplest model of a constant-velocity waveguide with a perfectly rigid bottom and in terms of the paraxial approximation used for the mode representation of the field in this waveguide, the spatial period R_H of the periodic focusing along the horizontal axis is determined by the formula

$$R_H = 4H^2/\lambda, \tag{1}$$

where H is the depth of the water layer and λ is the sound wavelength. A detailed review of the publications concerned with the description of this effect in optics, electrodynamics, and acoustics can be found in the preprint written by the author of this paper [6]. Here, it is important to note that, in contrast to the refraction focusing of the fields in oceanic waveguides stratified in depth [7], the spatial period R_H (1) of the aforementioned focusing is fundamentally determined by the radiation wavelength. Hence, we will call it diffraction focusing (as in [5, 6]). Naturally, the diffraction focusing should also be observed in oceanic waveguides stratified in depth [6]. Therefore, this paper is devoted to the generalization of the analytical results obtained in earlier publications [1–4] to the refraction oceanic waveguides.

To solve this problem, we use the approach proposed in [6, 8] for analyzing the spatial interference structure of the acoustic field in an oceanic waveguide. We write the expression for the dependence of the field intensity $J(r)$ on the horizontal distance r in the form

$$J(r) = 2\pi p_0 \frac{R_0^2}{r}\left[\sum_{l=1}^{L(\omega)} |A_l|^2 + \sum_{l\neq l'}^{L(\omega)}\sum_{l'=1}^{L(\omega)} A_l A_{l'}^* \cos[(k_l - k_{l'})r]\right], \tag{2}$$

which is valid in the far zone $k_l r \gg 1$ of a CW point source operating at a cyclic frequency ω and positioned at the depth z_s. Here,

$$A_l = \psi_l(z_s)\psi_l(z)/\sqrt{k_l} \tag{3}$$

is the amplitude of the lth mode, k_l is the horizontal wave number of this mode, $\psi_l(z)$ represents the corresponding orthonormal eigenfunctions of the waveguide, $L(\omega) = \max(l)$ is the total number of excited modes, z is the depth of the reception, and p_0 is the amplitude of the pressure disturbance produced by a point source in a homogeneous medium at a spherical surface of radius R_0. From expression (2), it follows (see [6, 8]) that, in a waveguide, the acoustic field intensity orthonormalized to the geometric spread, $J_0(r) = rJ(r)$, is a function quasi-periodic in r with certain spatial periods (interference periods)

$$R_{l,l'} = 2\pi/(k_l - k_{l'}) \tag{4}$$

and the corresponding spatial periods of beats

$$R_g(l, l'; n, n') = R_{l,l'}R_{n,n'}/(|R_{l,l'} - R_{n,n'}|). \tag{5}$$

The latter will be called (as in [6, 8]) spatial periods of the rearrangement of the interference structure of the acoustic field in a waveguide.

Below, we consider only the well predicted (and, hence, being of most interest) large-scale interference structure of the acoustic field. This interference structure is formed by different pairs of adjacent modes for which expressions (4) and (5) take the form

$$R_{l,\,l+1} = 2\pi/(k_l - k_{l+1}), \tag{6}$$

$$R_g(l, l+1; n, n+1) = R_{l,\,l+1}R_{n,\,n+1}/\left|R_{l,\,l+1} - R_{n,\,n+1}\right|. \tag{7}$$

From the aforesaid, it follows that the spatial interference structure of the acoustic field in an oceanic waveguide will be rearranged with the maximum possible spatial period $R_{\max}$ (see [6, 8]). Evidently, the value of $R_{\max}$ must fall within the range of values of the spatial period of rearrangement for two adjacent pairs of modes from their entire possible set:

$$R_{\max} = \max[R_g(l, l+1; l+1, l+2)]. \tag{8}$$

The minimum spatial period $R_{\min}$ of the rearrangement of the field interference structure formed in the waveguide

$$R_{\min} = \min[R_g(l, l+1; l+1, l+2)] \tag{9}$$

is also of interest, because the rearrangement of the large-scale interference structure should be most pronounced in the intervals of horizontal distances determined by this very period:

$$mR_{\min} \le r \le mR_{\max} \quad (m = 1, 2, \ldots). \tag{10}$$

The diffraction focusing of the field should be observed in the same intervals of distances (10). This statement follows from the fact that the rearrangement of the interference structure with the spatial period $R_{\max}$ (8) implies at least a partial manifestation of its specific features observed at the distances $0 < r \ll R_{\min}$ including the immediate vicinity of the source. Here, it should be noted that it is the periodic diffraction focusing of the field within distances (10) that leads to the phenomenon of the periodic spatial rearrangement of the far zones of insonification in an underwater sound channel open toward the surface [8].

Now, we proceed to the derivation of an analytical expression for the spatial period of the diffraction focusing of the field in a stratified oceanic waveguide with a smooth, although somewhat arbitrary, depth dependence of the square of the refraction index for acoustic waves $n^2(z)$. We assume that the free surface $z = 0$ and the bottom $z = H$ are perfectly reflecting surfaces.

Since the phenomenon under study is most conspicuous in the case of multimode propagation (see [1–6]), we will solve the above-stated problem by using the WKB approach on the assumption that the conditions of its applicability are satisfied [7]. In the WKB approximation, the dispersion equation for horizontal wave numbers of modes has the form [7]

$$k\int_{z_1}^{z_2}\sqrt{n^2(z) - \beta_l^2}\,dz = \pi(l - \nu), \tag{11}$$

where

$$\beta_l = k_l/k = \cos\chi_l,\ z_1 = \begin{cases}0\\ z_{l\mathrm{u}},\end{cases}\quad z_2 = \begin{cases}z_{l\mathrm{l}}\\ H,\end{cases}\quad l = [1, L],$$

$$\nu = \begin{cases}1/2,\ z_1 = z_{l\mathrm{u}}, z_2 = z_{l\mathrm{l}}\\ 1/4,\ z_1 = 0, z_2 = z_{l\mathrm{l}},\end{cases}$$

$$\nu = \begin{cases}1/2,\ z_1 = 0, z_2 = H\\ 1/4,\ z_1 = z_{l\mathrm{u}}, z_2 = H.\end{cases}$$

Here, χ_l is the grazing angle of a Brillouin ray at the channel axis $z = z_0$; $z_{l\mathrm{u}}$ and $z_{l\mathrm{l}}$ are the upper and lower turning depths of Brillouin rays, respectively; $n(z) = c(z_0)/c(z)$, where $c(z)$ is the dependence of the sound velocity on depth; and $k = \omega/c(z_0)$.

With the use of the WKB approximation, the series expansion of the quantity β_{l+1} correct to the third order

$$\beta_{l+1} \approx \beta_l + \frac{d\beta_l}{dl} + \frac{d^2\beta_l}{2!dl^2} + \frac{d^3\beta_l}{3!dl^3}, \tag{12}$$

and the differential relation following from equation (11),

$$\frac{d\beta_l}{dl} = -\frac{2\pi}{kD_l}, \tag{13}$$

where D_l is the cycle length of the corresponding Brillouin ray

$$D_l = 2\beta_l\int_{z_1}^{z_2}\frac{dz}{\sqrt{n^2(z) - \beta_l^2}}, \tag{14}$$

we represent expression (6) in the form of an approximate equality at $D_l k \gg 1$:

$$R_{l,\,l+1} \approx D_l\left[1 + \frac{\pi}{kD_l^2}\frac{dD_l}{d\beta_l} - \frac{2\pi^2}{3k^2D_l^3}\left[\frac{d^2D_l}{d\beta_l^2} - \frac{3}{D_l}\left(\frac{dD_l}{d\beta_l}\right)^2\right]\right]^{-1}. \tag{15}$$

In the same way, using formulas (13) and (15) and the series expansion

$$D_{l+1} \approx D_l + \frac{dD_l}{dl} + \frac{d^2D_l}{2!dl^2} \tag{16}$$

we represent expression (7) in the form of an approximate equality:

$$R_g(l, l+1; l+1, l+2) \approx \frac{k}{2\pi} D_l^3 \left[1 - \frac{2\pi}{kD_l^2}\frac{dD_l}{d\beta_l}\right] \times \left[\left|\frac{dD_l}{d\beta_l} - \frac{2\pi}{kD_l}\left[\frac{d^2D_l}{d\beta_l^2} - \frac{2}{D_l}\left(\frac{dD_l}{d\beta_l}\right)^2\right]\right|\right]^{-1}. \quad (17)$$

For the following calculations, it is important to note that oceanic waveguides can be classified according to the dependences of D_l on the ray parameter β_l [9, 10]. Hence, for oceanic waveguides with a monotone dependence of D_l on β_l, i.e., in the absence of extrema when

$$\frac{dD_l}{d\beta_l} \neq 0, \quad (18)$$

we use relations (17) and (18) at $kD_l \gg 1$, and, from expressions (8) and (9), we obtain simple expressions for the minimum and maximum spatial periods of the diffraction focusing of the field:

$$R_{\min} = \frac{kH_g^2}{2\pi}\min\left[\bar{D}_l^3 \Big/ \left|\frac{d\bar{D}_l}{d\beta_l}\right|\right], \quad (19)$$

$$R_{\max} = \frac{kH_g^2}{2\pi}\max\left[\bar{D}_l^3 \Big/ \left|\frac{d\bar{D}_l}{d\beta_l}\right|\right]. \quad (20)$$

Here, $\bar{D}_l = D_l/H_g$ is the Brillouin ray cycle length normalized to the characteristic vertical scale of the waveguide H_g.

Thus, the dependences (19) and (20) suggest that, in an oceanic waveguide with a monotone dependence of the Brillouin ray cycle on the ray parameter, the spatial period of the diffraction focusing of the field is directly proportional to the square of the characteristic vertical scale of the waveguide and inversely proportional to the radiation wavelength.

In an oceanic waveguide with a nonmonotone dependence $D_l(\beta_l)$, which at some $\beta_l = \beta_c$ exhibits extrema satisfying the condition

$$\left(\frac{dD_l}{d\beta_l}\right)_{\beta_l = \beta_c} = 0 \quad (21)$$

and corresponding to the formation of weakly divergent acoustic beams [9, 10], we use relations (17) and (21), and, from expression (8), we obtain the desired expression for the spatial period of the diffraction focusing of the field:

$$R_{\max} = \frac{k^2 H_g^3}{4\pi^2} \times \left[\bar{D}_l^4(\beta_c) \Big/ \left|\left(\frac{d^2\bar{D}_l}{d\beta_l^2}\right)_{\beta_l = \beta_c}\right|\right]. \quad (22)$$

In such oceanic waveguides, the spatial period (22) of the diffraction focusing of the field is directly proportional to the cube of the characteristic vertical scale of the waveguide and inversely proportional to the square of the radiation wavelength.

Now, using the analytical calculations and the WKB approximation, we will prove that the spatial rearrangement of the interference structure of the acoustic field in waveguides leads to the diffraction focusing of the field with the same spatial period $R_{\max}$: (20) or (22). For this purpose, we use the results of the analysis of the mode structure of the field in a waveguide [4, 10, 11]. To simplify the intermediate calculations, we consider an oceanic waveguide with a sound channel open toward the surface and with an acoustically transparent bottom. Such a simplification causes no loss of generality for the resulting expressions for $R_{\min}$ and $R_{\max}$.

Using the WKB approximation, we obtain the following expression for the pressure field formed by the refracted modes, $1 \leq l \leq L_r$, and the modes interacting with the ocean surface, $L_r + 1 \leq l \leq L$, [7, 8]:

$$p' = 4p_0 R_0 \sqrt{\frac{2\pi i}{kr}} \exp(-i\omega t) \times \sum_{l=1}^{L(\omega)} \frac{\sqrt{\beta_l}\exp(ikr\beta_l)}{D_l\sqrt{\gamma_l(z_s)\gamma_l(z)}} \sin[\varphi_l(z_s)]\sin[\varphi_l(z)], \quad (23)$$

where

$$\gamma_l(z) = \sqrt{n^2(z) - \beta_l^2}, \quad (24)$$

$$\varphi_l(z) = \begin{cases} k\int_{z_{lu}}^{z} \gamma_l(z)dz + \pi/4 = F_l(z), & 1 \leq l \leq L_r \\ (n(0) \leq \beta_l \leq n(z_s)) & \\ k\int_{0}^{z} \gamma_l(z)dz = \Phi_l(z), & L_r + 1 \leq l \leq L \\ (n(H) \leq \beta_l \leq n(0)) & \end{cases} \quad (25)$$

and t is time. The total number of the refracted modes L_r and the number of all excited modes L can be determined from the dispersion equation (11) with the corresponding values of the parameters $z_{lu} = 0$, $\beta_l = n(0)$, $z_{ll} = H$, and $\beta_l = n(H)$:

$$L_r = \frac{k}{\pi}\int_0^{H_r} \sqrt{n^2(z) - n^2(0)}dz + \frac{1}{2}, \quad L = \frac{k}{\pi}\int_0^{H} \sqrt{n^2(z) - n^2(H)}dz + \frac{1}{4}, \quad (26)$$

where H_r is the characteristic width of the underwater sound channel, this quantity being determined from the equation $n(0) = n(H_r)$.

In the case of multimode propagation with the points of transmission and reception being far from the interfaces, the field in the waveguide has a beam structure determined by the oscillatory dependence of the absolute value of the excitation coefficient of modes on their numbers [4, 10, 11]. For each beam, there exists a certain number of a refracted mode $l_{\max}(q) = l_{r\max}(q_r)$ or a mode reflected from the ocean surface $l_{\max}(q) = l_{s\max}(q_s)$ at which the mode amplitude reaches its maximum absolute value $|A_l|$ at the source depth $z = z_s$. Therefore, the equations for the determination of $l_{\max}(q)$ follow from the equality $\sin^2[\varphi_l(z_s)] = 1$ [10] and have a relatively simple form:

$$F_l(z_s)\big|_{l = l_{r\max}} = \frac{\pi}{2}(2q_r - 1), \tag{27}$$

$$\Phi_l(z_s)\big|_{l = l_{s\max}} = \frac{\pi}{2}(2q_s - 1). \tag{28}$$

Here, $q_r = [1, Q_r]$ and $q_s = [Q_r + 1, Q]$ are the corresponding numbers of the refracted and surface-reflected mode beams, Q_r is the total number of refracted mode beams, Q is the total number of all mode beams, and $q = [1, Q]$.

It should be kept in mind that, in the case of the excitation of a large number of refracted modes $L_r \gg 1$, the depth interval $\Delta z_{l\mathrm{u}} = z_{l+1\mathrm{u}} - z_{l\mathrm{u}}$ between the turning depths of the adjacent modes becomes fairly small, and there will always exist some depth $z_{l\mathrm{u}}$ that is quite close to z_s. In this case, the mode number $l_r = l_{r\max}$ (1) corresponding to the first refracted mode beam will be determined not from equation (27), but from the dispersion equation (11) under the condition of the coincidence of the depths $z_{l\mathrm{u}} = z_s$:

$$l_r = \frac{k}{\pi}\int_{z_s}^{z_*}\sqrt{n^2(z) - n^2(z_s)}\,dz + \frac{1}{2}, \tag{29}$$

where z_* is the depth corresponding to the source depth and determined from the equality $n(z_s) = n(z_*)$. Evidently, the solutions to equations (27) and (28) should satisfy the conditions:

$$\begin{aligned} l_r \le l_{r\max}(q_r) \le L_r, \\ L_r + 1 \le l_{s\max}(q_s) \le L. \end{aligned} \tag{30}$$

Each of the mode beams is formed by a certain group of modes:

$$\begin{aligned} L_q &= L_{1q} + L_{2q} - 1; \\ L_{1q} &= l_{\max}(q) - l_{\min}(q-1), \\ L_{2q} &= l_{\min}(q) - l_{\max}(q). \end{aligned} \tag{31}$$

In each of these groups, the values of the mode numbers $l_{\min}(q) = l_{r\min}(q_r)$ and $l_{\min}(q) = l_{s\min}(q_s)$ correspond to the positions of the $|A_l|$ minima following after $l_{\max}(q) = l_{r\max}(q_r)$ and $l_{\max}(q) = l_{s\max}(q_s)$, respectively, and these values are determined from the equations

$$F_l(z_s)\big|_{l = l_{r\min}} = \pi q_r, \tag{32}$$

$$\Phi_l(z_s)\big|_{l = l_{s\min}} = \pi q_s, \tag{33}$$

where $q_r = [0, Q_r]$ and $q_s = [Q_r, Q]$. Equations (32) and (33) follow from the evident equality $\sin[\varphi_l(z_s)] = 0$, and their solutions must satisfy the conditions similar to conditions (30):

$$\begin{aligned} 1 \le l_{r\min}(q_r) \le L_r, \\ L_r + 1 \le l_{s\min}(q_s) \le L. \end{aligned} \tag{34}$$

Then, expression (23) for the pressure field can be represented in the form of a sum of the corresponding mode beams:

$$\begin{aligned} p' &= p_0 R_0 \sqrt{\frac{2\pi i}{kr}}\exp(-i\omega t) \\ &\times \sum_{q=1}^{Q}\sum_{j=1}^{4}\exp[i\pi(1 + \mu_j - \chi_j)]\Pi_{jq}, \end{aligned} \tag{35}$$

where

$$\Pi_{jq} = \sum_{l = l_{\min}(q-1)}^{l = l_{\min}(q)} \frac{\sqrt{\beta_l}\exp(i\Psi_{jl})}{D_l\sqrt{\gamma_l(z_s)\gamma_l(z)}}, \tag{36}$$

$$\Psi_{jl} = k\beta_l r + \mu_j\varphi_l(z_s) + \chi_j\varphi_l(z), \tag{37}$$

$$\mu_j, \chi_j = \begin{cases} 1,\ 1;\ j = 1 \\ 1,\ -1;\ j = 2 \\ -1\ \ 1;\ j = 3 \\ -1,\ -1;\ j = 4. \end{cases} \tag{38}$$

In the case of multimode propagation, we can use the series expansion of the function Ψ_{jl} (37) in l near $l = l_{\max}(q)$ correct to the third power of $\Delta l/L = [l - l_{\max}(q)]/L$:

$$\begin{aligned} \Psi_{jl} &\approx \Psi_{jl_{\max}(q)} + \left(\frac{\partial\Psi_{jl}}{\partial l}\right)\Big|_{l = l_{\max}(q)}\Delta l \\ &+ \frac{1}{2!}\left(\frac{\partial^2\Psi_{jl}}{\partial l^2}\right)\Big|_{l = l_{\max}(q)}(\Delta l)^2 + \frac{1}{3!}\left(\frac{\partial^3\Psi_{jl}}{\partial l^3}\right)\Big|_{l = l_{\max}(q)}(\Delta l)^3. \end{aligned} \tag{39}$$

Using the differential relation (13) and the approximate equality (39), we represent expression (35) for the pressure field in the form

$$\begin{aligned} p' &= p_0 R_0 \sqrt{\frac{2\pi i}{kr}} \\ &\times \sum_{q=1}^{Q}\sum_{j=1}^{4}\frac{\sqrt{\beta_l}\exp[i(\Psi_{jl_{\max}(q)} - \omega t + \pi(1 + \mu_j - \chi_j))]}{(D_l\sqrt{\gamma_l(z_s)\gamma_l(z)})\big|_{l = l_{\max}(q)}}P_{jq}, \end{aligned} \tag{40}$$

where

$$P_{jq} = \sum_{\Delta l = -L_{1q}+1}^{\Delta l = L_{2q}-1} \exp[-i(\zeta_1 \Delta l + \zeta_2(\Delta l)^2 + \zeta_3(\Delta l)^3)]; \quad (41)$$

$$\zeta_1 = 2\pi\left(\frac{r_{jl}}{D_l}\right)\Bigg|_{l = l_{\max}(q)}, \quad r_{jl} = r + \mu_j D_l(z_s) + \chi_j D_l(z), \quad D_l(z) = \beta_l \int_{z_1}^{z} \frac{dz}{\gamma_l(z)}; \quad (42)$$

$$\zeta_2 = \frac{2\pi^2}{k}\left[\frac{r_{jl}}{D_l^3}\left[\frac{dD_l}{d\beta_l} - \frac{D_l}{r_{jl}}\left(\mu_j \frac{dD_l(z_s)}{d\beta_l} + \chi_j \frac{dD_l(z)}{d\beta_l}\right)\right]\right]\Bigg|_{l = l_{\max}(q)}; \quad (43)$$

$$\zeta_3 = \frac{4\pi^3}{3k^2}\left[\frac{r_{jl}}{D_l^4}\left[\left[\frac{d^2 D_l}{d\beta_l^2} - \frac{3}{D_l}\left(\frac{dD_l}{d\beta_l}\right)^2\right] + \frac{3}{r_{jl}}\frac{dD_l}{d\beta_l}\left(\mu_j \frac{dD_l(z_s)}{d\beta_l} + \chi_j \frac{dD_l(z)}{d\beta_l}\right) - \frac{D_l}{r_{jl}}\left(\mu_j \frac{d^2 D_l(z_s)}{d\beta_l^2} + \chi_j \frac{d^2 D_l(z)}{d\beta_l^2}\right)\right]\right]\Bigg|_{l = l_{\max}(q)}. \quad (44)$$

If, in the exponent in (41), we take into account only the term proportional to ζ_1 (see [11]), we can perform an elementary summation with the use of the formula for a geometric progression. Then, we obtain that every mode beam is formed near two reference Brillouin rays whose grazing angles at the source depth are opposite in sign, such a mode beam propagating without any diffraction distortions. The equations for the ray paths of these rays have the form

$$r = R_{jm}^{(1)} = m_1 D_{l_{\max}(q)} - \mu_j D_{l_{\max}(q)}(z_s) - \chi_j D_{l_{\max}(q)}(z), \quad (45)$$

and they are found from the equality

$$\zeta_1 = 2\pi m_1 \quad (m_1 = 1, 2, \ldots), \quad (46)$$

which means an in-phase summation of the mode group forming the given beam along the corresponding Brillouin rays (45).

The inclusion of the second term of the exponent in (41), i.e., the term proportional to ζ_2, leads to a dephasing of the modes forming the corresponding beam, i.e., to its diffraction spread along the propagation path [4]. However, according to expressions (41) and (43), at the distances $r = R_{jm}^{(2)}$ determined by the expression

$$R_{jm}^{(2)} = \left[\frac{k}{2\pi}\frac{D_l^3}{\left|\frac{dD_l}{d\beta_l}\right|} \times \left[m_2 + \frac{2\pi}{kD_l^2}\left(\mu_j \frac{dD_l(z_s)}{d\beta_l} + \chi_j \frac{dD_l(z)}{d\beta_l}\right)\right] - \mu_j D_l(z_s) - \chi_j D_l(z)\right]\Bigg|_{l = l_{\max}(q)}, \quad (47)$$

which follows from the equality

$$|\zeta_2| = \pi m_2, \quad (m_2 = 1, 2, \ldots), \quad (48)$$

a diffraction focusing of the corresponding mode beam will be observed. For odd L_q and m_2, the beam will be focused in phase at odd L_{1q} and L_{2q} and in antiphase at even L_{1q} and L_{2q}. For even m_2, the beam will always be focused in phase independently of L_{1q} and L_{2q}. Only for the beam formed by an even number of modes at odd m_2 will a considerable defocusing be observed.

Assuming that the condition $kD_l \gg 1$ and condition (18) are valid, from expression (47) we obtain the approximate relation

$$R_{jm}^{(2)} \approx m_2 R_g(l_{\max}(q)), \quad (49)$$

where the quantity

$$R_g(l_{\max}(q)) = \frac{kH_g^2}{2\pi}\left[\bar{D}_l^3 \Big/ \left|\frac{d\bar{D}_l}{d\beta_l}\right|\right]\Bigg|_{l = l_{\max}(q)} \quad (50)$$

is the spatial period of the diffraction focusing of the corresponding mode beam. From all values of the quantity $R_g(l_{\max}(q))$ that are possible at $q = [1, Q]$, we always can select the minimum $R_{\min}$ and maximum $R_{\max}$ values of the spatial period of the diffraction focusing of the field:

$$R_{\min} = \frac{kH_g^2}{2\pi}\min\left[\left[\bar{D}_l^3 \Big/ \left|\frac{d\bar{D}_l}{d\beta_l}\right|\right]\Bigg|_{l = l_{\max}(q)}\right], \quad (51)$$

$$R_{\max} = \frac{kH_g^2}{2\pi}\max\left[\left[\bar{D}_l^3 \Big/ \left|\frac{d\bar{D}_l}{d\beta_l}\right|\right]\Bigg|_{l = l_{\max}(q)}\right]. \quad (52)$$

From formulas (51) and (52), one can see that the corresponding values are determined by the expressions that are analogous to the expressions for the minimum $R_{\min}$ (19) and maximum $R_{\max}$ (20) spatial periods of the rearrangement of the field interference structure in an oceanic waveguide.

Hence, the spatial rearrangement of the interference structure of the acoustic field in an oceanic waveguide

gives rise to the diffraction focusing of the field with the corresponding spatial periods.

It should be noted that, from the equality

$$|\zeta_2|(\Delta l)^2 = \pi, \tag{53}$$

which fundamentally differs from (48), Virovlyanskii *et al.* [12] obtained the following expression for the evaluation of the limiting allowable number of modes that are combined in phase and form the mode beam:

$$\Delta l = \sqrt{R_g(l_{\max}(q))/r}, \tag{54}$$

where $R_g(l_{\max}(q))$ is determined by formula (50). On the basis of expression (54), these authors [12] made a fundamentally wrong conclusion that, at the distances $r \geq R_g(l_{\max}(q))$, all modes cease to interfere along the reference Brillouin rays, and the initially narrow beam formed by these rays is totally spread. Such a conclusion was made without taking into account an important fact: although different modes $(-L_{1q} + 1 \leq \Delta l \leq L_{2q} - 1)$ become dephased at different distances $r = R_g(l_{\max}(q))/(\Delta l)^2$, they will be in a certain way phased owing to the integer values of the quantity $(\Delta l)^2$, and their phasing will occur at the distances $R_{jm}^{(2)}$ (49) with the corresponding characteristic spatial period $R_g(l_{\max}(q))$ (50).

The spatial periodicity of the diffraction focusing of the field in oceanic waveguides does not mean an exact reproduction of its values in the corresponding focal planes because of the effect of the third term, i.e., the term proportional to ζ_3, in the exponent in expression (41). This term plays a crucial role in the diffraction spread and focusing of weakly divergent acoustic beams [8–10]. If equality (21) is satisfied for some mode number $l = l_{\max}(q) = l_c = l(\beta_c)$, i.e., $\zeta_2 = 0$, then, from the equation

$$|\zeta_3| = \pi m_3 \quad (m_3 = 1, 2, \ldots) \tag{55}$$

we obtain another expression for the determination of the distances $r = R_{jm}^{(3)}$ at which the diffraction focusing of a weakly divergent mode beam will be observed:

$$R_{jm}^{(3)} = \left[\frac{3k^2 D_l^4}{4\pi^2\left|\frac{d^2 D_l}{d\beta_l^2}\right|}\right.$$
$$\times\left[m_3 + \frac{4\pi^2}{3k^2 D_l^3}\left(\mu_j\frac{d^2 D_l(z_s)}{d\beta_l^2} + \chi_j\frac{d^2 D_l(z)}{d\beta_l^2}\right)\right] \tag{56}$$
$$\left.\left. - \mu_j D_l(z_s) - \chi_j D_l(z)\right]\right|_{l = l_c}.$$

From expression (56) at $kD_l \gg 1$, we derive a simple expression

$$R_{jm}^{(3)} \approx m_3 R_g(l_c), \tag{57}$$

where the quantity

$$R_g(l_c) = \frac{3k^2 H_g^3}{4\pi^2}\left[\bar{D}_l^4 \Big/ \left|\frac{d^2\bar{D}_l}{d\beta_l^2}\right|\right]\Bigg|_{l = l_c} \tag{58}$$

is the spatial period of the diffraction focusing of a weakly divergent mode beam. The focusing of every beam in phase or in antiphase depends on the same conditions, which are formulated above for m_3, L_q, l_{1q}, and L_{2q} with allowance for only two terms in the exponent in expression (41), i.e., the terms proportional to ζ_1 and ζ_2.

The comparison of the expression for $R_{\max}$ (22) with the one for $R_g(l_c)$ (58) shows that these quantities differ only by the integer coefficient $R_g(l_c)/R_{\max} = 3$. Thus, the approach based on the analysis of the beam structure of the acoustic field in an oceanic waveguide suggests the conclusion that the diffraction focusing of weakly divergent acoustic beams manifests itself at intervals equal to three spatial periods of the rearrangement of the interference structure of the field. However, this result does not rule out the possibility of a partial diffraction focusing of the field with the spatial period $R_{\max}$ (22). The reason is that the conclusions made on the basis of analyzing the spatial rearrangement of the interference structure of acoustic field in oceanic waveguides are more general ones. This statement may be confirmed by the fact that the correctness of the aforementioned conclusions does not depend on the validity of the equality $l_{\max}(q) = l_c$ characteristic of weakly divergent acoustic beams.

In closing, we formulate the main results of this study, which may be useful for a correct description of a long-range sound transmission in the ocean [13, 14].

First, it is shown that the periodic rearrangement of the spatial interference structure of acoustic field along an oceanic waveguide is accompanied by the diffraction focusing of the field with the corresponding spatial period.

Second, it is found that, for an oceanic waveguide with a monotone angular dependence of the Brillouin ray cycle on the ray parameter, the spatial period of the diffraction focusing of acoustic field is proportional to the square of the characteristic vertical scale of the waveguide and inversely proportional to the sound wavelength.

Third, for an oceanic waveguide with a nonmonotone dependence of the Brillouin ray cycle on the ray parameter (i.e., a dependence with extrema), the spatial period of the diffraction focusing of acoustic field is proportional to the cube of the characteristic vertical scale of the waveguide and inversely proportional to the square of the sound wavelength.

ACKNOWLEDGMENTS

This work was supported by the Russian Foundation for Basic Research (project nos. 96-02-16116a and 98-02-16402) and the Competitive Center of Basic Natural Sciences (project no. 97-8.2-78).

REFERENCES

1. A. B. Wood, J. Acoust. Soc. Am. **31**, 1213 (1959).
2. A. B. Wood, in *Underwater Acoustics*, Ed. by V. M. Albers (Plenum, New York, 1963; Mir, Moscow, 1965).
3. D. E. Weston, J. Acoust. Soc. Am. **32**, 647 (1960).
4. D. E. Weston, J. Acoust. Soc. Am. **44**, 1706 (1968).
5. D. I. Abrosimov and Yu. V. Petukhov, Preprint No. 466, IPF RAN (Institute of Applied Physics, Russian Academy of Sciences, Nizhni Novgorod, 1998).
6. Yu. V. Petukhov, Preprint No. 443, NIRFI (Research Radiophysical Institute, Nizhni Novgorod, 1998).
7. L. M. Brekhovskikh and Yu. P. Lysanov, *Fundamentals of Ocean Acoustics* (Gidrometeoizdat, Leningrad, 1982; Springer, Berlin, 1982).
8. Yu. V. Petukhov, Akust. Zh. **42**, 688 (1996) [Acoust. Phys. **42**, 606 (1996)].
9. Yu. V. Petukhov, Akust. Zh. **41**, 807 (1995) [Acoust. Phys. **41**, 712 (1995)].
10. D. I. Abrosimov and Yu. V. Petukhov, Akust. Zh. **43**, 437 (1997) [Acoust. Phys. **43**, 373 (1997)].
11. V. N. Kulakov, N. E. Mal'tsev, and S. D. Chuprov, Akust. Zh. **29**, 74 (1983) [Sov. Phys. Acoust. **29**, 41 (1983)].
12. A. L. Virovlyanskiĭ, S. A. Kirilov, and I. A. Shereshevskiĭ, Izv. Vyssh. Uchebn. Zaved., Radiofiz. **31**, 726 (1988).
13. K. Prada, J. L. Spiesberger, and E. Terray, J. Acoust. Soc. Am. **95**, 3654 (1994).
14. D. E. Norris, D. W. Merdes, and J. L. Spiesberger, J. Acoust. Soc. Am. **103**, 182 (1998).

Translated by E. M. Golyamina

Acoustical Physics, Vol. 46, No. 3, 2000, pp. 334–341. Translated from Akusticheskiĭ Zhurnal, Vol. 46, No. 3, 2000, pp. 392–400.

Nonlinear Phenomena Accompanying the Development of Oscillations Excited in a Layer of a Linear Dissipative Medium by Finite Displacements of Its Boundary

O. V. Rudenko and A. V. Shanin

Moscow State University, Vorob'evy gory, Moscow, 119899 Russia

e-mail: shanin@ort.ru

Received January 26, 1999

Abstract—A method of describing oscillations in resonators on the basis of evolution equations is proposed. The latter are obtained by simplifying the functional equations under the assumption that the distortions of travelling waves within the resonator length are small, that the Mach number for the moving boundary oscillations is small, and that the frequency is close to one of the natural frequencies of the resonator. The problems of nonstationary oscillations of a layer with a moving boundary are solved. The law that should govern the wall oscillations to provide the development of steady-state linear resonance oscillations is determined. The shape of the resonance curve formed in the presence of a boundary nonlinearity is calculated. The method of matching of asymptotics is applied to the singularly perturbed problem with small dissipation. It is shown that a boundary nonlinearity leads to a distortion of the temporal profile of the standing wave and to the generation of higher harmonics in the process of the development of steady-state oscillations. In contrast to the classical linear problems where the resonance occurs at the coincidence of the external force frequency with one of the natural frequencies, in the case under study the resonance behavior is observed in frequency bands, which are wider the higher the amplitude of the boundary oscillations is. © *2000 MAIK "Nauka/Interperiodica"*.

INTRODUCTION

Most publications concerned with nonlinear acoustics are devoted to the studies of bulk nonlinear effects, which lead to progressive distortions of the profiles and spectra of waves in the course of their propagation through a nonlinear medium. However, in some cases, it is necessary to take into account local distortions that are related to the nonlinearity of the boundary condition at a surface performing finite-amplitude oscillations.

In the framework of the problems concerned with wave radiation, the effects of the boundary nonlinearity are not accumulated and, therefore, manifest themselves only when the motion occurs with the velocities comparable to the velocity of sound [1]. However, these effects may be important in resonators where their accumulation with time is possible. In this case, the nonlinear effects are determined by the ratio of the two small parameters: the acoustic Mach number M and the detuning, i.e., the dimensionless departure Δ from the exact resonance frequency. This ratio can be relatively large in high-Q resonators or in the presence of intense pumping.

The accumulation of the effects of the boundary nonlinearity in a resonator was considered in the previous paper [2]. The results reported there were obtained on the basis of the solution of the functional equations and applicable only to steady-state oscillations without considering the processes of their development. However, in the case $M > |\Delta|$, the steady-state solution exhibits some singularities, which makes it necessary to analyze the process of the development of oscillations. It is also fundamentally important to take into account the dissipative properties of the medium, i.e., the properties that limit the field growth in the layer.

In this paper, we present the solution of a more general nonstationary problem on the basis of a simplified evolution equation that allows for the dissipation, the detuning, and the finiteness of the boundary motion.

The results presented below contribute to the theory of nonlinear oscillations of linearly deformed systems with moving boundaries [3–6].

Our interest in this problem was inspired by the development of superhigh-Q resonators for subtle physical measurements [7] and by the technical achievements in the excitation of highly nonlinear oscillations with the suppression of the process of the shock front formation [8]. The formulation of the problem was discussed in detail in the introduction to the cited paper [2].

EVOLUTION EQUATION. DEVELOPMENT OF LINEAR OSCILLATIONS IN THE LAYER

This section outlines the scheme of the derivation of the evolution equation for describing the process of a slow (relative to the oscillation period) development of steady-state oscillations in a layer of a dissipative

1063-7710/00/4603-0334$20.00

medium. A number of formulas presented here are used in the following sections for solving the moving-boundary problem.

We consider a layer whose left boundary ($x = 0$) performs harmonic oscillations (e.g., according to the law $X = -(A/\omega)\cos(\omega t)$), and the right boundary ($x = L$) is immobile. Then, for the particle velocity in the medium we have

$$v(x = 0, t) = \frac{dX}{dt} = A\sin(\omega t), \qquad v(x = L, t) = 0. \tag{1}$$

Plane waves propagating in a viscous heat-conducting medium are described by the equation [9]

$$\frac{\partial^2 v}{\partial t^2} - c^2\frac{\partial^2 v}{\partial x^2} = \frac{b}{\rho}\frac{\partial^3 v}{\partial t \partial x^2}. \tag{2}$$

Here, c and ρ are the equilibrium values of the sound velocity and density of the medium and b is the effective dissipation factor [9]. We assume that the absorption is weak, and the travelling wave attenuates only weakly within distances of the order of the wavelength. In this case, for the wave propagating in the positive direction along the x axis, equation (2) yields a simplified parabolic equation [9]

$$\frac{\partial v}{\partial x} = \frac{b}{2c^3\rho}\frac{\partial^2 v}{\partial \tau_1^2}, \quad \tau_1 = t - \frac{x}{c}. \tag{3}$$

For the wave propagating in the opposite direction (leftward), the corresponding equation will have the form

$$\frac{\partial v}{\partial x} = -\frac{b}{2c^3\rho}\frac{\partial^2 v}{\partial \tau_2^2}, \quad \tau_2 = t + \frac{x}{c}. \tag{4}$$

In the approximation indicated above, the general solution to equation (2) can be represented as a sum of the solutions to equations (3) and (4). Specifically, for boundary conditions (1), the solution can be represented in the form

$$v = e^{-\delta\omega^2(x-L)}F\left(t - \frac{x-L}{c}\right) - e^{\delta\omega^2(x-L)}F\left(t + \frac{x-L}{c}\right), \tag{5}$$

where $\delta = b/(2c^3\rho)$ and F is an unknown function; here, $F(t)$ is a linear combination of $\sin(\omega t)$ and $\cos(\omega t)$ with the coefficients that may slowly vary with time.

The corresponding expression for the acoustic pressure has the form

$$\frac{p}{\rho c} = e^{-\delta\omega^2(x-L)}F\left(t - \frac{x-L}{c}\right) + e^{\delta\omega^2(x-L)}F\left(t + \frac{x-L}{c}\right). \tag{6}$$

Formula (5) is written so as to automatically satisfy condition (1) at the fixed boundary. Condition (1) at the oscillating boundary ($x = 0$) reduces expression (5) to the functional equation

$$A\sin\omega t = e^{D}F\left(t + \frac{L}{c}\right) - e^{-D}F\left(t - \frac{L}{c}\right), \tag{7}$$

where $D = \delta\omega^2 L$.

For steady-state linear oscillations, the function $F(t)$ is a harmonic one. In this case, equation (7) can be easily solved. The solution has the form

$$F = \frac{A}{2} \times \frac{\cos(kL)\mathrm{sh}(D)\sin(\omega t) - \sin(kL)\mathrm{ch}(D)\cos(\omega t)}{\cos^2(kL)\mathrm{sh}^2(D) + \sin^2(kL)\mathrm{ch}^2(D)}. \tag{8}$$

Let the frequency ω of the boundary oscillations be close to the fundamental resonance frequency $\omega_0 = \pi c/L$. In this case, we can write $kL = \pi + \Delta$, where $\Delta = \pi(\omega - \omega_0)/\omega_0$ represents the small detuning. The attenuation within the resonator length is also assumed to be small: $D = \delta\omega^2 L \ll 1$. Under these assumptions, solution (8) is considerably simplified:

$$F = \frac{A}{2}\frac{\cos\left(\omega t + \arctan\dfrac{D}{\Delta}\right)}{\sqrt{\Delta^2 + D^2}}. \tag{9}$$

From solution (9), one can easily derive the known facts: the amplitude of forced oscillations at resonance and the width of the resonance curve are finite and determined by the attenuation; the phase of the oscillations changes as the frequency ω passes through ω_0.

Now, we return to the functional equation (7) in order to analyze the process of the development of steady-state oscillations. In the vicinity of the fundamental resonance, $kL = \pi + \Delta$, equation (7) takes the form

$$A\sin\omega t = e^{D}F(\omega t + \pi + \Delta) - e^{-D}F(\omega t - \pi - \Delta). \tag{10}$$

For small detuning Δ and attenuation D, we expand the right-hand member of equation (10) in a series and retain only the terms of the zero and first orders of smallness:

$$A\sin(\omega t) \approx (F_+ - F_-) + D(F_+ + F_-) + \Delta(F_+' + F_-'). \tag{11}$$

Here, $F_+ = F(\omega t + \pi)$, $F_- = F(\omega t - \pi)$, and the prime means the differentiation with respect to the argument.

Since F is a nearly periodic function with the period 2π, and it slowly varies from one period to another, we can write the following approximate expression for the difference $F_+ - F_-$:

$$F_+ - F_- \approx 2\pi\frac{\partial F}{\partial(\omega t)} = 2\frac{\partial F}{\partial T}, \tag{12}$$

where $T = \omega t/\pi$ is the "slow" time. We note that the slowness (in comparison with the oscillation period) of

the variation of the quantity F as a function of T is determined by the presence of the small coefficients M, Δ, and D in all remaining terms of the derived evolution equation.

In the second and third terms of expansion (11), which contain small coefficients D and Δ, the deviation of the function F from strict periodicity can be neglected. Then, the functional equation (10) can be reduced to the following differential equation:

$$\frac{\partial F}{\partial T} + DF(\omega t + \pi) + \Delta\frac{\partial}{\partial(\omega t)}F(\omega t + \pi) = \frac{A}{2}\sin(\omega t). \tag{13}$$

Introducing the notations $U = F/c$, $M = A/c$, and $\xi = \omega t + \pi$, we represent the partial differential equation (13) in the final form

$$\frac{\partial U}{\partial T} + DU + \Delta\frac{\partial U}{\partial \xi} = -\frac{M}{2}\sin\xi. \tag{14}$$

The process of the development of steady-state oscillations in the layer is described by the solution to equation (14) with the zero initial condition $U(T = 0, \xi) = 0$. This solution is as follows:

$$U = B(T)\cos(\xi + \varphi(T)), \tag{15}$$

$$B = \frac{M}{2}\left[\frac{1 - 2e^{-DT}\cos(\Delta T) + e^{-2DT}}{\Delta^2 + D^2}\right]^{1/2}, \tag{16}$$

$$\varphi = \arctan\frac{D}{\Delta} + \arctan\left[\frac{e^{-DT}\sin(\Delta T)}{1 - e^{-DT}\cos(\Delta T)}\right]. \tag{17}$$

For small T, solution (15)–(17) is reduced to the expression

$$U \approx -\frac{1}{2}MT\sin\xi, \tag{18}$$

which describes the beginning of the process of the oscillation development with a linear growth of amplitude. As $T \longrightarrow \infty$, solution (15)–(17) tends to a steady-state form

$$U \approx \frac{M}{2}\frac{\cos(\xi + \arctan(D/\Delta))}{\sqrt{\Delta^2 + D^2}}, \tag{19}$$

which coincides with expression (9).

LAYER WITH A MOVING BOUNDARY: EQUATION AND THE INVERSE PROBLEM

To derive the evolution equation with allowance for the boundary motion, we use a scheme similar to that used for the derivation of the differential equation (14) from the initial functional equation (7). The only difference is that the new boundary condition (compare with (1))

$$v(x = X(t), t) = \frac{dX}{dt} \tag{20}$$

set at the wall moving according to the law $x = X(t)$ leads to the appearance of nonlinear field distortions. Therefore, the function F in solution (5) will contain higher harmonics:

$$F(\omega t) = \sum_{n=0}^{\infty} B_n(t)\exp(-in\omega t) \tag{21}$$

even when the law $X(t)$ is a harmonic one. The corresponding generalization of functional equation (7) has the form

$$\frac{dX}{dt} = A\sin(\omega t) = \sum_{n=0}^{\infty} B_n\left(t - \frac{X(t) - L}{c}\right) \times \exp\left\{-\delta n^2\omega^2(X(t) - L) - in\omega\left(t - \frac{X(t) - L}{c}\right)\right\} - \sum_{n=0}^{\infty} B_n\left(t + \frac{X(t) - L}{c}\right) \times \exp\left\{\delta n^2\omega^2(X(t) - L) - in\omega\left(t + \frac{X(t) - L}{c}\right)\right\}. \tag{22}$$

As before, we assume that the attenuation within the resonator length is weak ($D = \delta\omega^2 L \ll 1$) and consider the oscillations that are close to the fundamental mode of the resonator ($kL = \pi + \Delta$, $|\Delta| \ll 1$). In addition, we assume that the displacement of the wall is small in comparison with the wavelength ($k|X| \ll 1$).

Expanding all functions involved in equation (22) into series and retaining only the terms of the zero and first orders of smallness, we arrive at the relation

$$\frac{A}{2}\sin(\omega t) = \sum_{n=0}^{\infty}\left[\frac{L}{c}\frac{\partial B_n}{\partial t} + \left(\delta n^2\omega^2 L - in\frac{A}{c}\cos(\omega t) - in\Delta\right)B_n\right]\exp\{-in(\omega t + \pi)\}. \tag{23}$$

Here, we note that, firstly, the multiplication of the terms of the series by $(-in\omega)$ corresponds to the differentiation of the exponent with respect to the variable t, and, secondly, in the vicinity of the fundamental resonance, we have $L/c \approx \pi/\omega$. Taking into account these two facts and expression (21) for F, we represent relation (23) in the form

$$\frac{A}{2}\sin(\omega t) = \left(\frac{\partial}{\partial T} - \delta L\frac{\partial^2}{\partial t^2} + \frac{A}{\omega c}\cos(\omega t)\frac{\partial}{\partial t} + \frac{\Delta}{\omega}\frac{\partial}{\partial t}\right)F(T, \omega t + \pi). \tag{24}$$

Using notation (14), we arrive at the sought-for equation

$$\frac{\partial U}{\partial T} - D\frac{\partial^2 U}{\partial \xi^2} - M\cos\xi\frac{\partial U}{\partial \xi} + \Delta\frac{\partial U}{\partial \xi} = -\frac{M}{2}\sin\xi. \tag{25}$$

If the wall motion $X(t)$ is nonharmonic but periodic with the period 2π, equation (25) allows the following generalization:

$$\frac{\partial U}{\partial T} - D\frac{\partial^2 U}{\partial \xi^2} - Mf(\xi)\frac{\partial U}{\partial \xi} + \Delta\frac{\partial U}{\partial \xi} = \frac{M}{2}f'(\xi), \quad (26)$$

where $Mf(\xi) = kX(\xi - \pi)$.

Now, as in the cited paper [2], we consider the direct and inverse problems on the basis of the equations obtained above.

The direct problem consists in the determination of the form $U(T, \xi)$ of the wave excited in the layer from the known law $X(t)$ of the layer boundary motion. For this purpose, it is necessary to solve equations (25) and (26), which are inhomogeneous second-order partial differential equations with variable coefficients. This problem is fairly complicated.

The inverse problem is a simpler one. It consists in the determination of the law $X(t)$ that should govern the boundary motion to provide the development of a given process $U(T, \xi)$ in the resonator. In this case, it is necessary to solve equation (26) for $f(\xi)$, i.e., to solve an ordinary first-order equation.

It is easy to verify that the expression

$$f = C_1(T) + C_2(T)$$
$$\times \exp\left\{-2U_0 e^{-DT}\cos\left[\xi - \Delta T + M\int_0^T C_1(y)dy\right]\right\} \quad (27)$$

will be an exact solution to equation (26), and this solution will be periodic in the variable ξ, provided that the process has the form

$$U = U_0 e^{-DT}\cos\left[\xi - \Delta T + M\int_0^T C_1(y)dy\right]. \quad (28)$$

Here, C_1 and C_2 are arbitrary functions of the "slow" time T and U_0 is a constant.

Assuming that in expressions (27) and (28) we have

$$C_1 = \frac{\Delta}{M}, \quad C_2 = -\frac{\Delta}{M}I_0^{-1}\left(\frac{M}{\Delta}e^{-DT}\right), \quad U_0 = \frac{M}{2\Delta}, \quad (29)$$

where I_0 is a zero-order modified Bessel function, we obtain the solution to the inverse problem in the form:

$$Mf(\xi) = kX(\xi - \pi)$$
$$= \Delta\left[1 - \frac{\exp\left(-\frac{M}{\Delta}e^{-DT}\cos\xi\right)}{I_0\left(\frac{M}{\Delta}e^{-DT}\right)}\right], \quad (30)$$

$$U = \frac{M}{2\Delta}e^{-DT}\cos\xi. \quad (31)$$

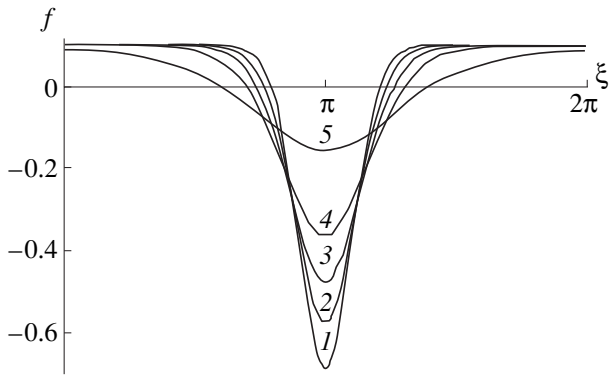

Fig. 1.

It is remarkable that, in the absence of attenuation ($D = 0$), solution (30), (31) correct to the notation coincides with the solution obtained by treating the inverse problem in an entirely different way in the previous paper [2] (formulas (9) and (4)). In the cited paper [2], the best way of the excitation of steady-state waves is determined; namely, the law of the wall motion that effectively maintains resonance harmonic oscillations is derived. In the case of a small ratio M/Δ, the wall can be moved according to a harmonic law, while, at greater ratios M/Δ, the wall motion should be modified in a special way. For example, to maintain harmonic oscillations in the layer at large values of M/Δ, it is necessary to excite the resonator by short "jerks" following one after another with the period 2π.

In contrast to the solution obtained in [2], solution (30) is a nonstationary one. It describes the dissipation-caused transition from "highly nonlinear" (for $M/\Delta \gg 1$) wall oscillations at the initial instant of time $T = 0$ to purely harmonic linear oscillations at $T \longrightarrow \infty$. In the course of the evolution of law (30) governing the wall motion, oscillations (31) excited in the layer remain harmonic; as $T \longrightarrow \infty$, these oscillations attenuate.

Figure 1 shows the temporal profiles of the periodic boundary motion (30) providing a harmonic mode of oscillations (31). The profiles are plotted for $M/\Delta = 10$ and the instants of time $DT = 0$, 0.3, 0.6, 1, and 2 (curves *1–5*, respectively).

Let us determine the dependence $f(T, \xi)$ that provides the formation of the linear solution (15)–(17). Using the fact that solution (15)–(17) satisfies equation (14), we can simplify the differential equation for f. Subtracting (14) from (26), we obtain

$$\frac{df}{d\xi} = 2fB\sin(\xi + \varphi) - \sin\xi. \quad (32)$$

The solution to this equation is

$$f(\xi) = -e^{-2B\cos(\xi + \varphi)}\int \sin\xi e^{2B\cos(\xi + \varphi)}d\xi. \quad (33)$$

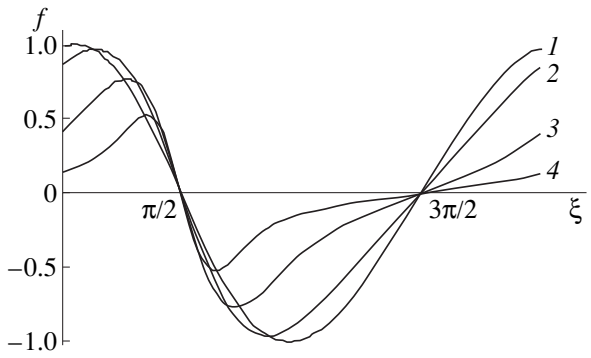

Fig. 2.

The integration constant involved in the latter expression is arbitrary, which means that, for a single dependence $U(T, \xi)$, we obtain a family of solutions. However, in our calculations, the integration constant was selected so as to obtain a zero time-average displacement of the piston.

The results of the calculations are presented in Fig. 2. We selected the parameters $\Delta = 0$, $D = 0.01$, and $T = 10^{-1}$, 1, 10, and 10^2 (curves *1–4*, respectively). From this figure, one can see that, for small values of T, the wall motion is similar to that in the linear case, while, for greater values of T, the piston motion should be fairly complicated.

FIELD IN A RESONATOR WITHOUT DISSIPATION. THE DIRECT NONSTATIONARY PROBLEM

We begin with the solution of equation (25) for a medium without dissipation, i.e., with $D = 0$. In this case, the order of the evolution equation is reduced, and it takes the form

$$\frac{\partial U}{\partial T} + (\Delta - M\cos\xi)\frac{\partial U}{\partial \xi} = -\frac{M}{2}\sin\xi. \qquad (34)$$

In the problem of the development of steady-state forced oscillations, we should set a zero initial condition (at $T = 0$) and the condition of periodicity in the variable ξ:

$$U(T = 0, \xi) = 0, \quad U(T, \xi + 2\pi) = U(T, \xi). \qquad (35)$$

The solution to the Cauchy problem (34), (35) can be found by the conventional method of characteristics. However, the symmetry of equation (34) makes it possible to use a simpler method. In equation (34), we set

$$U = -\frac{1}{2}\ln[A(T)\cos\xi + B(T)\sin\xi + C(T)]. \qquad (36)$$

The unknown functions A, B, and C must satisfy the system of ordinary equations

$$\frac{dA}{dT} + \Delta B = 0, \quad \frac{dB}{dT} - \Delta A = MC, \quad \frac{dC}{dT} = MB, \qquad (37)$$

which can be easily solved. With allowance for the initial condition (35), we have

$$A = \frac{M\Delta[1 - \mathrm{ch}(\sqrt{M^2 - \Delta^2}\,T)]}{M^2 - \Delta^2},$$

$$B = \frac{M\,\mathrm{sh}(\sqrt{M^2 - \Delta^2}\,T)}{\sqrt{M^2 - \Delta^2}}, \qquad (38)$$

$$C = \frac{M^2\,\mathrm{ch}(\sqrt{M^2 - \Delta^2}\,T) - \Delta^2}{M^2 - \Delta^2}$$

for small detuning, i.e., for $\Delta^2 < M^2$, and

$$A = \frac{M\Delta[\cos(\sqrt{\Delta^2 - M^2}\,T) - 1]}{\Delta^2 - M^2},$$

$$B = \frac{M\sin(\sqrt{\Delta^2 - M^2}\,T)}{\sqrt{\Delta^2 - M^2}}, \qquad (39)$$

$$C = \frac{\Delta^2 - M^2\cos(\sqrt{\Delta^2 - M^2}\,T)}{\Delta^2 - M^2}$$

for greater detuning $\Delta^2 > M^2$.

Let us discuss the results obtained above. First, we consider the case $|\Delta| < M$. From formulas (36) and (38), it follows that in this case the expression under the logarithm is positively definite, and, hence, the solution has no singularities. For $T \longrightarrow \infty$, it takes the form

$$U = -\frac{1}{2}\ln S, \quad S = \frac{1}{2}\frac{e^{M\sin\xi_* T}}{\sin^2\xi_*}[1 - \cos(\xi + \xi_*)], \qquad (40)$$

where $\sin\xi_* = \sqrt{1 - \Delta^2/M^2}$. Analyzing formulas (40), we conclude that, as $T \longrightarrow \infty$, the quantity U tends to the function with a logarithmic singularity at $\xi = -\xi_*$, while, at any finite T, no singularities are present.

We introduce the notation

$$u_e(\xi) = \lim_{T\to\infty}\left\{U(T, \xi) + \frac{MT}{2}\sin\xi_*\right\}$$
$$= -\ln\left|\sin\frac{\xi + \xi_*}{2}\right| + \ln\sin\xi_*. \qquad (41)$$

Figure 3 presents the plots of $u_e(\xi)$ and $U + (MT/2)\sin\xi_*$ for $\Delta = 0$, $M = 0.1$, and $T = 10$, 20, 30, and 40 (curves *1–4*, respectively). One can see that a sharp peak is formed near the point $\xi = -\xi_*$, and the height of this peak increases with time. Evidently, the growth of this peak is limited by dissipation, and, for $T \longrightarrow \infty$, it is necessary to take into account the term $D\partial^2 U/\partial\xi^2$,

which was discarded when passing from the evolution equation (25) to its simplified version (34).

In the second case, for greater detuning $|\Delta| > M$, the solution to equation (34) has the form (36), (39). Evidently, this solution is periodic in T with the period $2\pi/\sqrt{\Delta^2 - M^2}$. The profiles of the wave $U(T, \xi)$ are shown in Fig. 4 for $M = 0.1$ and $\Delta = 0.15$ and for different T selected according to the formula $T = 2\pi n/(6\sqrt{\Delta^2 - M^2})$, where $n = 1, 2, 3, 4$, and 5. One can see that the solution has no singularities.

The analysis of Figs. 3 and 4 reveals some fundamental differences between the oscillations of a layer with a moving boundary and those of a layer with an infinitesimal displacement of its wall.

Figure 4 shows the "beats" whose frequency depends on the amplitude A of the wall oscillations (or on $M = A/c$); this frequency decreases as M approaches $|\Delta|$. Similar beats are observed in the classical problem when the excitation frequency does not coincide with the resonance frequency. These beats result from the summation of forced and natural oscillations, and their frequency does not depend on M and is exactly equal to Δ.

In an ordinary resonator, when the excitation frequency coincides with the resonance frequency, the oscillation amplitude increases with time (see (15)–(17)). A similar behavior is observed in Fig. 3. The difference lies in the form of the wave, which now contains higher harmonics; at longer times T, a sharp peak is formed, and in the limit $T \longrightarrow \infty$, it is transformed to a logarithmic singularity. Such "resonance" behavior is observed not only at $\Delta = 0$, but also within the band $|\Delta| < M$.

STEADY-STATE OSCILLATIONS IN A RESONATOR WITH SMALL DISSIPATION

In the previous section, we have shown that, for $|\Delta| < M$, the function U exhibits a sharp peak whose height is limited by dissipation. Let us determine the height of this peak in the case of small dissipation. In addition, we assume that the small parameters D and M obey the relation $D/M \ll 1$. The physical meaning of this relation is evident. Two concurrent processes occur in the resonator: the accumulation of "nonlinearity," which leads to the formation of the peak, and the dissipation, which destroys this peak. If M and D will be of the same order of magnitude or D will be greater than M, the peak will never be formed, and, qualitatively, the solution will be the same as in the classical linear case.

Let us assume that the oscillations in the resonator are fully developed, i.e., the boundary nonlinearity and the dissipation are in balance. We need to determine the field in the resonator. At first glance, it may seem that for this purpose it is sufficient to drop the term containing the derivative with respect to T in equation (25) and to solve the resulting ordinary differential equation.

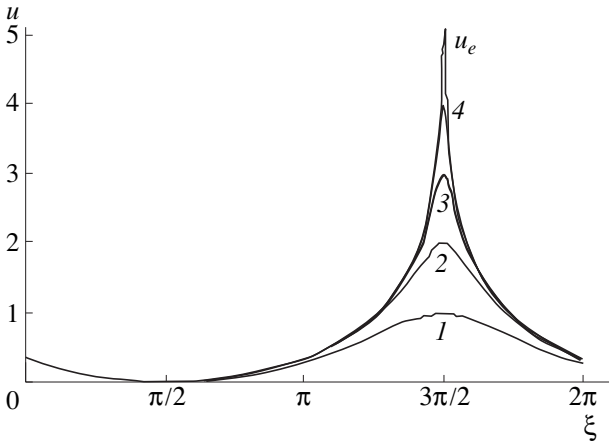

Fig. 3.

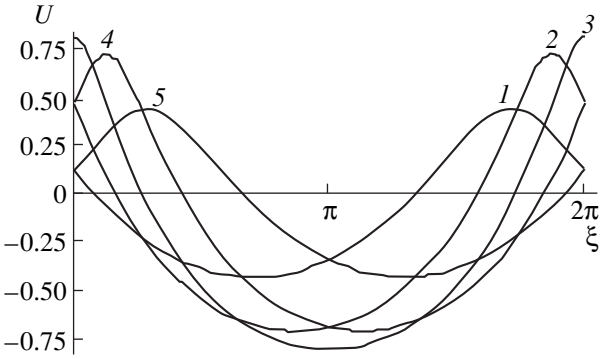

Fig. 4.

However, the solution is not that simple. The analysis of expressions (40) and (41) shows that the solution to the equation without dissipation contains a secular (slowly increasing with T) term, which is equal to $-(MT\sin\xi_*)/2$. The same term is present in the solution to the equation with dissipation (this follows from the analysis of the singularity at $\xi = \xi_*$). Hence, we seek the "steady-state" solution to equation (25) in the form

$$U(T, \xi) = u(\xi) - \frac{MT\sin\xi_*}{2}. \qquad (42)$$

The presence of the linearly increasing term is a theoretical problem. This term disappears with the passage (5) from the auxiliary function U to the particle velocity v in the layer; however, this term is present in the expression for the pressure p (see (6)).

The problem of the appearance of a nonzero mean in a nonlinear oscillatory motion is well known (see [10], pp. 362 and 524). In purely one-dimensional problems, constant or slowly varying mean values are usually unrelated to the mass transfer; they only slightly change the "background" on which the oscillations are observed. Presumably, the linear growth can

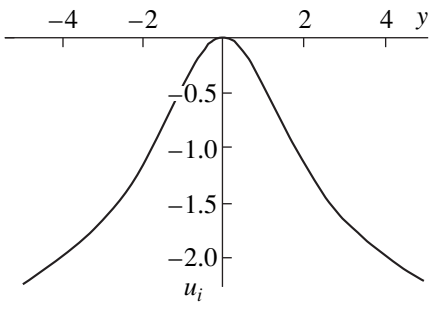

Fig. 5.

be eliminated by considering an equation of motion that is more realistic than equation (2). Here, we do not solve this problem, because the presence of such a disadvantage does not prevent us from getting correct results. Besides, such difficulties do not arise in other similar problems concerned with the oscillations of a string or a rod with moving ends [3, 4].

For the function $u(\xi)$, we have an ordinary differential equation

$$D\frac{d^2u}{d\xi^2} - (\Delta - M\cos\xi)\frac{du}{d\xi} + \frac{M}{2}(\sin\xi_* - \sin\xi) = 0. \quad (43)$$

This equation can be solved by conventional methods, but such a solution is cumbersome and requires an extra analysis to determine of its asymptotic characteristics. In our case, it is more convenient to use an approximate solution obtained by the method of matching of asymptotics.

For small ratios D/M, it is possible to ignore the term with the second derivative everywhere except the vicinity of the point $\xi = -\xi_*$ and to use the quantity u_e determined by formula (41) as the approximate solution. In terms of the perturbation theory [11], u_e is the first term of the "external" solution to the problem. Near the point $\xi = -\xi_*$, the external solution cannot be used, and, therefore, it is necessary to construct an internal expansion that allows for the dissipation but is valid only in the vicinity of the singular point. For this purpose, we derive a differential equation of type (43) with simplified coefficients.

We introduce the "internal" variable

$$y = \sqrt{\frac{M\sin\xi_*}{D}}(\xi + \xi_*). \quad (44)$$

We expand the second and third terms in equation (43) in powers of $\xi + \xi_*$ and pass to the independent variable y. Retaining only the terms of the expansion that are leading in $\sqrt{D/M}$, we obtain the equation that determines the approximate internal solution:

$$\frac{d^2u_i}{dy^2} + y\frac{du_i}{dy} + 1 = 0. \quad (45)$$

The even (with respect to y) solution to equation (45) can be expressed through Dawson's integral $F(z)$ [12]:

$$u_i(y) = K - \sqrt{2}\int_0^y F\left(\frac{z}{\sqrt{2}}\right)dz, \quad F(z) = e^{-z^2}\int_0^z e^{t^2}dt, \quad (46)$$

where K is an arbitrary constant. This solution describes the form of the peak of the steady-state wave profile at any values of the parameters Δ, M, and D satisfying the above assumptions. The curve representing this solution for $K = 0$ is shown in Fig. 5.

The functions u_e and u_i describe the behavior of u in different regions, and, therefore, it is necessary that they are matched in a certain sense [11]. One can use the condition of the matching of asymptotics, which, in our case, is as follows: when expressed through the variable ξ, the asymptotics of u_i for $y \longrightarrow \infty$ should coincide with the asymptotics of u_e for $\xi \longrightarrow -\xi_*$. The application of this condition provides a correct choice of the parameter K.

The asymptotics of u_e for $\xi \longrightarrow -\xi_*$ can be easily obtained from formula (41):

$$u_e \sim -\ln|\xi + \xi_*| + \ln(2\sin\xi_*). \quad (47)$$

The asymptotics of the internal solution (46) is given by the formula

$$u_i(y) \sim K - \ln|y| - \eta = -\ln|\xi + \xi_i| + K - \eta - \frac{1}{2}\ln\frac{M\sin\xi_*}{D}, \quad (48)$$

where the asymptotics of Dawson's integral $F(z \longrightarrow \infty) \sim (2z)^{-1}$ is used, and the constant

$$\eta = \lim_{y\to\infty}\left[\sqrt{2}\int_0^y F\left(\frac{x}{\sqrt{2}}\right)dx - \ln y\right] \quad (49)$$

is determined numerically: $\eta = 0.635181$. Correlating formulas (47) and (48), we obtain

$$K = \eta + \ln\left(2\sqrt{\frac{M}{D}}\sin^{3/2}\xi_*\right). \quad (50)$$

The curves representing the external and internal expansions are shown in Fig. 6 for different D. The selected parameters are $M = 0.1$ and $D = 2 \times 10^{-4}$, 1×10^{-3}, and 5×10^{-3} (curves *1–3*, respectively). From this figure, it follows that, for small D/M, the internal expansion describing the shape of the resonance pulse smoothly passes into the external expansion describing the rest of the signal. Comparing Figs. 3 and 6, one can see that the steady-state wave profiles formed in a resonator with dissipation are similar to the wave profiles formed in a medium without dissipation at different instants of time T. This result makes it possible to qual-

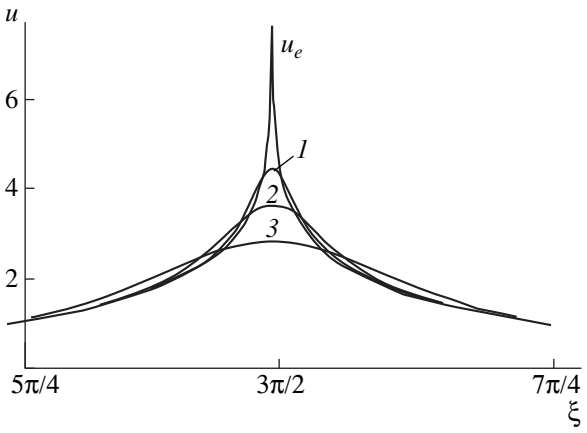

Fig. 6.

itatively describe the process of the development of oscillations in a resonator with dissipation. For small T, dissipation is insignificant, and the growth of the wave profile is observed, as in Fig. 3. At some time, the profile becomes close to the limiting distribution (see Fig. 6) and, then, exponentially tends to it (varying insignificantly). We note that the calculated value of the constant K is the peak value of the wave profile. Hence, relation (50) represents the resonance curve for the system with dissipation.

Let us estimate the time of the development of the mode of oscillation described by formulas (41) and (46). For this purpose, we determine the time that is necessary for the formation of a peak of height (50) in the absence of dissipation. Equation (34) allows us to directly calculate the values of $U(T, \pm\xi_*)$. We note that, at the given values of the variable ξ, the coefficient of the derivative with respect to ξ is equal to zero. The peak value of the wave profile calculated by using equation (34) is as follows:

$$U(-\xi_*) = \frac{MT}{2}\sin\xi_*. \tag{51}$$

Comparing this quantity with relation (50) and taking into account the linearly increasing term, we obtain the estimate

$$T_{\text{est}} \sim \frac{1}{M\sin\xi_*}\ln\left(\sqrt{\frac{M}{D}}\sin^{3/2}\xi_*\right). \tag{52}$$

ACKNOWLEDGMENTS

This work was supported by the Russian Foundation for Basic Research, the INTAS, and the program "Universities of Russia."

REFERENCES

1. O. V. Rudenko, Akust. Zh. **44**, 786 (1998) [Acoust. Phys. **44**, 717 (1998)].
2. O. V. Rudenko, Akust. Zh. **45**, 397 (1999) [Acoust. Phys. **45**, 351 (1999)].
3. A. I. Vesnitskiĭ and A. I. Potapov, Prikl. Mekh. **11** (4), 98 (1975).
4. A. I. Vesnitskiĭ, S. V. Krysov, and A. I. Potapov, Mekh. Tverd. Tela, No. 6, 128 (1978).
5. V. A. Pozdeev, *Nonstationary Wave Fields in Regions with Moving Boundaries* (Naukova Dumka, Kiev, 1985).
6. V. S. Krutikov, *One-Dimensional Problems of Mechanics of Continua with Moving Boundaries* (Naukova Dumka, Kiev, 1985).
7. V. B. Braginskiĭ, V. P. Mitrofanov, and V. I. Panov, *Systems with Small Dissipation* (Nauka, Moscow, 1981; Chicago Univ. Press, Chicago, 1985).
8. C. C. Lawrenson, B. Lipkens, T. S. Lucas, *et al.*, J. Acoust. Soc. Am. **104**, 623 (1998).
9. M. B. Vinogradova, O. V. Rudenko, and A. P. Sukhorukov, *Theory of Waves* (Nauka, Moscow, 1990).
10. L. D. Landau and E. M. Lifshits, *Hydrodynamics* (Nauka, Moscow, 1986).
11. A. H. Nayfeh, *Introduction to Perturbation Techniques* (Wiley, New York, 1981; Mir, Moscow, 1984).
12. *Handbook of Mathematical Functions with Formulas, Graphs and Mathematical Tables*, Ed. by M. Abramowits and J. A. Stegun (Dover, New York, 1968; Nauka, Moscow, 1979).

Translated by E.M. Golyamina

Acoustical Physics, Vol. 46, No. 3, 2000, pp. 342–347. Translated from Akusticheskiĭ Zhurnal, Vol. 46, No. 3, 2000, pp. 401–407.

Calculation of the Spectra of Pseudosound Wall-Pressure Fluctuations in Turbulent Boundary Layers

A. V. Smol'yakov

Krylov Central Research Institute, Moskovskoe sh. 44, St. Petersburg, 196158 Russia

e-mail: albert@krylov.spb.su

Received March 16, 1999

Abstract—A simple method is developed for calculating the wall-pressure spectra in turbulent boundary layers. The method is based on the modeling of the wave-number spectrum of the sources that are caused by the interaction of the turbulence–mean shear type. The sources are described in the framework of the semiempirical theory of turbulence. The calculations reveal four characteristic frequency ranges; for these ranges, the specific features of the wall-pressure spectra are determined, and the most general ways of their scaling are found. The calculated spectra and rms values of pressure fluctuations are compared with the experimental data, and a good agreement between the calculations and the experiment is observed. © *2000 MAIK "Nauka/Interperiodica".*

The frequency spectrum of pseudosound (in the Blokhintsev sense) pressure fluctuations in a turbulent boundary layer is one of the most important statistical characteristics that are used in calculating the flow noise and the vibrations excited by turbulent flows in airplane fuselages, ship hulls, and other engineering structures. In the last 40 years, numerous measurements of pressure spectra in turbulent boundary layers were carried out for various flow conditions. Comprehensive reviews of such measurements can be found in the literature [1, 2]. The studies concerned with the theoretical calculations of such spectra are much fewer in number. In some recent publications, the statistical characteristics of a turbulent wall-pressure field were determined by numerical integration of the Navier–Stokes equations [3, 4]. However, this approach requires a great deal of calculation, and one has to consider only the case of low Reynolds numbers even if modern efficient computers are used. Earlier attempts at analytical studies of the problem for high Reynolds numbers originate from Kraichnan's publication [5]. The latter study was based on the use of the Poisson equation, which was obtained by taking the divergence of the Navier–Stokes equations for an incompressible fluid, and on the assumption that the pressure sources caused by the interaction of turbulence with the mean shear (the turbulence–mean shear sources) predominate over the turbulence–turbulence sources. With this method, the greatest progress was achieved by Panton and Lineberger [6]: they integrated the spectral form of the Poisson differential equation by the Monte-Carlo method with the help of a computer the performance of which corresponded to the time of their work. The main problems encountered by these authors [6] were related to the fact that the integrand function contained fairly complex and, in the general case, unknown spectral and correlation characteristics of the velocity field formed in the boundary layer. To overcome this difficulty, one has to rely on scanty and disconnected experimental data by supplementing them with many speculative hypotheses whose validity is not always evident, and, therefore, the results of such studies are not sufficiently reliable. Possibly, this was the reason why Blake, in his fundamental monograph [7], gave up a detailed description of the integrand and restricted his consideration to the evaluation of the orders of magnitude of different terms and to only qualitative predictions about the shape of the spectrum in different frequency ranges (see p. 528 and Fig. 8.14 in [7]).

For the pseudosound region ($k \gg \omega/c$), Blake [7] used the following expression (first proposed in [8]) for the pressure produced at a flat plate in a turbulent boundary layer by the turbulence–mean shear sources:

$$p(k_1, k_3, \omega) \sim \rho \frac{k_1}{k} \int_0^\infty \frac{dU}{dy} \tilde{u}_2(k_1, y, k_3\omega) \exp(-ky) dy, \quad k \gg \omega/c. \tag{1}$$

Here, ω is the circular frequency; c is the sound velocity; $p(k_1, k_3, \omega)$ is the wavenumber-frequency spectrum of the amplitudes of pressure fluctuations; k_1 and k_3 are the wave numbers in the planes parallel to the plate, where k_1 corresponds to the flow direction, k_3 corresponds to the direction across the flow, and $k = (k_1^2 + k_3^2)^{1/2}$; ρ is the density of liquid; y is the distance from the plate along the normal to it; U is the average velocity in the boundary layer at the level y; and $\tilde{u}_2(k_1, y, k_3, \omega)$ is the Fourier transform of the velocity fluctuations $u_2(x, y, z, t)$ normal to the plate in the planes y = const, where x and z are the Cartesian coordinates along the flow and across it, respectively, and t is time.

1063-7710/00/4603-0342$20.00 © 2000 MAIK "Nauka/Interperiodica"

The wavenumber-frequency spectrum of energy $E(\mathbf{k}, \omega)$ is related to the amplitude spectrum:

$$E(\mathbf{k}, \omega)\delta(\mathbf{k}-\mathbf{k}')\delta(\omega-\omega') = \langle p(\mathbf{k}, \omega)p(\mathbf{k}', \omega')\rangle, \quad (2)$$

where $\delta(x)$ is the Dirac delta-function, $\mathbf{k}'$ and ω' are variables independent of $\mathbf{k}$ and ω, and angular brackets denote averaging over the ensemble. The multiplication of integrals (1) and their subsequent averaging in conformity with (2) yields an expression containing unknown wavenumber-frequency spectra and spatial correlations of velocity fluctuations, which are to be integrated twice with respect to the independent coordinates y and y' normal to the wall along with the average velocity gradients.

The main idea of this work is to avoid the aforementioned manipulations with unknown functions. For this purpose, based on the structures of formulas (1) and (2), we construct a simplified expression on the assumption that the necessary averaging and one integration with respect to y have already been performed:

$$E(\mathbf{k}, \omega) \sim \rho^2\left(\frac{k_1}{k}\right)^2 \int_0^\infty \left(\frac{dU}{dy}\right)^2 G(\mathbf{k}, \omega, y)\exp(-2ky)dy. \quad (3)$$

Here, $G(\mathbf{k}, \omega, y)$ is a generalized wavenumber-frequency function of the pressure sources located in the boundary layer at the distance y from the wall. Now, the only problem consists in an adequate modeling of the function G. For this function, we adopt the Taylor frozen turbulence hypothesis (however, in our case, this hypothesis is not extended to the wall pressure field [8]):

$$G(k_1, k_3, \omega, y) = B(k_1, k_3, y)\delta(k_1 - \omega/U), \quad (4)$$

where $B(k_1, k_3, y)$ is the wave-number spectrum of the sources; at small k, this spectrum is proportional to k^2, and, at $k \longrightarrow \infty$, it tends to zero (see [8]). Such behavior is in particular characteristic of the function

$$B(k_1, k_3, y) = f(y)(k_1^2 + \beta^2 k_3^2) \times \exp\{-\alpha l[k + |k_1|(\beta - 1)]\}. \quad (5)$$

In the geometric interpretation, function (5) has the form of an elongated crater oriented along k_3 at $\beta > 1$, where β is the asymmetry coefficient. In formula (5), l is the typical size of eddy structures (the length scale) at the distance y from the wall, and α is the dimensionless coefficient that determines the rate of decrease of spectrum (5) at high wave numbers. It would appear natural to have the maximum energy at the wave number $k_3 = 2\pi/l$; for this purpose, we set $\alpha = 1/\pi$.

Based on the dimensional considerations, we can represent the function of the distance in (5) as $f(y) \sim v l^5$, where v is the characteristic value of turbulent velocity fluctuations at the level y. Using this relation and substituting formulas (4) and (5) into expression (3), we perform the integration of the latter over the wave numbers and obtain the following expression for the frequency spectrum of turbulent pressures:

$$P(\omega) = \int_{-\infty}^{\infty}\int E(k_1, k_3, \omega)dk_1 dk_3 = A\rho^2 \int_0^\infty F(\mu) v l^5 \left(\frac{dU}{dy}\right)^2 \left(\frac{\omega}{U}\right)^3 \exp\left[-\frac{l\omega}{\pi U}(\beta - 1)\right]dy. \quad (6)$$

Here, A is a dimensionless constant,

$$F(\mu) = \beta^2 \int_1^\infty \frac{se^{-\mu s}ds}{\sqrt{s^2-1}} - (\beta^2 - 1)\int_1^\infty \frac{e^{-\mu s}ds}{s\sqrt{s^2-1}} = \beta^2 K_1(\mu) - (\beta^2 - 1)I(\mu), \quad (7)$$

$\mu = (\omega l/\pi U)[1 + (2\pi y/l)]$, $s^2 = 1 + (k_3 U/\omega)^2$, $K_1(\mu)$ is the first-order modified Bessel function of the second kind, and $I(\mu)$ is the second integral from relation (7).

For the characteristic scales of the velocity and length of turbulent motion in a shear flow, we use the expressions [9, 10]:

$$v \sim \langle u_1 u_2\rangle^{1/2}, \quad l = \langle u_1 u_2\rangle^{1/2}/(dU/dy). \quad (8)$$

Here, $\langle u_1 u_2\rangle$ is the correlation of the longitudinal and the transverse (i.e., normal to the wall) components of turbulent velocity fluctuations. This quantity is proportional to the Reynolds stresses. We note that the second expression (8) agrees well with the Prandtl hypothesis $l = \kappa y$ about the path of mixing ($\kappa = 0.41$ is the Karman constant).

Using turbulent scales (8) and simple relations obtained from the semiempirical theory of turbulence, we can determine the contributions of different parts of the boundary layer to the wall pressure field; namely, the contributions of the parts characterized by different dependences of the motion on the viscous and inertial forces acting in the flow.

In a turbulent boundary layer, two regions of the flow can be distinguished: the layer of constant stresses and the outer part of the boundary layer. Each of these parts has its own specific features that will be used below in calculating the spectra of pressure fluctuations in a turbulent flow.

In the constant stress layer, which lies next to the wall and occupies about 13–15% of the boundary layer thickness, the equilibrium of forces is described by the relation [11, 12]

$$(dU/dy)(\nu + \varepsilon) = U_\tau^2 = \text{const}, \quad (9)$$

where ν is the molecular viscosity, $\varepsilon = \langle u_1 u_2\rangle/(dU/dy)$ is the eddy viscosity, $U_\tau = (\tau_w/\rho)^{1/2}$ is the friction velocity, and τ_w is the viscous friction stress at the wall. Using

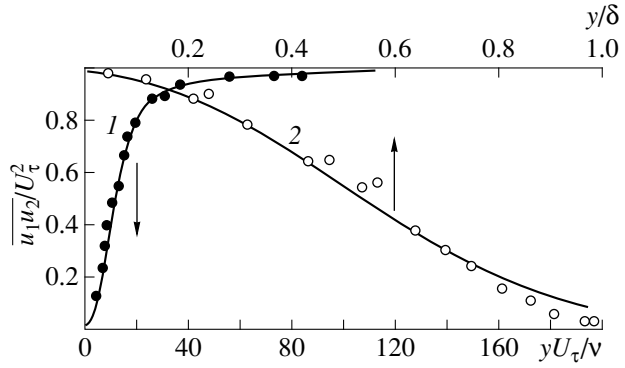

Fig. 1. Distribution of Reynolds stresses across the boundary layer: (○, ●) experimental and (—) computational data.

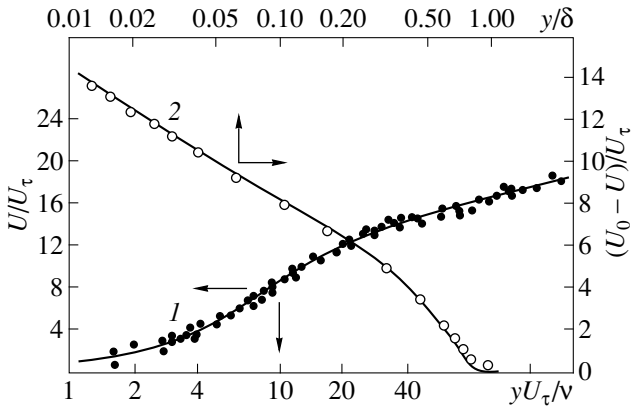

Fig. 2. Distribution of the average velocity and velocity defect across the boundary layer. Notations are the same as in Fig. 1.

expression (9), we can represent turbulent scales (8) in the form

$$\nu \sim U_\tau[(\varepsilon/\nu)/(1+\varepsilon/\nu)]^{1/2},$$
$$l = (\nu/U_\tau)[(\varepsilon/\nu)(1+\varepsilon/\nu)]^{1/2}. \quad (10)$$

According to Townsend [11], the eddy viscosity increases with distance from the wall, first, as the cube of the distance and, then, in direct proportion to it. Therefore, we set:

$$\varepsilon/\nu = b(yU_\tau/\nu)^3 \text{ at } yU_\tau/\nu \le (\kappa/b)^{1/2};$$
$$\varepsilon/\nu = \kappa(yU_\tau/\nu) \text{ at } yU_\tau/\nu \ge (\kappa/b)^{1/2}, \quad (11)$$

where b is a constant. We do not use the more complicated expression [9] that combines both these cases, because it is not necessary for our calculations. Figure 1 compares the results, which were obtained by calculating the quantity $\langle u_1u_2\rangle/U_\tau^2$ (curve *1*) on the basis of the definition $\varepsilon = \langle u_1u_2\rangle/(dU/dy)$ and formulas (9) and (11), with the experimental data taken from Hinze's monograph [12]. The use of dependences (11) for the determination of the average velocity profile $U/U_\tau = f(yU_\tau/\nu)$ by integrating formula (9) yields the results that also agree well with the experimental data in all parts of the constant stress layer; i.e., in the viscous part ($\varepsilon \ll \nu$), the buffer part ($\varepsilon \approx \nu$), and the part with fully developed turbulence ($\varepsilon \gg \nu$) (see curve *1* in Fig. 2); in this case, the experimental data were taken from the same monograph [12]. A good agreement of the calculations with the experiment is achieved at $b = 6.14 \times 10^{-4}$, which is quite close to the initial estimate $b = 6 \times 10^{-4}$ given by Townsend [11] and corresponds to the widely used constant 4.9 in the logarithmic profile $U/U_\tau = \kappa^{-1}\ln(yU_\tau/\nu) + 4.9$. In other coordinates, this profile corresponds to the logarithmic dependence of the velocity defect [11, 12] $(U_0 - U)/U_\tau = -k^{-1}\ln Y + 2.5$, where $Y = y/\delta$, U_0 is the velocity at the upper boundary of the boundary layer, and δ is its thickness. The latter can easily be determined from the comparison of the two logarithmic dependences:

$$\delta = (\nu/U_\tau)\exp[\kappa(U_0/U_\tau - 7.4)]. \quad (12)$$

For the outer part of the boundary layer, which occupies 85–87% of the boundary layer thickness, the concept of a constant eddy viscosity is valid [9–12]:

$$\varepsilon = U_\tau\delta/\gamma = \text{const}, \quad (13)$$

where γ is a constant. In this region, the correlation $\langle u_1u_2\rangle$ is adequately approximated by a square exponent [12]

$$\langle u_1u_2\rangle = U_\tau^2\exp(-2.5Y^2), \quad (14)$$

which is illustrated by curve *2* in Fig. 1. Since the correlation is related to the gradient of the average velocity, $\langle u_1u_2\rangle = \varepsilon(dU/dy)$, we obtain the expression

$$dU/dy = \gamma(U_\tau/\delta)\exp(-2.5Y^2). \quad (15)$$

Substituting formulas (14) and (15) into expressions (8), we obtain the following turbulence scales in the outer part of the boundary layer:

$$\nu \sim U_\tau\exp(-1.25Y^2), \quad l = (\delta/\gamma)\exp(1.25Y^2). \quad (16)$$

The boundary y_0 between the constant stress layer and the outer part of the boundary layer can be found from the condition of equality of the eddy viscosities determined by formula (13) and the second formula (11). This boundary is described by the dimensionless expressions

$$y_0U_\tau/\nu = (U_\tau\delta/\nu)/(\kappa\gamma), \quad Y_0 = y_0/\delta = (\kappa\gamma)^{-1}. \quad (17)$$

Performing the integration of gradient (15) and the comparison of the resulting defect of the average velocity in the outer part of the layer with the experimental data, one can see that a good agreement between the calculations and the experiment is achieved at $\gamma = 17.9$ (curve *2* in Fig. 2). This value was used for calculating

the pressure spectra. The substitution of this value in the second formula (17) at $\kappa = 0.41$ shows that the thickness of the constant stress layer lying next to the wall is about 14% of the total boundary layer thickness.

The values of the displacement thickness δ^* and the momentum thickness θ, which were necessary for different kinds of the pressure spectra scaling, were obtained by the integration of the corresponding expressions, $(1 - U/U_0)$ and $(U/U_0)(1 - U/U_0)$, over the entire thickness of the boundary layer (12). The friction velocity U_τ and the related local friction τ_w and the friction coefficient c_w were calculated by the Falkner formula $c_w = 2\tau_w/(\rho U_0^2) = 2(U_\tau/U_0)^2 = 0.0263 R_x^{-1/7}$, where $R_x = U_0 x/\nu$ is the Reynolds number along the x coordinate measured downstream from the leading edge of the plate.

The proportionality factors implied in formulas (10) and (16) are included in the constant A of the main computational formula (6), and the value of A is determined from the comparison of the calculated and measured pressure spectra. The same is true for the second unknown constant, i.e., the asymmetry coefficient β of the wave-number spectrum of the pressure sources (5). The best suitable values were found to be $A = 1.6$ and $\beta = 6$.

Figure 3 presents the pressure fluctuation spectra measured in laboratory conditions by Schewe [13], Emmerling [14], Farabee [15], Bull and Thomas [16], and Manoha [17], as well as the spectra measured by Efimtsov [18] at airplane fuselages. The scaling variables for the spectral levels are the outer scales of the boundary layer, i.e., the scales that characterize the inertial forces in the flow. The same figure shows the results of the calculations by formula (6) for the Reynolds numbers corresponding to the conditions of measurements. Despite the slight scatter of data, the computational and experimental results are in a relatively good agreement. In the region of low and mid-frequencies, the spectra (with the aforementioned scaling) form a dense group for a wide range of Reynolds numbers. At high frequencies, the spectra become separated according to the Reynolds numbers (this effect was first noticed by Efimtsov [18]). In Fig. 4, the scaling variables for the same computational and experimental results are the inner scales, which characterize the viscous forces in the flow. One can see that, at high dimensionless frequencies, all these spectra tend to a single dependence (judging from the review [1], this fact is well known), while, at low and mid-frequencies, they become separated according to the Reynolds numbers. In the calculated spectra, smooth peaks are observed, with their heights depending on the Reynolds number. Figure 5 shows the calculated heights of these peaks versus the quantity $R_\theta = U_0\theta/\nu$ (curve *1*) along with the experimental data [13, 15, 16, 19–21] borrowed from the review [2] and complemented with the results of the aforementioned experiments [14, 17, 18]. One can see that the results of calculations agree well with those of measurements. Figure 6 presents only the calculated frequency spectra in order to demonstrate the specific features of their behavior at different frequencies and different Reynolds numbers. The lower group of curves

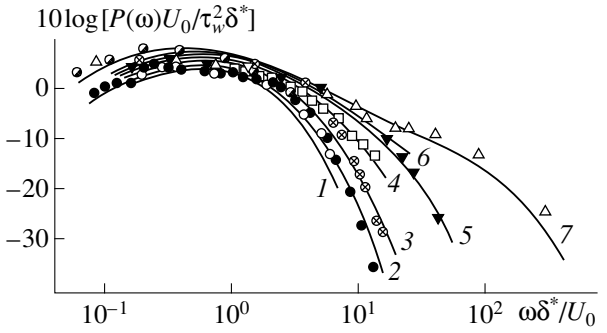

Fig. 3. Pressure spectra with the outer scaling. Measurements: R_θ = (○) 1.4×10^3 [13]; (●) 2×10^3 [14]; (⊗) 3.4×10^3 [15]; (□) 7×10^3 [16]; (◑) 2.9×10^4 [17]; (▼) 1.73×10^4 [18]; and (△) 2.93×10^5 [18]. Solid curves *1–7* correspond to the calculations for the aforementioned values of R_θ in increasing order.

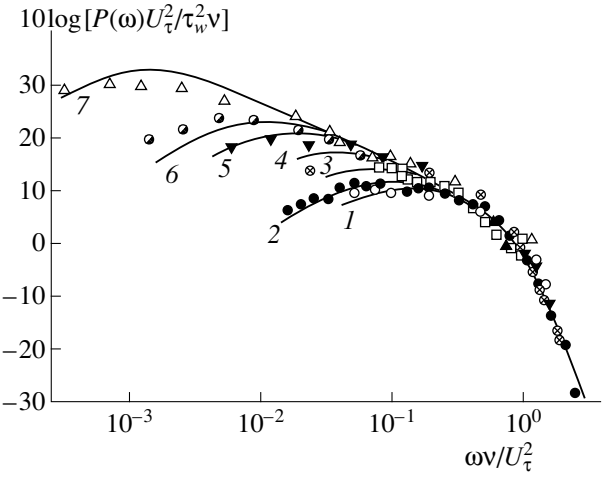

Fig. 4. Pressure spectra with the inner scaling. Notations are the same as in Fig. 3.

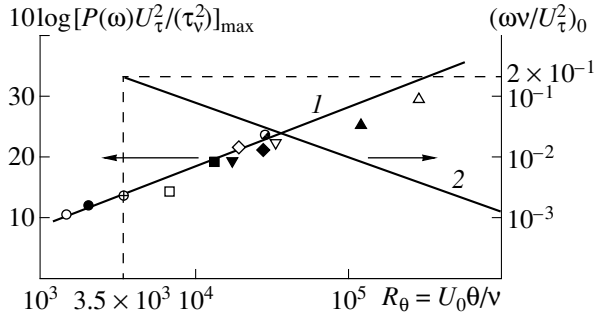

Fig. 5. Peaks of the pressure spectra (curve *1*) and the initial point of the universal range (curve *2*) versus the Reynolds number. Notation: (○), (●), (⊗), (□), (▼), (△), (◑), as in Fig. 3; (■) [19], (◇) 20; (◆) [21]; (▽), (▲) [18]; (—) calculations.

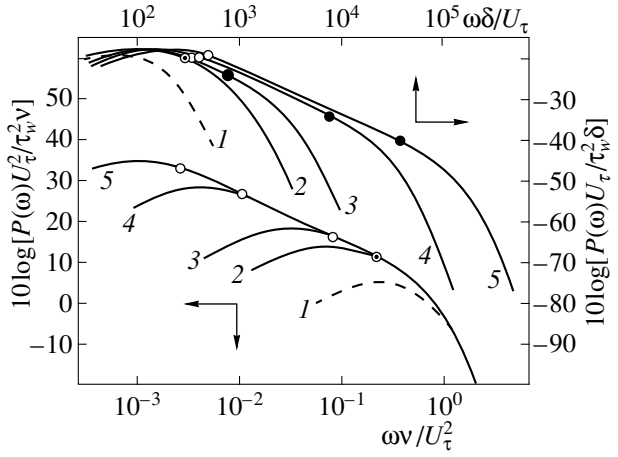

Fig. 6. Calculated pressure spectra with different scaling for different Reynolds numbers R_θ = (*1*) 560; (*2*) 3.5×10^3; (*3*) 10^4; (*4*) 10^5; and (*5*) 5×10^5.

represents the spectra with the inner scaling. According to the classification proposed in [1, 7, 22], four characteristic frequency ranges can be distinguished in the spectra at high Reynolds numbers.

At low frequencies, a decrease in the spectral levels is observed with decreasing frequency, and this decrease gradually passes into the quadratic dependence $P(\omega) \sim \omega^2$ theoretically predicted in [7, 8]. The authors of the experiments [22] believe that, in this frequency range, the most general scaling variable for the spectral levels is the quantity $\rho^2 U_0^3 \delta^*$, while the most general scaling variable for the frequencies is U_0/δ^*. Our calculations confirm this assumption: such a scaling provides a coincidence (within 1 dB) of the low-frequency spectra in a wide range of Reynolds numbers $10^3 < R_\theta < 10^6$.

The mid-frequency range lies in the region of the peaks of the spectra. According to [1, 2, 18, 22], the most suitable scaling variables in this region are the quantity $\tau_w^2 \delta/U_\tau$ for the spectra and U_τ/δ for the frequencies, which is confirmed by the computational results, namely, by the upper group of curves in Fig. 6. An exception is the spectrum corresponding to the lowest Reynolds number $R_\theta = 560$ ($R_x \approx 2 \times 10^5$) at which the notion of a fully developed turbulent boundary layer loses its meaning. The frequency range following the mid-frequencies was called the "universal" range by Bradshaw [23]. Using the dimensional analysis, Bradshaw predicted that, in this frequency range, the wave-number spectrum of pressures should decrease in inverse proportion to the wave number $P(k_1) \sim 1/k_1$. Such a dependence was also obtained by calculations for some range of wave numbers in [6]. If we assume that the turbulent pressure field is frozen and carried with a constant convection velocity, the prediction made by Bradshaw [23] for the wave-number spectrum is equivalent to a similar prediction for the frequency spectrum: $P(\omega) \sim \omega^{-1}$. Our calculations yield the dependence $P(\omega) \sim \omega^{-1.11}$, which slightly deviates from ω^{-1}, and this deviation can be easily explained by the presence of an incompletely frozen pressure field and the dependence of the convection velocity on the wave number. The calculations showed that the pressure spectrum in the universal range is determined by the turbulent motion in the logarithmic zone of the boundary layer, and the width of this region essentially depends on the Reynolds number. It decreases with decreasing Reynolds number, and at $R_\theta \le 3.5 \times 10^3$ the universal range vanishes. In Fig. 6, empty circles indicate the points corresponding to the beginning of this region, and the full circles indicate its end points at $\omega\nu/U_\tau^2 \approx 0.2$. The calculated lowest frequency of the universal range versus the Reynolds number is shown by curve *2* in Fig. 5.

At high frequencies $\omega\nu/U_\tau^2 > 0.2$, the calculated spectral levels with the inner scaling are characterized by a single curve independent of the Reynolds number, which is also observed in the experiment (Fig. 4).

To make the proposed computational scheme (which can be realized within minutes with the simplest IBM PC) applicable to other situations, one can use the approximating formulas that at $R_\theta > 10^3$ ($R_x > 5 \times 10^5$) yield the spectra deviating from the computer calculated ones by no more than ±0.6 dB:

$$\bar{P}(\omega) = 1.49 \times 10^{-5} R_\theta^{2.74} \bar{\omega}^2 (1 - 0.117 R_\theta^{0.44} \bar{\omega}^{1/2}) \quad \text{at } \bar{\omega} < \bar{\omega}_0,$$

$$\bar{P}(\omega) = 2.75 \bar{\omega}^{-1.11} \{1 - 0.82 \exp[-0.51(\bar{\omega}/\bar{\omega}_0 - 1)]\} \quad \text{at } \bar{\omega}_0 < \bar{\omega} < 0.2, \qquad (18)$$

$$\bar{P}(\omega) = (38.9 e^{-8.35\bar{\omega}} + 18.6 e^{-3.58\bar{\omega}} + 0.31 e^{-2.14\bar{\omega}}) \times \{1 - 0.82 \exp[-0.51(\bar{\omega}/\bar{\omega}_0 - 1)]\} \quad \text{at } \bar{\omega} > 0.2,$$

where $\bar{P}(\omega) = P(\omega) U_\tau^2/(\tau_W^2 \nu)$ and $\bar{\omega} = \omega\nu/U_\tau^2$, $\bar{\omega}_0 = 49.35 R_\theta^{-0.88}$. Knowing the values of δ, δ^*, and θ, one can easily pass to other forms of the frequency spectra scaling. The first factors in these formulas describe the main laws governing the behavior of the spectra in the low-frequency, universal, and high-frequency ranges, respectively. The second factors (in parentheses) provide a smooth matching of the levels in the regions between these ranges.

For the spectra at high frequencies, there exists a wide variety of concepts in the literature: from $P(\omega) \sim \omega^{-1}$ [26] to $P(\omega) \sim \omega^{-5}$ [7]. Some publications provide intermediate estimates like $\sim\omega^{-3/2}$ or $\sim\omega^{-7/3}$. The experimental data shown in Fig. 4 on a bilogarithmic scale are represented in Fig. 7 as a function of frequency

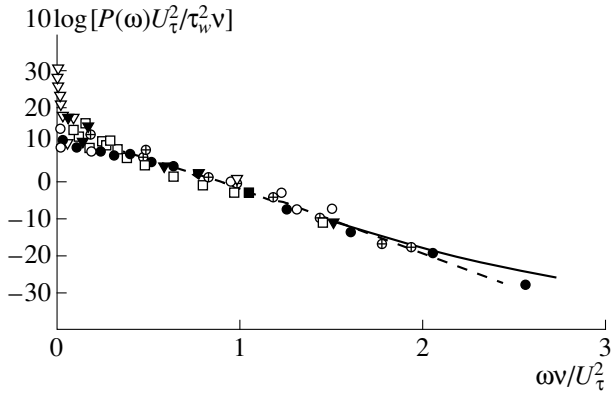

Fig. 7. High-frequency part of the pressure spectrum in semilogarithmic coordinates. Notations are the same as in Fig. 3; (----) exponential approximation and (—) calculation.

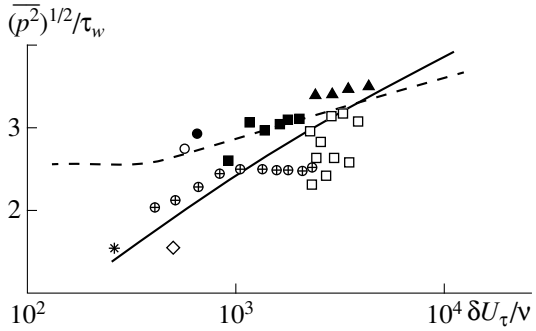

Fig. 8. Root-mean-square values of pressure fluctuations. Measurements: (∗) [4], (○) [13], (●) [14], (□) [16], (■) [22], (▲) [24], (◇) [25], and (⊕) [27]; (----) approximation [22] and (—) calculation.

instead of its logarithm. One can see that, in the frequency range $\omega\nu/U_\tau^2 > 0.2$, a tendency toward a linear dependence of the logarithm of the spectrum on frequency is observed (dashed line), which testifies to an exponential form of the spectrum rather than a power-law one. The results of the calculation by formula (6) are shown by a solid line in Fig. 7, and they are also quite close to an exponential dependence. Evidently, different portions of the exponent can be approximated by the power-law dependences of type ω^{-m} with the exponent m increasing with increasing frequency.

Figure 8 presents the experimental rms values $\langle p^2\rangle^{1/2}$ of the turbulent pressures from different publications [4, 13, 14, 16, 22, 24, 25, 27]. The solid line shows the computational results obtained by the integration of spectrum (6) with respect to frequency. The dashed line corresponds to the dependence proposed in [22]. Both computational and experimental data testify that the ratio $\langle p^2\rangle^{1/2}/\tau_w$ increases with increasing Reynolds number.

Thus, the proposed computational scheme is consistent with the experimental data reported in the literature. With formulas (6) or (18), it can be used for predicting the frequency spectra of pressures in turbulent boundary layers at different Reynolds numbers.

REFERENCES

1. M. K. Bull, J. Sound Vibr. **190**, 299 (1996).
2. W. L. Keith, D. A. Hurdis, and B. M. Abraham, Trans. ASME, J. Fluids Eng. **114**, 338 (1992).
3. J. Kim, J. Fluid Mech. **205**, 421 (1989).
4. H. Choi and P. Moin, Phys. Fluids A **2**, 1450 (1990).
5. R. H. Kraichnan, J. Acoust. Soc. Am. **28**, 378 (1956).
6. R. L. Panton and J. H. Lineberger, J. Fluid Mech. **65**, 261 (1974).
7. W. K. Blake, *Mechanics of Flow-Induced Sound and Vibration* (Academic, New York, 1986).
8. J. E. Ffowcs Williams, J. Fluid Mech. **22**, 507 (1965).
9. A. V. Smol'yakov, Akust. Zh. **19**, 251 (1973) [Sov. Phys. Acoust. **19**, 165 (1973)].
10. A. V. Smol'yakov, Akust. Zh. **19**, 420 (1973) [Sov. Phys. Acoust. **19**, 271 (1973)].
11. A. A. Townsend, *The Structure of Turbulent Shear Flow* (Cambridge Univ. Press, 1956).
12. J. O. Hinze, *Turbulence, an Introduction to Its Mechanism and Theory* (McGraw-Hill, New York, 1959).
13. G. S. Schewe, J. Fluid Mech. **134**, 311 (1983).
14. R. Emmerling, Mitteilungen aus dem Max-Plank-Inst. fur Stromungsforshung, No. 9, 1 (1973).
15. T. M. Farabee, David Taylor Res. Center Tech. Rep., No. 86/047 (1986), pp. 1–15.
16. M. K. Bull and A. S. Thomas, Phys. Fluids **19**, 597 (1976).
17. E. Manoha, in *Proceedings of AIAA Aeroacoustic Conference, 1996*, pp. 96–98.
18. B. M. Efimtsov, Akust. Zh. **30**, 58 (1984) [Sov. Phys. Acoust. **30**, 33 (1984)].
19. W. L. Keith and J. C. Bennet, J. AIAA **29**, 526 (1991).
20. M. K. Bull, J. Fluid Mech. **28**, 719 (1967).
21. W. W. Willmarth and C. E. Wooldridge, J. Fluid Mech. **14**, 187 (1962).
22. T. M. Farabee and M. J. Casarella, Phys. Fluids A **3**, 2410 (1991).
23. P. Bradshaw, J. Fluid Mech. **30**, 241 (1967).
24. W. K. Blake, J. Fluid Mech. **44**, 637 (1970).
25. G. C. Lauchle and M. A. Daniels, Phys. Fluids **30**, 3019 (1987).
26. D. M. Chase, J. Sound Vibr. **112**, 125 (1987).
27. M. K. Bull and Th. Langenheineken, Mitteilungen aus dem Max-Plank-Inst. fur Stromungsforshung, No. 73, 15 (1981).

Translated by E.M. Golyamina

Acoustical Physics, Vol. 46, No. 3, 2000, pp. 348–356. Translated from Akusticheskiĭ Zhurnal, Vol. 46, No. 3, 2000, pp. 408–416.

Conditions of Similarity of the Cross-Spectra of Pseudosound Pressures in Turbulence

V. M. Tkachenko

Krylov Central Research Institute, Moskovskoe sh. 44, St. Petersburg, 196158 Russia

e-mail: albert@krylov.spb.su

Received March 29, 1999

Abstract—Nondimensional cross-spectra of pseudosound wall-pressures in turbulence are considered in the framework of model fields of progressively increasing complexity. Conditions for the existence of the similarity of the nondimensional cross-spectra for frequency and spacing are studied; factors that lead to the violation of this similarity are considered. It is shown that, for the similarity of both longitudinal and transverse spectra, a wide distribution of the field energy in the wave numbers is necessary in combination with a small dispersion of the transport velocity of the wave components of the field. For the longitudinal spectrum, this condition is also a sufficient one. For the similarity of the transverse spectrum, the wave-number spectrum of the field should have some special form. The absence of the field energy in some region of the wave space leads to the violation of similarity of the cross-spectra at the corresponding frequencies. The results of the calculations of the longitudinal and transverse spectra are presented. The calculations are performed in the framework of the proposed model; they illustrate the effects of different parameters of the field on the properties of the cross-spectra. © *2000 MAIK "Nauka/Interperiodica".*

The field of pressure fluctuations that occur in a turbulent boundary layer at a flat or weakly curved surface at high Reynolds numbers is usually considered as a statistically uniform and steady-state field. An important characteristic of such a field is its cross-spectrum or, more precisely, the frequency cross-spectrum $P(\boldsymbol{\xi}, \omega)$ that describes the statistical correlation at different time-domain frequencies and different spacings. This spectrum is determined as the Fourier transform of the space-time correlation function $R(\boldsymbol{\xi}, \tau)$:

$$P(\boldsymbol{\xi}, \omega) = \frac{1}{2\pi}\int_{-\infty}^{\infty} R(\boldsymbol{\xi}, \tau)\exp(-i\omega\tau)d\tau, \qquad (1)$$

where $\boldsymbol{\xi} = \{\xi_1, \xi_2\}$ is the vector of the spacing between the points at the plane with the components ξ_1 and ξ_2, ω is the cyclic frequency, τ is the time delay, and i is the imaginary unit. From here on, the subscript 1 indicates the vector component along the flow, and the subscript 2 corresponds to the direction across the flow. In practice, it is more common to use the nondimensional cross-spectrum $\gamma(\boldsymbol{\xi}, \omega)$ determined as function (1) scaled on its value at $\boldsymbol{\xi} = 0$, i.e., on the power spectrum:

$$\gamma(\boldsymbol{\xi}, \omega) = P(\boldsymbol{\xi}, \omega)/P(0, \omega). \qquad (2)$$

Both functions, (1) and (2), are complex functions of real variables, which is peculiar to a streamwise field transfer. The objects usually studied by researchers are the real γ_{re} and imaginary γ_{im} parts of the nondimensional cross-spectrum (2), as well as its absolute value $|\gamma| = (\gamma_{re}^2 + \gamma_{im}^2)^{1/2}$ and phase $\varphi = \arctan(\gamma_{im}/\gamma_{re})$.

The property of similarity of the cross-spectrum for spacing and frequency was first revealed by Corcos [1] with the help of the empirical approach and later verified by other researchers. According to this property, spectrum (2) is a function of the product of the two variables, $\gamma(\boldsymbol{\xi}, \omega) = \gamma(\omega\boldsymbol{\xi}/U_c)$, where U_c is a factor with the velocity dimension; this factor is usually called the convection velocity. Later, along with the experimental justification of the similarity of cross-spectra, it was found that this similarity may be violated in the low-frequency range [2–4]. The theoretical studies carried out by Smol'yakov [5] showed that the condition of incompressibility of a medium leads to the fundamental impossibility of the similarity of cross-spectra at $\omega \longrightarrow 0$. Owing to recent progress in experimental and computational methods, it has become possible to measure the cross-spectra of turbulent pressures for a wide range of spacings [6, 7]. Such measurements made the violation of similarity of the cross-spectra even more evident. However, the physical mechanism of this phenomenon is still poorly understood. According to the hypothesis put forward by Farabee and Casarella [6], the deviation from similarity of the cross-spectra is a result of the low-wave-number cutoff of the wavenumber-frequency spectrum of turbulence. Some questions still have to be answered: whether the nature of the similarity is the same for the longitudinal and transverse cross-spectra? What are the factors that determine the damping decre-

1063-7710/00/4603-0348$20.00 © 2000 MAIK "Nauka/Interperiodica"

ment for the cross-spectrum level? Which parameters of the field govern the violation of similarity of the cross-spectra at low frequencies? Is a violation of similarity possible at high frequencies? In this paper, we use the convective field model [8] to answer these questions.

Construction of the model. Let us consider a pair of plane waves at the $x_1 0 x_2$ plane, this pair being an elementary component of the field of wall-pressures in a turbulent boundary layer. Along each wave, the pressure varies according to a harmonic law with the amplitude p_o. The wavelength and the orientation of the waves on the plane are determined by the wave vectors $\mathbf{k}^o = \{k_1^o, k_2^o\}$ and $\mathbf{k}'^o = \{k_1^o, -k_2^o\}$. Both waves are transferred in the aforementioned plane with a fixed convection velocity $\mathbf{U}^o = \{U_1^o, U_2^o\}$. Their transport velocity is assumed to be much less than the sound velocity, so the results should be attributed to incompressible flows. Because of the transference of waves, the pressure p produced at the point $\mathbf{x} = \{x_1, x_2\}$ (in Cartesian coordinates on the plane) will be a function of the spatial coordinates and time t:

$$p(\mathbf{x}, t, \mathbf{k}^o, \mathbf{U}^o) = \frac{1}{2} p_o \{ \exp[i\mathbf{k}^o(\mathbf{x} + \mathbf{U}^o t)] + \exp[-i\mathbf{k}^o(\mathbf{x} + \mathbf{U}^o t)] + \exp[i\mathbf{k}'^o(\mathbf{x} + \mathbf{U}^o t)] + \exp[-i\mathbf{k}'^o(\mathbf{x} + \mathbf{U}^o t)] \}.$$

For this pressure field, we can determine the space-time correlation function

$$R(\boldsymbol{\xi}, \tau, \mathbf{k}^o, \mathbf{U}^o) = \langle p^*(\mathbf{x}, t, \mathbf{k}^o) p(\mathbf{x} + \boldsymbol{\xi}, t + \tau, \mathbf{k}^o) \rangle = \frac{1}{4} p_o^2 \{ \exp[i\mathbf{k}^o(\boldsymbol{\xi} + \mathbf{U}^o \tau)] + \exp[-i\mathbf{k}^o(\boldsymbol{\xi} + \mathbf{U}^o \tau)] + \exp[i\mathbf{k}'^o(\boldsymbol{\xi} + \mathbf{U}^o \tau)] + \exp[-i\mathbf{k}'^o(\boldsymbol{\xi} + \mathbf{U}^o \tau)] \}, \quad (3)$$

where $*$ denotes the complex conjugation, $\langle\ \rangle$ denotes the averaging over time and space for a multiple of the spatial and temporal periods, and the point between the vectors means scalar multiplication. The field components with different wave vectors are statistically orthogonal to each other in the sense that their average products equal zero. Therefore, for more complicated fields consisting of a great or infinite number of wave components, the space-time correlation and other two-point characteristics determined by the Fourier transform can be obtained by the summation or integration over the corresponding characteristics of the elementary pair of waves. Fourier transform (1) of expression (3) yields the cross-spectrum of the pair of pressure waves, which are symmetric about the longitudinal axis and transferred with the velocity $\mathbf{U}^o$:

$$P(\boldsymbol{\xi}, \omega, \mathbf{k}^o, \mathbf{U}^o) = \frac{1}{4} p_o^2 [[\exp[i(k_1^o \xi_1 + k_2^o \xi_2)] \times \delta(\omega - k_1^o U_1^o - k_2^o U_2^o) + \exp[-i(k_1^o \xi_1 + k_2^o \xi_2)] \times \delta(\omega + k_1^o U_1^o + k_2^o U_2^o) + \exp[i(k_1^o \xi_1 - k_2^o \xi_2)] \delta(\omega - k_1^o U_1^o + k_2^o U_2^o) + \exp[-i(k_1^o \xi_1 - k_2^o \xi_2)] \delta(\omega + k_1^o U_1^o - k_2^o U_2^o)], \quad (4)$$

where $\delta(\ldots)$ is the Dirac delta-function. From expression (4), one can easily derive the nondimensional spectrum (2) of the elementary pair of waves for the case of their transfer along the longitudinal axis, i.e., at $U_2^o = 0$. Let us separately consider the longitudinal cross-spectrum ($\xi_2 = 0$)

$$\gamma(\xi_1, 0, \omega, \mathbf{k}^o, U_1^o) = \begin{cases} \exp(i\omega\xi_1/U_1^o) & \text{at } \omega = \pm k_1^o U_1^o \\ 0 & \text{at } \omega \neq \pm k_1^o U_1^o \end{cases} \quad (5)$$

and the transverse spectrum ($\xi_1 = 0$)

$$\gamma(0, \xi_2, \omega, \mathbf{k}^o, U_1^o) = \begin{cases} \cos k_2^o \xi_2 & \text{at } \omega = \pm k_1^o U_1^o \\ 0 & \text{at } \omega \neq \pm k_1^o U_1^o. \end{cases} \quad (6)$$

Although expressions (5) and (6) bear little resemblance to the cross-spectra of the real pressure field in turbulence (they differ from zero at a single frequency and are represented by undamped functions), they suggest some useful conclusions. Firstly, both longitudinal and transverse spectra differ from zero at the same single frequency determined by the longitudinal component k_1^o of the wave vector and by the transport velocity U_1^o. Secondly, expression (5) for the longitudinal spectrum does not contain any transverse components of the initial wave vectors. This means that, in the longitudinal cross-spectrum, the contributions made by the waves with identical longitudinal k_1^o and different transverse k_2^o components are indistinguishable, and the longitudinal spectrum for a set of such waves will be the same as the spectrum for one pair of waves with the same k_1^o. As for the transverse cross-spectrum (6), its form is determined by the transverse components k_2^o of the wave vectors. For several pairs of waves with the same k_1^o and different k_2^o, the form of the transverse

spectrum will depend on the distribution of the field energy in the wave space along the transverse direction.

Let us consider the dependence of the transverse cross-spectrum on the spacing in more detail. We consider a field formed by n pairs of waves with the wave vectors $\mathbf{k}^j = \{k_1^o, \pm k_2^j\}$, $j = 1, 2, \ldots, n$. Without loss of generality, we can assume that the amplitudes of all waves are equal; in this case, the nonuniformity of the field energy distribution in the wave space can be introduced through the nonuniformity of the distribution of the wave vectors over the plane. Then, instead of expression (6), for the nondimensional transverse spectrum of such a field we obtain the expression

$$\gamma(0, \xi_2, \omega, \mathbf{k}^j, U_1^o) = \begin{cases} \frac{1}{n}\sum_{j=1}^{n} \cos k_2^j \xi_2 & \text{at } \omega = \pm k_1^o U_1^o \\ 0 & \text{at } \omega \neq \pm k_1^o U_1^o. \end{cases} \quad (7)$$

If the components k_2^j of the wave vectors are continuously distributed in space, the sum involved in expression (7) can be replaced by an integral:

$$\gamma(0, \xi_2, \omega, k_1^o, U_1^o) = \begin{cases} \int_{-\infty}^{\infty} \cos k_2 \xi_2 W(k_2) dk_2 & \text{at } \omega = \pm k_1^o U_1^o \\ 0 & \text{at } \omega \neq \pm k_1^o U_1^o, \end{cases} \quad (7')$$

where $W(k_2)$ is the probability distribution function describing the distribution of the transverse components in the wave space:

$$\int_{-\infty}^{\infty} W(k_2) dk_2 = 1. \quad (8)$$

To this point, the wave composition of the model field was limited to the components containing only one longitudinal component k_1^o. At a single transport velocity U_1^o, the spectral characteristics of the field were nonzero at a single frequency $\omega = \pm k_1^o U_1^o$, which did not allow us to pose the problem of similarity of the cross-spectra. In what follows, the wave composition of the field will be extended by adding wave components with different longitudinal components k_1. Even if all field components are transported with the same velocity, such a field structure will provide the existence of the field characteristics in a wide frequency range and will allow us to consider the similarity or dissimilarity of the dependences of the cross-spectra on the spacing and frequency.

Similarity of the longitudinal cross-spectrum. Let the projections k_1 of the wave vectors fill the whole longitudinal axis. Every wave number k_1 makes a contribution to the frequency $\omega = \pm k_1 U_1^o$, and the set of frequencies, as well as the set of wave numbers k_1, is everywhere dense. Then, according to expression (5), the longitudinal cross-spectrum will, for all frequencies, have the form

$$\gamma(\xi_1, \omega) = \exp(\pm i k_1 \xi_1) = \exp(i\omega \xi_1 / U_1^o);$$

i.e., it will be similar for the frequency and spacing. We note that, for a field where the projections of the wave vectors on the longitudinal axis form an everywhere dense set only within a segment $k_1' \le \omega \le k_1''$, the longitudinal cross-spectrum has the form

$$\gamma(\xi_1, \omega) = \begin{cases} \exp(i\omega \xi_1 / U_1^o) & \text{at } k_1' U_1^o \le |\omega| \le k_1'' U_1^o \\ 0 & \text{at other } \omega. \end{cases}$$

The latter expression testifies that the similarity of the cross-spectrum occurs only within some limited frequency range. Thus, at a constant convection velocity, for the similarity of the longitudinal cross-spectrum, it is sufficient that the field energy be continuously distributed along the longitudinal (i.e., coincident with the direction of the field transfer) axis of the wave space. Below, it will be shown that this statement is also valid for a variety of transport velocities of the field components with a small dispersion relative to the average value.

Similarity of the transverse spectrum. The conditions of similarity can be most easily determined by using the example of two pairs of coupled waves, one of which is determined by the wave vectors $\mathbf{k}' = \{k_1', \pm k_2'\}$ and the other by the wave vectors $\mathbf{k}'' = \{k_1'', \pm k_2''\}$, so that $k_1' \neq k_1''$. According to expression (6), the transverse cross-spectrum of these waves transferred with the velocity U_1^o has the form

$$\gamma(\xi_2, \omega, \mathbf{k}', \mathbf{k}'') = \begin{cases} \cos k_2' \xi_2 & \text{at } \omega = \pm k_1' U_1^o \\ \cos k_2'' \xi_2 & \text{at } \omega = \pm k_1'' U_1^o \\ 0 & \text{at other } \omega. \end{cases}$$

To judge the similarity of the cross-spectrum, it is necessary that its frequency dependence be an explicit one. We denote $\lambda' = k_2'/k_1'$ and $\lambda'' = k_2''/k_1''$. Then, it is evident that, for a local similarity of the transverse spectrum at these two frequencies, it is sufficient that the equality $\lambda' = \lambda''$ be valid; i.e., that the wave vectors $\mathbf{k}'$ and $\mathbf{k}''$ be collinear. This statement holds for any number of wave vectors. When the longitudinal components

of all wave vectors continuously fill the k_1 axis so that every value of k_1 corresponds to a single pair of vectors $\{k_1, \pm k_2\}$, the transverse spectrum is determined at all frequencies. It has the form

$$\gamma(\xi_2, \omega) = \cos k_2 \xi_2 \quad \text{at} \quad \omega = \pm k_1 U_1^o. \tag{9}$$

However, the similarity of the spectrum will occur only when the wave vectors are collinear. In this case, we have $k_2 = \pm \lambda k_1$, $\lambda = \text{const}$, and, at all frequencies, we obtain

$$\gamma(\xi_2, \omega) = \cos \lambda \omega \xi_2 / U_1^o. \tag{9'}$$

If the wave vectors are collinear but their projections only partially fill the longitudinal axis within the segment $k_1' \le k_1 \le k_1''$, the transverse spectrum will be similar only within a limited frequency range:

$$\gamma(\xi_2, \omega) = \begin{cases} \cos \lambda \omega \xi_2 / U_1^o & \text{at} \quad k_1' U_1^o \le |\omega| \le k_1'' U_1^o \\ 0 & \text{at other} \quad \omega, \end{cases}$$

as in the analogous case for the longitudinal spectrum.

The undamped dependence (9') on the transverse spacing is not typical of turbulent fields. Such a dependence occurs because, at each frequency, the pressure fluctuations are produced by only one pair of waves. As indicated above, the presence of a great number of wave components with a given longitudinal component k_1^o will change the dependence of the transverse spectrum on the spacing, and this dependence will be determined by expression (7) or (7'). Below, we consider two specific examples of the energy distribution in the wave space.

Case 1. We assume that, at every k_1 in the wave space, the energy is uniformly distributed in k_2 within the segment $[-k_2^m, k_2^m]$ and is absent outside this segment, the quantity k_2^m depending on k_1: $k_2^m = k_2^m(k_1)$. The corresponding distribution function has the form

$$W(k_2) = \begin{cases} 1/2k_2^m & \text{at} \quad 0 \le |k_2| \le k_2^m \\ 0 & \text{at} \quad |k_2| > k_2^m. \end{cases}$$

The calculation of the transverse spectrum by formula (7') yields

$$\gamma(\xi_2, \omega) = \begin{cases} \sin(k_2^m \xi_2)/k_2^m \xi_2 & \text{at} \quad \omega = \pm k_1 U_1^o \\ 0 & \text{at} \quad \omega \ne \pm k_1 U_1^o. \end{cases} \tag{10}$$

In contrast to expression (6), the transverse spectrum (10) decreases with increasing spacing ξ_2 but fluctuates near the zero value, which makes it different from the typical dependence for turbulent pressure fields.

Case 2. Now, assume that at every k_1 the energy is uniformly distributed within the angle $0 \le |\theta| \le \theta^m$, where $\theta = \arctan(k_2/k_1)$, and is absent outside this angle; i.e., the distribution function for the angle θ has the form

$$W(\theta) = \begin{cases} 1/2\theta^m & \text{at} \quad 0 \le |\theta| \le \theta^m \\ 0 & \text{at} \quad |\theta| > \theta^m. \end{cases}$$

The corresponding distribution function for the transverse components of the wave numbers can be determined by the formula known from the theory of random functions:

$$W(k_2) = W(\theta) \frac{1}{\left| \frac{dk_2}{d\theta} \right|}$$

$$= \begin{cases} \frac{1}{\theta^m} \frac{k_1}{k_1^2 + k_2^2} & \text{at} \quad 0 \le |k_2| \le k_2^m = k_1 \tan \theta^m \\ 0 & \text{at} \quad |k_2| > k_2^m, \end{cases}$$

which at $\theta^m = \pi/2$ yields

$$W(k_2) = \frac{2}{\pi} k_1 / (k_1^2 + k_2^2). \tag{11}$$

Applying expression (7') to this case, we obtain the transverse spectrum $\gamma(\xi_2, \omega) = \exp(-k_1|\xi_2|)$; since $\omega = \pm k_1 U_1^o$, we obtain the spectrum

$$\gamma(\xi_2, \omega) = \exp(-\omega|\xi_2|/U_1^o). \tag{12}$$

Spectrum (12) has an exponential form that is commonly used in the Corcos model [1]. Thus, the exponential dependence of the transverse spectrum on the spacing is a consequence of a uniform distribution of the wave vectors with the same longitudinal component throughout the directions.

On the basis of the analysis described above, we can determine the general form of the distribution function $W(k_1, k_2)$ that describes the energy distribution in the wave space at which the similarity of the transverse spectrum takes place. The condition of collinearity of the wave vectors requires an affine expansion of the function in proportion to the distance from the origin of coordinates, which, in combination with condition (8), requires a corresponding compression of the function in height. The function satisfying these requirements has the form

$$W(k_1, k_2) = \frac{1}{k_1} W(k_2/k_1). \tag{13}$$

Thus, in a convected field where the distribution of energy in wave numbers is expressed by formula (13),

the transverse cross-spectrum will exhibit similarity. Since the function $W(k_1, k_2)$ has the meaning of the wave-number spectrum, we can conclude that, for the similarity of the transverse cross-spectrum, the wave-number spectrum of the field must have the form determined by expression (13). It is easy to verify that, in the first of the examples presented above, the transverse spectrum (10) will be a similar one only when k_2^m is proportional to k_1. Function (11) from the second example satisfies condition (13), and, hence, spectrum (12) is a similar one. As predicted by Farabee and Casarella [6], in the absence of energy in some region of the wave space, or, more specifically, in the region of longitudinal wave numbers, the similarity of the cross-spectrum is partially violated.

Field model with a random convection velocity. The field model considered above was based on a single transport velocity of the field components. This assumption simplified the analysis and allowed us to derive important qualitative conclusions concerning the conditions of similarity of the cross-spectra. To obtain a closer approximation to the real pressure fields in turbulence, it is necessary to introduce a variety of transport velocities. Let us assume that the transport velocity $\mathbf{U}^o$ of the field components in spectrum (4) is a random variable that takes one or another value with a probability determined by the distribution function $W(\mathbf{U}^o)$. The cross-spectrum of such a field has the form

$$P(\boldsymbol{\xi}, \omega, \mathbf{k}^o) = \int_{-\infty}^{\infty}\int_{-\infty}^{\infty} P(\boldsymbol{\xi}, \omega, \mathbf{k}^o, \mathbf{U}^o) W(\mathbf{U}^o) d\mathbf{U}^o.$$

The specific form of the distribution function is unknown; however, it seems reasonable to use the two-dimensional normal law

$$W(U_1^o, U_2^o) = \frac{1}{2\pi\sigma_1\sigma_2}\exp[-(U_1^o - U_c)^2/2\sigma_1^2] \times \exp(-U_2^{o2}/2\sigma_2^2),$$

where U_c is the average convection velocity, and σ_1^2 and σ_2^2 describe its dispersion in the longitudinal and transverse directions. The adopted distribution law allows the integration of expression (4) by quadratures; as a result, the cross-spectrum of a pair of pressure waves symmetric about the longitudinal axis can be represented in the form

$$P(\boldsymbol{\xi}, \omega, \mathbf{k}^o) = \frac{p_o^2}{2\sqrt{\pi}s}\{\exp(ik_1^o\xi_1) \times \exp[-(\omega - k_1^o U_c)^2/s^2] + \exp(-ik_1^o\xi_1) \times \exp[-(\omega + k_1^o U_c)^2/s^2]\}\cos k_2^o\xi_2, \quad (14)$$

where $s^2 = 2(\sigma_1^2 k_1^2 + \sigma_2^2 k_2^2)$. If instead of one pair of coupled waves, a denumerable set of such pairs is present in the field, the cross-spectrum can be obtained by summing the corresponding expressions (14). For a field with a continuous distribution of energy in the wave numbers, the cross-spectrum can be obtained by defining the parameters k_1^o and k_2^o as random variables with a given probability distribution function $W(k_1^o, k_2^o)$. Then, the cross-spectrum of the field will be obtained by the integration of contributions (14) over the entire wave space with the weight factor $W(k_1^o, k_2^o)$. It can easily be shown that the quantity $(p_o^2/2)W(k_1^o, k_2^o)$ is equivalent to the wave-number spectrum of the field $B(k_1^o, k_2^o)$. Using this result, we obtain the final expression for the cross-spectrum:

$$P(\boldsymbol{\xi}, \omega) = \frac{1}{\sqrt{\pi}}\int_0^{\infty}\int_0^{\infty} B(k_1^2, k_2^2) \times \frac{1}{s}\{\exp(ik_1\xi_1)\exp[-(\omega - k_1U_c)^2/s^2] + \exp(-ik_1\xi_1)\exp[-(\omega + k_1U_c)^2/s^2]\} \times \cos k_2\xi_2 dk_1 dk_2. \quad (15)$$

On the basis of expression (15), a number of nondimensional cross-spectra were calculated with the use of a PC. Before the calculations, a passage to the nondimensional variables was performed: $\bar{\omega} = \omega\delta^*/U_1$, $\bar{U}_c = U_c/U_1$, $\bar{\sigma}_i^2 = \sigma_i^2/U_1^2$, and $\bar{k}_i = \bar{k}_i\delta^*$ ($i = 1, 2$), where δ^* and U_1 are the characteristic scales of length and velocity; e.g., the displacement thickness of the boundary layer and the velocity at its outer boundary. It is assumed that the wave-number spectrum and the cross-spectrum involved in expression (15) are scaled on some characteristic quantities, but the specific values of the latter are unimportant, because they are absent in the final result. The frequency, the spacing, the dispersion of the convection velocity, and the form of the wave-number spectrum of the field were varied in the course of the calculations. The average convection velocity was assumed to be constant and equal to $\bar{U}_c = 0.8$. The dispersion of the convection velocity was assumed to be small: $\bar{\sigma}_1^2$ from 0.0017 to 0.017 and $\bar{\sigma}_2^2$ from 0.0001 to 0.0004.

The integration was performed by the Simpson method within the region $0 \le \bar{k}_1 \le 20$, $0 \le \bar{k}_2 \le 50$ with a precision no lower than 1–2%. The region of the

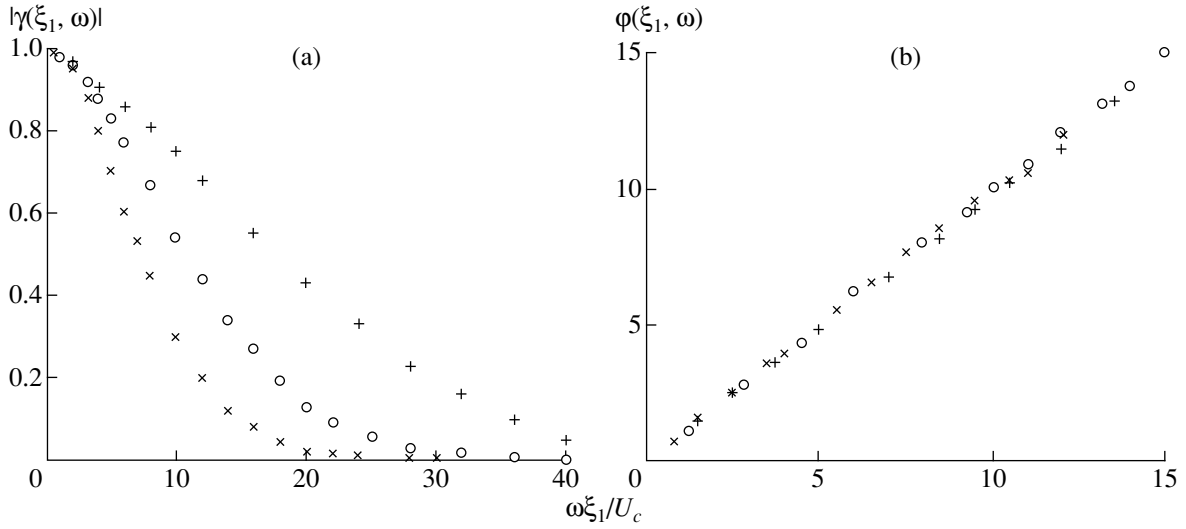

Fig. 1. (a) Absolute value and (b) phase of the longitudinal cross-spectrum at different values of the convection velocity dispersion: $\bar{\sigma}_1^2$ = (○) 0.0170, (+) 0.0065, and (×) 0. 0017; $\bar{\sigma}_2^2$ = 0.0001. The wave-number spectrum is determined by expression (16); $\bar{k}_1^{\min}$ = 0.05 and $\bar{k}_1^{\max}$ = 20.0.

existence of the wave-number spectrum was bounded by the wave numbers $\bar{k}_1^{\min}$ from below and $\bar{k}_1^{\max}$ from above, which made it possible to demonstrate the violation of similarity of the cross-spectra and to avoid the singularity at the origin of coordinates. The wave-number spectrum was determined by the expression

$$\bar{B}(\bar{k}_1, \bar{k}_2) = \begin{cases} \frac{2}{\pi}|\bar{k}_1|/(\bar{k}_1^2 + \bar{k}_2^2) & \text{at } \bar{k}_1^{\min} \le |\bar{k}_1| \le \bar{k}_1^{\max} \\ 0 & \text{at other } k_1. \end{cases} \quad (16)$$

The results obtained by calculating the nondimensional cross-spectra are shown in Figs. 1–3 (the longitudinal spectrum: its absolute value and the phase) and Figs. 4–6 (the transverse spectrum). Figure 1 illustrates the effect of the dispersion of the transport velocity of the field components on the absolute value and the phase of the longitudinal spectrum. When the wave-number spectrum is determined in a wide range of wave numbers ($\bar{k}_1^{\min}$ = 0.05, $\bar{k}_1^{\max}$ = 20.0), the absolute value of the longitudinal cross-spectrum as the function of the phase exhibits the property of similarity at every fixed value of the dispersion of the transport velocity of the field components (Fig. 1a). The calculations were performed for three values of the dispersion of the transport velocity in the longitudinal direction: $\bar{\sigma}_1^2$ = 0.0017, 0.0065, and 0.0170. It was found that the less the dispersion, the less the attenuation of the absolute value of the longitudinal spectrum. This is natural, because, in the case of a zero dispersion, the absolute value of the longitudinal spectrum does not attenuate at all. In contrast to the absolute value, the phase of the cross-spectrum is not affected by the dispersion of the transport velocity, and, for all frequencies and spacings, it is proportional to $\omega\xi_1/U_c$ (Fig. 1b). The low values of the transverse convective velocity dispersion $\bar{\sigma}_2^2$ do not affect the longitudinal spectrum.

Figures 2 and 3 illustrate the violation of similarity of the longitudinal cross-spectrum in the absence of energy in some region of the wave space. If the field contains no wave components with longitudinal components below some $k_1^{\min}$, the violation of similarity occurs at small values of the quantity $\omega\xi_1/U_c$ and, correspondingly, at low frequencies (Figs. 2a, 2b). The absence of the field energy at high wave numbers when k_1 exceeds some $k_1^{\max}$ leads to the violation of similarity at large values of the quantity $\omega\xi_1/U_c$ and, correspondingly, at high frequencies (Figs. 3a, 3b). For both the absolute value and the phase of the cross-spectrum, the violation of similarity is observed as the deviation of the curves from the general law.

Figure 4 displays the transverse cross-spectrum for the field with the wave-number spectrum determined by expression (16) in a wide range of longitudinal wave numbers. According to the results obtained above, the spectrum has an exponential form and is a similar one. We note that the variation in the dispersion of the trans-

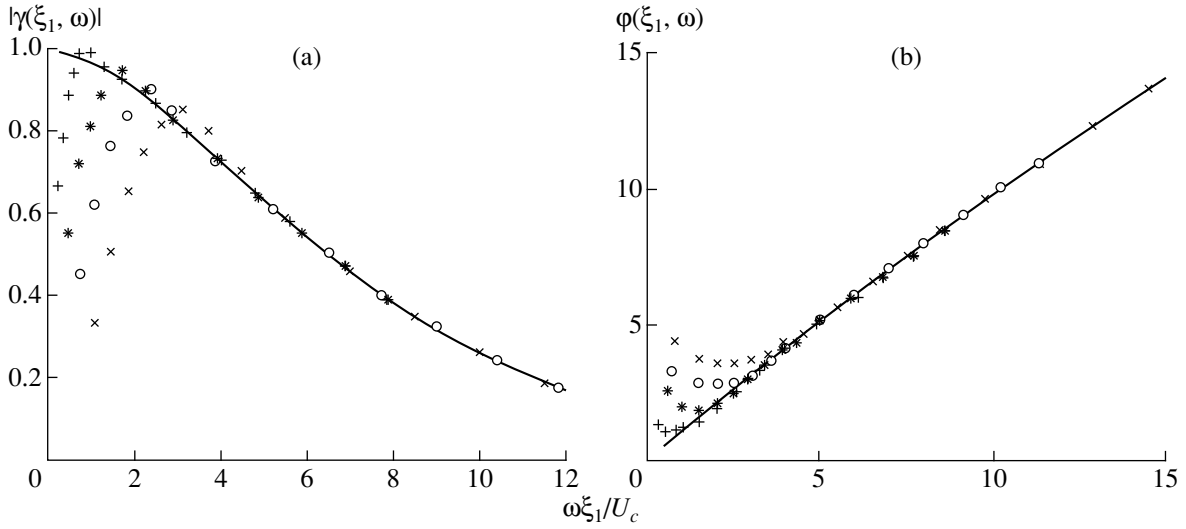

Fig. 2. Violation of similarity of (a) the absolute value and (b) the phase of the longitudinal cross-spectrum at low frequencies in the absence of the field energy in the low-wave-number region. The wave-number spectrum is determined by expression (16); $\bar{k}_1^{\max} = 20.0$; $\bar{\xi}_1$ = (+) 2, (*) 4, (○) 6, and (×) 8 at $\bar{k}_1^{\min} = 0.4$; the solid line corresponds to the same values of $\bar{\xi}_1$ at $\bar{k}_1^{\min} = 0.05$; $\bar{\sigma}_1^2 = 0.017$ and $\bar{\sigma}_2^2 = 0.0001$.

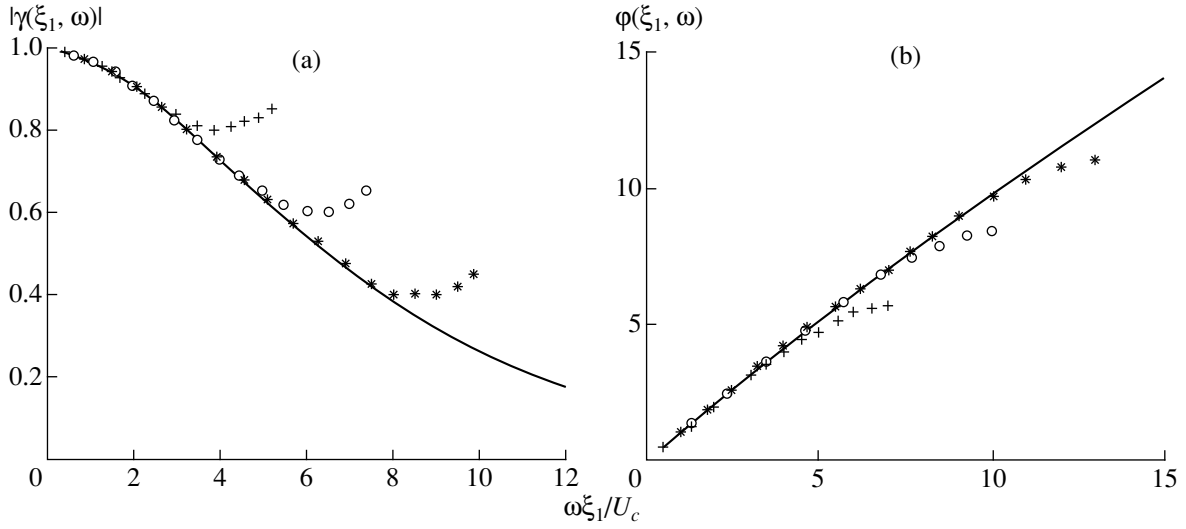

Fig. 3. Violation of similarity of (a) the absolute value and (b) the phase of the longitudinal cross-spectrum at high frequencies in the absence of the field energy in the high-wave-number region. The wave-number spectrum is determined by expression (16); $\bar{k}_1^{\min} = 0.05$; $\bar{\xi}_1$ = (+) 2, (○) 3, and (*) 4 at $\bar{k}_1^{\max} = 3$; the solid line corresponds to the same values of $\bar{\xi}_1$ at $\bar{k}_1^{\max} = 20.0$; $\bar{\sigma}_1^2 = 0.017$ and $\bar{\sigma}_2^2 = 0.0001$.

port velocity of the field components does not affect the value of the transverse spectrum. Figure 5 presents an example of a complete absence of similarity of the transverse spectrum when the wave-number spectrum of the field does not satisfy condition (13). In this case, the wave-number spectrum was set in the form

$$\bar{B}(\bar{k}_1, \bar{k}_2) = \frac{2}{\pi}\bar{k}_1/(\bar{k}_1^2 + \bar{k}_2^4) \qquad (17)$$

at $\bar{k}_1^{\min} < \bar{k}_1 < \bar{k}_1^{\max} = 20.0$. Finally, Fig. 6 shows an example of the violation of similarity of the transverse

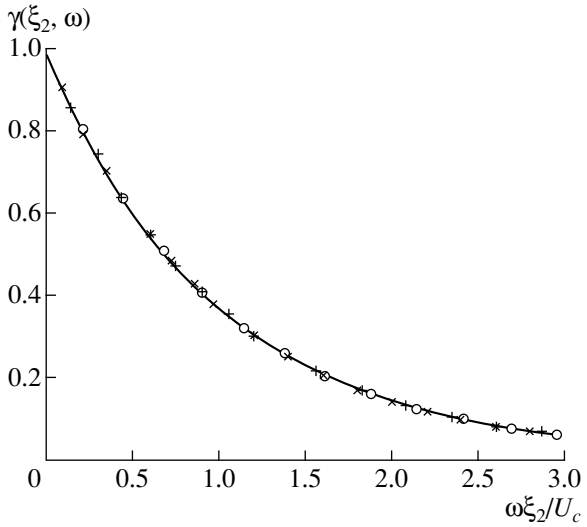

Fig. 4. Similarity of the transverse cross-spectrum and the absence of the dependence on the convection velocity dispersion. The wave-number spectrum is determined by expression (16); $\bar{k}_1^{\min} = 0.05$ and $\bar{k}_1^{\max} = 20.0$; $\bar{\sigma}_1^2 = 0.0017$–$0.0170$; $\bar{\sigma}_2^2 = 0.0001$–$0.0004$; $\overline{\xi_2}$ = (+) 0.1, (○) 0.3, and (×) 0.5; the solid line corresponds to $\exp(-\omega\xi_2/U_c)$.

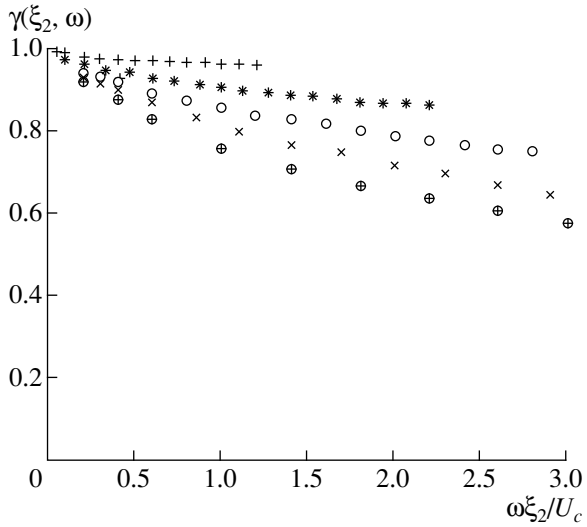

Fig. 5. Absence of similarity of the transverse cross-spectrum when condition (13) imposed on the form of the wave-number spectrum fails. The wave-number spectrum is determined by expression (17); $\bar{k}_1^{\min} = 0.05$ and $\bar{k}_1^{\max} = 20.0$; $\bar{\sigma}_1^2 = 0.017$; $\bar{\sigma}_2^2 = 0.0001$; $\overline{\xi_2}$ = (+) 0.1, (*) 0.2, (○) 0.3, (×) 0.4, and (⊕) 0.5.

spectrum in the low-frequency range when the wave-number spectrum is determined by expression (16), and part of the wave space of the field at low $\bar{k}_1$ contains no energy.

The purpose of this work was the determination of the relation between the structure of the convected field and its cross-spectral characteristics; therefore, it presents no direct comparison of the computational results with the experimental data. However, the qualitative behavior of the calculated dependences agrees well with the known results of the cross-spectral measurements. In closing, we present some additional speculations on the correlation between the results of this study and the properties of real pressure fields in turbulence. It is reasonable to assume that the dispersion of the transport velocity of the pressure field components is closely related to the intensity of the velocity fluctuations in the boundary layer. Therefore, the damping decrement of the absolute value of the longitudinal cross-spectrum should be a function of the Reynolds number. It would appear natural to expect that, in the boundary layer, no components with the wave numbers well below than the inverse of the boundary layer thickness will be present. This leads to the violation of similarity observed in the experiments at low frequencies in both longitudinal and transverse cross-spectra. At the same time, no such limitation exists at high wave numbers. Hence, there is no reason to believe that the similarity of the longitudinal cross-spectrum will be violated at high frequencies. However, the violation of similarity of the transverse spectrum is quite possible, because the conditions of similarity for this spectrum are more rigid, and, hence, they may fail. The speculations described above may be useful for the develop-

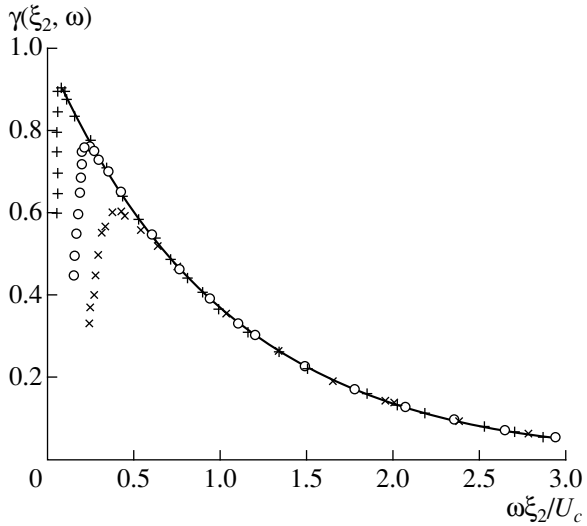

Fig. 6. Violation of similarity of the transverse cross-spectrum at low frequencies in the absence of the field energy in the low-wave-number region. The wave-number spectrum is determined by expression (16); $\bar{k}_1^{\max} = 20.0$; $\bar{\sigma}_1^2 = 0.017$; $\bar{\sigma}_2^2 = 0.0001$; $\overline{\xi_2}$ = (+) 0.1, (○) 0.3, and (×) 0.5 at $\bar{k}_1^{\min} = 0.8$; the solid line corresponds to the same values of $\overline{\xi_2}$ at $\bar{k}_1^{\min} = 0.05$.

ment of new cross-spectrum models that would provide a more adequate description of real processes.

REFERENCES

1. J. M. Corcos, J. Acoust. Soc. Am. **35**, 192 (1963).
2. M. K. Bull, J. Fluid Mech. **28**, 719 (1967).
3. B. M. Efimtsov and S. E. Shubin, Proc. TsAGI (Zhukovskiĭ Central Institute of Aerohydrodynamics, Moscow, 1974), No. 1539.
4. A. V. Smol'yakov and V. M. Tkachenko, Akust. Zh. **37**, 1199 (1991) [Sov. Phys. Acoust. **37**, 627 (1991)].
5. A. V. Smol'yakov, Akust. Zh. **16**, 291 (1970) [Sov. Phys. Acoust. **16**, 241 (1970)].
6. T. M. Farabee and M. J. Casarella, Phys. Fluids A **3**, 2410 (1991).
7. B. M. Abraham and W. L. Keith, Trans. ASME, J. Fluids Eng. **120**, 29 (1998).
8. A. V. Smol'yakov and V. M. Tkachenko, *Measurement of Turbulent Fluctuations* (Énergiya, Leningrad, 1980).

Translated by E.M. Golyamina

Acoustical Physics, Vol. 46, No. 3, 2000, pp. 357–363. Translated from Akusticheskiĭ Zhurnal, Vol. 46, No. 3, 2000, pp. 417–423.

Helmholtz Equation Solutions Corresponding to Multiple Roots of the Dispersion Equation for a Waveguide with Impedance Walls

E. L. Shenderov

Morfizpribor Central Research Institute, Chkalovskiĭ pr. 46, St. Petersburg, 197376 Russia

e-mail: shend@fs.spb.su

Received February 8, 1999

Abstract—The Helmholtz equation solutions corresponding to multiple roots of the dispersion equation are considered for a waveguide with impedance walls. It is shown that in this case the eigenfunctions are determined by expressions that cannot be obtained by the separation of variables. In addition to exponential or trigonometric factors, such functions involve factors linear in coordinates. Equations for calculating the multiple roots are obtained, and the relationships that determine the impedance values at which the multiple roots appear are presented. The Green's function is constructed for the case of the appearance of multiple roots. A plane waveguide and a circular waveguide with axially symmetric modes are considered. © *2000 MAIK "Nauka/Interperiodica".*

An extensive literature (see, e.g., [1–14]) is devoted to the investigation of sound wave propagation in a waveguide with impedance walls. The solutions are usually written as series expansions in normal waves whose eigenvalues, which determine the normal wave velocities, and eigenfunctions are found from the solution to a complex transcendental equation. In papers [10], [13], and [14], it was noted that such equations may have multiple roots. As is shown in [15], such roots can appear for the normal waves in a thin elastic strip. In the case of the appearance of multiple roots, the solutions to the Helmholtz equation involve some additional factors linearly depending on the coordinates. This leads to the nonseparable solutions. We note that the nonseparable solutions to the Helmholtz equation have already been described in the literature [16–19]. However, we found no works describing the specific features of the wave field representation in an impedance waveguide in the presence of multiple roots. In this paper, we analyze some properties of the sound fields in an impedance waveguide in the special case that the above-mentioned equation has multiple roots.

The sound field in a waveguide is usually represented as the superposition of normal waves, which are determined by the separation of variables. A normal wave that propagates in the positive direction along the x axis is represented as the combination of functions that are partial solutions to the Helmholtz equation. For example, for a plane waveguide, this wave has the form

$$\exp(\pm i\beta x/d + ik\gamma y), \tag{1}$$

where x and y are the coordinates along and across the waveguide, respectively; d is the waveguide width; k is the wave number; and $\gamma = \sqrt{1 - \beta^2/(kd)^2}$. The time dependence is taken as $\exp(-i\omega t)$. Such a wave is described by the product of two factors, one of them depending only on x and the other depending only on y. Below, it is shown that, in addition to the separable solutions, nonseparable solutions to the Helmholtz equation are also possible. However, before describing such solutions, we summarize the main properties of the conventional solutions to the Helmholtz equation for a plane waveguide with impedance walls by using the results and notations from the paper [13].

The boundary conditions are written as

$$p = \frac{w_1}{ik}\frac{\partial p}{\partial x}\bigg|_{x = d/2}, \quad p = -\frac{w_2}{ik}\frac{\partial p}{\partial x}\bigg|_{x = -d/2}, \tag{2}$$

where p is the sound pressure in the waveguide, $w_1 = Z_1/\rho c$ and $w_2 = Z_2/\rho c$ are the dimensionless impedances normalized to the wave impedance of the medium ρc, and $k = \omega/c$ is the wave number in the medium. A partial solution to the Helmholtz equation obtained by separation of variables has the form

$$s_n(x, y) = \psi_n(x)\exp(ik\gamma_n y). \tag{3}$$

Here, $\gamma_n = \sqrt{1 - (\beta_n/kd)^2}$ and β_n are the eigenvalues of the nth mode. The function $\psi_n(x)$ is the eigenfunction that satisfies the Helmholtz equation

$$\partial^2\psi_n(x)/\partial x^2 + (\beta_n/d)^2\psi_n(x) = 0 \tag{4}$$

1063-7710/00/4603-0357$20.00 © 2000 MAIK "Nauka/Interperiodica"

and boundary conditions (1). The equation for the eigenvalues is

$$F(\beta) = (u_1 u_2 \beta^2 - 1)\sin\beta - \beta(u_1 + u_2)\cos\beta = 0, \quad (5)$$

where $u_1 = w_1(-ikd)$ and $u_2 = w_2/(-ikd)$. Each eigenvalue is referred to the eigenfunction

$$\psi_n(x) = u_2\beta_n\cos(\beta_n(x/d) + \beta_n/2) + \sin(\beta_n(x/d) + \beta_n/2). \quad (6)$$

The functions $\psi_n(x)$ satisfy the orthogonality condition within the interval $(-d/2, d/2)$

$$\frac{1}{d}\int_{-d/2}^{d/2} \psi_n(x)\psi_m(x)dx = \begin{cases} 0 & \text{at } m \neq n \\ H_n & \text{at } m = n, \end{cases} \quad (7)$$

where H_n is defined as

$$H_n = [1 + u_2 + \beta_n^2 u_2^2 - u_2\cos(2\beta_n) + (\beta_n^2 u_2^2 - 1)\sin(2\beta_n)/(2\beta_n)]/2. \quad (8)$$

Note that, in the integrand of expression (7), the sign of the complex conjuction for one of the functions is absent. The Green's function in the waveguide with the impedance walls is determined by the expansion (see, e.g., [11])

$$G(x, y, x_0, y_0) = \frac{i}{2kd}\sum_{n=1}^{\infty} \frac{\psi_n(x)\psi_n(x_0)}{H_n\gamma_n}\exp(ik\gamma_n|y - y_0|). \quad (9)$$

Consider now the nonseparable solutions to the Helmholtz equation, for example, a function of the form

$$(\pm x - \beta(y/(kdy)))\exp(\pm i\beta x/d + ik\gamma y), \quad (10)$$

which also satisfies the Helmholtz equation. In the latter expression, one needs to take either upper or lower signs. Note that function (10) correct to a constant factor is the derivative of function (1) with respect to the parameter β. Let us introduce a new function $t_q(x, y, \beta_q)$ as the derivative of the function $s_q(x, y, \beta_q)$ with respect to β_q:

$$t_q(x, y, \beta_q) = \frac{\partial s_q(x, y, \beta_q)}{\partial\beta_q} = \left[\frac{\partial\psi_q(x, \beta_q)}{\partial\beta_q} - i\frac{\beta_q y}{kd^2\gamma_q}\psi_q(x, \beta_q)\right]\exp(ik\gamma_q y). \quad (11)$$

We will denote all quantities related to such a solution by the subscript q. Function (11) satisfies the Helmholtz equation, the second term in the square brackets satisfying also boundary conditions (2), since the eigenfunction $\psi_q(x, \beta_q)$ satisfies these conditions. Let us find out in which cases the first term also satisfies these conditions. Denoting this term by $\varphi_q(x)$ and using expression (6), we obtain

$$\varphi_q(x) = \partial\psi_q(x, \beta_q)/\partial\beta_q = u_2\cos(\beta_q x') - u_2\beta_q x'\sin(\beta_q x') + x'\cos(\beta_q x'), \quad (12)$$

where $x' = x/d + 0.5$. It is easy to verify that expression (12) satisfies the second boundary condition (2). Using the first boundary condition (2), we obtain the expression, which coincides with the derivative of function (5) with respect to β. Thus, for function (12) to satisfy the boundary conditions, it is necessary that β_q be a root of the two equations

$$F(\beta_q) = (u_1 u_2 \beta_q^2 - 1)\sin\beta_q - \beta_q(u_1 + u_2)\cos\beta_q = 0,$$
$$\partial F(\beta_q)/\partial\beta_q = \beta_q\sin\beta_q(2u_1u_2 + u_1 + u_2) + \cos\beta_q(u_1u_2\beta_q^2 - u_1 - u_2 - 1) = 0. \quad (13)$$

Because, in this case at $\beta = \beta_q$, not only the function F, but also its derivative becomes zero, β_q is a double root. The corresponding solution to the Helmholtz equation has the form

$$t_q(x, y, \beta_q) = [\varphi_q(x, \beta_q) - i\psi_q(x, \beta_q)\beta_q y/(kd^2\gamma_q)]\exp(ik\gamma_q y). \quad (14)$$

Eigenfunction (14) is the product of the exponential function and an expression involving the x and y coordinates as factors (x enters into this expression as a factor through expression (12)). Thus, eigenfunction (14) is a nonseparable solution.

Consider now the orthogonality relationships connecting the functions ψ_n, ψ_q, and φ_q. Recall that by the subscript n we denote all functions for which β satisfies only the first equation (13), while the functions for which β satisfies both equations (13) are denoted by the subscript q. First of all, we note that H_q vanishes, i.e.,

$$H_q = \frac{1}{d}\int_{-d/2}^{d/2} \psi_q^2(x)dx = 0. \quad (15)$$

This relationship can be derived by two methods: first, by direct integration with allowance for equations (13), and, second, without any integration, taking into account that the equality $H_q = 0$ follows directly from equations (13) if we eliminate u_1 from them and compare the result with expression (8). Thus, the function $\psi_q(x)$ is orthogonal to itself. We note that H_q can vanish in spite of the sign of the squared function in the integrand. This is explained by the fact that the eigenfunctions are complex quantities, and, as it was noted above, the sign of the complex conjugation is absent in the orthogonality relation.

In addition, the following relationships have place

$$\frac{1}{d}\int_{-d/2}^{d/2}\psi_m(x)\psi_n(x)dx = \begin{cases}0 \text{ at } m\neq n \text{ and at } m = n = q\\ H_n\neq 0 \text{ at } m = n\neq q,\end{cases} \tag{16}$$

$$\frac{1}{d}\int_{-d/2}^{d/2}\psi_n(x)\varphi_q(x)dx = \begin{cases}0 \text{ at } n\neq q\\ L_q\neq 0 \text{ at } n = q,\end{cases} \tag{17}$$

$$\frac{1}{d}\int_{-d/2}^{d/2}\varphi_q^2(x)dx = P_q. \tag{18}$$

Here,

$$L_q = [4\beta_q^3u_2^2 + 2\beta_q(\beta_q^2u_2^2-1)\cos(2\beta_q) + (1+4\beta_q^2u_2+\beta_q^2u_2^2)\sin(2\beta_q)]/(8\beta_q^2), \tag{19}$$

$$P_q = [4\beta_q^3(1+3u_2+3u_2^2+\beta_q^2u_2^2) + 6\beta_q(1+2\beta_q^2u_2+\beta_q^2u_2^2)\cos(2\beta_q) + 3(-1+2\beta_q^2+\beta_q^2u_2^2-2\beta_q^4u_2^2)\sin(2\beta_q)]/(24\beta_q^3). \tag{20}$$

Using these relationships, we can write Green's function in a waveguide with impedance walls when one of the roots of equation (5) is multiple. In this case, the normalizing factor H_n in one of the terms in series (9) vanishes. Let us assume that, in a waveguide cross-section $y = y_0$, the distribution of the y-component of the particle velocity has the form of a delta-function

$$v_y = Q\delta(x-x_0)/2, \tag{21}$$

where Q is the strength of the source. Here, we introduced the factor 1/2 for the following reason. Distribution (21) corresponds to a concentrated source, i.e., in the two-dimensional case, to a linear source with the axis normal to the xy-plane and located near an acoustically hard plane. The acoustic pressure is then doubled. However, for calculating Green's function, we need to deem that sound waves are radiated both in positive and negative directions of the y-axis. In other words, the source as though is cut in two by the plane $y = y_0$.

The acoustic pressure generated by a concentrated source is related to Green's function by the relationship

$$p(x, y, x_0, y_0) = -ik\rho cQG(x, y, x_0, y_0). \tag{22}$$

We represent the acoustic field at $y > y_0$ as

$$p(x,y) = \sum_{n=1,\,n\neq q}^{\infty}a_n\psi_n(x)\exp(ik\gamma_n y) + a_q\psi_q(x)\exp(ik\gamma_q y) + b[\varphi_q(x) - i\psi_q(x)\beta_q y/(\gamma_q kd^2)]\exp(ik\gamma_q y), \tag{23}$$

where a_n, a_q, and b are unknown coefficients. From the sum in this expression, we select the term with $n = q$ and add function (14). This yields

$$v_y = \frac{1}{i\omega\rho}\frac{\partial p}{\partial y}\bigg|_{y=y_0} = \frac{1}{\rho c}\sum_{n=1,\,n\neq q}^{\infty}a_n\gamma_n\psi_n(x) \times\exp(ik\gamma_n y_0) + \frac{1}{\rho c}a_q\gamma_q\psi_q(x)\exp(ik\gamma_q y_0) + b\frac{1}{\rho c}\left[\frac{-i\beta_q}{kd^2\gamma_q}\psi_q(x) + \gamma_q\left(\varphi_q(x) - y_0\frac{-i\beta_q}{kd^2\gamma_q}\psi_q(x)\right)\right] \times\exp(ik\gamma_q y) = Q\delta(x-x_0)/2. \tag{24}$$

Let us multiply the left-hand and right-hand sides by $\psi_m(x)$ at $m \neq q$, integrate over the waveguide cross-section, and set $y = y_0$. By virtue of orthogonality relations (16) and (17), only the term with $n = m$ remains in the sum. Then, we obtain

$$a_m = \rho cQ\exp(-ik\gamma_m y_0)\psi_m(x_0)/(2H_m\gamma_m d) \quad \text{at } m\neq q. \tag{25}$$

After this, we multiply the left-hand and right-hand sides of expression (24) by $\psi_q(x)$ and integrate. In this case, all terms of the sum vanish. Then, we obtain

$$b = \rho cQ\exp(-ik\gamma_q y_0)\psi_q(x_0)/(2L_q\gamma_q d). \tag{26}$$

It remains for us to find the coefficient a_q. To do this, we multiply both sides of expansion (24) by $\varphi_q(x, y_0)$ and integrate. Using equalities (16), (17), and (26), we find

$$a_q = \frac{\rho cQ}{2L_q\gamma_q d}\exp(-ik\gamma_q y_0) \times\left[\varphi_q(x_0) - \psi_q(x_0)\left(\frac{\beta_q}{(kd)^2\gamma_q} - \frac{P_q}{L_q} + y_0\frac{i\beta_q}{kd^2\gamma_q}\right)\right]. \tag{27}$$

Using (22), (23), and (25)–(27), we obtain Green's function

$$G(x,y,x_0,y_0) = \frac{i}{2kd}\left\{\sum_{n=1,\,n\neq q}^{\infty}\frac{\psi_n(x)\psi_n(x_0)}{H_n\gamma_n}\exp(ik\gamma_n|y-y_0|) + \frac{\exp(ik\gamma_q|y-y_0|)}{L_q\gamma_q}\left[\psi_q(x)\varphi_q(x_0) + \psi_q(x_0)\varphi_q(x) + \psi_q(x)\psi_q(x_0)\left(\frac{\beta_q}{(kd)^2\gamma_q} - \frac{P_q}{L_q} - |y-y_0|\frac{i\beta_q}{kd^2\gamma_q}\right)\right]\right\}. \tag{28}$$

In the last expression in (28), we replaced $(y - y_0)$ by $|y - y_0|$, so that it would be valid for both $y > y_0$ and $y < y_0$.

Consider now some examples. It is clear that equations (13) cannot simultaneously be satisfied at arbitrary values of u_1 and u_2, but only at some definite relations between them. The algorithm for finding these

The first two double roots of the dispersion equation and the normalized impedances at which the double roots appear (a plane waveguide)

Type of the waveguide	q	β_q	w_1/kd
Symmetric waveguide, $w_1 = w_2 = w$,	1	4.212392 – i 2.250729	0.1478164 + i 0.1184415
Symmetric waves	2	10.712537 – i 3.103149	0.0815858 + i 0.0314714
Symmetric waveguide, $w_1 = w_2 = w$,	1	7.497676 – i 2.768678	0.1067190 + i 0.0543799
Antisymmetric waves	2	13.899960 – i 3.352210	0.0656290 + i 0.0206384
One acoustically soft wall, $w_2 = 0$	1	3.748838 – i 1.384339	0.2134380 + i 0.1087599
	2	6.499799 – i 1.676105	0.1312580 + i 0.0412769
One acoustically hard wall, $w_2 = \infty$	1	2.106196 – i 1.125364	0.2956329 + i 0.2368831
	2	5.356269 – i 1.551574	0.1631717 + i 0.0629429

values is as follows. For a given u_2, we need to solve the equation

$$H_q = [1 + u_2 + u_2^2\beta_q^2 - u_2\cos(2\beta_q) + (u_2^2\beta_q^2 - 1)\sin(2\beta_q)/(2\beta_q)]/2 = 0 \quad (29)$$

for β_q and then find u_1 from any of equations (13). Thus, for a given impedance of one wall, we can find the impedance of the other wall so that the root becomes multiple. The question of the possibility to always find such a value of β_q that would a have physical meaning, as well as the question about the number of possible values of u_1 for one value of u_2, requires further investigation.

For a symmetric waveguide ($u_1 = u_2 = u$), from the second equation (13), we obtain two solutions

$$u = \frac{\cos\beta_q \pm 1}{\beta_q \sin\beta_q}. \quad (30)$$

Substitution of this expression in the first equation (13) yields two equations

$$\sin\beta_q = \mp\beta_q. \quad (31)$$

In expressions (30) and (31), one needs to take simultaneously either the upper or the lower signs. The upper signs correspond to symmetric waves, while the lower signs refer to antisymmetric waves. Besides the trivial solution $\beta_q = 0$, equations (31) have a number of other solutions. The first two of them are given in the table. Using the values of β_q, from formulas (30) we can find such values u at which multiple roots exist. In a similar way, for a waveguide with one acoustically soft wall ($u_2 = 0$), we obtain the equation

$$\sin(2\beta_q) = 2\beta_q \quad (32)$$

and the formula for determining the impedance

$$u_1 = -\tan\beta_q/\beta_q. \quad (33)$$

For a waveguide with one acoustically hard wall ($u_2 = \infty$), we obtain

$$\sin(2\beta_q) = -2\beta_q \quad (34)$$

and

$$u_1 = \cot\beta_q/\beta_q. \quad (35)$$

Let us represent expression (30) as

$$u = \cot(\beta_q/2)/\beta_q, \quad u = -\tan(\beta_q/2)/\beta_q, \quad (36)$$

where the first formula refers to symmetric waves in a symmetric waveguide and the second formula refers to antisymmetric waves in the same waveguide. Comparing expressions (31), (32), and (34), we find that the multiple root values corresponding to the symmetric waves in a symmetric waveguide equal doubled values of the roots for the waveguide with an acoustically hard wall, while the roots for the antisymmetric waves in a symmetric waveguide equal doubled values of the roots for a waveguide with an acoustically soft wall. The values of the impedances at which multiple roots appear for a symmetric waveguide are less by a factor of 2 than the corresponding values for the waveguides with one acoustically hard or acoustically soft wall.

The values of the first two multiple roots and the corresponding impedances for the above-mentioned cases are given in the table.

In paper [13] for the waveguide with one acoustically hard wall with $kd = 5$, the impedance value, at which the multiple root $w_1 = 1.47816 + i1.18441$ appears, was presented. The value $w_1/(kd) = 0.29563 + i0.23688$ almost coincides with that presented in the table.

Figure 1 exhibits the behavior of the eigenvalues of two modes for the wall impedances that satisfy the condition of multiple root appearance. The curves for the imaginary parts of $\beta_{1,2}$ (Fig. 1b) intersect, while the curves for the real parts in Fig. 1a are only tangent to one another at the point corresponding to the appearance of the multiple root. For the given impedance values, the multiple root appears at $kd = 1$. Note that if both curves in Fig. 1a were drawn by solid lines, they might seem to intersect. Even small changes in the impedance values lead to that the real parts of β_1 and β_2 are no longer tangent to one another (Figs. 1 c, 1d).

Figure 2 shows the dispersion curves for the same modes as in Fig. 1. The dispersion curves intersect, but,

passing through the point $kd = 1$, the modes switch places. As an illustration, the upper and lower parts of Fig. 2 exhibit the modes $\psi_{1,2}(x)$ corresponding to different points of the dispersion curves. As is seen, the modes with monotone amplitude variations correspond to the points *a*, *b*, and *c*, the point *c* lying on the dotted line rather than on the solid line. Similarly, a mode with the amplitude oscillating along the *x* coordinate passes from the dotted line to the solid line.

A wave corresponding to the multiple root can be considered as a result of the interference of two normal waves with very close phase velocities.

The question as to whether to introduce or not an additional function $t_q(x, y)$ in the field expansion depends on the desired accuracy of calculations. To answer this question, we present the following reasoning. If we need to calculate the difference $f(x + \varepsilon) - f(x)$, where $\varepsilon \ll x$, we can do it by the direct calculation of this difference when the accuracy of the calculation is high enough. However, such a calculation is related to loss in accuracy. Therefore, if the accuracy is insufficient, we can calculate the quantity $\varepsilon df(x)/dx$ instead. In this case, the calculations may be performed with lower accuracy. The eigenfunctions of the type (6) may be calculated by a similar method in the vicinity of the parameter values u_1 and u_2 at which the multiple root appears. However, in this case, a loss in accuracy is possible. Using expansion (28) instead of (9), such a loss can be avoided.

From the above results, it follows that multiple roots appear only for some particular values of the complex impedances of the walls. In practice, the probability that in real problems the impedances will take precisely these values is very low. The question arises as to how much the impedances must differ from the above-mentioned values to make the introduction of the additional function $t_q(x, y)$ in expansion (9) unnecessary. In the example, shown in Fig. 1, it was sufficient to introduce a change in the third decimal place in the imaginary part of the impedance to obtain a noticeable difference in the values of β for different modes.

We consider now a circular waveguide and restrict ourselves to the axially symmetric modes. For a circular waveguide with an impedance inner surface, the partial solution to the Helmholtz equation satisfying the boundary condition

$$p = \frac{w}{ik}\frac{\partial p}{\partial r}\bigg|_{r=a} \tag{37}$$

has the form

$$s_n(r, y) = J_0(\beta_n r/a)\exp(ik\gamma_n y). \tag{38}$$

In what follows, $\gamma_n = \sqrt{1 - \beta_n^2/(ka)^2}$, $w = Z/(\rho c)$, $u = w/(-ika)$, and β_n is the root of the equation

$$F(\beta) = J_0(\beta) - u\beta J_1(\beta) = 0. \tag{39}$$

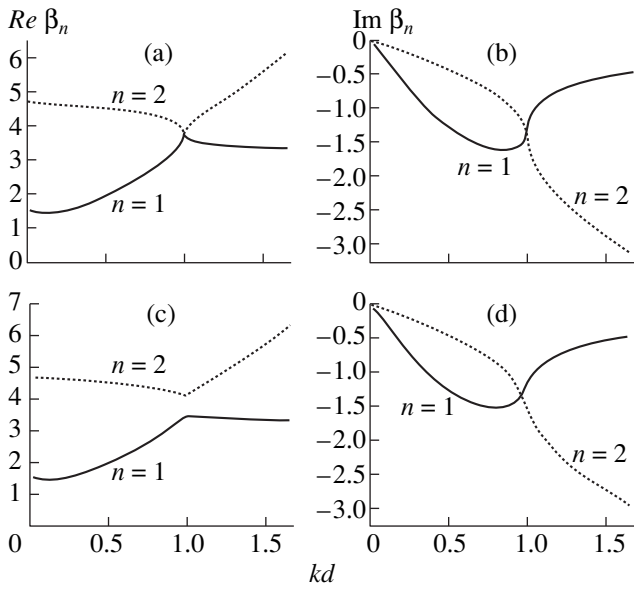

Fig. 1. Eigenvalues versus *kd* for two modes in the vicinity of the value $kd = 1$ corresponding to the double root for $w_2 = 0$; (a, b) $w_1 = 0.2134380 + i0.1087599$; (c, d) $w_1 = 0.2134380 + i0.1$.

Besides solution (38), there exists another solution

$$t_q(r, y) = \partial s_q/\partial\beta = [\varphi(r) - \psi(r)i\beta_q y/ka^2\psi_q], \tag{40}$$

where

$$\psi(r) = J_0(\beta_q r/\alpha);$$
$$\varphi(r) = \partial\psi/\partial\beta = -J_1(\beta_q r/a)r/a. \tag{41}$$

The function $\psi(r)$ satisfies condition (37). The function $\varphi(r)$ satisfies this boundary condition if β_q is the root of the equation

$$\partial F/\partial\beta = -(J_1(\beta) + u\beta J_0(\beta)) = 0. \tag{42}$$

Thus, β_q is the double root of equation (39). Eliminating *u* from equations (39) and (42), we obtain the equation for determining the multiple roots

$$J_0^2(\beta) + J_1^2(\beta) = 0. \tag{43}$$

As before, we will denote the multiple roots by the index *q*. Using equation (39), we obtain the impedance values at which multiple roots appear

$$w = -ikaJ_0(\beta_q)/(\beta_q J_1(\beta_q)). \tag{44}$$

We present the values of the two first roots of equation (43) and the respective values of the normalized impedances

$$\beta = 2.98038241 - i\ 1.27960254,$$
$$w = (0.28330464 + i\ 0.12163450)ka;$$
$$\beta = 6.17515307 - i\ 1.61871738,$$
$$w = (0.15152723 + i\ 0.03972043)ka.$$

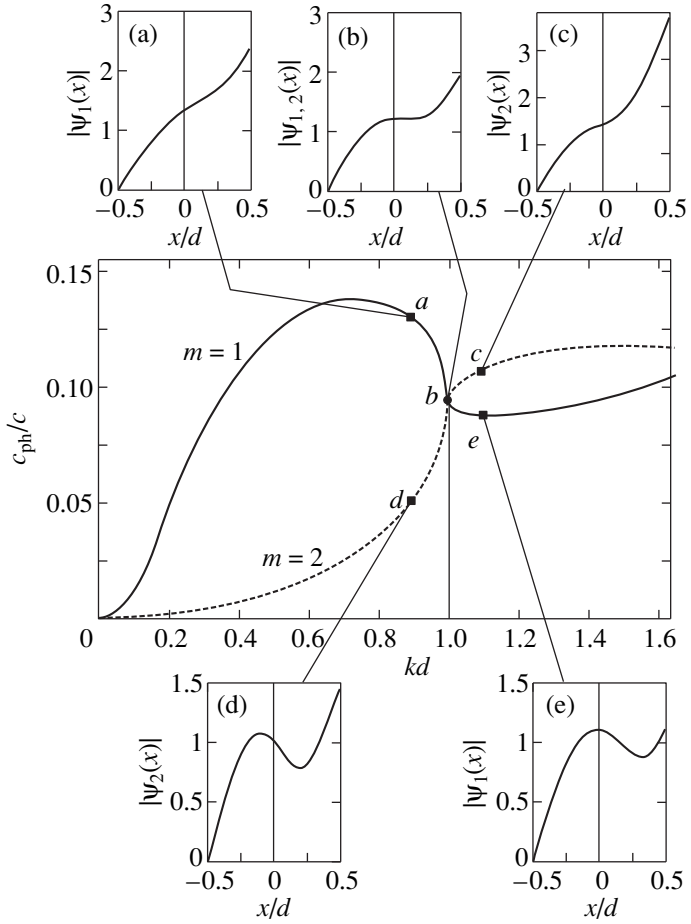

Fig. 2. Dispersion curves for two modes in the vicinity of the value $kd = 1$ corresponding to the double root for $w_2 = 0$ and $w_1 = 0.2134380 + i0.1087599$. The middle part of the figure exhibits the dispersion curves; the upper and lower parts exhibit the acoustic pressure distribution over the waveguide width, i.e., the absolute values of the eigenfunctions.

The functions φ and ψ satisfy the following relations of the orthogonality and normalization:

$$\int_0^a \psi_n(r)\psi_m(r)rdr = \begin{cases} 0 \text{ at } n \neq m \text{ at } n = m = q \\ a^2 H_n \text{ at } n = m \neq q, \end{cases} \quad (45)$$

where

$$H_n = [J_0^2(\beta_n) + J_1^2(\beta_n)]/2. \quad (46)$$

Note that H_n vanishes for $n = m = q$, i.e., the function $\psi_q(r)$ is orthogonal to itself,

$$\int_a^0 \varphi_n(r)\psi_q(r)rdr = \begin{cases} 0 \text{ at } n \neq q \\ a^2 L_q \text{ at } n = q, \end{cases} \quad (47)$$

$$\int_0^a \varphi_q^2(r)rdr = a^2 P_q, \quad (48)$$

where

$$L_q = -[J_0(\beta_q)J_1(\beta_q) + J_1(\beta_q)J_2(\beta_q)]/(4\beta_q), \quad (49)$$

$$P_q = [J_1^2(\beta_q) + J_2^2(\beta_q)]/(6\beta_q). \quad (50)$$

The Green's function for the axially symmetric case (i.e, one of the corresponding points lies on the axis) is determined by expression (28) where one has to replace x by r, d by a, and use relationships (41), (46), (49), and (50).

ACKNOWLEDGMENTS

This work was supported by the Russian Foundation for Basic Research, project no. 98-02-16017

REFERENCES

1. N. N. Andreev, Izv. Akad. Nauk SSSR, Ser. Fiz., No. 5, 625 (1936).
2. Ph. M. Morse, J. Acoust. Soc. Am. **11**, 205 (1939).
3. L. Cremer, Akustische Beihefte, Acustica **3** (2), 249 (1953).

4. A. D. Lapin, Akust. Zh. **36**, 375 (1990) [Sov. Phys. Acoust. **36**, 209 (1990)].
5. A. D. Lapin, Akust. Zh. **37**, 581 (1991) [Sov. Phys. Acoust. **37**, 302 (1991)].
6. A. D. Lapin, Akust. Zh. **22**, 400 (1976) [Sov. Phys. Acoust. **22**, 224 (1976)].
7. A. D. Lapin, Akust. Zh. **21**, 215 (1975) [Sov. Phys. Acoust. **21**, 136 (1975)].
8. A. D. Rawlins, Proc. R. Soc. **A-361**, 65 (1978).
9. A. Cabelly, J. Sound Vibr. **103**, 13 (1985).
10. Yu. A. Lavrov, Akust. Zh. **36**, 308 (1990) [Sov. Phys. Acoust. **36**, 167 (1990)].
11. Ph. M. Morse and K. U. Ingard, in *Handbook of Physics* (Springer, Berlin, 1961), Vol. 11/1, pp. 1–128.
12. M. A. Isakovich, *General Acoustics* (Nauka, Moscow, 1973).
13. E. L. Shenderov, Akust. Zh. **45**, 661 (1999) [Acoust. Phys. **45**, 589 (1999)].
14. B. J. Tester, J. Sound Vibr. **23**, 477 (1973).
15. Yu. I. Bobrovnitskiĭ, Akust. Zh. **23**, 34 (1977) [Sov. Phys. Acoust. **23**, 18 (1977).
16. Yu. P. Lysanov, in *Proceedings of the 6th All-Union Acoustical Conference* (Acoustics Institute, Moscow, 1968), Section A.
17. F. E. Grigoryan, Akust. Zh. **20**, 214 (1974) [Sov. Phys. Acoust. **20**, 132 (1974)].
18. D. S. Moseley, Quart. Appl. Math. **27**, 451 (1970).
19. A. Chakrabarti, J. Math. Analysis Appl. **42**, 198 (1973).

Translated by Yu.P. Lysanov

Acoustical Physics, Vol. 46, No. 3, 2000, pp. 364–366. Translated from Akusticheskiĭ Zhurnal, Vol. 46, No. 3, 2000, pp. 424–426.

SHORT COMMUNICATIONS

Experimental Study of the Vibration Characteristics of Railroad Ties

N. A. Vasil'ev and S. I. Dvornikov

Andreev Acoustics Institute, Russian Academy of Sciences, ul. Shvernika 4, Moscow, 117036 Russia

e-mail: bvp@akin.ru

Received December 30, 1998

Abstract—Vibration characteristics of railroad ties are investigated by the method of shock excitation. The feasibility of estimating the quality of railroad tracks from the harmonic analysis of these vibrations is demonstrated. © *2000 MAIK "Nauka/Interperiodica".*

Monitoring the condition of railroad tracks is essential for maintaining trouble-free operation of railroads. Well-timed detection and elimination of defects of tracks is not only profitable from an economical point of view, but also assures the safety of this kind of transportation.

It is known that the quality of tracks largely depends on the tightness of contact between the ties and ballast, which serves as a damper and usually consists of a layer of crushed stone 20–30 cm thick. Today's methods of track monitoring do not always make it possible to detect in time the ties hanging on rails, due to subsidence of the ballast.

In routine maintenance work, the detection of gaps between the ties and the ballast is carried out by a special-purpose train. While the train is moving along the rails, it detects the tie deflection under a known load. This method requires a specially equipped heavy-loaded train and an interruption in the railway traffic for the time of measurements. In the opinion of specialists, this method does not always provide an exact estimate of the quality of the contact between the ties and the ballast.

In this paper, we propose a simple method of detecting ties that have lost tight contact with the ballast and are hanging on the rails. This method is based on a shock excitation of tie vibrations, a remote recording of vibrations by an acoustic microphone, and a subsequent harmonic analysis of the signal.

The railroad track is usually considered as a distributed elastic system contacting with an elastic base [1, 2]. The dynamics of this system depends not only on the elastic parameters of the ties and rails, their dimensions, the density of materials and the way of their fastening, but also on the properties of the elastic base, such as its density, coefficient of restitution, coupling constant, and coefficient of external friction. Evidently, for the parts of the track where the ties are not in tight contact with ballast or even hang above it, some of these characteristics will differ from the values and properties of the corresponding characteristics for tracks with a tight contact. It is reasonable to expect that this difference will lead to a change in the amplitude-frequency characteristic of the track vibration.

An efficient method widely used for studying the amplitude-frequency characteristics of mechanical systems is the method of shock excitation, with subsequent recording and analysis of the excited vibrations [3]. In this process, the amount of energy spent for vibration and its spectral components depends in a complicated way on the mass, the material, and the form of the impact tool, the ratio of the initial velocity of impact tool to the sound velocity in the system, the mass of the system, the properties of the surface at the impact site, and the place of the latter in the system.

The experimental studies of the vibration processes generated in reinforced concrete ties by shock excitation were carried out at a railroad testing ground. The vibrations were detected by RFT vibration transducers attached to the tie and also by a remote method with the use of a Bruel and Kjaer capacitor microphone. The signals were recorded by a multichannel magnetograph and subjected to computer processing in laboratory conditions.

For the excitation of vibrations in ties, we used steel impact tools of mass from 200 g to 4 kg. In the experiments, it was found that the fundamental frequency of vibration of a tie fastened to the rail track was most efficiently excited by an impact tool of mass no less than 1 kg, on the condition that the impact occurred at the center or at the end of the tie.

If we consider a tie fastened to a massive rail track as a beam hinged at two points (Fig. 1), then, neglecting the elasticity of the rail track, we can expect that the main mode of its vibration will be a symmetric periodic motion about the points of fastening. The ends of the tie and its center have maximum amplitudes and are the points of the most efficient excitation of this type of

1063-7710/00/4603-0364$20.00

vibration. The frequency of vibration is determined by the well-known relation [4, 5]

$$w = \frac{\pi^2}{l^2}\left(\frac{EJ}{m}\right)^{1/2}, \quad (1)$$

where E is Young's modulus, J is the moment of inertia with respect to the tie center line, l is the track gauge, and m is the tie mass per unit length.

The objective of the experiments was to study the dynamics of the changes in the amplitude-frequency characteristic of the tie vibration with a decrease in the area of contact between the tie and the ballast. For this purpose, we initially chose an arbitrary tie, which was in tight contact with the ballast, and measured its vibration generated by impacts at various points. Then, the tie was undermined on one end for 1/8 of its length, and the measurements were repeated. The subsequent measurements were carried out with the tie undermined for 1/4 and 1/3 of its length. In addition, at a certain distance from this tie, six successive ties were chosen for which similar measurements were performed. However, these ties were not undermined, and the measurements were aimed at gathering some statistical data.

Figure 2 shows the power spectra of the signals detected by the capacitor microphone after the shock excitation of the ties. The spectra are averaged over ten realizations and displayed in dimensionless values on a linear scale along the ordinate axis for the following cases: (a) a tie in tight contact with the ballast, (b) a tie with ballast removed for 1/8 of its length, (c) a tie with the ballast removed for 1/4 of its length, (d) a tie with ballast removed for 1/3 of its length, and (e) a power spectrum averaged over six ties being in tight contact with the ballast.

It is seen that, when a tie is in tight contact with the ballast, the spectrum of its vibration is practically uniform with quasi-discrete components in the frequency range from 50 to 1000 Hz.

However, even slight, for 1/8 of its length, release of the tie from the contact with the ballast results in the appearance of a spectral component with a frequency of about 100 Hz and a power far exceeding all other components.

An increase in the length of undermining to 1/4 and 1/3 of the tie length makes this effect more pronounced with the aforementioned spectral maximum being shifted toward lower frequencies.

It should be noted that, by simply listening to the strokes on ties, it is possible to detect the change in sound when there is a hollow under a tie. The change consists in the appearance of a specific "hollow" sound and may be explained by the presence of intense components in the low-frequency part of the spectrum.

The calculations by equation (1) confirm that the frequency of about 100 Hz is the fundamental frequency of vibration of a tie considered as a beam hinged at two points. As is shown in [5], when such a

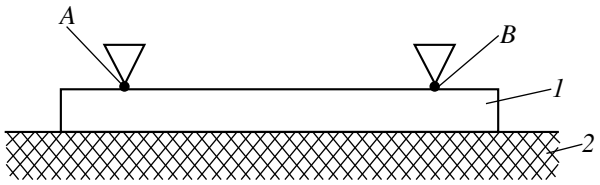

Fig. 1. Representation of a railroad tie fastened to the rail track and lying on the ballast as (*1*) an elastic beam hinged at the points *A* and *B* and (*2*) lying on an elastic base.

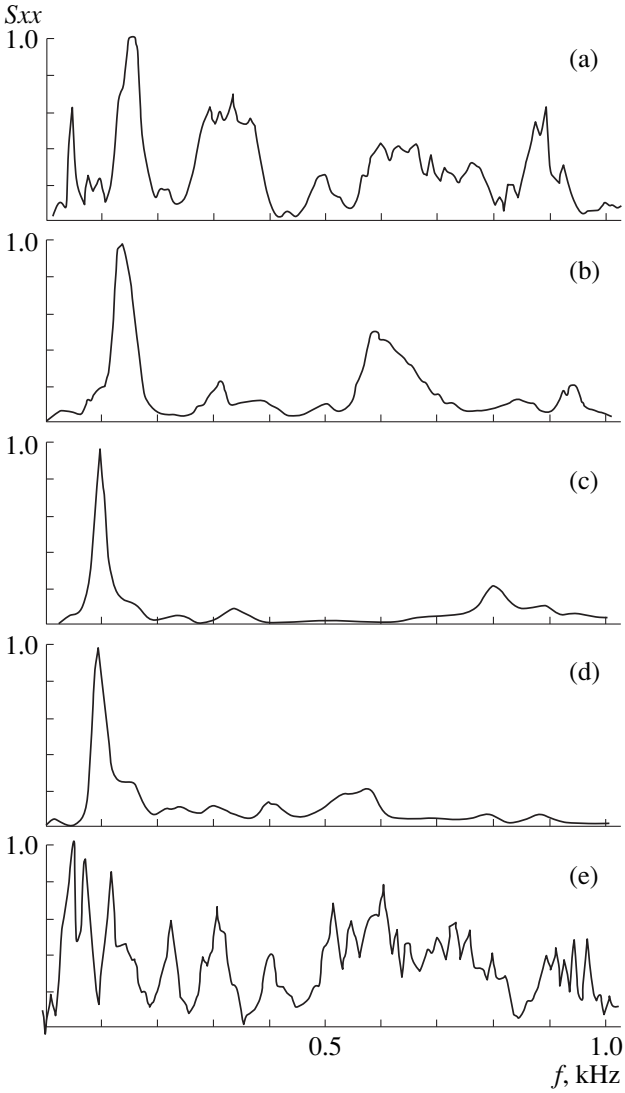

Fig. 2. Power spectra of the railroad tie vibrations for various areas of contact with the ballast.

beam lies on an elastic base, its fundamental frequency is determined by the formula

$$w = \left[\left(\frac{\pi^4 EJ}{l^4} + K_0\right)\frac{1}{m}\right]^{1/2}, \quad (2)$$

where K_0 is the stiffness coefficient of the base and other parameters are the same as in relation (1).

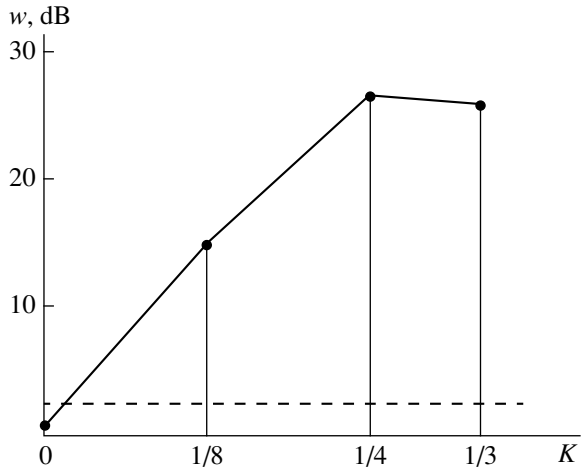

Fig. 3. Dependence of the energy of the fundamental mode of tie vibrations on the quantity K characterizing the loss of contact between tie and the ballast.

As is seen from (2), the reduction in K_0 (in our case, it corresponds to the increase in the area of undermining under a tie) must lead to a decrease in the fundamental frequency, which was observed in the experiment. If we perform the integration of the power spectra presented in Fig. 2 over some frequency band Δf, the resulting quantity may be interpreted as the energy of the tie vibration in this frequency band.

Figure 3 shows the change in the energy of the tie vibration at a frequency of 100 Hz in a 40-Hz frequency band as a function of the degree of its release from the contact with the ballast. The dashed line shows the averaged energy of vibration for ties being in tight contact with the ballast for the same frequency range. It is seen from the figure that the ratio of energies changes from $\simeq 12$ dB, which corresponds to the case of the loss of contact with the ballast within 1/8 of the tie length, to $\simeq 25$ dB for the loss of contact within 1/4 of the tie length.

Thus, the performed experimental study shows that, when a tie is in tight contact with the ballast, the fundamental frequency of its vibration, which is about 100 Hz, is damped by the ballast and practically not excited by impact. The loss of contact with the ballast results in the appearance of the fundamental frequency in the spectrum of the tie vibrations. This effect can be used as the basis for estimating the quality of the contact between the ties and the ballast in railroad tracks.

ACKNOWLEDGMENTS

We thank V.A. Aleksashenko from GOS NII RTI for organizing the field measurements and R.Yu. Popov, E.V. Simakina, and I.I. Baranova from the Andreev Acoustics Institute for helpful remarks and discussion of the results.

REFERENCES

1. A. P. Filippov, *Vibrations of Deformable Systems* (Mashinostroenie, Moscow, 1970).
2. L. Gry, J. Sound Vibr. **195**, 477 (1996).
3. Lin Viching, Lai Wei-Kuang, and Lin Kuo-Lung, J. Acoust. Soc. Am. **103**, 1468 (1998).
4. K. T. Chan, T. P. Leung, and W. O. Wong, J. Sound Vibr. **191**, 590 (1996).
5. Yu. N. Novichkov and D. A. Grishin, Prikl. Mekh. **24** (3), 91 (1988).

Translated by A.V. Svechnikov

Acoustical Physics, Vol. 46, No. 3, 2000, pp. 367–369. Translated from Akusticheskiĭ Zhurnal, Vol. 46, No. 3, 2000, pp. 427–429.

SHORT COMMUNICATIONS

Radiation Impedance of a Piston in a Waveguide

A. D. Lapin

Andreev Acoustics Institute, Russian Academy of Sciences, ul. Shvernika 4, Moscow, 117036 Russia

e-mail: bvp@akin.ru

Received March 25, 1999

Abstract—The radiation of a piston in a rectangular waveguide whose wall is a baffle for the piston is considered. Simple asymptotic formulas for the real and imaginary parts of the piston radiation impedance are derived. © *2000 MAIK "Nauka/Interperiodica".*

Efficiency of a radiator is usually characterized by its radiation impedance [1, 2]. It depends not only on the radiator design, but also on the medium in which it operates. The impedance of a particular radiator operating in a free medium is significantly different from that in a waveguide [3]. In a waveguide, the radiator impedance increases without limit when the sound frequency approaches one of the waveguide critical frequencies. In order to calculate the impedance of a radiator in a waveguide, it is necessary to solve a complex diffraction problem of finding the field at the surface of this radiator [4–6]. At present, the radiation impedance is calculated only for the simplest radiators—a piston in a rectangular waveguide [7] and a ring transducer in a circular waveguide [8]. The exact formulas obtained contain infinite sums and take into account the contribution of all normal waveguide modes. For practical purposes, simple asymptotic formulas that allow one to approximately estimate the impedance of the radiator are necessary. Below, we derive such asymptotic formulas for the real and imaginary parts of the radiation impedance for a piston in a rectangular waveguide.

Consider a rectangular waveguide with perfectly rigid walls. Choose a Cartesian coordinate system such that two waveguide walls are coincident with the coordinate planes $y = 0$ and $z = 0$. Denote the side lengths of the waveguide cross-section by H_y and H_z. The lower wall ($z = 0$) contains a rectangular opening ($|x| < L$, $0 < y < H_y$), into which a piston with an area $S_0 = 2LH_y$ is inserted without a clearance. The piston oscillates harmonically with a velocity $u\exp(-i\omega t)$. It is necessary to find the radiation impedance of this piston.

Denote the sound pressure in the waveguide by p. Using the standard Fourier method [4], one can obtain the following integral representation for p:

$$p(x, z) = i\omega\rho\frac{u}{\pi} \times \int_{-\infty}^{\infty} \frac{\sin(\xi L)\cos[\sqrt{k^2 - \xi^2}(H - z)]}{\xi\sqrt{k^2 - \xi^2}\sin[\sqrt{k^2 - \xi^2}H]}\exp(i\xi x)d\xi,$$

where $H = H_z$, $k = \omega/c$, and ρ and c are the density of the medium filling the waveguide and the sound velocity in it, respectively; the $\exp(-i\omega t)$ time dependence is omitted. Using the residue theory, we obtain the expressions

$$\begin{aligned} p(x, z) &= 2\omega\rho u\sum_{n=0}^{\infty}\frac{\sin(\xi_n L)}{\theta_n\xi_n^2 H} \\ &\times \exp(i\xi_n|x|)\cos(\zeta_n z), \quad |x| \geq L, \\ p(x, z) &= i\omega\rho u\left\{\frac{\cos[k(H - z)]}{k\sin(kH)} - 2\sum_{n=0}^{\infty}\frac{\exp(i\xi_n L)}{\theta_n\xi_n^2 H}\right. \\ &\left.\times \cos(\xi_n x)\cos(\zeta_n z)\right\}, \quad |x| \leq L, \end{aligned} \tag{1}$$

where

$$\zeta_n = n\pi/H, \quad \xi_n = \sqrt{k^2 - \zeta_n^2},$$
$$\theta_0 = 2, \quad \theta_n = 1 \text{ at } n \neq 0.$$

The sound field acts upon the piston with the force

$$F = \iint_{S_0} p(x, 0)dxdy. \tag{2}$$

The ratio of this force to the piston velocity is referred to as the radiation impedance Z. By virtue of formulas (1) and (2), we obtain the following expression:

$$Z = F/u = i\rho c S_0\left\{\cot(kH)\right.$$
$$\left. + \sum_{n=0}^{\infty}\frac{2k}{\theta_n\xi_n^2 H}\frac{\sin(\xi_n L)}{(\xi_n L)}\exp(i\xi_n L)\right\}.$$

1063-7710/00/4603-0367$20.00

The real and imaginary parts of the radiation impedance are as follows:

$$R = \mathrm{Re}\,z = \rho c S_0^2/S \sum_{n=0}^{N-1} \frac{k}{\theta_n \xi_n} \frac{\sin^2(\xi_n L)}{(\xi_n L)^2},$$

$$X = \mathrm{Im}\,z = \rho c S_0 \Bigg\{ \cot(kH) - \sum_{n=0}^{N-1} \frac{2k}{\theta_n \xi_n^2 H} \frac{\sin(\xi_n L)}{(\xi_n L)} \cos(\xi_n L) + \sum_{n=N}^{\infty} \frac{2k}{\theta_n \kappa_n^2 H} \frac{\sinh(\kappa_n L)}{(\kappa_n L)} \exp(-\kappa_n L) \Bigg\}, \quad (3)$$

where $\kappa_n = i\xi_n = \sqrt{\zeta_n^2 - k^2}$, $S_0 = 2LH_y$ and $S = H_y H_z$ are the areas of the piston and waveguide cross-sections, respectively; and N is the number of homogeneous modes in a two-dimensional waveguide (layer) of width H.

The quantity R is called the radiation resistance; the piston radiation power averaged over a period is equal to $1/2Ru^2$. In a single-mode waveguide ($kH < \pi$), the radiation resistance is equal to $\rho c S_0^2/(2S)\sin^2(kL)/(kL)^2$. The radiation resistance of a narrow piston ($2kL \ll 1$) at any kH can be calculated from the formula

$$R = \rho c S_0^2/S \sum_{n=0}^{N-1} k/(\theta_n \xi_n). \quad (4)$$

Assume that the following conditions are valid: $2kL \ll 1$ and $kH \gg \pi$ (a narrow piston in a multimode waveguide). Then a simple asymptotic formula for R can be obtained. With this aim, we separate the resonance term with the index $N-1$ and replace the sum from $n = 0$ to $n = N-2$ by an integral

$$R = \rho c S_0^2/S \Bigg\{ k/\xi_{N-1} + kH/\pi \sum_{n=0}^{N-2} \frac{\pi/kH}{\theta_n \sqrt{1-\alpha_n^2}} \Bigg\} \approx \rho c S_0^2/S \Bigg\{ k/\xi_{N-1} + kH/\pi \int_0^{\alpha_{N-2}} \frac{d\alpha}{\sqrt{1-\alpha^2}} \Bigg\},$$

where $\alpha_n = n\pi/(kH)$. Calculating the integral, we obtain

$$R \approx \rho c S_0^2/S \{ k/\xi_{N-1} + kH/\pi \arcsin \alpha_{N-2} \}. \quad (5)$$

As $kH \longrightarrow \infty$, the relationship $\alpha_{N-2} \approx 1$ becomes valid, and formula (5) takes the form

$$R \approx \rho c (2L)^2 k H_y/2\{1 + 2/(\xi_{N-1} H)\}.$$

When the frequency ω is well away from all waveguide critical frequencies, the radiation resistance of a narrow piston in a wide waveguide coincides with the radiation resistance of the corresponding region of an infinite strip in the free halfspace.

Let us study the behavior of the reactive component of the radiation impedance. In the general case, X can be positive (an elastic-type load) or negative (a mass-type load). For $kL \gg 1$, formula (3) yields

$$X \approx \rho c S_0 \cot(kH)$$

and iX coincides with the impedance of a section of a pipe of the length H and cross-section S_0 closed by a rigid cap at the end.

Now, we calculate X for a narrow piston ($2kL \ll 1$, $2L/H \ll 1$). For this purpose, we expand the standing wave field formed in the layer into the Fourier cosine series

$$\cos[k(H-z)] = 2k\sin(kH) \sum_{n=0}^{\infty} \frac{\cos(\zeta_n z)}{\theta_n \xi_n H},$$

which, at $z = 0$, yields

$$\cot(kH) = \sum_{n=0}^{\infty} \frac{2k}{\theta_n \xi_n^2 H}.$$

By virtue of this relationship, formula (3) for the narrow piston can be reduced to the form

$$X = -\rho c S_0 \sum_{n=N}^{\infty} \frac{2k}{\kappa_n^2 H} \Bigg\{ 1 - \frac{\sinh(\kappa_n L)}{(\kappa_n L)} \exp(-\kappa_n L) \Bigg\}. \quad (6)$$

Separate the resonance term with the index N in formula (6) and replace the sum taken from $n = N+1$ to $n = \infty$ by an integral:

$$X = -2LS_0 \rho c k \Bigg\{ \frac{1}{\kappa_N H} + \frac{1}{\pi} \sum_{n=N+1}^{\infty} \frac{1}{(\kappa_n L)^2} \times \Bigg[1 - \frac{\sinh(\kappa_n L)}{(\kappa_n L)} \exp(-\kappa_n L) \Bigg] \frac{\pi L}{H} \Bigg\}$$

$$\approx -2LS_0 \rho c k \Bigg\{ \frac{1}{\kappa_N H} + \frac{1}{\pi} \int_{\beta_{N+1}}^{\infty} \frac{1}{\gamma^2} \Bigg[1 - \frac{\sinh\gamma}{\gamma} \exp(-\gamma) \Bigg] d\beta,$$

where

$$\pi L/H \ll 1, \quad \beta_n = n\pi L/H,$$

$$\gamma_n = (\kappa_n L) = \sqrt{\beta_n^2 - (kL)^2}, \quad \gamma = \sqrt{\beta^2 - (kL)^2}.$$

Divide the integration interval into the subintervals $\beta_{N+1} < \beta < \beta_{2N}$ and $\beta_{2N} < \beta < \infty$. In the first subinterval, the inequality $\gamma \ll 1$ is valid, and the integrand is approximately equal to $1/\gamma$. In the second subinterval, one can assume $\gamma \approx \beta$. As result of these simplifying transformations, we obtain standard integrals [9],

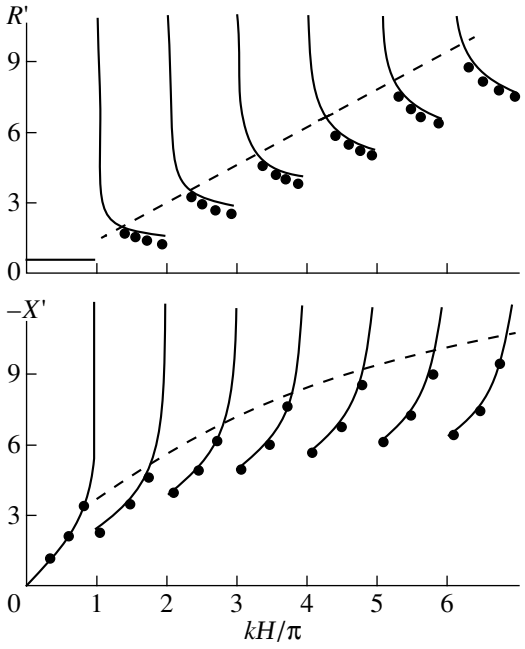

Real and imaginary parts of the normalized piston radiation impedance as functions of kH/π.

which can be calculated to obtain the approximate formula

$$X \approx -2LS_0\rho ck/\pi \times \{\pi/(\kappa_N H) + 1.6 - \ln[2L(\zeta_{N+1} + \kappa_{N+1})]\}. \quad (7)$$

The reactive component of the radiation impedance of a narrow piston in a waveguide always exhibits mass-type behavior; the added mass of this piston is equal to $-X/\omega$. When $kH \longrightarrow \infty$, the relationships

$$\kappa_{N+1} \ll \zeta_{N+1} \approx k$$

are valid, and formula (7) takes the form

$$X \approx -2LS_0\rho ck/\pi\{\pi/(\kappa_N H) + 1.6 - \ln(2kL)\}. \quad (8)$$

When the operating frequency is well away from the waveguide critical frequencies, formula (8) coincides with the expression for the reactive impedance of the corresponding section of an infinite strip in the free halfspace.

Compare the results given by the exact and asymptotic formulas. The figure presents the real and imaginary parts of the normalized radiation impedance $R' = R[S/(\rho c S_0^2)]$ and $X' = X[S/(\rho c S_0^2)]$ as functions of kH/π at $2L/H = 0.05$. The solid lines are calculated from exact formulas (4) and (6); the points represent the results calculated from asymptotic formulas (5) and (7). The results for X' agree for all kH/π, the results for R' converge as kH/π increases (note that asymptotic formula (5) is derived under the condition $kH/\pi \gg 1$). For the sake of comparison, the dashed lines show R' and X' for a strip in free space.

Thus, asymptotic formulas (5) and (7) provide a good description of the real and imaginary parts of the radiation impedance, and they can be used in practice to estimate the efficiency of a piston radiator.

REFERENCES

1. E. Skudzyk, *The Foundation of Acoustics* (Springer, Vienna, 1971; Inostrannaya Literatura, Moscow, 1958), Vol. 1.
2. S. N. Rzhevkin, *A Course of Lectures on the Theory of Sound* (Mosk. Gos. Univ., Moscow, 1960).
3. M. A. Isakovich, *General Acoustics* (Nauka, Moscow, 1973).
4. P. M. Morse and H. Feshbach, *Methods of Theoretical Physics* (McGraw-Hill, New York, 1953; Inostrannaya Literatura, Moscow, 1960), Vol. 2.
5. J. D'hooge, J. Nuyts, B. Bijnens, *et al.*, J. Acoust. Soc. Am. **102**, 78 (1997).
6. W. S. Hwang, J. Acoust. Soc. Am. **101**, 3330 (1997).
7. A. D. Lapin, in *Progress in Construction Physics. Acoustics. Scientific Works of the Construction Physics Research Institute* (Moscow, 1970), No. 1 (13).
8. A. D. Lapin, in *Acoustoaerodynamic Research* (Nauka, Moscow, 1975), pp. 57–62.
9. I. S. Gradshteĭn and I. M. Ryzhik, *Tables of Integrals, Series, and Products*, 4th ed. (Nauka GIFML, Moscow, 1962; Academic, New York, 1965).

Translated by A.D. Khzmalyan

Acoustical Physics, Vol. 46, No. 3, 2000, pp. 370–372. Translated from Akusticheskiĭ Zhurnal, Vol. 46, No. 3, 2000, pp. 430–432.

SHORT COMMUNICATIONS

Negative Role of Paraxial Sound Rays in Lithotripsy

I. A. Urusovskiĭ

Andreev Acoustics Institute, ul. Shvernika 4, Moscow, 117036 Russia

e-mail: bvp@akin.ru

Received July 12, 1999

Methods of sound focusing intended for medical applications have considerably advanced during the last decade [1–5].

As applied to extracorporeal lithotripsy, it is important to reduce the size of the focal spot of focused sound in order to diminish the risk of damage for the tissues surrounding the stone to be disintegrated by intense sound. However, the size of this spot along the axis of the focusing system is much greater than its transverse size. This is caused by the fact that the misphasing of sound waves propagating at small angles to the system axis, i.e., waves corresponding to paraxial sound rays, occurs at relatively large distances. The elimination of paraxial sound rays from the process of formation of the focal spot leads to a reduction of its size and an increase in the sound pressure gradient along the system axis. If the size of the focal spot decreases, the nonlinear distortions of the sound field also decrease. Northeved and Toftkjaer [3] achieved such an elimination by deflecting the paraxial sound rays by a special plate positioned in their path. A focusing system in which paraxial sound rays are totally absent in the vicinity of the focus was described by Reichenberger [5]. In this system, because of a special design, an auxiliary mirror (a cone) deflects the primary beam through an angle of 90°, thus distributing the rays over all directions perpendicular to its axis and directing them at a focusing coaxial parabolic mirror.

Since the effect of the elimination of paraxial rays upon the size of the focal spot has not been studied theoretically until the present time, let us consider this effect by using as an example a linear problem of the field generated at the symmetry axis of a focusing mirror, which has the form of a part of an ellipsoid of revolution, by a harmonic point source of unit volume velocity placed at one of the focuses of this ellipsoid. The mirror is the part of an ellipsoid confined between the planes $x = x_-$ and $x = x_+$, where x is the coordinate along the ellipsoid axis. The axial section of the mirror is shown in Fig. 1. The source of sound is positioned at the focal point $x = \varepsilon a$, where $\varepsilon = \sqrt{1-(b/a)^2}$ is the eccentricity; a and b are the large and small semiaxes of the ellipsoid, respectively; and y is the distance from the axis. The distance from the source to the variable point $\mathbf{r}'(x', y')$ at the mirror surface is equal to $r_1 = a - \varepsilon x'$. The second focus is at the point $x = -\varepsilon a$. We assume that $-\varepsilon a < x_- < x_+$. Since the rays reflected from the mirror and transmitted through the second focus do not get back to the mirror, and the radii of the mirror curvature are large compared to the wavelengths of interest, we may assume (ignoring the contribution of the edge modes originating from the mirror edge to the field at the mirror) that the sound pressure at an acoustically rigid mirror is equal to twice the sound pressure in the incident field $2p_i(\mathbf{r}')$, where $p_i(\mathbf{r}') = -i\rho\omega\exp(ikr_1)/(4\pi r_1)$, ρ is the medium density, ω is the cyclic frequency, and k is the wave number. At a rigid mirror, the normal derivative of sound pressure vanishes. Then, in the approximation at hand, according to the Green formula, the sound pressure $p(x)$ at the mirror axis is reduced to the form

$$p(x) = \int_S 2p_i(\mathbf{r}')\frac{\partial}{\partial n}G(x, \mathbf{r}')dS', \qquad (1)$$

where

$$G(x, \mathbf{r}') = \exp(ikR)/(4\pi R),$$

$R = \sqrt{(x-x')^2 + y'^2}$, $\partial/\partial n$ means differentiation with respect to the inner normal to the mirror, $dS' = 2\pi y'\sqrt{1+(dy'/dx)^2}$ is the element of the area of the

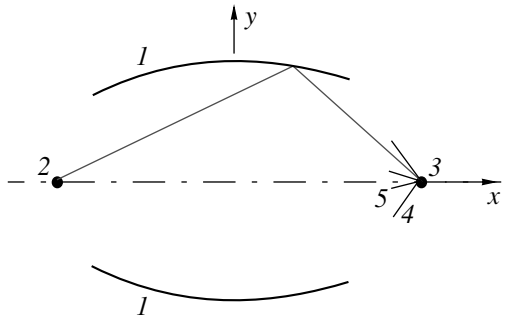

Fig. 1. (*1*) Axial section of a mirror shaped as a part of an ellipsoid. A sound source is positioned at (*3*) its right-hand focus, and sound is focused at (*2*) the left-hand focus. (*4*, *5*) Cones, forming the walls of a horn directing the radiation only at the mirror.

1063-7710/00/4603-0370$20.00

mirror surface, and the integration is performed over the mirror surface from x_- to x_+. From the equation for the ellipsoid

$$(x'/a)^2 + (y'/b)^2 = 1,$$

by differentiation we obtain: $dy'/dx = x'b^2/(y'a^2)$. In this case, we have

$$\frac{\partial R}{\partial n} dS' = -\frac{2\pi}{R} b^2 \left(1 - \frac{xx'}{a^2}\right) dx'.$$

Substituting the determined factors into the integrand in formula (1), we obtain an expression for the field at the mirror axis

$$p(x) = \frac{i}{4\pi}\left(\frac{b}{a}\right)^2 \rho c k \int_{\zeta_-}^{\zeta_+} F(x, x') \left(ika - \frac{a}{R}\right)(a - x\zeta) d\zeta,$$

where

$$F(x, x') = \exp\left[ika\left(1 - \varepsilon\zeta + \frac{R}{a}\right)\right] \frac{1}{(1 - \varepsilon\zeta)R^2},$$

$$\frac{\partial p(x)}{\partial x} = \frac{i}{4\pi}\left(\frac{b}{a}\right)^2 \rho c k \int_{\zeta_-}^{\zeta_+} F(x, x') \left\{\left(ika - \frac{a}{R}\right)\zeta \right.$$

$$\left. + \frac{x - a\zeta}{R}\left(1 - \zeta\frac{x}{a}\right)\left[(ka)^2 + i3ka\frac{a}{R} - 3\left(\frac{a}{R}\right)^2\right]\right] d\zeta.$$

Removal of a part of the mirror does not necessarily mean the loss of a corresponding part of the energy of focused sound. If we place a plane rigid wall of large wave dimensions (the dimensions may be small in comparison with the distance from the source to the mirror) next to the source (on the side of the ellipsoid vertex closest to it) and perpendicularly to the mirror axis, we obtain a doubling of the focused field. We obtain an even greater increase in this field if we replace the plane wall by a rigid cone with the vertex at the point of the source and the generating lines passing through the mirror edge closest to the cone vertex, i.e. to the source. And, finally, the maximum increase in the field can be obtained by installing one more rigid conic screen with the vertex at the point of the source and with the generating lines passing through the far edge of the mirror (see Fig. 1). The dimensions of the conic screens must be large in comparison with the wavelengths of the operating range, but, preferably, small in comparison with the distance from the source to the mirror. In these conditions, almost all radiation is directed at the mirror, the emitted sound propagates within a kind of horn formed by the outer and inner coaxial cones, and the inner cone does not shade the mirror. In this case, the sound field increases by a factor of

$$\frac{4\pi}{\Omega} = \frac{2}{\cos\theta_+ - \cos\theta_-} = \frac{2(a - \varepsilon x_-)(a - \varepsilon x_+)}{aL(1 - \varepsilon^2)}, \quad (2)$$

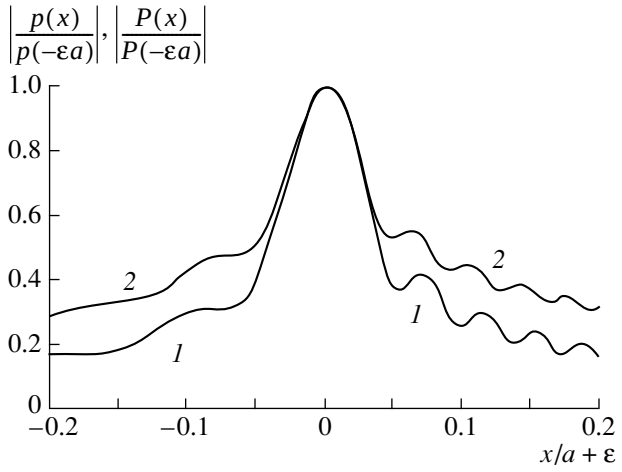

Fig. 2. Relative values of the sound pressure at the axis of a mirror with a truncated (curve *1*) and a nontruncated (curve *2*) part on the side of the source; $ka = 200$.

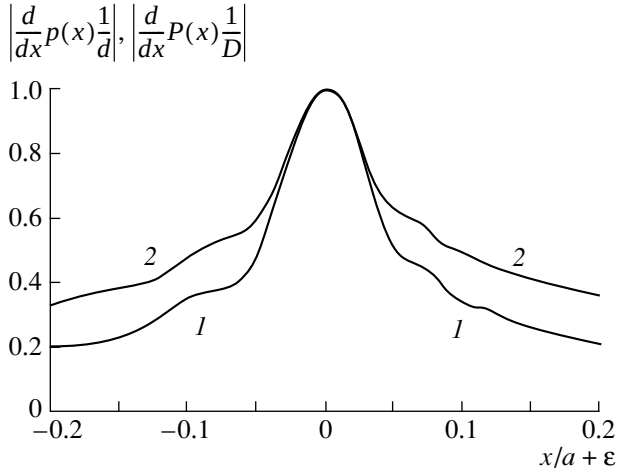

Fig. 3. Curves analogous to those in Fig. 2 for the sound pressure gradient along the mirror axis; *d* and *D* are the maximum values of the corresponding quantities.

where Ω is the spatial angle at which one can see the mirror from the observation point; θ_- and θ_+ are the angles between the x axis and the directions from the source to the corresponding edge; and $L = x_- - x_+$ is the distance between the mirror focuses. For the mirror configuration shown in Fig. 1 ($a/b = 2$, $\varepsilon = \sqrt{3/4}$, $\zeta_-/a = -\varepsilon$, and $\zeta_+/a = \varepsilon$), the right-hand member of formula (2) is equal to 5.8. Curve *1* in Fig. 2 shows the relative absolute values of sound pressure at the mirror axis in the vicinity of the focal point for the mirror parameters specified above and for $ka = 200$. For comparison, curve *2* presents the corresponding values for a mirror with the nontruncated part on the side of the sound source. Figure 3 shows analogous curves for the sound pressure gradient along the mirror axis. The removal of the indicated right-hand part of the mirror leads to a decrease in the dimension of the focal spot

along the mirror axis at the level of half the field amplitude by a factor of 1.58 for sound pressure and by a factor of 1.88 for its derivative along the mirror axis.

REFERENCES

1. O. Weiss, Patent No. 4570634 (Class 128/328); J. Acoust. Soc. Am. **80**, 1001 (1986).
2. Wessels *et al.*, Patent No. 4697579 (Class 128/24A); J. Acoust. Soc. Am. **85**, 2696 (1989).
3. A. Northeved and G. Toftkjaer, Patent No. 4844081 (Class 128/660.03); J. Acoust. Soc. Am. **86**, 1209 (1989).
4. D. Cathignol and O. A. Sapozhnikov, J. Acoust. Soc. Am. **105**, 2612 (1999).
5. H. Reichenberger, Patent No. 4664111 (Class 128/328); J. Acoust. Soc. Am. **86**, 1209 (1989).

Translated by M.L. Lyamshev